Doctoral Dissertation
Doctoral Program in Chemical Engineering (31th cycle)

Continuous Freeze-Drying of Pharmaceuticals

by

Luigi Carlo Capozzi

Supervisors:
Prof. Roberto Pisano, Supervisor
Prof. Antonello A. Barresi, Co-Supervisor

Doctoral Examination Committee:
Prof. Vincenza Calabrò, *Università della Calabria*
Prof. Davide Manca, *Politecnico di Milano*
Prof. Kyuya Nakagawa, *Kyoto University*
Prof. Franco Pattarino, *Università degli Studi del Piemonte Orientale*

Politecnico di Torino
2019

Summary

Continuous manufacturing is becoming increasingly important in pharmaceutical manufacturing. Lyophilization, as a downstream process in the pharma industry, also needs to move from batch to continuous. In this thesis, the drawbacks of batch lyophilization and their impact on the production of drugs and biotech drugs are discussed. Some continuous technologies are currently under development to address the more stringent requirement of quality set by regulatory authorities and enhance process efficiency and profitability. Three new recent concepts of continuous are presented and discussed: Active freeze-drying by Hosokawa Micron BV, continuous lyophilization of spin-frozen unit-doses by RheaVita Ghent University and continuous lyophilization of VISF-based unit-doses proposed by Politecnico di Torino - MIT.

In this work, a new concept for freeze-drying of pharmaceuticals in unit-doses is presented in response to the current trends in the pharmaceutical industry. The configuration studied in this work realizes a continuous freeze-drying process that produces a final product with similar characteristics to the parenteral products and biopharmaceuticals which are already commercialized, avoiding the backward of conventional, batch, freeze-drying. Moreover, this technology is also able to process other dosage forms, e.g., granular products, and alternate packaging, e.g., dual chamber cartridges/syringe and ampoules. This thesis is focused on liquid solutions and particle-based products in vials, which is a promises dosage form that is emerging in the last year for pulmonary and epidermal delivery.

The main idea behind this process is that a constant flow of vials enters and leaves the apparatus, passing through different, specialized, chambers. The process starts from the filling in continuous of vials, which, at that point, are suspended over a moving track and move into the conditioning module. Here, the flow of a cryogenic gas cools down the vial, bringing the product to the desired temperature. At the end of this module, the vial moves into a special chamber, the nucleation chamber, where the pressure is low enough to induce nucleation; VISF was extensively studied by the authors for the batch configuration, and here applied to continuous lyophilization. After that, the vial moves in the freezing module, where, again, a cryogenic gas cools down the vial, achieving the complete solidification of product. It is possible to create customizable freezing protocols by changing the gas velocity, and so, modulating the freezing rate. The vial is then transferred to the drying module by mean of a load-lock system, which allows the passage of the vial from a module at a higher pressure to another at lower pressure without breaking the vacuum. In the drying module, vials are suspended over a track and move in the module following "snake"-type path. The module is constituted of temperature-controlled walls that supply heat to the product via radiation. It is possible to modulate heat transferred to the product by changing wall temperature, and, hence, to carry out both gentle and aggressive cycles. The last step of this process consists of the backfilling and vial stoppering. The entire process

is carried out in continuous, without breaks between phase or manually intervention.

The concept proposed for performing freeze-drying in continuous is a completely new concept which needs to be deeply investigated to demonstrate its feasibility. In this sense, the experimental campaign was accompanied by modeling work. The experimental campaign was essential to give some insight into this new process, i.e., heat and mass transfer phenomena, product quality and cycle time. On the other hand, the modeling tools developed in this thesis have been essential to evaluate the pros and cons of this technology, such as to support the design of the apparatus. The multi-scale approach was, then, seen as a powerful technique to investigate different aspects of continuous lyophilization and its related products. The modeling of freeze-drying at the macro-scale has been coupled with other techniques in order to estimate some product characteristics and better understand mass transport into products during the drying process. More specifically, X-ray micro-computed tomography coupled to CFD and image analysis was used for analyzing bulk material in vials, and discrete element method coupled to CFD for particle-based materials.

In this thesis, it is shown that the main advantages of this technology are the complete control of product structure, which can be reached using VISF, and the perfect control and uniformity of heat supplied to the product during drying. In fact, using VISF, nucleation temperature is the same for every sample, avoiding any differences in freezing history of the product, and, thus, in the final product structure. This technique allows the production of freeze-dried products with the desired morphological attributes by changing the cooling rate after nucleation has occurred. In recent year, VISF has become increasingly popular among researchers, and a wide literature already exists, making VISF a ready-to-use technique also in continuous.

A further advantage is the perfect control and uniformity of heat supplied to products during primary and secondary drying. In fact, no edge-vial effect can be identified any longer because every vial follows the same path and experiences identical conditions. Moreover, contrary to batch lyophilization, small variations in the geometry of the vials have no significant effect on the heat supplied by radiation. Moreover, heat by radiation is completely independent of chamber pressure, allowing to reduce pressure and, hence, increasing the sublimation rate further.

This method draws its strength from producing very uniform products, with the same characteristics because they undergo the same process conditions. It is extremely flexible because can also treat particle-based materials in vials, and it does not have a limitation in the shape of vessels. Our firsts results suggested that the drying duration is shortened by 2 to 4 times, and the total cycle times, including the elimination of dead time.

Acknowledgments

Contents

PART I

Towards continuous lyophilization

1

Introduction

1.1 Current trends in the Pharmaceutical Industry

The pharmaceutical industry is facing a period of significant changes: new drugs and dosage forms, the patent expiration of some high-profit drugs, new competitors and markets, and more stringent standards set by regulatory authorities. To respond to this wave of competing challenge and, at the same time, to a period of stagnant growth rate, many pharmaceutical companies are consolidating their position by demonstrating the clinical and the economic value of their products, adopting new technologies, elevating their quality standards and, finally, rethinking their production and distribution structures (Gautam and Pan, 2016).

If the 1990s are considered the golden era in the pharmaceutical industry because of the revenues of some 'blockbuster' drugs, the current market has seen $120 billion loss due to patent expirations between 2009 and 2014, and $215 billion losses in sales are forecasted for the period 2015-2020. Moreover, the pricing policy of pharmaceutical companies has been questioned not only in some developing countries but also in the UK and USA (Ghinea et al., 2016). In this climate, the pharmaceutical industry is trying to reduce its productions costs and optimize its processes.

From the processing point of view, the main challenge to be faced is the competition for cost-effective drugs and the increasing of regulatory authority scrutiny (Molenberghs, 2017). In this perspective, the strategy adopted by some big Pharma is the so-called "Toyota model", which consists of moving from a traditional production model to highly responsive, lean, manufacturing (Figure 1.1). The next step is naturally to move from batch to continuous production. Some companies are still moving in this direction, also thanks to the support of regulatory authorities, such as U.S. Food and Drug Administration (FDA) and European Medicines Agency (EMA).
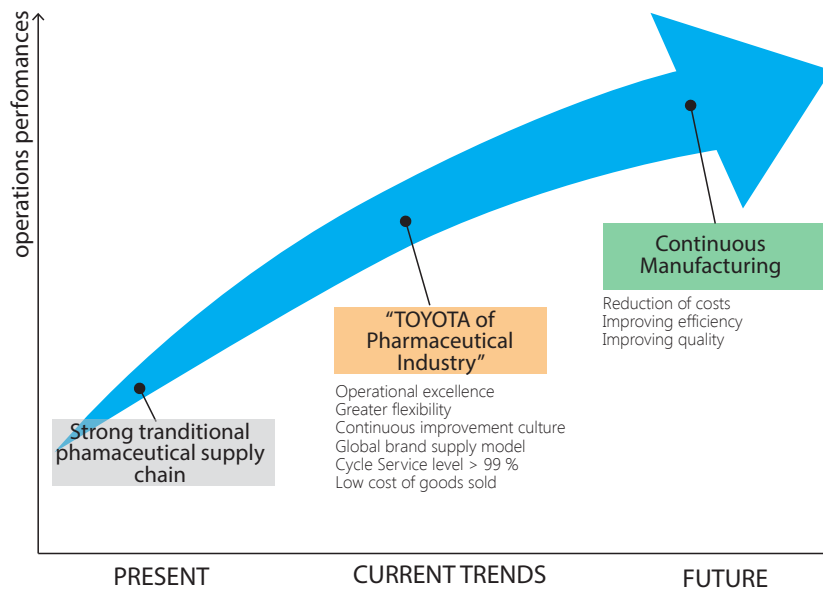
Figure 1.1 Present and current trends in the pharmaceutical industry.

1.2 Continuous manufacturing of pharmaceuticals

The pharmaceutical industry typically uses batch manufacturing, which consists of a series of separate unit operations.

- A batch process is constituted of a predefined sequence of discrete tasks, in which raw products are charged into the system at the beginning and discharged after a preset time.

- In a continuous process, raw materials are continuously fed and discharged during the operation. Continuous processes operate 24 h/day, 7 days/week, with infrequent planned maintenance shutdown. No transient or dead time is present.

The main advantages of continuous processes over batch ones are the following (Kleinebudde et al., 2017):

- Operation flexibility

- Shortening the time to react to changes in market demand

- Reduced scale-up issues, or no scale-up at all

- Real-time quality assurance

- Reduction of footprint, investment, and operative costs

1.2.1 Early implementations of continuous processes in the pharmaceutical industry

There exist a number of potential processes that can significantly benefit from shifting from batch to continuous productions (Leuenberger, 2001; Plumb, 2005; Byrn et al., 2015; Schaber et al., 2011; McKenzie et al., 2006; Poechlauer et al., 2012), and recently a growing number of manufacturers are converting their processes to adopt continuous production for their commercial drugs. Vertex is using a continuous manufacturing technology for the production of the cystic fibrosis drug tablets, Orkambi, since 2015 (Yu, 2016). In 2016, FDA approved of switching from batch to continuous manufacturing of Prezista, a tablet drug produced by Janssen Supply Chain for the treatment of HIV-1 infection (Lee, 2017). That conversion to continuous was the result of a partnership of Janssen Supply Chain with Rutgers University, the University of Puerto Rico and the Engineering Research Center for Structured Organic Particulate Systems (C-SOPS). A further example of a commercial drug produced by continuous manufacturing and already available in the market is Severin, nimesulide tablets produced by Chinoin (Jessen, 2016; Teżyk et al., 2016). In addition to these private initiatives, many pharmaceutical companies have increased their efforts in developing new continuous processes in collaboration with universities. *Novartis-MIT Center for Continuous Manufacturing*, a 10-year research collaboration project between Novartis and Massachusetts Institute of Technology (MIT), developed a fully integrated, continuous manufacturing plant for synthesizing Aliskiren and producing coated tablets (Heider et al., 2014). In Europe, the Centre for Innovative Manufacturing for Continuous Manufacturing and Crystallisation (CMAC) at University of Strathclyde is collaborating with many industries to develop new continuous processes. Other initiatives are ongoing in Singapore, where GlaxoSmithKline is building a continuous manufacturing plant for antibiotics production (Hernandez, 2015), and Amgen introduced a continuous purification process in its production lines.

1.2.2 Regulatory perspectives

Regulatory authorities, such as FDA and EMA, and Pharmaceuticals and Medical Devices Agency (PMDA) are promoting the integration of continuous manufacturing for the pharmaceutical production (Allison et al., 2015). FDA is strongly encouraging the modernization of the pharmaceutical manufacturing, with particular emphasis on Pharmaceutical Quality Systems (PQS), Quality by Design (QbD), Process Analytical Technology (PAT) and Real Time Release Testing (RTRT), and, of course, continuous manufacturing (Woodcock, 2014). As concerns this technology, FDA formally encouraged the pharmaceutical community to move toward continuous processing in order to improve efficiency and manage variability (FDA, 2015; Lee, 2017). In 2016, the US government's National Science and Technology Council (NSTC) included continuous manufacturing of pharmaceuticals among the priority objectives of the US industry, and as a candidate for Federal investment and public-private collaborations (Subcommittee for Advanced Manufacturing of the National Science and Technology Council, 2016). Although there is not an EU initiative that subsidizes continuous manufacturing in the pharmaceutical industry, EMA repeatedly confirmed his favorable position to innovation in manufacturing, and specifically to continuous approaches (Hernán, 2017). In Japan, PMDA is encouraging industry to introduce innovative continuous

manufacturing technologies based on science- and risk-based approaches (Matsuda, 2016).

1.3 Motivation for the continuous freeze-drying

The future trends and challenges of the pharmaceutical freeze-drying will see the emerging of new technologies for the continuous production of lyophilized products (Langford et al., 2018), new personalized drugs (Schellekens et al., 2017) and new dosage forms (Korpus and Friess, 2017), and new strict requirements on product quality and standardization (Molenberghs, 2017), see Fig. 1.2.

Moving from batch to continuous process

Integrated processing with fewer steps

Smaller equipment/Shorter processing times

More flexible operation

Production of personalized drugs and new dosage forms

Quick design of lyophilized products with desired characteristics

Standardization and product quality

Increase of the requirements of quality, safety and efficiency set by regulatory authorities

Quality by Design
Design of cycles (freezing and drying) that produce dried products with the desired final attributes, to predict its variability within a production and the losses due to undesired off-target products

Process Analytical Technology
Design, analize and control manufacturing through timely measurements of critical quality and performance attributes of raw and in-process materials and processes with the goal of ensuring final product quality

Figure 1.2 The future paradigm of freeze-drying of pharmaceuticals

Continuous processing is the next paradigm of pharmaceutical manufacturing and, hence, of lyophilization as a downstream operation. The motivation for shifting from robust, well known, batch processes to a completely new, continuous process resides on the advantages that continuous technology can give in terms of process agility and flexibility, product quality, processing costs, and efficiency. Modern pharmaceutical manufacturing is still moving in the direction of assuring a robust QbD, PAT, PQS, and RTRT, to guarantee the quality of final products. In this perspective, continuous manufacturing can address the new stringent requirements set by regulatory authorities better than batch processes (Allison et al., 2015).

In recent years, the lyophilization community is working on the improvement of processing control, scale-up, product quality and uniformity, and APIs stability (Lim et al., 2016; Goshima et al., 2016). New PAT tools have been developed, such as software sensors, wireless product temperature monitoring systems, infrared thermography, and miniature mass spectrometers (Vollrath et al., 2017; Fissore, 2017; De Beer et al., 2009; Pisano et al., 2014; Velardi et al., 2008; Barresi et al., 2009b). Despite these continuous improvements, batch lyophilization still presents serious limitations, which are discussed in the following chapter.

1.4   Overview of thesis

1.4.1   Scope of the present thesis

In this work, a new concept for freeze-drying of pharmaceuticals in unit-doses is presented in response to the current trends in the pharmaceutical industry. The configuration studied in this work realizes a continuous freeze-drying process that produces a final product with similar characteristics to the parenteral products and biopharmaceuticals which are already commercialized, avoiding the backward of conventional, batch, freeze-drying. Moreover, this technology is also able to process other dosage forms, i.g., granular products, and alternative packaging, e.g., dual chamber cartridges/syringe and ampoules. This thesis is focused on liquid solutions and particle-based products in vials; the latter is a promising dosage form that is emerging in the last year for pulmonary and epidermal delivery.

1.4.2   Questions to be answered

There are some crucial questions to be answered to demonstrate the feasibility of the new concept of continuous lyophilization proposed in this thesis. In the years spent working on this research project, academics and professionals from the industry helped us with their questions and doubts which came out during meetings and conferences. I have, so, decided to put all these questions together and resume them into 8 main questions. The questions to be answered are the following,

1. Is continuous manufacturing really useful and necessary in the pharmaceutical industry and, specifically, in freeze-drying?

2. What are the solutions proposed for performing freeze-drying in continuous or semi-continuous modes? What the pros and cons of these technologies?

3. In what consists the continuous technology proposed in this thesis? What are the main problems that it aims to solve?

4. Is continuous freeze-drying of suspended-vial able to control heat transferred to the product and reduce its variability?

5. Is continuous freeze-drying of suspended-vial able to reduce the vial-to-vial variability of product structure? Is it able to design products with specific characteristics?

6. Is continuous freeze-drying of suspended-vial able to reduce drying time and the variability of sublimation rates? Is also able to reduce variability in final residual moisture?

7. Is continuous freeze-drying of suspended-vial beneficial for sensitive APIs?

8. Can continuous freeze-drying of suspended-vial respond to the request of flexibility and modularity of the pharmaceutical industry? Is it possible to reduce the footprint and increase throughput?

1.4.3 Methodology

The concept proposed for performing freeze-drying in continuous is a completely new concept which needs to be deeply investigated to demonstrate its feasibility. In this sense, the experimental campaign was accompanied by modeling work. The experimental campaign was essential to give some insight into this new process, i.e., heat and mass transfer phenomena, product quality and cycle time. Moreover, in some industry environments, along the lines of the saying *"a simulation is something nobody believes, except the person who made it; an experiment is something everybody believes, except the person who made it"*, the experimental proof is believed a "harder" evidence that the simulation one. On the other hand, the modeling tools developed in this thesis have been essential to evaluate the pros and cons of this technology, such as to support the design of the apparatus. Although this work may be seen as the result of a linear research process, the reality is that experiments and simulations came together, and they were used to decide how moving forward a certain pathway or step back.

The multi-scale approach was, then, seen as a powerful technique to investigate different aspects of continuous lyophilization and its related products, see Fig. 1.3.
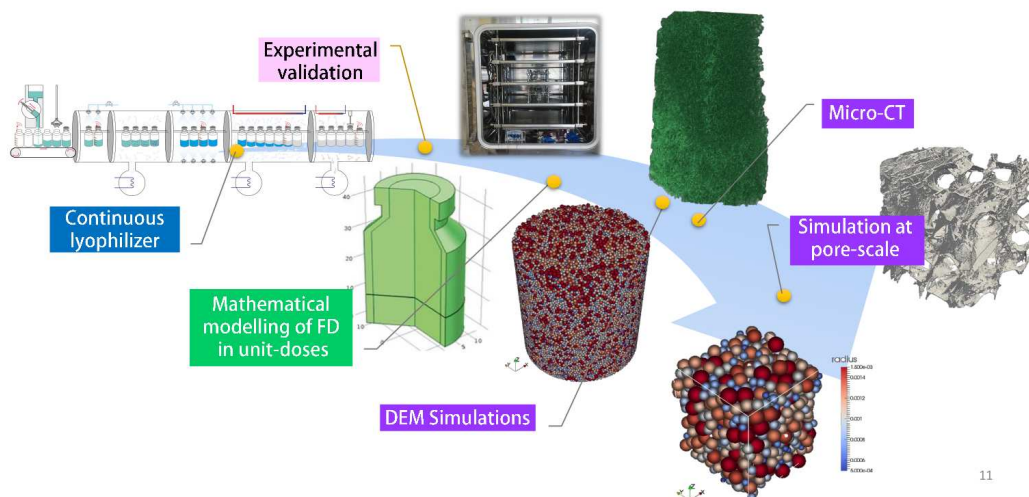
Figure 1.3   Schematic of the project implementation and scales.

The simulation at the pore-scale was used to estimate some product characteristics and better understand mass transport into products during the drying process. More specifically, X-ray micro-computed tomography (μ-CT) coupled to CFD was used for analyzing bulk material in vial, and DEM coupled to CFD for particle-based materials. After that, mathematical modeling of the process at the macro-scale was implemented to better design the process without using long experimental tests.

Once these modeling tools have been developed, they were used to compare the continuous technology with the existing batch processes or some alternative continuous processes proposed in the literature; a preliminary economic analysis will also be presented at the end of the thesis.

1.4.4   Outline of the work

This thesis is divided into four part.

Part I introduces the reader to the pharmaceutical industry and freeze-drying. *Chapter 1* surveys major trends in the pharmaceutical industry and discusses the role of continuous manufacturing for improving the quality and profitability of pharmaceutical products. *Chapter 2* introduces the general concepts of freeze-drying, briefly surveys the current trends in the research, shows the drawbacks of batch freeze-drying and, finally, examines early and current attempts to realize a continuous freeze-drying process.

Part II presents the new concept of continuous freeze-drying. *Chapter 3* has a specific focus on the technology proposed for moving from batch to continuous. *Chapter 4* concerns the feasibility study of continuous freeze-drying by using a functional prototype that reproduces very similar conditions expected in the continuous apparatus.

Part III concerns the multi-scale modeling of continuous freeze-drying and its related products from the macro- to the pore-scale. *Chapter 5* is focused on the modeling at the macro-scale of continuous freezing, and *Chapter 6* of continuous drying. *Chapter 7* deals with the modeling of lyophilized products at the pore-scale using X-Ray Computed Tomography coupled with CFD to understand product characteristics better. *Chapter 8* studies the characteristics of particle-based products using DEM and CFD.

In *Chapter 9* of **Part IV**, batch and continuous technologies are compared for some case studies, with particular emphasis on the economic aspects. The thesis ends with the final remarks and conclusions.

1.4.5   Contribution of the thesis

This dissertation contributes to the area of emerging technologies for the production of pharmaceutical and biopharmaceuticals, and in particular to the continuous manufacturing. Specifically, it introduces a novel continuous freeze-drying process as an alternative to conventional batch one. Since the control of product quality is one of the most important features of that technology, this dissertation introduces innovative methods for predicting and analyzing product structure.

Some of the results presented in this thesis have been already presented in the following papers and conference proceedings,

- Capozzi, L.C., Boccardo, G., Barresi, A. A., Pisano, R. (2015). Coupled bullet physics and computational fluid dynamics as a tool for modelling the freeze-drying of microparticles. In: *Proceedings of the 5th European Drying Conference, October 21–23, Budapest*, pp. 75–83.

- Pisano, R., Barresi, A.A., Capozzi, L.C., Novajra, G., Oddone, I., Vitale Brovarone, C. (2015). Modeling and characterization of intra-vial heterogeneity of lyophilized products using X-ray computed tomography. In: *Proceedings of the 5th European Drying Conference, October 21–23, Budapest*, pp. 314–321.

- Capozzi, L.C., Pisano, R. (2016) Freeze-drying of suspended vials: a first step toward continuous manufacturing. In: *Proceedings of the 2nd International Symposium on Continuous Manufacturing of Pharmaceuticals, Cambridge (MA, USA), September 26–27, 2016*

- Capozzi, L.C., Boccardo, G., Barresi, A. A., Pisano, R. (2016). Computer-aided property estimation of micro-particles in packed-beds for freeze-drying applications. In: *Proceedings of the 20th International Drying Symposium, Gifu (Japan), August 7–10, 2016*, pp. 1–8.

- Pisano, R., Capozzi, L.C., Trout, B.L., (2017). Continuous freeze-drying and its relevance to the pharma/biotech industry. In: *Proceedings of Integrated Continuous Biomanufacturing III, Cascais (Portugal), September 17–21, 2017*, pp. 1–26.

- Capozzi, L.C., Arsiccio, A., Pisano, R. (2017). Looking inside the 'black box': freezing engineering for assuring quality of freeze-dried biopharmaceuticals. In: *Proceedings of the 8th International Conference on Lyophilization and Freeze-Drying, Havana, (Cuba), April 24–28, 2017*.

- Pisano, R., Napoletano, F., Paladini, A., De Beer, T., Capozzi, L.C. (2017). Influence of the freezing protocol on the activity of lactate dehydrogenase after freeze-drying. In: *Proceedings of the 6th European Drying Conference - EuroDrying 2017, June 19-21, 2017*.

- Pisano, R., Barresi, A.A., Capozzi, L.C., Novajra, G., Oddone, I., Vitale Brovarone, C. (2017). Characterization of the mass transfer of lyophilized products based on X-ray micro-computed tomography images. *Drying Technology*, 35(8), 933-938.

- Pisano, R., Capozzi, L. C. (2017). Prediction of product morphology of lyophilized drugs in the case of Vacuum Induced Surface Freezing. *Chemical Engineering Research and Design*, 125, 119-129.

- Capozzi, L.C., Pisano, R. (2018). Looking inside the black box: Freezing engineering to ensure the quality of freeze-dried biopharmaceuticals. *European Journal of Pharmaceutics and Biopharmaceutics*, 129, 58–65.

- Capozzi, L.C., Arsiccio, A., Sparavigna, A. C., Pisano, R., Barresi, A.A. (2018). Image Segmentation and 3D reconstruction for improved prediction of the sublimation rate during freeze drying. In: *Proceedings of the 21st International Drying Symposium - IDS 2018., Valencia (Spain), September 11–14, 2018*, pp. 411–418.

- Capozzi, L.C., Montalbano, G., Novajra, G., Vitale Brovarone, C. Pisano, R., CFD modelling based on X-Ray microtomography reconstruction of lyophilized products. In: Freeze Drying of Pharmaceuticals & Biopharmaceuticals, Garmisch-Partenkirchen (Germany), September 18–21, 2018.

- Capozzi, L.C., Barresi, A.A., Pisano, R. (2019). Supporting data and methods for the multi-scale modelling of freeze-drying of microparticles in packed-beds. *Data in Brief*, 22, 722–755.

- Capozzi, L.C., Barresi, A. A., Pisano, R. (2019). A multi-scale computational framework for modeling the freeze-drying of microparticles in packed-beds. *Powder Technology*, 343, 834-846.

- Capozzi, L.C., Trout, B.L., Pisano, R. (2019). From batch to continuous: freeze-drying of suspended vials for pharmaceuticals in unit-doses. *Industrial & Engineering Chemistry Research*, 58.4: 1635-1649.

Acronyms

API Active Pharmaceutical Ingredient; **CFD** Computational Fluid Dynamics; μ**-CT** X-Ray Micro Computed Tomography; **DEM** Discrete Element Method; **EMA** European Medicines Agency; **FDA** U.S. Food and Drug Administration; **PAT** Process Analytical Technology; **PMDA** Pharmaceuticals and Medical Devices Agency; **PQS** Pharmaceutical Quality Systems; **QbD** Quality by Design; **RTRT** Real Time Release Testing.

References

Allison, G., Cain, Y. T., Cooney, C., Garcia, T., Bizjak, T. G., Holte, O., Jagota, N., Komas, B., Korakianiti, E., Kourti, D., et al. (2015). Regulatory and quality considerations for continuous manufacturing. May 20–21, 2014 Continuous Manufacturing Symposium. *Journal of Pharmaceutical Sciences* 104 (3), pp. 803–812.

Barresi, A. A., Pisano, R., Fissore, D., Rasetto, V., Velardi, S. A., Vallan, A., Parvis, M., and Galan, M. (2009b). Monitoring of the primary drying of a lyophilization process in vials. *Chemical Engineering and Processing: Process Intensification* 48 (1), pp. 408–423.

Byrn, S., Futran, M., Thomas, H., Jayjock, E., Maron, N., Meyer, R. F., Myerson, A. S., Thien, M. P., and Trout, B. L. (2015). Achieving continuous manufacturing for final dosage formation: Challenges and how to meet them. May 20–21, 2014 Continuous Manufacturing Symposium. *Journal of Pharmaceutical Sciences* 104 (3), pp. 792–802.

De Beer, T., Vercruysse, P., Burggraeve, A., Quinten, T., Ouyang, J, Zhang, X, Vervaet, C., Remon, J. P., and Baeyens, W. (2009). In-line and real-time process monitoring of a freeze drying process using Raman and NIR spectroscopy as complementary process analytical technology (PAT) tools. *Journal of Pharmaceutical Sciences* 98 (9), pp. 3430–3446.

FDA (2015). *Advancement of Emerging Technology Applications to Modernize the Pharmaceutical Manufacturing Base Guidance for Industry*. Draft guidance.

Fissore, D. (2017). Model-based PAT for quality management in pharmaceuticals freeze-drying: state of the art. *Frontiers in Bioengineering and Biotechnology* 5, p. 5.

Gautam, A. and Pan, X. (2016). The changing model of big pharma: impact of key trends. *Drug Discovery Today* 21 (3), pp. 379 –384.

Ghinea, N., Lipworth, W., and Kerridge, I. (2016). Propaganda or the cost of innovation? Challenging the high price of new drugs. *BMJ: British Medical Journal (Online)* 352.

Goshima, H., Do, G., and Nakagawa, K. (2016). Impact of ice morphology on design space of pharmaceutical freeze-drying. *Journal of Pharmaceutical Sciences* 105 (6), pp. 1920–1933.

Heider, P. L., Born, S. C., Basak, S., Benyahia, B., Lakerveld, R., Zhang, H., Hogan, R., Buchbinder, L., Wolfe, A., Mascia, S., et al. (2014). Development of a multi-step synthesis and workup sequence for an integrated, continuous manufacturing process of a pharmaceutical. *Organic Process Research & Development* 18 (3), pp. 402–409.

Hernandez, R. (2015). Continuous manufacturing: a changing processing paradigm. *BioPharm International* 28 (4), pp. 20–27.

Hernán, D. (2017). Continuous manufacturing: challenges and opportunities. EMA perspective. In: *Proceedings of the 3rd FDA/PQRI Conference on Advancing Product Quality, March 22–24, 2017, Rockville, MD, USA*.

Jessen, V. (2016). Continuous manufacturing, A qualitative analysis of challenges and opportunities for introducing continuous manufacturing in pharmaceutical companies. In: *Proceedings of the ISPE Network Meeting - Biotechnology CoP. Continuous Manufacturing, June 16, 2016, Bagsværd, Denmark*.

Kleinebudde, P., Khinast, J., and Rantanen, J. (2017). *Continuous Manufacturing of Pharmaceuticals*. Vol. 7703. John Wiley & Sons.

Korpus, C. and Friess, W. (2017). Evaluation of different holder devices for freeze-drying in dual-chamber cartridges with a focus on energy transfer. *Journal of Pharmaceutical Sciences* 106 (4), pp. 1092–1101.

Langford, A., Bhatnagar, B., Walters, R., Tchessalov, S., and Ohtake, S. (2018). Drying technologies for biopharmaceutical applications: Recent developments and future direction. *Drying Technology* 36 (6), pp. 677–684.

Lee, S. (2017). Present and future for continuous manufacturing: FDA perspective. In: *Proceedings of the 3rd FDA/PQRI Conference on Advancing Product Quality, March 22–24, 2017, Rockville, MD, USA*.

Leuenberger, H. (2001). New trends in the production of pharmaceutical granules: batch versus continuous processing. *European Journal of Pharmaceutics and Biopharmaceutics* 52 (3), pp. 289–296.

Lim, J. Y., Kim, N. A., Lim, D. G., Kim, K. H., Choi, D. H., and Jeong, S. H. (2016). Process cycle development of freeze drying for therapeutic proteins with stability evaluation. *Journal of Pharmaceutical Investigation* 46 (6), pp. 519–536.

Matsuda, Y. (2016). Continuous Manufacturing: PMDA Perspective. In: *International Symposium on Continuous Manufacturing of Pharmaceuticals, September 26-27, 2016, MIT, Cambridge, MA, USA.*

McKenzie, P., Kiang, S., Tom, J., Rubin, A. E., and Futran, M. (2006). Can pharmaceutical process development become high tech? *AIChE Journal* 52 (12), pp. 3990–3994.

Molenberghs, G. (2017). Discussion: Is the FDA in need of a major change in the way it regulates? *Biostatistics* 18 (3), pp. 408–410.

Pisano, R., Fissore, D., and Barresi, A. A. (2014). A new method based on the regression of step response data for monitoring a freeze-drying cycle. *Journal of Pharmaceutical Sciences* 103 (6), pp. 1756–1765.

Plumb, K. (2005). Continuous processing in the pharmaceutical industry: changing the mind set. *Chemical Engineering Research and Design* 83 (6), pp. 730–738.

Poechlauer, P., Manley, J., Broxterman, R., Gregertsen, B., and Ridemark, M. (2012). Continuous processing in the manufacture of active pharmaceutical ingredients and finished dosage forms: an industry perspective. *Organic Process Research & Development* 16 (10), pp. 1586–1590.

Schaber, S. D., Gerogiorgis, D. I., Ramachandran, R., Evans, J. M., Barton, P. I., and Trout, B. L. (2011). Economic analysis of integrated continuous and batch pharmaceutical manufacturing: a case study. *Industrial & Engineering Chemistry Research* 50 (17), pp. 10083–10092.

Schellekens, H., Aldosari, M., Talsma, H., and Mastrobattista, E. (2017). Making individualized drugs a reality. *Nature biotechnology* 35 (6), p. 507.

Subcommittee for Advanced Manufacturing of the National Science and Technology Council (2016). *Advanced Manufacturing: A Snapshot of Priority Technology Areas Across the Federal Government.* Report.

Teżyk, M., Milanowski, B., Ernst, A., and Lulek, J. (2016). Recent progress in continuous and semi-continuous processing of solid oral dosage forms: a review. *Drug Development and Industrial Pharmacy* 42 (8), pp. 1195–1214.

Velardi, S. A., Rasetto, V., and Barresi, A. A. (2008). Dynamic parameters estimation method: advanced manometric temperature measurement approach for freeze-drying monitoring of pharmaceutical solutions. *Industrial & Engineering Chemistry Research* 47 (21), pp. 8445–8457.

Vollrath, I., Pauli, V., Friess, W., Freitag, A., Hawe, A., and Winter, G. (2017). Evaluation of heat flux measurement as a new process analytical technology monitoring tool in freeze drying. *Journal of pharmaceutical sciences* 106 (5), pp. 1249–1257.

Woodcock, J. (2014). Modernizing pharmaceutical manufacturing–Continuous Manufacturing as a key enabler. In: *International Symposium on Continuous Manufacturing of Pharmaceuticals, May 2021, 2014, MIT, Cambridge, MA, USA.*

Yu, L. (2016). Continuous manufacturing has a strong impact on drug quality. *FDA Voice, April 12, 2016.*

<div align="right">

2

</div>

From batch to continuous freeze-drying

This chapter provides a brief overview of freeze-drying and its main features, with particular regard to the pharmaceutical applications. A brief historical perspective relating the discovery of various technological solutions to carry out the lyophilization process is presented, starting from the early, rudimentary, configuration to modern, sophisticated, applications. The fundamentals of freeze-drying are discussed, and particular emphasis is given to the industrial process, with a focus on the drawbacks of batch lyophilization and the future perspective. A brief literature review of continuous freeze-drying is provided to help the reader to better understand the context in which this work evolved.

2.1 Hystory of freeze-drying from early applications to current market perspective

Lyophilization, or freeze-drying, is a gentle process of drying based mainly on the sublimation of solvent, usually ice.

Ice can be removed from a frozen material via sublimation only if the partial pressure of water in the atmosphere is very low and there is a source of heat for sublimating ice. These conditions can be realized only in specific parts of the earth, such as in high mountains, and was completely unknown in most ancient civilization until the early 1900s.

Some traces of this process could suggestively already be observed in the prehistoric times of Eskimos (1250 BC), who dehydrated fish in the cold Arctic winds, or the process that ancient Peruvian Incas (1250-850 BC) used for preserving potatoes above Machu Picchu, at 3,000 m above sea level. Also, the ancient population of The Andes, the Buddhist monks of Mount Koya or Vikings, might have taken advantage of the cold and dry weather conditions, or the relatively low atmospheric pressure of the place where they were used to live on, to perform a rudimentary process of lyophilization (Varshney and Singh, 2015; Franks and Auffret, 2008).

Except for these examples within history and myth, it was in 1890 that the lyophi-

lization process was first tested by the German histologist Richard Altmann (Altmann, 1894), but only in the 1920s lyophilization became an established laboratory tool for preserving live microorganisms or tissues (Jennings, 1999). In 1933, S. Mudd and E. W. Flosdorf at University of Pennsylvania performed the first aseptic freeze-drying of blood serum, and, in their paper published in 1935, they called that material *lyophile* (from the Greek $\lambda\acute{v}o\varsigma$ and $\varphi\iota\lambda\epsilon\iota\nu$, solvent-loving) because of their great ability to rehydrate again (Flosdorf and Mudd, 1935).

In 1945, freeze-drying for large-scale production of penicillin was developed, and the process was performed using a single chamber, a mechanical refrigeration apparatus and vacuum pump, similar to the design used today (Flosdorf et al., 1945).

Early commercial lyophilized products were hemin by Abbott and corticotro-phin by Parker Davis and Rorer Pharmaceuticals. In the 1970s, new antibiotics were produced as lyophilized (penicillin G procaine by Wyeth Development, aminoglycosides by Wyeth, cephalosporins by Lilly, cefazolin by SKB and Lilly, β-lactams vancomycin HCl by Lilly, tetracycline by Pfizer), vaccines (IBV H-52 and H-120 for infectious bronchitis), oncolytics (dactinomycin by Merck, cisplatin by BMS), two corticosteroids by Upjohn Company, hydrocortisone sodium succinate by Cortef, and methylpred-nisolone sodium succinate by Solu-Medrol. In the 1980s and 1990s, new products were introduced for bacterial (Azactam by BMS, imipenem/ cilastatin by Merck) and viral infections (acyclovir by GSK, ganciclovir by Syntex/Roche, interferons ra-2A by Roche, interferons ra-2B by Schering), treatment for multiple sclerosis (interferon rB1b by Byers) and heart attack (alteplase by Genentech), and new vaccines (Cervarix by GSK for HPV treatment, Pentacel by Sanofi Pasteur for DPT + polio and hemophilus influenza b, Zostavax by Merck for herpes zoster (Trappler, 2013). Fig. 2.1 shows the freeze-dried drugs approved from 1990 to 2014.

Nowadays, roughly 40% of commercial biotherapeutics, including recombinant proteins, plasma, vaccines, and antibodies are freeze-dried (Akers, 2016). Moreover, according to BCC Research, 16% of the top 100 pharmaceutical drugs are lyophilized (LaTorre-Snyder, 2017). The single most lucrative product in 2017 was Enbrel (etanercept), a biologic product for autoimmune disease by Amgen and Pfizer, which generated global sales of $9 billion and that will lose its patent protection in 2019. Other examples of highest-revenue products were Remicade (infliximab) produced by Johnson and Johnson and Merck ($8 billion; patent expires in 2018); Herceptin (trastuzumab) a monoclonal antibody produced by Roche ($6.5 billion; patent expires in 2019); Copaxone (glatiramer acetate) manufactured by Teva Pharmaceuticals ($4.2 billion, patent expired in 2014).

As a result of the rapid development of biopharma industry and the introduction of new drugs and biosimilars, also lyophilization equipment market is forecasted to double its value from $2.7 billion to $4.8 billion in 2020, with a compound annual growth rate of 8.5% (Keenan, 2014).

2.2 Pharmaceutical freeze-drying

Lyophilization, or freeze-drying, is a drying process based on the removal of ice or other frozen solvents via sublimation, and removal of water molecules bonded to the solid matrix via desorption.

A typical lyophilization cycle of pharma/biopharma drugs consists of three main
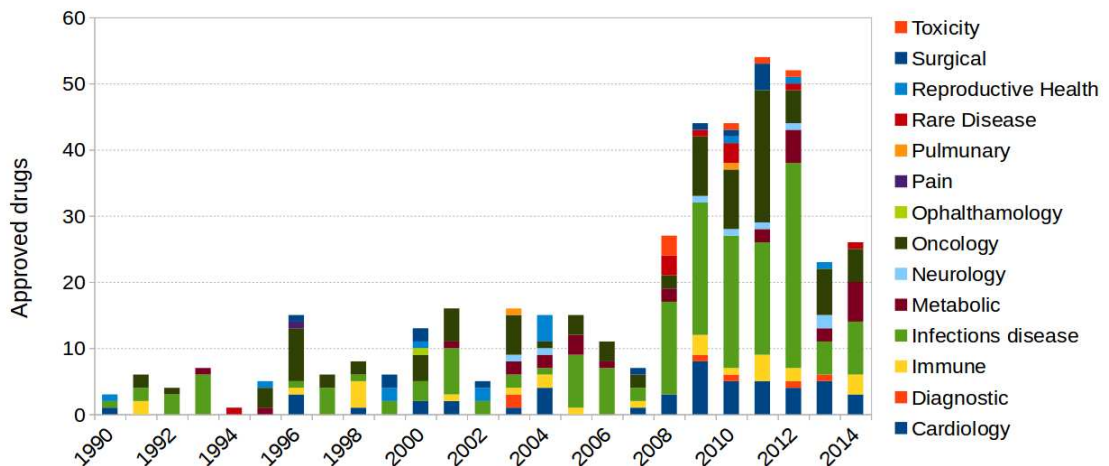
Figure 2.1 Freeze-dried drugs approved by year. Data from Debus (2017).

stages:

1. Freezing: the solution is cooled down until complete solidification occurs. During freezing, water is separated from drug and excipients, forming multiple phases separated by interfaces between ice and the other solid components. This process may induce stresses in some protein drugs destabilizing or deactivating them. Moreover, it has a significant influence on the drying time because it determines the structure of the product, and, hence, its mass transfer resistance during the drying phase.

2. Primary drying: chamber vacuum is reduced, and heat is supplied from heating shelves to promote ice sublimation. Heat input and sublimation rate have to be adjusted to keep product temperature below the collapse temperature and, hence, avoid back melting, puffing or collapse of the product.

3. Secondary drying: the residual water, mostly unfrozen and adsorbed in the solid matrix of the product, is removed by desorption. The critical attribute to be controlled is the residual moisture content within the product, while the adjustable process variables are shelf temperature and secondary drying duration.

The fishbone of lyophilization shown in Fig. 2.2 points out the complexity of the process and the variables to be controlled. Some of these drawbacks are presented in the following sections.

2.2.1 Fundamentals of freezing

Freezing is the principal dehydration step, as the solvent is separated from the solute, creating multiple solid phases. The liquid solution is cooled down much below the equilibrium freezing temperature until the solution is completely frozen. Freezing is a crucial phase because it influences the physicochemical properties and the morphology of the product. Moreover, it determines the drying performance, the product characteristics and their inter- and intra-vial variability, and, finally, can affect the stability of many APIs (Tang and Pikal, 2004).
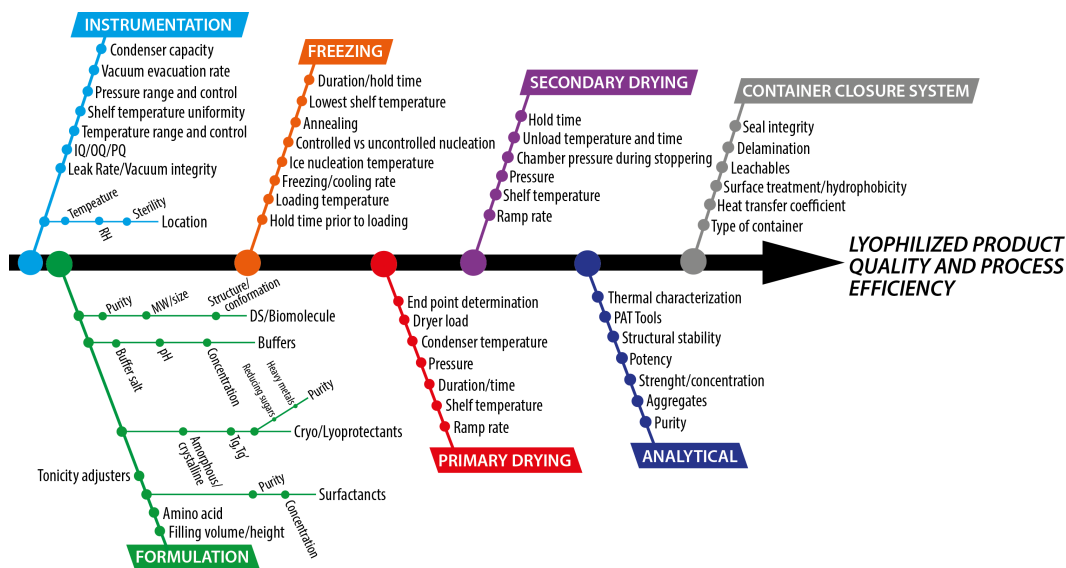
Figure 2.2 Fishbone of freeze-drying process based on Korang-Yeboah (2017).

As shown in Fig. 2.3a, freezing involves (AB) the supercooling of the solution, (BC) the formation of stable nuclei and (CD) crystal growth. At the end of this process, once the product is completely frozen, the temperature drops (E).
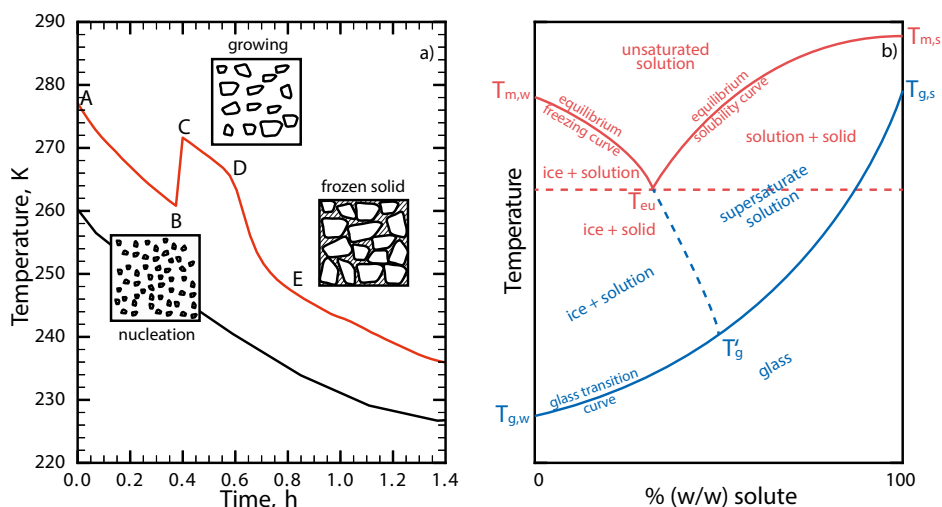
Figure 2.3 a) Temperature profile of a solution being frozen during shelf-ramped freezing (the red line represents the product temperature and black line the shelf temperature); b) State diagram for water (w)/solute (s) systems.

Supercooling is the difference between the temperature at which stable nuclei form and the equilibrium freezing temperature. During supercooling, which is a metastable, non-equilibrium phase, the solution is cooled to a sub-zero temperature without liquid-solid transition occurs. It is reported that supercooling ranges from 10 to 15 °C in a no-GMP environment (Liu, 2006) and 30 °C or more in a GMP manufacturing equipment with a low particulate environment (Tang and Pikal, 2004; Konstantinidis et al., 2011); supercooling depends on solution property and the process conditions.

During this phase, water molecules form clusters that break up rapidly because they are thermodynamically unfavorable, but their probability of reaching the critical radius increases as the degree of supercooling increases (Franks and Auffret, 2008). The temperature/time at which stable nuclei form is stochastic. In lyophilization process, heterogeneous nucleation takes place instead of homogeneous nucleation because of the presence of nucleants, such as foreign impurity, dust particles, the surface of the container or even the sites on large molecules in solution (Kasper and Friess, 2011).

Crystal growth follows the nucleation event. The growing process consists in the addition of water molecules to the crystal interface; this process is controlled by the latent heat release and the cooling rate. In this context, it is essential to point out the difference between cooling rate, defined as the rate at which the solution is cooled down, and the freezing rate, which is the post-nucleation cooling rate (Searles et al., 2001). As a general rule, slow cooling produces bigger ice crystals than a fast cooling protocol (Hottot et al., 2007).

As ice crystals grow, the solute concentration in the interstitial regions increases until a critical concentration is reached, leading to eutectic freezing or vitrification, see Fig. 2.3b. Some solutes, i.g., mannitol, glycine, sodium chloride or phosphate buffer, crystallize when the freeze-concentrated solution is below the eutectic melting temperature (T_{eu}); different polymorphs or hydrates can co-exist in the solid matrix depending on the process conditions or the starting formulation. On the other hand, some other solutes, such as sucrose, do not crystallize forming an amorphous solid matrix; in this case, ice crystals continue to grow also below the eutectic melting temperature at the expenses of the solution, which becomes increasingly supersaturated and viscous. This process ends when the solution reaches the glass transition temperature (T'_g).

A further fundamental temperature that characterizes a formulation is the critical temperature (T_c), which is defined as the temperature at which the frozen matrix loss its physical structure (Kasper and Friess, 2011).

Characterization of formulations

The first step in the design of a lyophilization cycle is always the determination of T'_g, T_{eu}, and T_c. In the common practice, the critical temperature is determined using differential scanning calorimetry (DSC) for detecting T_{eu} and T'_g and freeze-drying microscopy (FDM) for T_c. Other methods can be used for characterizing the formulation, i.e., differential thermal analysis (DTA), thermo electric analysis (TEA), dynamic mechanical thermal analysis (DMA), thermo mechanical analysis (TMA), dielectric analysis (DEA), and thermally stimulated current spectrometry (TSC) (Rey, 2016).

Freezing methods

Shelf-ramped freezing. The freezing method that is most often used in lyophilization is *shelf-ramped freezing*, which consists of cooling down vials placed on the shelves by decreasing the shelf temperature linearly. The cooling rate is usually between 0.1 and 5 °C, and the final shelf temperature is between -50 and -40 °C. Usually, the final temperature is held for 1-2 h to assure complete solidification. Moreover, before starting the cooling ramp, the vials usually are equilibrated at 5-10 °C for 15-30 min to

assure more homogeneous freezing (Kasper and Friess, 2011; Tang and Pikal, 2004).

Pre-cooled shelf freezing. A further possibility is to use *pre-cooled shelf method*, which consists of loading the vials on pre-cooled shelves; here, shelf temperature is set at the final shelf temperature, i.g., -40 °C.

Quench freezing. It is reported that *quench freezing method* can be advantageous in some specific cases when a very high freezing rate is needed, i.g., to reduce the detrimental effect of a freeze-concentration induced phase separation on protein secondary structure (Heller et al., 1999). Quench freezing consists of immersing vials into a cryogenic fluid (liquid nitrogen or propane) or in a dry ice bath; the freezing is very fast, i.e., within 2 min, but totally uncontrolled and results in the formation of small heterogeneous ice crystals (Geidobler and Winter, 2013).

Annealing. After freezing is completed, it is possible to perform a further step called *annealing*, which consists in increasing the product temperature between T'_g and T_{eu} and hold products at that temperature for several hours. Annealing promotes the crystallization of solutes and further growth of ice crystals (Tang and Pikal, 2004)

Spin freezing. *Spin-freezing* consists in rotating the vials with the solution along with their longitudinal axis and, at the same time, immerse them in a cryogenic fluid or a dry ice bath. The product is, so, spread all around the vial wall side, forming a cylindrical shell of 1-5 mm thick (De Meyer et al., 2015). The advantage of this method lies in the sharp increase of sublimation rate during primary drying due to the higher surface area compared to traditional products in vials. On the other hand, there is poor or no control of freezing and product heterogeneity.

Gap freezing. Gap freezing consists of inserting a thermally insulating spacer between the vials and the shelf and cooling down vials mainly by radiation. It is reported that the nucleation temperature is higher and products show larger pores compared to traditional shelf-ramped freezing (Kuu et al., 2013). Unfortunately, its implementation in the industry appears to be challenging (Geidobler and Winter, 2013).

Methods to induce ice nucleation

Vacuum-induced surface freezing (VISF). The idea of inducing ice formation by evaporative self-cooling of the sample was firstly proposed by Kramer et al. (2002). It consists of reducing the local temperature at the water surface at sub-zero temperature, creating a thin film of ice that triggers the nucleation in the entire sample. VISF, as proposed by Oddone et al. (2014), consists of (i) cooling down the product at given temperature (T_n), (ii) maintaining the product at T_n for 1 hour, (iii) decreasing chamber pressure for a short time to induce nucleation, (iv) cooling down the product until complete solidification occurs; further details are reported in (Oddone, 2016; Arsiccio et al., 2018b). Using this procedure, nucleation is induced by evaporation of water at the top of the solution and then propagates downward. Once nucleation has occurred, ice crystals begin to grow until T'_g is reached. During this phase, the freezing front moves upward, forming three different regions, an icy zone at the bottom and a liquid zone at the top, divided by a mushy zone where ice crystals are in suspension in the

undercooled solution.

High Pressure Shift Freezing / depressurization technique. In the high-pressure shift freezing method, also known as depressurization method, the pressure is increased to lower the thermodynamic freezing temperature. Once the sample is cooled down at the equilibrium freezing temperature corresponding to that pressure, the pressure is quickly released to the atmospheric value. At that point, the equilibrium freezing temperature increases and the ice nucleation takes place. The method as patented by Gasteyer et al. (2007) consists of pressurizing the chamber at about 3.5 bar, cooling down and equilibrating the solutions and, finally, depressurizing the chamber to induce nucleation.

Ice fog technique. This technique was proposed by Rowe (1990) and consists of perturbating the solution within vials with ice fog. The ice fog is generated by injecting cold nitrogen into the chamber and triggering the condensation of air moisture into small ice particles. These particles penetrate into the vials and, in contact with the solution surface, induce nucleation. Many variations of this method are reported in the literature and aim to mitigate the drawbacks related to the up-scale of the process from laboratory to industrial equipment.

Ultrasound induced freezing. Ice nucleation can be induced using ultrasounds, as they are able to lead to the cavitation of the solution and produce gas bubbles into the whole volume; once these bubbles collapse, ice starts nucleating. This method was introduced in lyophilization by Nakagawa et al. (2006), but its diffusion at the industrial level is difficult because up-scaling is quite complicated.

Impact of the freezing on the final product

Sample morphology. The freezing conditions directly influence the number, size, and shape of ice crystals, and, consequently, the dried structure. In particular, the main parameters that set ice crystal properties are nucleation temperature T_n (or equivalently, the degree of supercooling) and freezing rate, which is related to the rate of ice formation. As a general rule, a high degree of supercooling results in a frozen matrix with a high number of small crystals, while a low degree of supercooling results in a small number of larger ice crystals (Geidobler and Winter, 2013). Besides, also the crystal shape is affected by the degree of supercooling, i.e., sponge-like structure in the case of a high degree of supercooling vs. lamellar pores for samples with a low degree of supercooling. The freezing rate has a great impact on crystal size; the higher the freezing rate, the smaller crystal size (Kasper and Friess, 2011). To some extent, product morphology can be controlled using VISF and choosing the nucleation temperature. To give you an example, inducing nucleation at $5\,°C$ as proposed by Kramer et al. (2002) produces chimney-like pores of more than 200 µm as diameter, whereas if T_n is below $-5\,°C$ the pore size ranges from 80 to 150 µm (Pisano, 2018).

Vial-to-vial variability. Vial-to-vial variability in the product characteristics has a tremendous impact on product quality and the process efficiency, and it is mainly connected to the stochastic nature of nucleation. In the GMP conditions, supercooling ranges up to $30\,°C$ or more (Tang and Pikal, 2004; Konstantinidis et al., 2011), pro-

19

ducing high product variability and poor control of the product quality. Freezing affects specifically vial-to-vial variability in the product structure, and, finally the sublimation rate, final residual moisture, and activity recovery for those APIs affected by surface-induced denaturation. On the other hand, VISF dramatically reduces vial-to-vial variability because nucleation is induced at the same temperature in the whole batch, and all the samples have the same thermal history (Pisano, 2018).

Intra-vial variability. Intra-vial variability mainly depends on a non-uniform growth rate during freezing and in the distribution of solutes across the vial. This variability is especially present when there is not a uniform temperature in the sample (Liu et al., 2005). As shown by Oddone et al. (2016), also VISF in some circumstances, such as high filling height or high nucleation temperature, can generate intra-vial variability within the samples; the perfect control of freezing conditions is, then, required to reduce intra-vial variability.

Primary drying performance. Freezing determines product structure and, finally, pore size, shape, and connectivity of the dried matrix. During primary drying, sublimation rate is strongly affected by product structure, as it determines the resistance to vapor flow from the sublimation interface to the top of the product (R_p) and, consequently, primary drying duration. Generally speaking, the smaller the crystals (equivalently, the pores) the higher the mass transfer resistance during primary drying and the longer the primary drying duration.

Secondary drying performance. Opposite to primary drying, in the secondary drying phase, the main mechanism of water removal is the desorption from the solid matrix. The desorption rate is correlated to the thickness of the wall of the interstitial matrix and its surface area, which means that the larger are the ice crystals the lower is the specific surface area (SSA) and, thus, the lower desorption rate (Passot et al., 2009). VISF usually produces samples with much lower SSA compared to uncontrolled nucleation, lowering desorption rate during secondary drying.

Protein activity. The main stress factors that can impact protein stability are cold denaturation, ice formation, and freeze-concentration. Cold denaturation is often considered marginal in lyophilization, whereas the ice formation, and so the creation of an ice-water surface, and the freeze-concentration, which leads to the increase of reaction rates, the shift in the pH value and the phase separation, are usually considered the main causes of protein denaturation (Bhatnagar et al., 2007; Arsiccio et al., 2019). Adsorption onto the ice-water interface is considered the predominant cause of protein denaturation so that the lower SSA, the higher the activity recovery (Jiang and Nail, 1998); VISF is then able to increase activity recovery after freeze-drying compared to uncontrolled nucleation (Pisano et al., 2017a; Fang et al., 2018).

2.2.2 Primary drying

Once the solution in all vials is completely frozen, the solvent (usually water) is removed via sublimation by lowering chamber pressure to values that typically range between 5 and 20 Pa, and supplying heat from the heating shelves. During primary drying, ice sublimates producing a dried cake, which needs to be rigid enough not to

collapse and guarantee pharmaceutical elegance, e.g., avoiding excessive shrinkage of the cake. To avoid melting or collapse, the product is maintained below its collapse temperature, which is usually some degree above its glass transition temperature for amorphous solutes, or below the eutectic temperature for crystalline solutes (Tang and Pikal, 2004). Usually, a target product temperature is chosen as the maximum temperature that product can reach during the primary drying; this temperature is between 2 and 5 °C below collapse temperature. Optimized cycles aim to achieve this temperature as quickly as possible and hold it constant throughout primary drying.

Heat and mass transfer

During primary drying, water vapor moves from the sublimation interface and condense again over the cold surfaces of the condenser. The dried cake offers the highest resistance to vapor (R_p), as the vapor moves through an interconnected network of pores with a size in the micron range, whereas the contribution of the stopper (R_s) and the chamber (R_c) to the total resistance (R_T) is usually considered negligible, see Fig. 2.4.

The sublimation rate is defined as the mass of ice that sublimates per unit time and can be expressed as (Pikal et al., 1984),

$$\frac{\mathrm{d}m}{\mathrm{d}t} = A_\mathrm{p}\frac{p_{\mathrm{w},i} - p_{\mathrm{w},c}}{R_\mathrm{p}} \tag{2.1}$$

where $\mathrm{d}m/\mathrm{d}t$ is the sublimation rate, A_p is the internal cross-sectional area of the vial, $p_{\mathrm{w},i}$ is the vapor pressure over ice and $p_{\mathrm{w},c}$ is the partial pressure of water in the chamber.

Heat is supplied to the product by temperature-controlled shelves to make ice sublimate; the heat flow is defined by,

$$\dot{Q}_\mathrm{d} = A_\mathrm{v}K_\mathrm{v}(T_\mathrm{fluid} - T_\mathrm{b}) \tag{2.2}$$

where A_v is the outer cross-sectional area of the vial, K_v is the overall heat transfer coefficient, T_fluid is the heating fluid temperature and T_b it the temperature at the bottom of the vial.

As shown in Fig. 2.4, heat is supplied by various mechanisms in parallel, i.e., (i) direct contact between the shelf and vial bottom at the points of contact, (ii) gas conduction through the gap between the shelf and the bottom of the vial and (iii) radiation from the shelves. The heat transfer coefficient between the heating shelf and the vial bottom reads,

$$K_\mathrm{v}' = K_\mathrm{c} + K_\mathrm{g} + K_\mathrm{r} \tag{2.3}$$

If the conduction in the glass at vial bottom and the resistance to heat transfer through the shelf are also considered, the overall heat transfer coefficient can be expressed as,

$$K_\mathrm{v} = \left(\frac{1}{K_\mathrm{v}'} + \frac{s_\mathrm{gl}}{\kappa_\mathrm{gl}} + \frac{1}{k_\mathrm{s}}\right)^{-1} \tag{2.4}$$
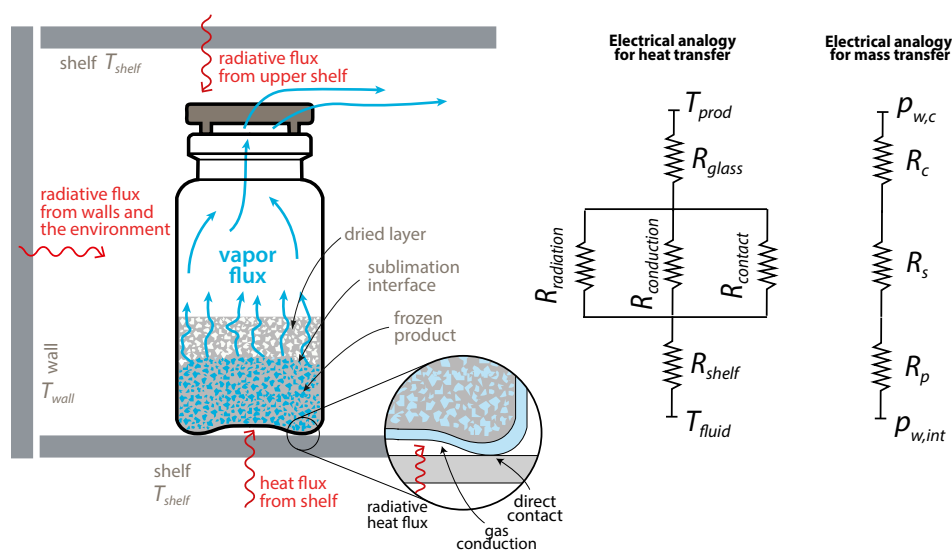
Figure 2.4 Schematic of heat and mass transfer in freeze-drying of pharmaceuticals.

Process Analytical Technology for monitoring primary drying

In QbD paradigm, PATs are fundamental tools for monitoring the process by measuring in-line and in real-time the critical process parameters (CPPs) and, finally, to guarantee the quality target product profile (QTPP) (Lawrence et al., 2014). Shelf and product temperature, chamber pressure, freezing, and heating ramp are examples of CPPs to measure during drying.

In freeze-drying of pharmaceuticals in unit-doses, PAT can be divided into methods that monitor single vials, i.g., temperature probe, conductivity probe, microbalance, in-line NIR/Raman probe, and methods that monitor the entire batch, i.g., pressure-rise test (PRT), barometric temperature measurement, mass spectroscopy and tunable diode laser absorption spectroscopy (TDLAS) (Fissore et al., 2018).

Product temperature monitoring. Monitoring and control of product temperature are crucial to assure product quality and avoid product collapse or excessive shrinkage. Alongside thermocouples and resistance temperature detectors (RTDs), non-invasive methods have also been proposed so far, e.g., methods based on the PRT. Various algorithms were proposed for coupling the pressure rise measurement in the chamber when the chamber is isolated from the condenser, and the product temperature, defined as an average value within the batch. The most known algorithms are Manometric Temperature Measurement (MTM) by Milton et al. (1997), the Dynamic Pressure Rise by Liapis and Sadikoglu (1998), the Pressure Rise Analysis (PRA) by Chouvenc et al. (2005), the Barometric Temperature Measurement (BTM) by Oetjen et al. (1999) and the Dynamic Parameters Estimation (DPE) by Velardi et al. (2008). Also, TDLAS can estimate the product temperature from the mass flow rate (Schneid and Gieseler, 2009). A further non-invasive method for monitoring product temperature consists of thin-film thermocouples (TFTCs) deposited onto the external wall of vials by low-pressure plasma processes (Oddone et al., 2015).

Primary drying endpoint. The detection of the end point of primary drying can be

achieved using several methods. Some of those are based on the measurement the gas composition in the drying chamber, i.e., comparing pressure measurement (Pirani vs. capacitance manometer), dew point monitoring (electronic moisture sensor), H_2O concentration from TDLAS and gas plasma spectroscopy. Product temperature response, condenser pressure, and PRT can be used as alternative methods (Patel et al., 2010). The comparative pressure measurement of Pirani and the capacitance manometer is the most popular among the methods for determining the primary drying end-point and consists in measuring the absolute pressure in the drying chamber using a capacitance manometer (i.e., MKS Baratron) and compare it with the value read by the Pirani gauge. The Pirani gauge is a thermal conductivity gauge and, so, its reading can be wrong if the composition of the gas within the drying chamber is different from that used for the calibration of the sensor, which is generally composed of 100% of N_2. Since the conductivity of water vapor is 1.6 times higher than nitrogen, the ratio of the Pirani and Baratron pressure detects an onset point, which indicates a change in the composition in the chamber from water vapor to nitrogen, and a offset, which indicates that gas in the chamber is essentially nitrogen as sublimation is not occurring anymore. Although the offset is often indicated as the end-point of primary drying, soak time is usually added to have a safety margin before starting secondary drying.

2.2.3 Secondary drying

During primary drying, ice is removed via sublimation, but the most part of water adsorbed on the solid surface is not removed during primary drying. The amount of residual moisture (RM) at the end of the primary drying is between 15 and 20 % for amorphous products (Hatley and Mant, 1993) and about 5-10 % for crystalline materials (Patel et al., 2010). At high RM, the glass transition temperature of the amorphous excipients results lowered, presumably leading to the collapse of the product. The perfect control of RM at the end of the secondary drying is fundamental as a high value in RM increases the rate of chemical degradation (Wang et al., 2015), but overdrying might also reduce the stability of some APIs (Cameron, 1997).

The steps in the removal of water from the dried cake are: (i) molecular diffusion of water from the interior to the surface of the glassy matrix, (ii) desorption from the solid interface, (iii) diffusion through the porous matrix, (iv) transport from vial headspace to the condenser. As shown by Pikal et al. (1990), transport in the vapor state (iii, iv) is not rate limiting as nor cake thickness or chamber pressure significantly affect drying rate. Desorption is presumably the controlling mechanism in the case of crystalline excipients; on the other hand, it is not clear whether (i) diffusion in the solid matrix or (ii) the desorption is the controlling mechanism in the case of amorphous products. The desorption rate is often described using one of the following equations (Fissore et al., 2011),

$$\frac{\mathrm{d}C_\mathrm{w}}{\mathrm{d}t} = -k_d(C_\mathrm{w} - C_\mathrm{w,eq}) \tag{2.5a}$$

$$\frac{\mathrm{d}C_\mathrm{w}}{\mathrm{d}t} = -k_d C_\mathrm{w} \tag{2.5b}$$

where the kinetic constant depends on the formulation, temperature and specific surface area of pores in the solid matrix. Its dependence on temperature follows an

Arrhenius-type equation,

$$k_d = k_0 \exp\left(-\frac{E_a}{RT}\right) \tag{2.6}$$

Although, as a general practice, chamber pressure is lowered during secondary drying, there is no evidence that pressure affects drying rate (Pikal et al., 1990).

Process Analytical Technology for monitoring secondary drying

Moisture content. The monitoring of residual moisture of the products during secondary drying can be achieved using a "samples thief", which is a sample periodically taken from the chamber and analyzed off-line using Karl Fisher titration, gravimetric analysis or NIR spectroscopy. PRT (Fissore et al., 2011) and TDLAS can also be used to measure the desorption rate (Schneid et al., 2011).

2.3 Batch equipment

Typically, a batch freeze-drier is composed of a chamber with controlled-temperature shelves connected to a cooling system, an ice condenser, and one or more vacuum pumps. The plant has to be equipped with control and monitoring instrumentation, cleaning, and sterilization system, and the stoppering system (Fig. 2.5a).

Pharmaceutical plants have to satisfy GMP requirements, which guarantee that the pharmaceutical products administrated to humans or animals meet the following attributes: (i) safety, (ii) identity, (iii) strength, (iv) purity and (v) quality (Akers, 2016). Therefore, freeze-drying of pharmaceuticals is strictly carried out under aseptic and dust-free conditions, see Fig. 2.5b.

Laboratory scale plants are often used during the pre-clinical phase; in this phase, no humans are involved in the experimentation. In the clinical phase, a pilot scale freeze-drier is used to produce the doses to be administrated to humans. In this phase, the drying chamber is about 0.1-0.2 m^3, and GMP conditions have to be satisfied. At the end of Phase III, final product specifications and process validation batch production are finalized in order to submit a new drug application (NDA). In this final phase, the scale-up of the process from pilot to commercial scale is required to guarantee the consistency and the robustness of the process. Commercial freeze-dryer can process from 50,000 to 100,000 vials and have a shelf area up to 20 m^2 (Akers, 2016; Oetjen, 1999; Kharaghani et al., 2000; Wang et al., 2015).

2.4 Research trends in freeze-drying

While much attention was placed on the advancement of continuous pharmaceutical manufacturing, the freeze-drying community is making extensive efforts to improve process robustness and achieve the stringent requirements of quality, safety, and efficiency set by regulatory authorities. In this perspective, research on freeze-drying was mainly focused on process control, monitoring (Fissore et al., 2011; Pisano et al., 2014; Pisano et al., 2016; De Beer et al., 2009; Oddone et al., 2015; Velardi et al., 2008; Barresi et al., 2009b; Barresi et al., 2009a; Pisano et al., 2010; Fissore et al., 2010), optimization (De Beer et al., 2011) and scale-up (Pisano et al., 2013a; Fissore and
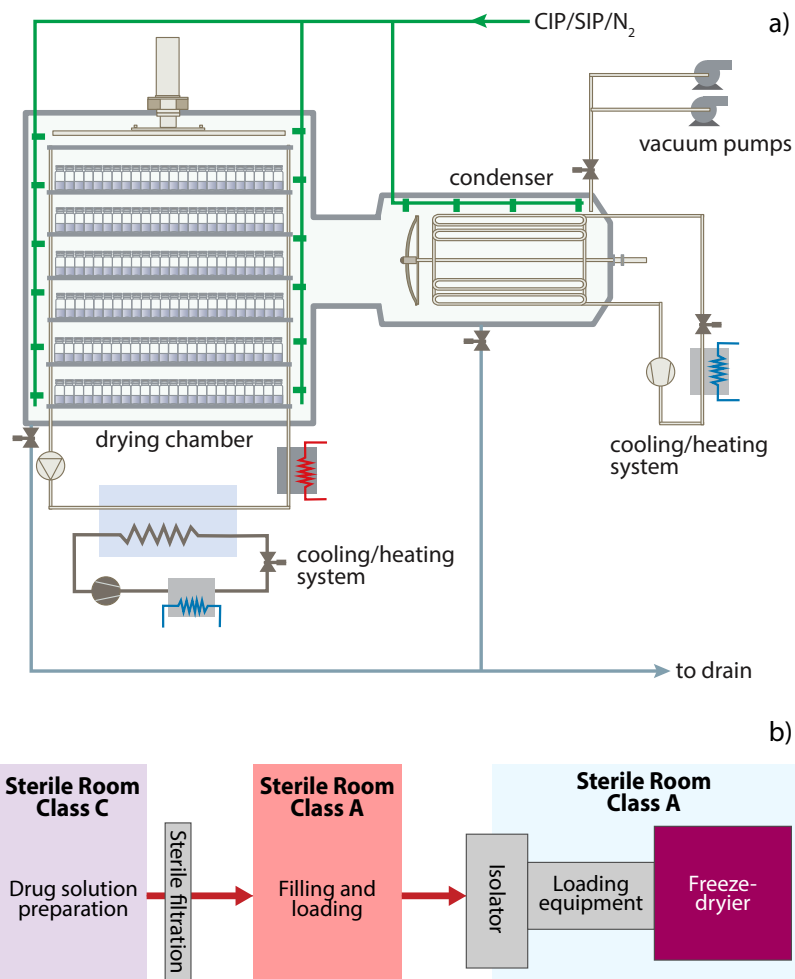
Figure 2.5 Schematic of a typical industrial freeze-drying plant.

Barresi, 2011; Pisano et al., 2013a). Many efforts have been made to improve the quality and uniformity of the product (Oddone et al., 2016; Goshima et al., 2016), as well on the development of cycles that guarantee the stability of APIs (Lim et al., 2016). Despite these efforts, conventional freeze-drying still presents serious limitations (Patel and Pikal, 2011) that call for a change in the mindset, shifting from conventional, batch, processes to innovative, continuous, modular ones. It is clear that freeze-drying needs to be completely rethought to be more integrated into the chain of production of drugs, more flexible in responding to variations in market needs and allowing online monitoring of product quality and overcome batch-to-batch variability (Lee et al., 2015).

2.5 Drawbacks of batch freeze-drying

2.5.1 Processing and dead times

The first drawback of lyophilization is the long processing time, which typically ranges from few hours, in the case of 'aggressive' cycles, to more than a week, in the case of

'gentle', conservative, cycles used for extremely heat-sensitive products. Besides the long processing time, batch lyophilization have some essential ancillary operations: (a) vial filling, loading, stoppering and unloading of vials in the drying chamber, (b) cleaning-in-place operation (CIP), (c) sterilization-in-place operation (SIP), (d) filter integrity test, (e) leak test of the unit, (f) venting/backfilling and (g) condenser defrosting. These operations need to meet the GMP guidelines and the stringent requirements set by regulatory authorities for sterile products.

Vial filling, loading, and unloading are performed using automatic systems with a capacity of 10,000-30,000 vials per hour (Oetjen, 1999), which means that, for a production of 100,000 vials, loading and unloading can range between 6 and 10 hours. Other auxiliary operations include line clearance, defrosting, CIP, SIP, water intrusion test, and leak testing, which take between 7 and 13 hours (Kharaghani et al., 2000). Thus, the overall downtime has a severe impact on the overall processing time, decreasing the efficiency and profitability of the process.

2.5.2   Control of the freezing process

Freezing is the first step of lyophilization, and it is fundamental in determining many product characteristics, of the final product such as the cake structure, the polymorph composition, and the stability of many APIs (Peters et al., 2016). Freezing can be responsible for batch-to-batch and vial-to-vial heterogeneity because of the stochastic nature of nucleation. The heterogeneity in the product structure causes large heterogeneity in the drying rate, the final moisture content, and in some cases in the API activity (Peters et al., 2016; Searles et al., 2001; Oddone et al., 2016). This effect can be mitigated using freezing control techniques, such as Vacuum Induced Surface freezing (VISF), ice-fog, high-pressure shift freezing/depressurization technique (Oddone et al., 2014; Rambhatla et al., 2004; Gasteyer et al., 2007), although significant concerns remain on the scaling and transfer them from laboratory/pilot to the industrial scale.

2.5.3   Primary and secondary drying

The non-uniformity of heat transfer within the batch is a crucial issue of primary drying because it has implications for product quality and performances of the process. During drying, heat is supplied to the product by direct contact between the shelf and the vial, conduction through the gas between the shelf and the bottom of the vial and radiation. As extensively shown in the literature, a small variation in vial geometry (Pikal et al., 1984; Scutellà et al., 2017) or the non-perfect planarity of the shelf have a significant impact on heat transfer. Vial position in the chamber represents a further cause of non-uniformity of heat transfer; the so-called edge-vial effect. In fact, vials placed at the side of the batch receive much more heat than those placed in the center (Pikal et al., 2016). Other issues in the batch apparatus are the non-uniformity in shelf surface temperatures (Cheng et al., 2014) and the non-uniformity of pressure in the drying chamber (Alexeenko et al., 2009; Barresi et al., 2010; Rasetto et al., 2010).

The non-perfect control of heat transferred to the product and, thus, of its temperature, have important implications on the final quality of the product, and in the robustness and efficiency of the process. When the product temperature exceeds the target temperature, the product could lose its structure, and the entire batch can be

rejected because of the lack of pharmaceutical elegance or, even worst, APIs activity is compromised (Wang et al., 2015; Patel et al., 2017).

Moreover, the non-uniformity of product structure and heat transfer cause a non-uniformity of the residual moisture in the product at the end of the secondary drying (Pikal and Shah, 1997). The control of this properties is, in certain cases, fundamental for the long storage of products without losing APIs activity (Breen et al., 2001; Chang et al., 2005). In batch lyophilization, this variability remains even if the product structure is well controlled, e.g., using the VISF protocol (Oddone et al., 2017).

2.5.4 Batch-to-batch variability

Similar to other batch-wise processes, lyophilization has to address batch-to-batch variations in product quality and characteristics. To mitigate these unpredictable variations, one might think that the perfect control of process parameters, i.e., chamber pressure or shelf temperature, is enough to maintain consistent product quality. Unfortunately, changes from batch-to-batch can be determined by a multitude of factors, such as ingredients or materials provided by new suppliers, different equipment with different performances, changes in the equipment efficiency due to aging, and, of course, changes introduced by operators (Galan, 2016).

2.5.5 Scale-up

During pre-clinical studies, lyophilization is usually carried out in small laboratory equipment, using from few to hundred vials per batch. At the end of this phase, the clinical and market production requires bigger apparatus, pilot or commercial scale equipment, assuring GMP conditions and preserving safety and efficacy of the product. Scale-up plays, at that point, a crucial role in developing a robust and efficient cycle, which can support process validation. Many approaches have been developed so far, but they all required extensive experimental campaigns, a perfect knowledge of the equipment characteristics and, usually, modeling tools. In recent years, Quality by Design (QbD) approach has been extensively used for the scale-up of cycles to mitigate the risks connected with the production of drugs (Pisano et al., 2013a; Pisano et al., 2013b; Van Bockstal et al., 2017a; Fissore et al., 2018).

2.6 Current status and perspectives in continuous freeze-drying

The idea of continuous lyophilization dates back to at least the 1940s when a pilot plant for continuous lyophilization of juice was proposed (Sluder et al., 1947), but only in the 1970s a fully continuous line, the Conrad freeze-dryer, was successfully introduced in the industry for the production of instant coffee (Goldblith et al., 1975). In the food industry, continuous lyophilization is evolving and more often applied to industrial, large-scale, productions.

Until now, many ideas regarding continuous lyophilization of pharmaceuticals have been proposed (Oetjen et al., 1971; Bruttini, 1993; Rey, 1999), but none of them has been successfully applied in the industry because of their complexity, the difficulty of guarantee product sterility or handling safety problems.

To give an example of an early application, Rey (1999) proposed a process in which the initial solution is frozen into spherical granules of a given size. This could be

done, for example, by dropping regular droplets of the liquid into a counter-current of cold air, as illustrated in Fig. 2.6. The granules are then loaded continuously, through a vacuum lock, onto a heated conveyor in a drying chamber. The tray may vibrate, for example, thus inducing a continuous motion of the granules towards the dryer exit. Here, a transfer lock discharges them into a second chamber, where secondary drying is performed. In this chamber, granules may be exposed to a well-controlled infrared or microwave heating to promote desorption. Finally, the dried particles are distributed into previously sterilized vials that are then capped. Thanks to the small size of the granules, the freeze-drying times can be reduced significantly, and, in that dispersed form, reconstitution would be very fast. However, the application of Rey's concept to very small granules (below a millimeter) would be technically difficult. Moreover, ensuring the sterility of the product would not be easy in the proposed apparatus, and, thus, Pisano et al. (2015) investigated the application of an e-beam sterilization treatment after the freeze-drying process. However, this treatment still requires further studies, as it may deactivate the active ingredients.
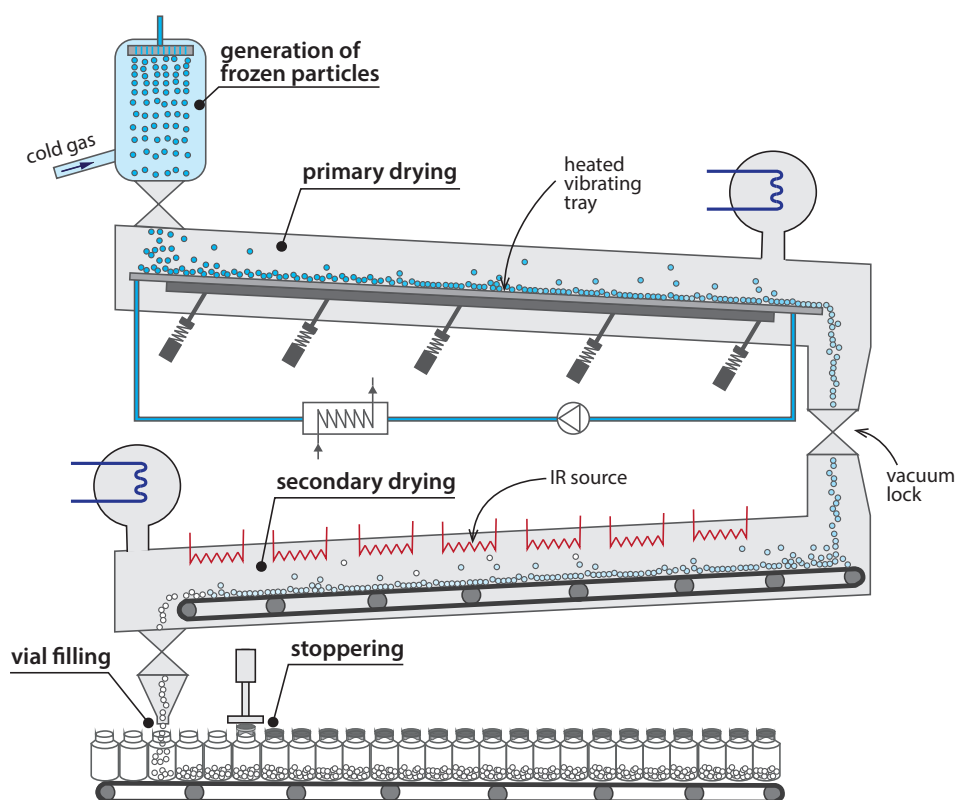
Figure 2.6   Scheme of the continuous freeze-dryer concept proposed by Rey (1999).

In recent years, three continuous technologies are emerging, which aim to address the drawbacks associated with batch lyophilization: lyophilization of granular material proposed by Hosokawa Micron BV (Van der Wel, 2005), and two continuous concepts of lyophilization in unit-doses, a first proposed by RheaVita and Ghent University (Corver, 2012), and a second proposed by Politecnico di Torino and Massachussetts Institute of Tecnology (Trout et al., 2018), which is discussed in this

work.

2.6.1 The Hosokawa Micron BV lyophilization concept

The Dutch company Hosokawa Micron BV proposes, for many years, an alternative to conventional lyophilization in vials by producing lyophilized products in the form of fine particle powder. In 2005, they patented the 'stirred freeze-drier' (Van der Wel, 2005), which was then commercialized as 'Active freeze-drying'. Contrary to classical spray-freeze drying, this process can be performed in batch or continuous/semi-continuous mode, although, to our best knowledge a pilot plant has been tested only in the batch mode (Touzet et al., 2018).

As shown in Fig. 2.7, a solution is fed into a conical chamber and continuously stirred; a heating/cooling jacket allows the removal of heat. During this stage, the solution solidifies into frozen, macroscopic, blocks of nano/micro crystals. In a second stirred tank, which can refer as 'stirred freeze-dryer', the pressure is lowered, and heat is supplied from the heating jacket, so that ice crystals in the external layers of the frozen blocks sublimate. At the same time, mixing stresses break the dried layer into small fragments, which moves out the chamber following the vapor flow. A filter cartridge is inserted between the tank and the vacuum system, allowing the collection of the dried powder and, finally, its extraction from the equipment. This system allows aseptic processes and is equipped with SIP/CIP systems.

This technology is particularly suitable for nanocrystal application, and, according to the manufacturer, can handle drying solutions, dispersions, pastes, and wet solids. In a recent paper, Active Freeze-Drying in batch-mode was tested for production of nanocrystal-based powder using Ketoconazole as a poorly water-soluble model drug (Touzet et al., 2018).

In a recent presentation at 8th International Conference of the International Society for Lyophilization and FreezeDrying, it has been shown that this process can allow a dramatic reduction of drying time due to the large surface area of the particles and fragments, and, therefore, to the high sublimation rate. To give you an example, this technology was able to reduce drying duration of skimmed milk powder from 50 to 15 h (Van der Wel, 2017). The company claims that the batch-wise process has been successfully tested for a wide range of materials, i.e., nutraceuticals, vitamins, herbal extracts, vegetables, meat products, herbs, milk derivatives, insects, fibers, soups, flavor and extracts (Van der Wel, 2015) but, to our best knowledge, none of these data have been disclosed. In our opinion, this lack of knowledge might represent a severe weakness for the diffusion of this process at the industrial level.

A similar concept has been patented by IMA Life North America in 2010. This technology uses spray-freezing followed by lyophilization in an agitated tank, which can potentially work in continuous or semi-continuous mode (Demarco and Renzi, 2010).

2.6.2 Continuous lyophilization in unit doses proposed by Rhea Vita Ghent University

A concept of continuous lyophilization in unit-doses was patented by J. Corver in 2013 (Corver, 2012), investigated later by the research group of Prof. T. De Beer at Ghent University (De Meyer et al., 2015). This process starts out from the spin-freezing
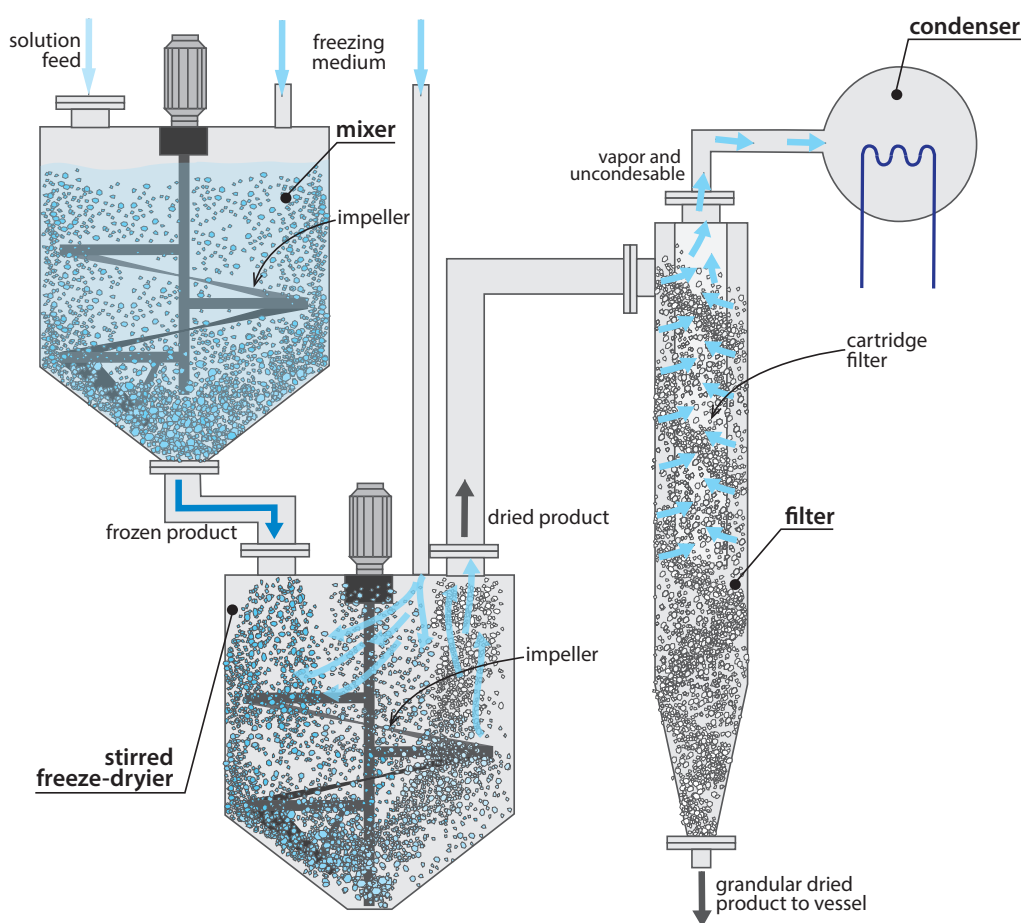
Figure 2.7 Schematic of the active freeze-drying plant.

of a liquid formulation in a vial, which occurs by rotating the vial longitudinally and removing heat by flowing a sterile cryogenic gas at controlled temperature around it; a second chamber is used to complete solidification of the product. During freezing, the vial is longitudinally rotated at about 2500 round per minute, to spread the product on the vial side wall as uniformly as possible. Because the drug is exposed to strong shear stresses during freezing, its stability could be compromised.

After that, the vial is transferred to a drying chamber at low pressure, where primary and secondary drying occurs. Here, the vial is not in contact with the shelf but it slowly rotates at about 5 rpm in front of an IR source, which supplies the heat required for ice sublimation. Vial rotation is fundamental for transfer heat homogeneously (Van Bockstal et al., 2017b). The weakness of this mode of supplying energy is that, up to now, there is not a robust way of monitoring and control product temperature during primary drying.

The movement of vials from chambers at different pressure is achieved by using load-lock systems. In Fig. 2.8, a schematic of this configuration is reported, but to our knowledge this might not be the final configuration. The authors proposed in-line NIR-based monitoring of the process that, coupled with the principal component analysis, can monitor primary and secondary drying, detecting the end point of each phase and, so, avoiding the typical soak time that affects batch lyophilization (De

Meyer et al., 2017).
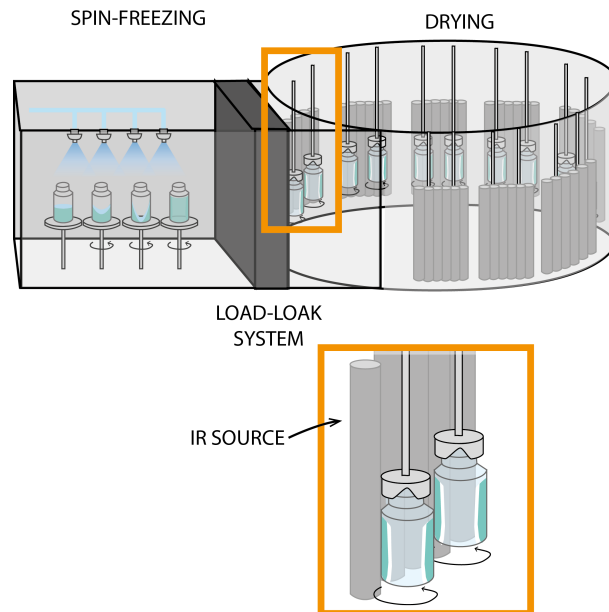
Figure 2.8 Schematic of Corver and De Meyer's spin freezing concept.

An important advantage of spin-freezing is that the frozen product is spread over the inner side wall of the vial, so that, the sublimation surface increases dramatically with respect to conventional freezing. That gives a significant advantage in performing primary and secondary drying in continuous because the sublimation rate is very high and drying duration is shortened by 5 to 15 times. On the other hand, there is no flexibility in the freezing protocol and poor control of the freezing process.

At the date of this writing, a functional prototype is used to simulate conditions similar to those of continuous. The next step would be the building of a one-vial prototype, then a multi-vial prototype, and finally, a GMP prototype that addresses all the requirements for the production of drugs for clinical testing and commercialization (Corver, 2017).

Acronyms

BTM Barometric Temperature Measurement; **CPP** Critical Process Parameter; **DEA** Dielectric Analysis; **DMA** Dynamic Mechanical Thermal Analysis; **DPE** Dynamic Parameter Estimation; **DSC** Differential Scanning Calorimetry; **DTA** Differential Thermal Analysis; **FDM** Freeze-Drying Microscopy; **GMP** Good Manufacturing Practice; **MTM** Manometric Temperature Measurement; **NDA** New Drug Application; **NIR** Near-Infrared Radiation; **PAT** Process Analytical Technology; **PRA** Pressure Rise Analysis; **PRT** Pressure-Rise Test; **QbD** Quality by Design; **QTPP** Quality Target Product Profile; **RM** Relative Moisture; **RTD** Resistance Temperature Detectors; **SSA** Specific surface area; **TDLAS** Tunable Diode Laser Adsorption Spectroscopy; **TEA** Thermo Electric Analysis; **TFTC** Thin-Film Thermocouples; **TMA** Thermo Mechanical Analysis; **TSC** Thermally Stimulated Current Spectrometry; **VISF** Vacuum-Induced Surface Freezing.

List of symbols

A_p inner cross-sectional area of the vial, m^2

A_v outer cross-sectional area of the vial, m^2

C_w residual moisture in the dried product, kg of water/kg of dried product

$C_{w,eq}$ weight fraction of sorbed water in the solid that would be in local equilibrium with the partial pressure of water in the drying chamber, kg of water/kg of dried product

E_a activation energy of the adsorption reaction, J mol^{-1}

K_c heat transfer coefficient due to direct conduction from the shelf to the glass at the points of contact, J s^{-1} m^{-2} K^{-1}

k_d kinetic constant of solvent desorption, s^{-1}

k_0 pre-exponential factor of the constant rate of desorption, s^{-1}

K_g heat transfer coefficient due to conduction in the gas between the shelf and the vial bottom, J s^{-1} m^{-2} K^{-1}

K_r heat transfer coefficient between the shelf and the vial due to radiation, J s^{-1} m^{-2} K^{-1}

k_s heat transfer coefficient between the technical fluid and the shelf, J s^{-1} m^{-2} K^{-1}

K_v overall heat transfer coefficient between the heating fluid and the product at vial bottom, J s^{-1} m^{-2} K^{-1}

K_v' heat transfer coefficient between the shelf and the vial bottom, J s^{-1} m^{-2} K^{-1}

m mass, kg

$p_{w,c}$ partial pressure of water in the drying chamber, Pa

$p_{w,i}$ partial pressure of water at the sublimating interface, Pa

$\dot{Q}_d$ heat flow supplied to the product during drying, J s^{-1}

R ideal gas constant, J mol^{-1} K^{-1}

R_p resistance of the dried layer to vapor flow, m s^{-1}

s_{gl} thickness of the glass at the bottom of the vial, m

T temperature, K

t time, s

T_b product temperature at vial bottom, K

T_c critical temperature, K

T_{eu} eutectic temperature, K

T_{fluid} temperature of the heating fluid, K

T_g' glass transition temperature, K

T_n nucleation temperature, K

Greek letters

κ_{gl} thermal conductivity of the glass, W m^{-1} K^{-1}

References

Akers, M. J. (2016). *Sterile Drug Products: Formulation, Packaging, Manufacturing and Quality.* Vol. 208. London/New York: CRC Press.

Alexeenko, A. A., Ganguly, A, and Nail, S. L. (2009). Computational analysis of fluid dynamics in pharmaceutical freeze-drying. *Journal of Pharmaceutical Sciences* 98 (9), pp. 3483–3494.

Altmann, R. (1894). *Die Elementarorganismen und ihre Beziehungen zu den Zellen.* Leipzig: Veit.

Arsiccio, A., Barresi, A., De Beer, T., Oddone, I., Van Bockstal, P.-J., and Pisano, R. (2018b). Vacuum Induced Surface Freezing as an effective method for improved inter-and intra-vial product homogeneity. *European Journal of Pharmaceutics and Biopharmaceutics* 128, pp. 210–219.

Arsiccio, A., Paladini, A., Pattarino, F., and Pisano, R. (2019). Designing the Optimal Formulation for Biopharmaceuticals: A New Approach Combining Molecular Dynamics and Experiments. *Journal of pharmaceutical sciences* 108 (1), pp. 431–438.

Barresi, A. A., Velardi, S. A., Pisano, R., Rasetto, V., Vallan, A., and Galan, M. (2009a). In-line control of the lyophilization process. A gentle PAT approach using software sensors. *International Journal of Refrigeration* 32 (5), pp. 1003–1014.

Barresi, A. A., Pisano, R., Fissore, D., Rasetto, V., Velardi, S. A., Vallan, A., Parvis, M., and Galan, M. (2009b). Monitoring of the primary drying of a lyophilization process in vials. *Chemical Engineering and Processing: Process Intensification* 48 (1), pp. 408–423.

Barresi, A. A., Pisano, R., Rasetto, V., Fissore, D., and Marchisio, D. L. (2010). Model-based monitoring and control of industrial freeze-drying processes: effect of batch nonuniformity. *Drying Technology* 28 (5), pp. 577–590.

Bhatnagar, B. S., Bogner, R. H., and Pikal, M. J. (2007). Protein stability during freezing: separation of stresses and mechanisms of protein stabilization. *Pharmaceutical Development and Technology* 12 (5), pp. 505–523.

Breen, E. D., Curley, J. G., Overcashier, D. E., Hsu, C. C., and Shire, S. J. (2001). Effect of moisture on the stability of a lyophilized humanized monoclonal antibody formulation. *Pharmaceutical Research* 18 (9), pp. 1345–1353.

Bruttini, R. (1993). Continuous freeze drying apparatus. U.S. pat. 5,269,077.

Cameron, P. (1997). *Good Pharmaceutical Freeze-Drying Practice*. Buffalo Grove, IL: CRC Press.

Chang, L., Shepherd, D., Sun, J., Tang, X., and Pikal, M. J. (2005). Effect of sorbitol and residual moisture on the stability of lyophilized antibodies: Implications for the mechanism of protein stabilization in the solid state. *Journal of Pharmaceutical Sciences* 94 (7), pp. 1445–1455.

Cheng, H.-P., Tsai, S.-M., and Cheng, C.-C. (2014). Analysis of heat transfer mechanism for shelf vacuum freeze-drying equipment. *Advances in Materials Science and Engineering* 2014, 515180.

Chouvenc, P, Vessot, S, Andrieu, J, and Vacus, P (2005). Optimization of the freeze-drying cycle: adaptation of the pressure rise analysis model to non-instantaneous isolation valves. *PDA Journal of Pharmaceutical Science and Technology* 59 (5), pp. 298–309.

Corver, J. (2017). A continuous and controlled pharmaceutical freeze-drying technology for unit doses. In: *8th International Conference of The International Society for Lyophilization and FreezeDrying*. Apr. 24–28, 2017. La Habana, Cuba.

Corver, J. A.W. M. (2012). Method and system for freeze-drying injectable compositions, in particular pharmaceutical compositions. U.S. pat. 20140215845 A1.

De Beer, T., Vercruysse, P., Burggraeve, A., Quinten, T., Ouyang, J, Zhang, X, Vervaet, C., Remon, J. P., and Baeyens, W. (2009). In-line and real-time process monitoring of a freeze drying process using Raman and NIR spectroscopy as complementary process analytical technology (PAT) tools. *Journal of Pharmaceutical Sciences* 98 (9), pp. 3430–3446.

De Beer, T., Wiggenhorn, M, Hawe, A, Kasper, J., Almeida, A., Quinten, T., Friess, W, Winter, G, Vervaet, C., and Remon, J. P. (2011). Optimization of a pharmaceutical freeze-dried product and its process using an experimental design approach and innovative process analyzers. *Talanta* 83 (5), pp. 1623–1633.

De Meyer, L, Van Bockstal, P.-J., Corver, J, Vervaet, C, Remon, J. P., and De Beer, T (2015). Evaluation of spin freezing versus conventional freezing as part of a continuous pharmaceutical freeze-drying concept for unit doses. *International Journal of Pharmaceutics* 496 (1), pp. 75–85.

De Meyer, L., Lammens, J., Mortier, S. T. F., Vanbillemont, B., Van Bockstal, P. J., Corver, J., Nopens, I., Vervaet, C., and De Beer, T. (2017). Modelling the primary drying step for the determination of the optimal dynamic heating pad temperature in a continuous pharmaceutical freeze-drying process for unit doses. *International Journal of Pharmaceutics* 532 (1), pp. 185–193.

Debus, K. (2017). 'Lyophilization Experiences Growth Spurt in Pharma'. *Pharmaceutical Processing* 32 (6), pp. 22–24.

Demarco, F. W. and Renzi, E. (2010). Bulk freeze drying using spray freezing and stirred drying. U.S. pat. 13811937.

Fang, R., Tanaka, K., Mudhivarthi, V., Bogner, R. H., and Pikal, M. J. (2018). Effect of controlled ice nucleation on stability of lactate dehydrogenase during freeze-drying. *Journal of Pharmaceutical Sciences* 107 (3), pp. 824–830.

Fissore, D. and Barresi, A. A. (2011). Scale-up and process transfer of freeze-drying recipes. *Drying Technology* 29 (14), pp. 1673–1684.

Fissore, D., Pisano, R., and Barresi, A. A. (2010). On the methods based on the Pressure Rise Test for monitoring a freeze-drying process. *Drying Technology* 29 (1), pp. 73–90.

Fissore, D., Pisano, R., and Barresi, A. A. (2011). Monitoring of the secondary drying in freeze-drying of pharmaceuticals. *Journal of Pharmaceutical Sciences* 100 (2), pp. 732–742.

Fissore, D., Pisano, R., and Barresi, A. A. (2018). Process analytical technology for monitoring pharmaceuticals freeze-drying–A comprehensive review. *Drying Technology*, pp. 1–27.

Flosdorf, E. W. and Mudd, S. (1935). Procedure and apparatus for preservation in lyophile form of serum and other biological substances. *The Journal of Immunology* 29 (5), pp. 389–425.

Flosdorf, E. W., Hull, L. W., and Mudd, S. (1945). Drying by sublimation. *The Journal of Immunology* 50, p. 21.

Franks, F. and Auffret, T. (2008). *Freeze-Drying of Pharmaceuticals and Biopharmaceuticals*. Cambridge, UK: Royal Society of Chemistry.

Galan, M. (2016). Monitoring and control of industrial freeze-drying operations: The challenge of implementing Quality-by-Design (QbD). In: *Freeze-Drying/Lyophilization of Pharmaceutical and Biological Products*. Ed. by L Rey and J. C. May. 3rd. New York: CRC Press. Chap. 19, pp. 453–471.

Gasteyer, T. H., Sever, R. R., Hunek, B, Grinter, N, and Verdone, M. L. (2007). Lyophilization system and method. U.S. pat. 20070186437.

Geidobler, R and Winter, G (2013). Controlled ice nucleation in the field of freeze-drying: fundamentals and technology review. *European Journal of Pharmaceutics and Biopharmaceutics* 85 (2), pp. 214–222.

Goldblith, S. A., Rey, L., and Rothmayr, W. W. (1975). *Freeze Drying and Advanced Food Technology*. London/New York: Academic Press.

Goshima, H., Do, G., and Nakagawa, K. (2016). Impact of ice morphology on design space of pharmaceutical freeze-drying. *Journal of Pharmaceutical Sciences* 105 (6), pp. 1920–1933.

Hatley, R. H. and Mant, A. (1993). Determination of the unfrozen water content of maximally freeze-concentrated carbohydrate solutions. *International Journal of Biological Macromolecules* 15 (4), pp. 227–232.

Heller, M. C., Carpenter, J. F., and Randolph, T. W. (1999). Protein formulation and lyophilization cycle design: Prevention of damage due to freeze-concentration induced phase separation. *Biotechnology and Bioengineering* 63 (2), pp. 166–174.

Hottot, A., Vessot, S., and Andrieu, J. (2007). Freeze drying of pharmaceuticals in vials: Influence of freezing protocol and sample configuration on ice morphology and freeze-dried cake texture. *Chemical Engineering and Processing: Process Intensification* 46 (7), pp. 666–674.

Jennings, T. A. (1999). *Lyophilization: introduction and basic principles*. New York: CRC Press.

Jiang, S. and Nail, S. L. (1998). Effect of process conditions on recovery of protein activity after freezing and freeze-drying. *European Journal of Pharmaceutics and Biopharmaceutics* 45 (3), pp. 249–257.

Kasper, J. C. and Friess, W. (2011). The freezing step in lyophilization: physico-chemical fundamentals, freezing methods and consequences on process performance and quality attributes of biopharmaceuticals. *European Journal of Pharmaceutics and Biopharmaceutics* 78 (2), pp. 248–263.

Keenan, J. (2014). 'Lyophilization market forecast to double in size by 2020'. *FiercePharma*. URL: https://www.pharmpro.com/blog/2017/09/lyophilization-experiences-growth-spurt-pharma.

Kharaghani, A., Tsotsas, E., Wolf, C., Beutler, T., Guttzeit, M., and Oetjen, G.-W. (2000). Freeze-Drying. In: *Ullmann's Encyclopedia of Industrial Chemistry*. Wiley-VCH, pp. 1–47.

Konstantinidis, A. K., Kuu, W., Otten, L., Nail, S. L., and Sever, R. R. (2011). Controlled nucleation in freeze-drying: Effects on pore size in the dried product layer, mass transfer resistance, and primary drying rate. *Journal of Pharmaceutical Sciences* 100 (8), pp. 3453–3470.

Korang-Yeboah, M. (2017). Advancing the formulation and manufacturing of lyophilized pharmaceuticals/biopharmaceuticals: Regulatory perspectives. In: *ISLFD East Coast Chapter Meeting*. Sept. 12, 2017. Cambridge, MA.

Kramer, M., Sennhenn, B., and Lee, G. (2002). Freeze-drying using vacuum-induced surface freezing. *Journal of Pharmaceutical Sciences* 91 (2), pp. 433–443.

Kuu, W. Y., Doty, M. J., Rebbeck, C. L., Hurst, W. S., and Cho, Y. K. (2013). Gap-freezing approach for shortening the lyophilization cycle time of pharmaceutical formulationsDemonstration of the concept. *Journal of Pharmaceutical Sciences* 102 (8), pp. 2572–2588.

LaTorre-Snyder, M. (2017). 'Lyophilization: The Basics. An overview of the lyophilization process as well as the advantages and disadvantages'. *Pharmaceutical Processing* 31 (1).

Lawrence, X. Y., Amidon, G., Khan, M. A., Hoag, S. W., Polli, J., Raju, G., and Woodcock, J. (2014). Understanding pharmaceutical quality by design. *The AAPS journal* 16 (4), pp. 771–783.

Lee, S. L., OConnor, T. F., Yang, X., Cruz, C. N., Chatterjee, S., Madurawe, R. D., Moore, C. M., Lawrence, X. Y., and Woodcock, J. (2015). Modernizing pharmaceutical manufacturing: from batch to continuous production. *Journal of Pharmaceutical Innovation* 10 (3), pp. 191–199.

Liapis, A. and Sadikoglu, H (1998). Dynamic pressure rise in the drying chamber as a remote sensing method for monitoring the temperature of the product during the primary drying stage of freeze drying. *Drying Technology* 16 (6), pp. 1153–1171.

Lim, J. Y., Kim, N. A., Lim, D. G., Kim, K. H., Choi, D. H., and Jeong, S. H. (2016). Process cycle development of freeze drying for therapeutic proteins with stability evaluation. *Journal of Pharmaceutical Investigation* 46 (6), pp. 519–536.

Liu, J. (2006). Physical characterization of pharmaceutical formulations in frozen and freeze-dried solid states: techniques and applications in freeze-drying development. *Pharmaceutical Development and Technology* 11 (1), pp. 3–28.

Liu, J., Viverette, T., Virgin, M., Anderson, M., and Dalal, P. (2005). A study of the impact of freezing on the lyophilization of a concentrated formulation with a high fill depth. *Pharmaceutical Development and Technology* 10 (2), pp. 261–272.

Milton, N., Pikal, M. J., Roy, M. L., and Nail, S. L. (1997). Evaluation of manometric temperature measurement as a method of monitoring product temperature during lyophilization. *PDA Journal of Pharmaceutical Science and Technology* 51 (1), pp. 7–16.

Nakagawa, K., Hottot, A., Vessot, S., and Andrieu, J. (2006). Influence of controlled nucleation by ultrasounds on ice morphology of frozen formulations for pharmaceutical proteins freeze-drying. *Chemical Engineering and Processing: Process Intensification* 45 (9), pp. 783–791.

Oddone, I. (2016). "Vacuum Induced Nucleation as a method for freeze drying optimization". PhD thesis. Politecnico di Torino.

Oddone, I., Pisano, R., Bullich, R., and Stewart, P. (2014). Vacuum-Induced nucleation as a method for freeze-drying cycle optimization. *Industrial & Engineering Chemistry Research* 53 (47), pp. 18236 –18244.

Oddone, I., Fulginiti, D., Barresi, A. A., Grassini, S., and Pisano, R. (2015). Non-invasive temperature monitoring in freeze drying: control of freezing as a case study. *Drying Technology* 33 (13), pp. 1621– 1630.

Oddone, I., Van Bockstal, P.-J., De Beer, T., and Pisano, R. (2016). Impact of vacuum-induced surface freezing on inter-and intra-vial heterogeneity. *European Journal of Pharmaceutics and Biopharmaceutics* 103, pp. 167–178.

Oddone, I., Barresi, A. A., and Pisano, R. (2017). Influence of controlled ice nucleation on the freeze-drying of pharmaceutical products: the secondary drying step. *International Journal of Pharmaceutics* 524 (1-2), pp. 134–140.

Oetjen, G.-W. (1999). Industrial freeze-drying for pharmaceutical applications. In: *Freeze Drying/ Lyophilization of Pharmaceutical and Biological Product*. Ed. by L Ray and J. C. May. 2nd. New York: Informa Healtcare.

Oetjen, G. W., Schmitz, F. J., and Eilenberg, H (1971). Continuous freeze dryer. U.S. pat. 3612411A.

Oetjen, G. W., Haseley, P, Klutsch, H, and Leineweber, M (1999). Method for Controlling a Freeze-Drying Process. U.S. pat. 6,163,979 A1.

Passot, S., Tréléa, I. C., Marin, M., Galan, M., Morris, G. J., and Fonseca, F. (2009). Effect of controlled ice nucleation on primary drying stage and protein recovery in vials cooled in a modified freeze-dryer. *Journal of Biomechanical Engineering* 131 (7), p. 074511.

Patel, S. M., Doen, T., and Pikal, M. J. (2010). Determination of end point of primary drying in freeze-drying process control. *AAPS Pharmscitech* 11 (1), pp. 73–84.

Patel, S. M. and Pikal, M. J. (2011). Emerging freeze-drying process development and scale-up issues. *AAPS PharmSciTech* 12 (1), pp. 372–378.

Patel, S. M., Nail, S. L., Pikal, M. J., Geidobler, R., Winter, G., Hawe, A., Davagnino, J., and Rambhatla Gupta, S. (2017). Lyophilized drug product cake appearance: what is acceptable? *Journal of Pharmaceutical Sciences* 106 (7), pp. 1706–1721.

Peters, B.-H., Staels, L., Rantanen, J., Molnár, F., De Beer, T., Lehto, V.-P., and Ketolainen, J. (2016). Effects of cooling rate in microscale and pilot scale freeze-drying -Variations in excipient polymorphs and protein secondary structure. *European Journal of Pharmaceutical Sciences* 95, pp. 72–81.

Pikal, M. J. and Shah, S (1997). Intravial distribution of moisture during the secondary drying stage of freeze drying. *PDA Journal of Pharmaceutical Science and Technology* 51 (1), pp. 17–24.

Pikal, M. J., Bogner, R., Mudhivarthi, V., Sharma, P., and Sane, P. (2016). Freeze-drying process development and scale-up: scale-up of edge vial versus center vial heat transfer coefficients, Kv. *Journal of Pharmaceutical Sciences* 105 (11), pp. 3333–3343.

Pikal, M., Roy, M., and Shah, S. (1984). Mass and heat transfer in vial freeze-drying of pharmaceuticals: Role of the vial. *Journal of Pharmaceutical Sciences* 73 (9), pp. 1224–1237.

Pikal, M., Shah, S, Roy, M., and Putman, R (1990). The secondary drying stage of freeze drying: drying kinetics as a function of temperature and chamber pressure. *International Journal of Pharmaceutics* 60 (3), pp. 203–207.

Pisano, R (2018). Alternative methods of controlling nucleation in freeze drying. In: *Lyophilization of Pharmaceuticals and Biologicals*. Ed. by K. R. Ward and P. Matejtschuk. New York: Springer.

Pisano, R., Rey, L., Kuntz, F., and Aoude-Werner, D. (2015). Effect of electron beam irradiation on remaining activity of lyophilized acid phosphatase with water-binding and non-water binding additives. *Drying Technology* 33, pp. 822–830.

Pisano, R, Napoletano, F, Paladini, A., De Beer, T., and Capozzi, L. C. (2017a). Influence of the freezing protocol on the activity of lactate dehydrogenase after freeze-drying. In: *Proceeding of EuroDrying2017 6th European Drying Conference, 19-21, 2017, Liège, Belgium.*

Pisano, R., Fissore, D., Velardi, S. A., and Barresi, A. A. (2010). In-line optimization and control of an industrial freeze-drying process for pharmaceuticals. *Journal of Pharmaceutical Sciences* 99 (11), pp. 4691–4709.

Pisano, R., Fissore, D., Barresi, A. A., Brayard, P., Chouvenc, P., and Woinet, B. (2013a). Quality by design: optimization of a freeze-drying cycle via design space in case of heterogeneous drying behavior and influence of the freezing protocol. *Pharmaceutical Development and Technology* 18 (1), pp. 280–295.

Pisano, R., Fissore, D., Barresi, A. A., and Rastelli, M. (2013b). Quality by Design: scale-up of freeze-drying cycles in pharmaceutical industry. *AAPS PharmSciTech* 14 (3), pp. 1137–1149.

Pisano, R., Fissore, D., and Barresi, A. A. (2014). A new method based on the regression of step response data for monitoring a freeze-drying cycle. *Journal of Pharmaceutical Sciences* 103 (6), pp. 1756–1765.

Pisano, R., Fissore, D., and Barresi, A. A. (2016). Noninvasive monitoring of a freeze-drying process for tert-butanol/water cosolvent-based formulations. *Industrial & Engineering Chemistry Research* 55 (19), pp. 5670–5680.

Rambhatla, S., Ramot, R., Bhugra, C., and Pikal, M. J. (2004). Heat and mass transfer scale-up issues during freeze drying: II. Control and characterization of the degree of supercooling. *AAPS Pharmscitech* 5 (4), pp. 54–62.

Rasetto, V., Marchisio, D. L., Fissore, D., and Barresi, A. A. (2010). On the use of a dual-scale model to improve understanding of a pharmaceutical freeze-drying process. *Journal of Pharmaceutical Sciences* 99 (10), pp. 4337–4350.

Rey, L. (1999). Glimpses into the realm of freeze-drying: classical issues and new ventures. In: *Freeze-Drying/Lyophilization of Pharmaceutical and Biological Products*. Ed. by L Rey and J. C. May. 3rd. New York: Marcel Dekker Inc.: New York. Chap. 1, pp. 1–30.

Rey, L. (2016). *Freeze-Drying/Lyophilization of Pharmaceutical and Biological Products*. CRC Press, New York.

Rowe, T. (1990). A Technique for the Nucleation of Ice. In: *International Symposium on Biological Product Freeze-Drying and Formulation*. Oct. 26, 1990. Geneva, Switzerland.

Schneid, S. and Gieseler, H. (2009). Process analytical technology (PAT) in freeze drying: tunable diode laser absorption spectroscopy as an evolving tool for cycle monitoring. *European Pharmaceutical Review* 13 (6), pp. 18–25.

Schneid, S. C., Gieseler, H., Kessler, W. J., Luthra, S. A., and Pikal, M. J. (2011). Optimization of the secondary drying step in freeze drying using TDLAS technology. *AAPS Pharmscitech* 12 (1), pp. 379–387.

Scutellà, B., Passot, S., Bourlés, E., Fonseca, F., and Tréléa, I. C. (2017). How vial geometry variability influences heat transfer and product temperature during freeze-drying. *Journal of Pharmaceutical Sciences* 106 (3), pp. 770–778.

Searles, J. A., Carpenter, J. F., and Randolph, T. W. (2001). The ice nucleation temperature determines the primary drying rate of lyophilization for samples frozen on a temperature-controlled shelf. *Journal of Pharmaceutical Sciences* 90 (7), pp. 860–871.

Sluder, J. C., Olsen, R. W., and Kenyon, E. M. (1947). A method for the production of dry powdered orange juice. *Food Tecnologists* 1, pp. 85–94.

Tang, X. C. and Pikal, M. J. (2004). Design of freeze-drying processes for pharmaceuticals: practical advice. *Pharmaceutical Research* 21 (2), pp. 191–200.

Touzet, A., Pfefferlé, F., Wel, P. van der, Lamprecht, A., and Pellequer, Y. (2018). Active freeze drying for production of nanocrystal-based powder: A pilot study. *International Journal of Pharmaceutics* 536 (1), pp. 222–230.

Trappler, E. H. (2013). Contemporary Approaches to Development and Manufacturing of Lyophilized Parenterals. In: *Sterile Product Development*. Ed. by P. Kolhe, M. Shah, and N. Rathore. Vol. 6. Springer, New York, NY, pp. 275–313.

Trout, B., Pisano, R., and Capozzi, L. C. (2018). Continuous freeze-drying methods and related products. Pat. req. International Application No. PCT/US2018/030629.

Van Bockstal, P. J., Mortier, S. T. F., De Meyer, L., Corver, J., Vervaet, C., Nopens, I., and De Beer, T. (2017a). Mechanistic modelling of infrared mediated energy transfer during the primary drying step of a continuous freeze-drying process. *European Journal of Pharmaceutics and Biopharmaceutics* 114, pp. 11–21.

Van Bockstal, P. J., Mortier, S. T. F., Corver, J., Nopens, I., Gernaey, K. V., and De Beer, T. (2017b). Quantitative risk assessment via uncertainty analysis in combination with error propagation for

the determination of the dynamic Design Space of the primary drying step during freeze-drying. *European Journal of Pharmaceutics and Biopharmaceutics* 121, pp. 32–41.

Van der Wel, P. G. J. (2005). Stirred freeze drying. Pat. WO2004073845A3.

Van der Wel, P. G. J. (2015). Active Freeze Drying. In: *Proceedings of 5th European Drying Conference*. Oct. 21–23, 2015. Budapest, Hungary.

Van der Wel, P. G. J. (2017). Active Freeze Drying. In: *8th International Conference of The International Society for Lyophilization and FreezeDrying*. Apr. 24–28, 2017. La Habana, Cuba.

Varshney, D. and Singh, M. (2015). History of Lyophilization. In: *Lyophilized Biologics and Vaccines*. Ed. by D. Varshney and M. Singh. New York: Springer. Chap. 1, pp. 3–10.

Velardi, S. A., Rasetto, V., and Barresi, A. A. (2008). Dynamic parameters estimation method: advanced manometric temperature measurement approach for freeze-drying monitoring of pharmaceutical solutions. *Industrial & Engineering Chemistry Research* 47 (21), pp. 8445–8457.

Wang, B., McCoy, T. R., Pikal, M. J., and Varshney, D. (2015). Lyophilization of therapeutic proteins in vials: process scale-up and advances in Quality by Design. In: *Lyophilized Biologics and Vaccines*. Ed. by D. Varshney and M. Singh. New York: Springer. Chap. 7, pp. 121–156.

PART II

A new concept of continuous freeze-drying of pharmaceuticals and biopharmaceuticals in unit doses

Presentation of the technology for continuous freeze-drying

In response to current trends in the pharmaceutical industry, a new concept for the freeze-drying of pharmaceuticals in unit-doses is presented: the continuous freeze-drying/ lyophilization of suspended vials. This configuration makes it possible to set up a continuous freeze-drying process that produces a final product with similar characteristics to those traditionally obtained by means of the batch process, but which avoids the drawbacks of conventional, batch freeze-drying. This chapter presents the description of the technology for performing freeze-drying in continuous, which is the result of a collaboration between Politecnico di Torino and Massachusetts Institute of Technology. The main component of the apparatus will be presented and discussed in detail. Conclusively, features and advantages of the proposed technology will be discussed*.

3.1 The importance of being continuous

The demands that a continuous process should be able to satisfy are the following: i) flexibility to process different products, dosage forms, and throughputs; ii) agility and reduction of scale-up efforts; iii) process monitoring and control in-line to assure the correct quality attributes (QAs), and, more specifically, the critical quality attributes (CQAs); iv) reduced floor space and investment costs (Kleinebudde et al., 2017; Byrn et al., 2015).

In the case of lyophilization, the main features that continuous freeze-drying have to address are i) the control of freezing to produce uniform products with the desired characteristics, ii) supply uniform heat during primary and secondary drying to

---

*Part of the work described in this chapter has been previously published in "Capozzi, L.C., Trout, B. and Pisano, R. (2018) From batch to continuous: freeze-drying of suspended vials for pharmaceuticals in unit-doses. *Industrial & Engineering Chemistry Research* (accepted)" and refers to the patent application "Trout, B., Pisano, R., and Capozzi, L. C. (2018). Continuous freeze-drying methods and related products. Pat. req. International Application No. PCT/US2018/030629".

avoid vial-to-vial differences and drying rate; iii) speed-up the process; iv) reduce operational risks connected to manual operation or product contamination; v) reduce the footprint of the equipment; vi) avoid batch-to-batch variability; vii) monitoring and control CQAs during the whole process; iix) eliminate scale-up and re-validation of the process.

In the following parts of this chapter, the technology for performing continuous freeze-drying as patented by Trout et al. (2018) will be shown and discussed in some of its technical detail.

3.2 Description of the technology

The basic concept of continuous freeze-drying consists of a sequence of modules, each of which is dedicated to a different operation, i.e., freezing, or primary and secondary drying, and are connected one to another to guarantee continuity of the vial flow and to be perfectly integrated with the downstream processes. The continuous flow of vials is achieved by suspending the vials over a track and moving them through chambers that have different conditions, i.e., pressures and temperatures, and which are separated by a sluice-gate system. This configuration makes the freezing and drying operations continuous. Moreover, the equipment can process various types of product with different dosage forms, i.e., solution or granules in vials or small containers. A schematic of the equipment is shown in Fig. 3.1.
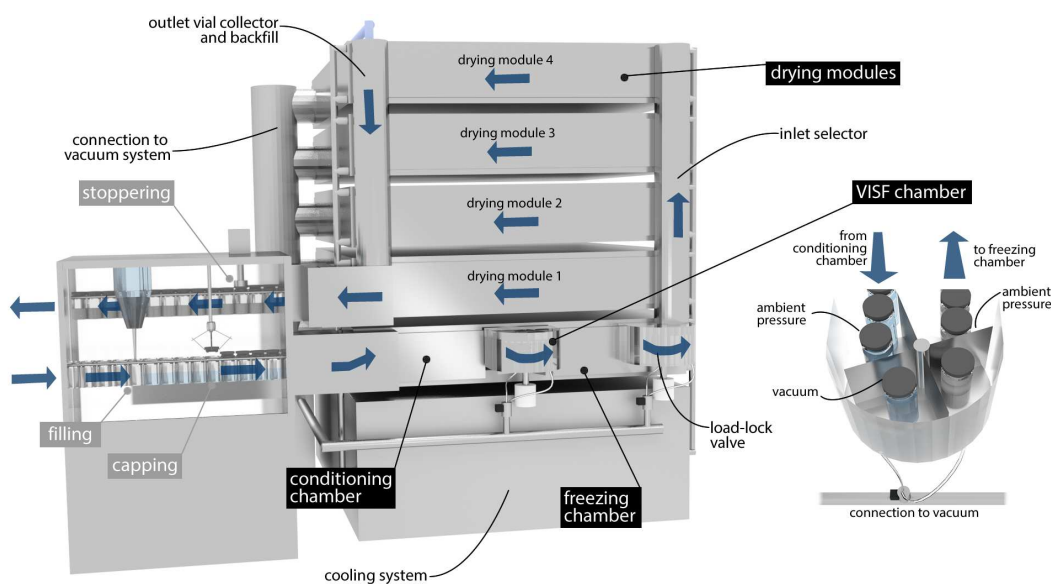
Figure 3.1 Schematic of the continuous freeze-dryer patented by the author (Trout et al., 2018).

3.2.1 Filling and loading module

The first step of the process is the continuous filling and loading of vials. This operation is naturally continuous and is already used in batch freeze-drying. Unfortunately, filling represents an unavoidable dead time in batch freeze-drying, although an automatic filler can process 30,000 vials per hour. In the batch configuration, loading

can cause problems related to the cooling/freezing of the products and, so, to its uniformity. Moreover, it can cause a loss in activity of some APIs, as, during the loading, some vials resides at ambient temperature for several hours (Cameron, 1997).

On the other hand, in the case of continuous mode, this operation does not require high-speed filling equipment, since vials are continuously loaded into the equipment. In the case of particle-based products, the frozen particles are continuously filled into vials and loaded, one by one, into the equipment.

Once filled, the vial is partially stoppered and then continuously loaded into the apparatus. A fully-automated system provides a sufficient number of vessels/minute to feed the freezing modules. These operations are carried out in a sterilized and temperature controlled environment to avoid contamination and deactivation of the APIs.

3.2.2   Freezing module

As shown in Fig. 3.1, the vial is filled with a pre-defined volume of liquid and then transferred, through a load-lock system, to the freezing module. Here, the vessels are suspended and moved over a moving track.

The freezing module consists of three sub-modules: (A) a conditioning module, (B) a load-lock system, where controlled nucleation can eventually take place, and (C) an equilibration/freezing module. The operations that the continuous freeze-dryer has to carry out depend on the dosage form of the product that has to be freeze-dried.

In the case of particle-based products, after filling, each vial is moved into the conditioning chamber and then directly into drying modules.

For liquid solutions, the vial is cooled down and equilibrated to the desired temperature by adjusting the temperature and flow rate of the cryogenic gas in the conditioning module. The vial then enters the load-lock system, where it is exposed to a vacuum that induces nucleation and is, then, transferred to the freezing module, where its temperature is lowered, and the solidification of the solution is completed. This operation is used to perform vacuum-induced surface freezing (VISF) in continuous mode, but the equipment can generally also perform uncontrolled nucleation.

Table 3.1 summarize the basic operations to be done for producing different solid dosage forms.

Table 3.1   Freezing operations for different types of material

Dosage form	Filling	Conditioning module	Nucleation chamber	Freezing module
Bulk, controlled nucleation	Yes	Yes	Yes	Yes
Bulk, uncontrolled nucleation	Yes	Yes (not compulsory)	No	Yes
Particle-base material	Yes	Yes (not compulsory)	No	No

The conditioning chamber

In the conditioning module, vials are conditioned to the desired temperature by flowing the cryogenic gas, nitrogen or another gas, at controlled temperature and flow rate. Vials are suspended over a moving track and moved along the module. The temperature and flow rate of the cryogenic fluid have to be adjusted to ensure that the vials reach their desired temperature before exiting from the module.

The pre-conditioning of the product that has to be freeze-dried is always compulsory in the case of VISF, but it is also suggested in the case of uncontrolled nucleation in order to improve product homogeneity.

Control of the nucleation temperature

The control of the nucleation temperature is essential to make both the drying behavior and product morphology perfectly uniform. Various methods are available to control the nucleation temperature, e.g., ultrasounds, ice fog, and pressure disturbance. All these methods can be integrated into the present technology, but we here propose the application of VISF technology, which uses the vacuum to instantaneously induce the nucleation event. VISF can easily be adapted, and it can be carried out directly in the load-lock systems used to load the vial into the freezing module. In fact, nucleation is induced by reducing the pressure directly inside the load-lock chamber; this pressure reduction promotes the partial evaporation of the solvent and hence cools down the solution, thus facilitating the formation of stable nuclei. This method guarantees the replication of the nucleation temperature in each sample and, thus, of ice morphology.

The freezing chamber

In the freezing modules, vials are cooled down by forced gas circulation until complete solidification of the product occurs. In this module, heat is prevalently transferred by gas convection and radiation from the surroundings.

In order to speed up and make the heat transfer between the equipment and the vessel more uniform, the cryogenic fluid can be forced to move along the freezing module, in a similar way to as in the conditioning chamber. In this manner, the external surfaces of the vials are flushed to the same extent by the cryogenic gas, thus reducing the heterogeneity of the heat flux that usually occurs in conventional batch freezing, where vials are loaded onto temperature-controlled shelves and receive different amounts of heat, depending on their position on the shelf.

Different freezing protocols can be performed by modulating the velocity of the cryogenic fluid and its temperature; moreover, these two process parameters can be adjusted to control the duration of the freezing and, thus, to design the final structure of the product.

3.2.3   Primary and secondary drying module

This module is connected to a vacuum system, condenser and vacuum pump, which guarantees the desired pressure, while the temperature of the equipment surfaces is controlled by adjusting the temperature of the heat transfer fluid, that is, silicon oil, by means of a refrigeration system. In this configuration, the vials are not in contact with the shelves, and heat is essentially transferred by radiation. In fact, a

low pressure, below 1 mbar, makes the heat transfer by convection and conduction negligible, with respect to the radiative contribution. This configuration allows the heat to be uniformly transferred to the vessel, thus avoiding those problems that are typical of batch freeze-drying, where individual vials behave differently, depending on their position within the batch and because of variations in the geometry of the vials themselves. Furthermore, the temperature and pressure gradients within the equipment no longer represent a cause of heterogeneity in the heat transfer, because the vials, following the same path, are exposed to exactly the same conditions.

In this module, heat is supplied by radiation through temperature-controlled surfaces, but can potentially be transferred using other technologies, such as IR radiation or microwaves. As heat is essentially transferred by radiation, the control of the temperature of the product being dried is much easier, and this allows uniformity in the heat transfer to be guaranteed and, thus, in the drying behavior.

The same equipment configuration is suitable for both the primary and secondary drying modules; the two modules are thus identical but operate at different pressures and temperatures.

3.3 Apparatus

3.3.1 Module design

The continuous freeze-drying apparatus is constituted by a number of modules specialized in performing the cooling/freezing and drying. These modules can have different shapes and dimension.

As shown in Fig. 3.2, a drying module is constituted of an upper and bottom temperature-controlled shelf and a number of fins to form a channel along with the whole module. These fins provide further heat to the product being drying by radiation. The module is provided with a track which is able to suspend vials and move them along the module. An example of design for a drying chamber is included in Table 3.2.

Table 3.2   Example of calculation for designing a drying module

Residence time	30 h	Determined by the process
Channel dimension	0.05x0.03 m	Determined by vial type
Dimension of the module	Length 1.82 Height 0.07 m Width 3.00 m	Designed
Total lenght of the path	35 m	Designed
Speed of travel	1.2 m/h	Determined from the total length of a path and residence time
Productivity	49 vials/h	

A cooling/freezing module has a similar shape, but heat is removed from the

a)

b)
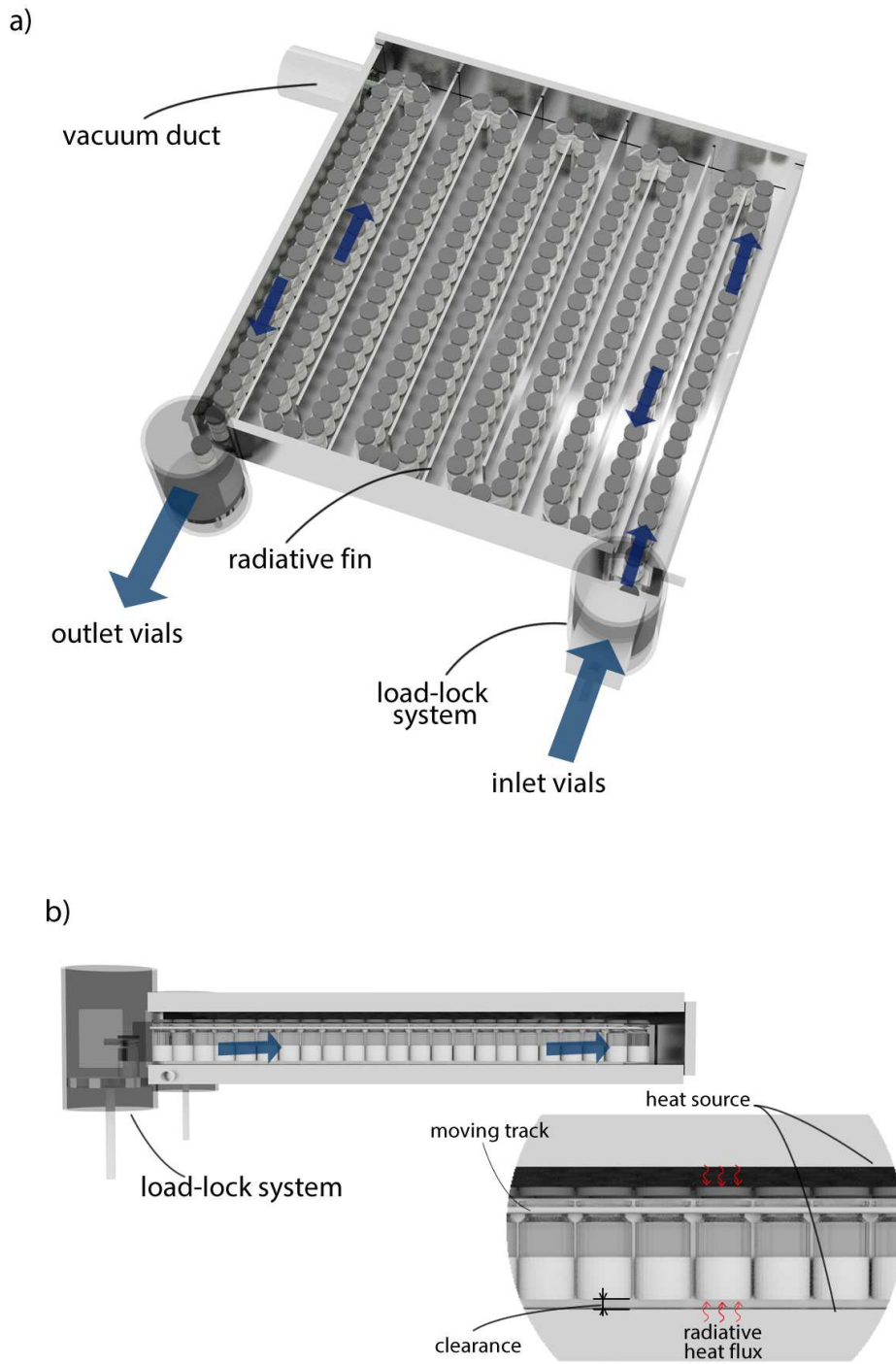
Figure 3.2   (a) Prospective view of a module, (b) side view of a module.

product by forced convection of a cryogenic gas.

3.3.2 Moving vials through the continuous freeze-drier

In the continuous apparatus, vials move through the module and are suspended to avoid heat transfer heterogeneity. Fig.3.3a-c shows three systems to suspend vials and move them through the module.

In Fig.3.3a, shows a first proposal for moving vials through the continuous freeze-dryer. As a vial enters a new module, a piston lift it up so that the vial is sufficiently close to a gripper. Then, the gripper grabs the vial and holds onto it until the end of the module. The gripper can effectively transport the vial along with the module through a trolley that moves over a track.

Fig.3.3b shows a configuration for the transport of the vials along with the equipment based on the use of conveyors. As a vial enters a new module, a piston lift it so that the vial is sufficiently close to two metallic semicircular parts. As the vial is in the right position, the two metallic parts join one another, forming a skate, and keep that position till the end of the module where the vial is left. The skate can effectively transport the vial along the module sliding over a track.

In Fig.3.3c, vials are directly suspended over a track. First, a vertical piston lifts the vial; then, a second piston pushes the vial along a track and, in this way, the entire row of vials is moved ahead.
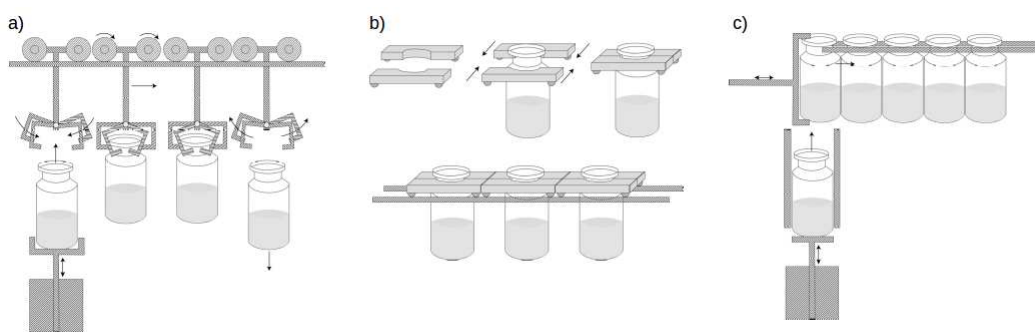
Figure 3.3 Schematic of the moving-vial systems based on the use of (a) a gripper, (b) a conveyor or (c) directly suspended over a track.

3.3.3 Moving vials between modules

The passage from modules at different pressure conditions requires special valves which are able to isolate the two environments. Some of these systems are shown in Fig.3.4a-c.

Fig.3.4a shows an example of a load-lock system to be used to transfer the vessels from one module to the subsequent one. At the end of each module, the vessel is picked up through a piston and transferred within an intermediate chamber. As the vessel is transferred into the intermediate chamber, a metallic sheet at the base of the piston isolates this chamber from the upstream module. After that, the pressure is reduced through a vacuum pump or increased by introducing a controlled flow rate of sterile gas at atmospheric pressure. Once the desired pressure has been reached, the intermediate chamber is open and a second piston pushes the vessel through the track of the downstream module. Once the vessel has been transferred, the intermediate chamber is closed, the pressure is adjusted according to that of the upstream module,

and finally is re-open through the first piston. This apparatus can also be used to induce nucleation by VISF.

Fig.3.4b shows the schematic of an alternative load-lock system to transfer the vessel between two modules. The apparatus is made of two coaxial cylinders: the inner cylinder can rotate, while the external one remains fixed. The vessel enters the load-lock system, through the upper opening; then, the inner cylinder of the apparatus rotates 90°. During rotation, the upper opening is closed, and then a new opening appears in the lower part. At this point, a piston pushes the vessels out of the load lock system over the track of the downstream module.

Fig.3.4c shows the schematic of a rotating load-lock system. As the vessel enters the load-lock apparatus, the rotary valve moves the vessel ahead. During this transition, the valve can undergo different values of pressure, decreasing or increasing pressure, depending on the request. Basically, this rotating load-lock system can also be used to induce the solvent nucleation by performing VISF. More specifically, the vessel (1), coming from the conditioning chamber which is at atmospheric pressure (2), moves into the rotary valve, where the pressure is decreased to the desired pressure. During its passage into the valve, the vessel experiences decreasing pressure (3, 5, 8, 10) assuring that nucleation occurs instantaneously. The valve is connected to a vacuum system and a controlled leakage line to regulate the final pressure (4, 6, 7, 9). After chamber 10, the vial exited the rotary valve and pushed, over a track, into the freezing module.

3.4 Features and advantages of the continuous freeze-dryer

The main advantages reached using the continuous technology proposed in this work are as follows,

1. improve product quality;

2. improve process efficiency and flexibility;

3. reduce processing costs;

4. eliminate the scale-up of a cycle from a laboratory unit to the manufacturing scale.

Product quality is a fundamental issue in the pharmaceutical industry, as marketed drugs need to be not only safe and therapeutically active, but their performance has to be consistent and predictable. In this perspective, the perfect control of every phase of the lyophilization is fundamental to obtain standardized products with the desired characteristics. The concept of continuous freeze-drying here proposed aims to produce lyophilized products with a specific product structure and characteristics. That is possible thanks to i) the control of nucleation via VISF and ii) the control process conditions during drying and, so, avoiding vial-to-vial variability.

The second main advantage of the proposed concept is the improvement in process efficiency and flexibility. Processing time is reduced, operations are more flexible and no manual handling is required during the whole process. Different materials and dosage forms can be processed, i.e., bulk materials in vials and particle-based materials. Moreover, innovative packaging can be processed, such as double-chamber cartridges, syringes, and ampoules.
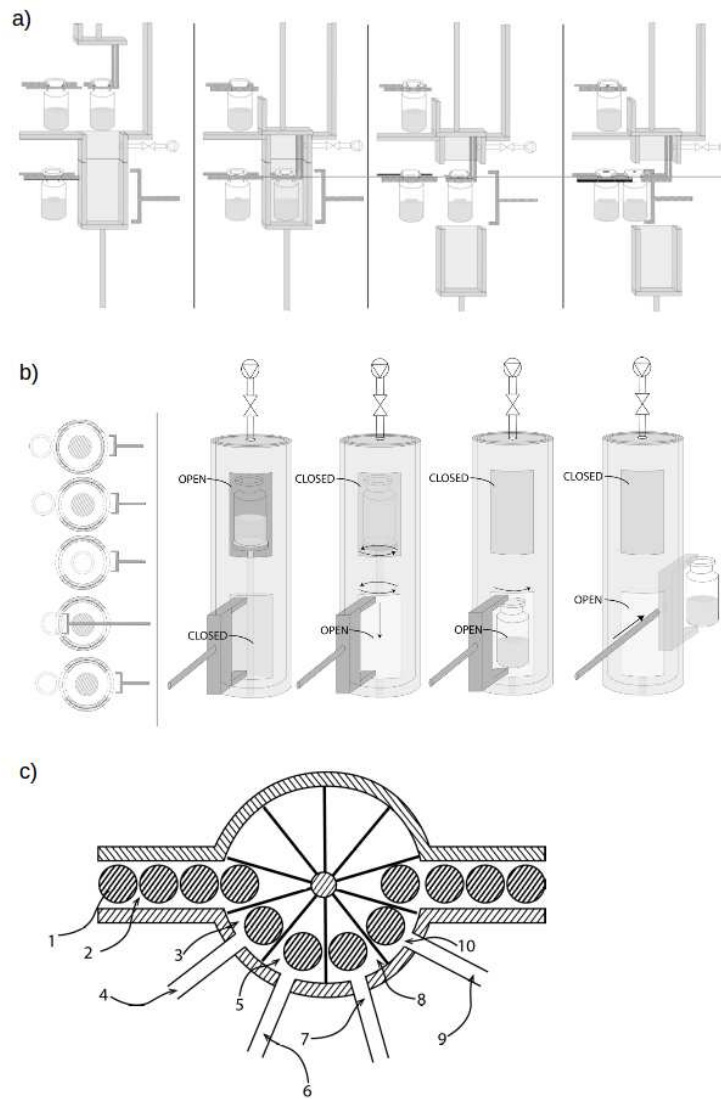
Figure 3.4 Schematic of the load-lock systems based on the (a) use of an elevator, (b) a rotary device and (c) a rotating load-lock system.

Operation flexibility is another important advantage of this continuous technology, as it uses different modules, which are specialized in a single operation. These modules can be combined in order to produce products from different upstream feeds and, eventually, in different dosage forms or with different characteristics, making this technology very flexible (see Fig.3.5).
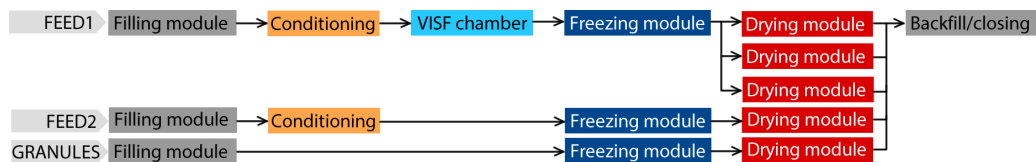
Figure 3.5 Example of potential configurations for the continuous lyophilizer

From the safety point of view, the continuous apparatus reduces the risk of

contamination of products and operators as no manual handling is needed during the whole process.

A further advantage resides in the reduction of processing costs and the increase in revenue due to the higher throughput capability than the batch apparatus, and the reduction of the scale-up efforts from the laboratory to production units. In fact, the scale-up consists of adding modules in parallel to achieve the desired throughput.

Acronyms

API Active Pharmaceutical Ingredient; **CQA** Critical Quality Attributes; **QA** Quality Attributes.

References

Byrn, S., Futran, M., Thomas, H., Jayjock, E., Maron, N., Meyer, R. F., Myerson, A. S., Thien, M. P., and Trout, B. L. (2015). Achieving continuous manufacturing for final dosage formation: Challenges and how to meet them. May 20–21, 2014 Continuous Manufacturing Symposium. *Journal of Pharmaceutical Sciences* 104 (3), pp. 792–802.

Cameron, P. (1997). *Good Pharmaceutical Freeze-Drying Practice*. Buffalo Grove, IL: CRC Press.

Kleinebudde, P., Khinast, J., and Rantanen, J. (2017). *Continuous Manufacturing of Pharmaceuticals*. Vol. 7703. John Wiley & Sons.

Trout, B., Pisano, R., and Capozzi, L. C. (2018). Continuous freeze-drying methods and related products. Pat. req. International Application No. PCT/US2018/030629.

<div style="text-align: right">

4

</div>

Experimental feasibility study of suspended-vial freeze-drying as a first step towards continuous

This chapter aims to demonstrate the feasibility and practical potential of the continuous lyophilizer described in Chapter 3. A laboratory scale lyophilizer has been modified so as to replicate the same heat and mass transfer conditions of the continuous apparatus. The continuous lyophilizer was found to improves heat and mass transfer uniformity, reduce primary and secondary drying time, and enhance vial-to-vial and intra-vial uniformity. Ultimately, the continuous lyophilizer has been tested upon an active molecule, lactate dehydrogenase (LDH), which is very sensitive to both freezing and drying stresses, showing very promising results[*].

4.1 Introduction

Over the past decades, many ideas regarding continuous freeze-drying have been proposed, but none of them has yet been successfully applied in the industry (Rey, 2016; Rhian et al., 1957; Jennings, 1999). In fact, these technologies do not allow either a perfect, precise control of product quality, or guarantee the sterility of the product, and, in the case of particle-based products, can potentially lead to safety problems, due to the exposure of operators to microparticles or allergenic dust in the air. New technologies have recently been proposed, i.e., *active freeze-drying* (Van der Wel, 2015), *fine-spray freeze-drying* (Bullich, 2015) and *spin-freezing* (Corver, 2012; De Meyer et al., 2015). Although these processes increase the efficiency of freeze-drying, some issues and concerns still remain, especially due to the lack of control and

---

[*]Part of the work described in this chapter has been previously published in "Capozzi, L.C., Trout, B. and Pisano, R. (2019) From batch to continuous: freeze-drying of suspended vials for pharmaceuticals in unit-doses. *Industrial & Engineering Chemistry Research*, 58.4: 1635-1649" and refers to the patent application "Trout, B., Pisano, R., and Capozzi, L. C. (2018). Continuous freeze-drying methods and related products. Pat. req. International Application No. PCT/US2018/030629".

standardization of the dried products. Moreover, the final product obtainable using the previous technologies is different from the traditional pharmaceutical dosage form of lyophilized products and may represent a further obstacle to their implementation in industry.

In this chapter, the feasibility of the continuous freeze-drying of suspended vials for pharmaceuticals in unit-doses is demonstrated by replicating the condition of the continuous process in a functional prototype. This chapter sets out the results of this experimental investigation.

The main objectives of this chapter are the following,

i. studying the freezing and drying behavior of products under similar conditions of the continuous apparatus, and compare it to the conventional, batch, process;

ii. investigating the heat transfer of the suspended-vial configuration, i.e., the role of pressure, shelf temperature, and clearance between shelf and vials;

iii. evaluating cycle performances of the suspended-vial configuration and the batch process in terms of primary and secondary drying duration, so as the final residual moisture and its vial-to-vial variability;

iv. exploring the possibility of using the vacuum-induced surface freezing (VISF) for controlling nucleation in the case of suspended-vial configuration;

v. evaluating the impact of suspended-vial configuration on product structure;

vi. demonstrating that the suspended-vial configuration has a beneficial impact on the activity of a model protein.

4.2   Materials and methods

4.2.1   Experimental setup

A functional prototype has been used to reproduce the same conditions that occur in the here proposed continuous process and to study the heat transfer process during freezing and primary drying, as well as their effect on the product quality and characteristics. Various process conditions have been investigated to understand the range of applicability of this new technology better. It should be pointed out that, in this functional version of the continuous lyophilizer, vials do not move along the plant, but undergo similar heat and mass transfer conditions to those of a continuous plant. The following configurations have been investigated,

(A) batch freeze-drying, uncontrolled freezing;

(B) batch freeze-drying of completely irradiated vials, uncontrolled freezing;

(C) suspended-vial freeze-drying, uncontrolled freezing;

(D) batch freeze-drying, controlled freezing;

(E) suspended-vial freeze-drying, controlled freezing.

In this context, 'batch freeze-drying' refers to the standard conventional batch cycles, whereas 'suspended-vial freeze-drying' refers to continuous freeze-drying but here performed in batch mode without moving vials.

We adapted the pilot-scale LyoBeta 25 freeze-dryer (Telstar, Terrassa, Spain) so that vials were suspended over the temperature-controlled shelves and underwent similar processing conditions to those that occur in a continuous lyophilizer (case C and E). The chamber pressure was measured by means of a capacitance manometer (MKS Baratron Type 626a) and a thermo-conductive gauge (PSG-101-S, Infcon, Bad Ragaz, Switzerland). The ratio between these two pressure readings was used to detect the primary drying endpoint.

Experimental runs were carried using two formulations, that is, aqueous solutions of mannitol 5% (w/w) and sucrose 5% (w/w). The solutions were prepared using water for injection (Fresenius Kabi Italia, Isola della Scala, Italy) and filtered using 0.2 μm filters. An aliquot of 3 ml of mannitol solution, or 2 ml of sucrose solution, was filled into tubing vials (10R 24.0 x 45.0, Nuova Ompi, Piombino Dese, Italy). Miniature thermocouples (T type, Tersid, Milano, Italy) were used to measure the product temperature as well as the temperature of the shelves, chamber walls and the air temperature within the chamber.

Handmade supports were used to suspend the vials and simulate similar heat transfer conditions as those of a continuous process. Each support was made of a plexiglass track and was sustained by screw pillars. The neck of the vial was held securely by the track and the vial remained suspended and fixed in the same position. The screw pillars also allowed the height of the tracks to be adjusted and therefore the clearance between the shelf and the vial.

As can be observed in Tab. 4.1, various configurations were studied by varying the vial loading, considering batch vs. continuous mode and uncontrolled versus controlled freezing.

Controlled nucleation was performed using VISF, as proposed by Oddone et al. (2015), see Fig. 4.1. Once the vials had been loaded into the lyophilizer, the shelf temperature was decreased from room temperature to a given $T_{sh,n}$ and was held for 1.5 h to stabilize the whole lot of vials at T_n. At this point, the pressure inside the chamber was reduced from ambient to a given pressure, i.e., 103 Pa for mannitol 5%, thus inducing nucleation in all the vials. The pressure was then released to atmospheric pressure; the shelf temperature decreased to $T_{sh,m}$ and was held at that temperature for 1.5 h, thus promoting ice crystal growth. The complete solidification of the product was achieved after lowering the shelf temperature to 228 K. $T_{sh,n}$ and $T_{sh,m}$ were set to 261 K and 251 K, respectively, for the mannitol 5% solution, and this resulted in T_n equal to 268 K, while the chamber pressure was 130 Pa. Test 10 and 11 were historical data obtained optimized the cycle using LyoDriver control system (Oddone et al., 2016; Fissore et al., 2009; Pisano et al., 2010). LyoDriver requires as input parameters (i) the maximum temperature that the technological fluid can reach during the cycle and (ii) the target temperature of the product; in test 10 and 11, those inputs were 273 K and 247 K respectively.

4.2.2 Characterization of the heat transfer

In the continuous lyophilizer, vials are not in contact with the temperature-controlled shelves, and heat is essentially transferred by radiation and convection.

Table 4.1   List of the experiments carried out to compare the batch and continuous freeze-drying modes.

Test	Solution		Configuration	Nucleation	T_{sh}	P_c
1	Mannitol 5%	(A)	Batch	Spontaneuous	263	10
2	Mannitol 5%	(B)	Contact+radiation	Spontaneuous	263	10
3	Mannitol 5%	(C)	Suspended	Spontaneuous	263	10
4	Mannitol 5%	(C)	Suspended	Spontaneuous	293	4
5	Mannitol 5%	(C)	Suspended	Spontaneuous	298	2
6	Mannitol 5%	(E)	Suspended	VISF (T_n=268 K)	263	3
7	Mannitol 5%	(E)	Suspended	VISF (T_n=268 K)	283	3
8	Mannitol 5%	(E)	Suspended	VISF (T_n=268 K)	293	3
9	Mannitol 5%	(E)	Suspended	VISF (T_n=268 K)	313	3
10	Mannitol 5%	(A)	Batch	Spontaneuous	Optimized	10
11	Mannitol 5%	(D)	Batch	VISF (T_n=268 K)	Optimized	10
12	Sucrose 5%	(A)	Batch	Spontaneuous	253	10
13	Sucrose 5%	(E)	Suspended	Spontaneuous	253	10
14	Sucrose 5%	(E)	Suspended	Spontaneuous	273	2
15	Sucrose 5%	(E)	Suspended	VISF (T_n=268 K)	293	2
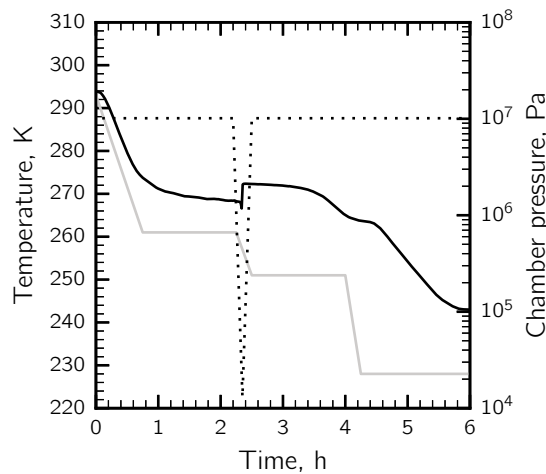
Figure 4.1   Evolution of the pressure (dashed line), shelf temperature (solid gray line) and product temperature (solid black line) when VISF is applied in the suspended-vial configuration.

Knowledge of the contribution of the various heat transfer mechanisms for the two plant configurations, that is, continuous vs. batch, is thus essential to identify their potential advantages and disadvantages. This analysis has to be carried out for both freezing and drying.

Heat transfer during freezing

During freezing, the heat power supplied to the solution was evaluated by monitoring the product temperature of 4 ml of deionized water, and in particular,

$$\dot{Q}_{\mathrm{f}} = m c_{p,\mathrm{ice}} \frac{\Delta T}{\Delta t} \tag{4.1}$$

where m is the mass of water introduced into the vial, $\Delta T / \Delta t$ is the decrease rate of the ice temperature and $c_{p,\mathrm{ice}}$ is the specific heat capacity of ice.

Heat transfer during primary drying

During drying, the heat power supplied to the product was evaluated using a gravimetric test, as described in Pisano et al. (2011). The heat power is given by,

$$\dot{Q}_{\mathrm{d}} = \Delta H_s \dot{m} \approx \Delta H_s \frac{\Delta m}{\Delta t} \tag{4.2}$$

where ΔH_s is the latent heat of ice sublimation and $\Delta m / \Delta t$ is the sublimation rate of ice. The mass of each vial was measured before and after each cycle, and its variation was used to estimate the sublimation rate.

As shown in Pisano et al. (2011), the heat power in conventional freeze-drying depends on the chamber pressure and shelf temperature. In fact, the temperature affects the heat transfer driving force but marginally the heat transfer coefficient, whereas the pressure mainly affects the heat transfer coefficient.

In batch freeze-drying, the heat is supplied by (i) direct conduction from the shelf to the glass at the points of contact, (ii) conduction through the gas in the gap at the bottom of the vial, (iii) radiation from the lower and upper shelves, and from the surroundings, i.e., the chamber walls and door, and (iv) by convection. The heat supplied by direct contact and radiation is independent of the chamber pressure, whereas convection and conduction both depend on the pressure. The heat power to the product reads (Pisano et al., 2011; Pikal et al., 1984),

$$\dot{Q}_{\mathrm{d}} = A_{\mathrm{v}} K_{\mathrm{v}}' (T_{\mathrm{sh}} - T_{\mathrm{b}}) \tag{4.3}$$

where T_{sh} is the temperature of the heating shelf, T_{b} is the product temperature at the bottom of the vial, and A_{v} is the bottom surface of the product. The heat transfer coefficient K_{v}' was determined using gravimetric tests and results from the combination of Eq. 4.2 and 4.3

In the case of suspended-vial freeze-drying, heat is supplied mainly by radiation from the temperature-controlled surfaces. A very simplified expression for the heat power supplied to the product is therefore proposed which consists of using the Stefan-Boltzmann law (Ganguly et al., 2013),

$$\dot{Q}_{\mathrm{d}} = K_{\mathrm{r}}^* (T_{\mathrm{sh}}^4 - T_{\mathrm{b}}^4), \text{ where } K_{\mathrm{r}}^* = A_{\mathrm{tot}} F \sigma_{\mathrm{SB}} \epsilon \tag{4.4}$$

where A_{tot} is the sum of the side, upper and bottom surfaces of the product, F is the view factor of the heating surfaces with respect to A_{tot}, σ_{SB} is the Stefan-Boltzmann constant, ϵ is the emission coefficient of the heating surfaces, T_{sh} is the temperature of the emitting surfaces and T_{b} is the temperature of the product. Once $\dot{Q}_{\mathrm{d}}$ has been

determined, using the gravimetric procedure, and Eq. 4.2 has been applied, it is easy to evaluate the overall radiative heat transfer coefficient K_r^*. It should be pointed out that the expression of the heat transferred in both batch and suspended-vial configuration is much more complicated than as proposed Eq. 4.3 and 4.4, and will be treated in details in Chapter 6.

4.2.3 Product resistance to the vapor flow

The sublimation rate can be expressed as follows,

$$\dot{m} = \frac{A_p}{R_p}(p_{w,i} - p_{w,c}) \tag{4.5}$$

where $p_{w,i}$ and $p_{w,c}$ are the vapor pressure at the sublimation interface and within the chamber, respectively, and R_p is the resistance to the vapor flow, which is mainly due to the dried layer, and A_p is the cross-section of the product.

The resistance to the vapor flow depends on the structure of the dried material, i.e., on the porosity, pore size, connectivity and tortuosity. This resistance can be measured through the product temperature response method using the following expression,

$$R_p = \frac{\Delta H_s(p_{w,i} - p_{w,c})}{K_v'(T_{sh} - T_b)} \quad \text{for batch freeze-drying} \tag{4.6}$$

$$R_p = \frac{A_p \Delta H_s(p_{w,i} - p_{w,c})}{K_r^*(T_{sh}^4 - T_b^4)} \quad \text{for suspended-vial freeze-drying} \tag{4.7}$$

where $p_{w,i}$ is estimated from the measurements of the product temperature at the bottom of the vial (T_b). The product resistance to the vapor flow was studied, for our model solution, for both suspended and non-suspended vials.

4.2.4 Characterization of lyophilized products

The porous structure of the dried product was analyzed using a Scanning Electron Microscope (SEM, FEI type, Quanta Inspect 200, Eindhoven, the Netherlands); the samples were metalized and examined at 15kV and under a high vacuum. The analysis was carried out at different points in the product (top, center, and bottom) to determine the intra-vial heterogeneity. The pore size distribution in the product was obtained from an analysis of the SEM images. Fifty to 150 pores were selected from each image and approximated as an ellipse; the pore dimension was calculated as the equivalent circle with the same area-to-perimeter ratio as that ellipse.

4.2.5 Residual Moisture Analysis

The Karl Fischer titration (KF, Karl Fischer Moisture Meter CA-31, Mitsubishi, Japan) was used to determine the residual moisture content of the sample vials. Hydranal titration solvent (Sigma Aldrich, Milano, Italy) was used in the case of sucrose, whereas formamide was added to those samples containing mannitol; the solution was then sonicated for 5 min. A titration blank was carried out to determine the moisture

concentration in formamide which was, then, subtracted from the net amount of water in each sample.

In the case of sucrose-based solutions, moisture content was analyzed for the batch cycle (test 12) and suspended-vial configuration in the case of both uncontrolled nucleation (test 14) and VISF (test 15). Residual moisture was analyzed at the end of primary drying and at different times during secondary drying; these tests were performed by stopping the cycle. The secondary drying step was carried out using a shelf temperature of 293 K and chamber pressure 2 Pa, whereas for the test 14 and 15 was also performed at 313 K.

4.2.6 Impact of the suspended-vial configuration on the LDH activity

Sample preparation

L-Lactic Dehydrogenase (LDH) was used as a model protein for studying the impact of freezing and drying on its activity and, finally, demonstrating proof-of-principle of the suspended-vial configuration. LDH was chosen as it was broadly studied in the literature and, so, it is particularly well suited to make comparisons between different freezing and drying protocols (Wang, 2000).

LDH from rabbit muscle (Sigma Aldrich, Milano, Italy) was purchased in form of a crystalline suspension in 3.2 M ammonium sulfate solution, pH 6.0. LDH was dialyzed against 100 mM potassium phosphate buffer (pH 7.3) using a dialysis membrane with a cut-off of 3.5 kDa (Pur-A-Lyzer Mega 3500 Dialysis Kit); LDH was dialyzed for 3 hours twice and a third time overnight at 277 K. After dialysis, UV absorbance at 280 nm (6850 UV/Vis spectrophotometer, Jenwa, Stone, Staffordshire, UK) was used to determine the concentration of LDH, using an extinction coefficient of 1.44 $\mathrm{ml\,mg^{-1}\,cm^{-1}}$ (Fang et al., 2018).

$10\ \mathrm{\mu g\,ml^{-1}}$ of LDH was diluted in 5 mM potassium phosphate buffer containing (i) 5% (w/w) sucrose , (ii) 3.5% (w/w) sucrose and 1.5% (w/w) trehalose and (iii) without excipient. Potassium phosphate buffer was prepared from potassium phosphate dibasic and potassium phosphate monobasic (Sigma Aldrich, Milano, Italy); water for injection (Fresenius Kabi Italia, Isola della Scala, Italy) was used for all the solutions. The solutions were filtered using a 0.2 μm filters, and then an aliquot of 2 ml was filled into tubing vials (10R 24.0 x 45.0, Nuova Ompi, Piombino Dese, Italy).

Freeze-thawing and freeze-drying

The following configurations have been investigated,

  (A) batch freeze-drying, uncontrolled freezing;

  (B) batch freeze-drying, controlled freezing;

  (C) suspended-vial freeze-drying, uncontrolled freezing;

  (D) suspended-vial freeze-drying, controlled freezing.

For each configuration, both freeze-thawing and freeze-drying cycles were performed to study the impact of freezing and drying on the LDH stability. Vials were loaded onto precooled shelves at 277 K and cooled down to 228 K using a ramp of about 0.8 K/min. In the case of VISF, nucleation was triggered at 267 K. Primary drying was

performed using a shelf temperature so that maximum product temperature did not exceded collapse temperature, i.e., 240 K. After primary drying was completed, shelf temperature was increased to 293 K in 4 h and hold for other 4 h.

LDH activity assay

The activity of LDH was measured using the Lactate Dehydrogenase Activity Assay Kit provided by Sigma-Aldrich (Milano, Italy). LDH catalyzes the conversion of lactate into pyruvate, and, so, reduces NAD to NADH. The 96-well plate spectrophotometer (Programmable MPT reader DV 990BV4, GDV, Italy) was used to follow the reduction of NAD to NADH by measuring the increase in absorbance at 450 nm.

0, 2.5, 5, 7.5, 10, and 12.5 nmol/well of NADH standards were prepared to generate a standard curve. Prior to measure activity, freeze-dried products were reconstituted with 10 ml of potassium phosphate buffer and, then, further diluted to ensure the readings were within the linear range of the standard curve. 50 µl of that solution and 50 µl of reaction mix (4% v/v of LDH substrate mix in LDH assay buffer) were added in each well; all samples were run in duplicate.

The plate was shaken into the spectrophotometer and incubate at 310 K for 2 min. After that, the initial measurement ($A_{450,ini}$) was taken at the initial time (t_{ini}). One measurement was taken every 5 min and the plate incubated at 310 K in the meanwhile of two consecutive measurements. The final measurement ($A_{450,fin}$) was the penultimate reading before the most active sample exceeded the end of the linear range of the standard curve (t_{fin}).

The decrease in absorption between t_{ini} and t_{fin} for a sample is,

$$\Delta A_{450} = A_{450,fin} - A_{450,ini} \tag{4.8}$$

where each value of absorbance where corrected subtracting the measurement of the background (0 nmol/well of NADH standards). At that point, the amount of NADH generated (n_{NADH}) was determined by comparing ΔA_{450} with the standard curve. The LDH activity of a sample reads,

$$\text{LDH activity} = \frac{n_{\text{NADH}}}{\Delta t_{RXN} V} \times \text{Sample Dilution Factor} \tag{4.9}$$

where Δt_{RXN} is the reaction time ($t_{fin} - t_{ini}$), V is the sample volume in ml added to each well.

4.3 Results

4.3.1 Freezing behavior

A typical temperature profile of the product, shelf, and air in the chamber is shown in Fig. 4.2a for the case of batch and suspended-vial freezing. In the case of batch freezing, the product temperature is always between the shelf temperature and the temperature of the surrounding air. In such a situation, heat is removed from the bottom, as a result of the direct contact between the shelf and the vial, but, at the same time, it is supplied to the vial side by air conduction and convection, thus creating a relatively large temperature gradient within the solution.
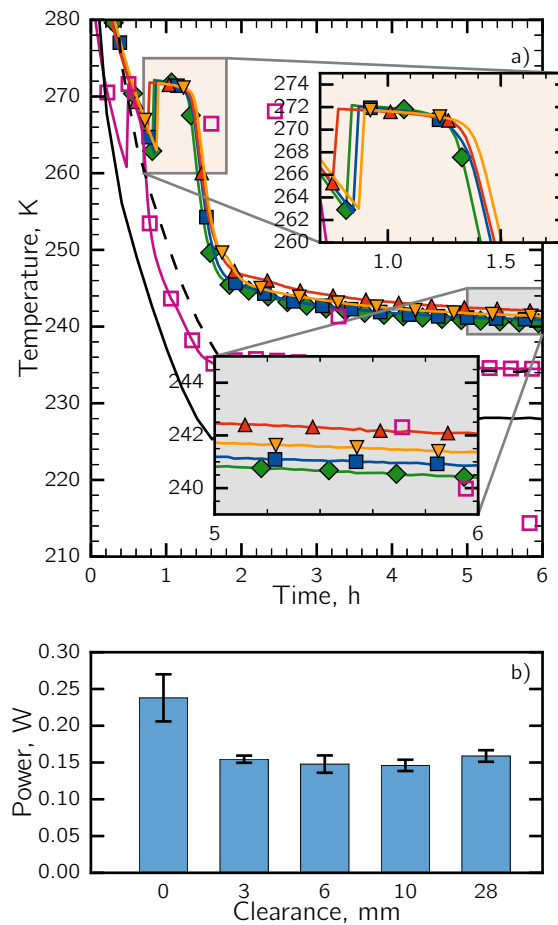
Figure 4.2 (a) Evolution of product temperature in the case of (□) non-suspended vials and suspended vials for different clearance value: (◆) 3 mm, (■) 6 mm, (▲) 10 mm, (▼) 28 mm. The evolution of (——) shelf temperature and that of (- - -) the air are also shown. (b) Average heat power removed during freezing as a function of the shelf-to-vial clearance

On the other hand, in the suspended-vial configuration, heat is essentially removed from the liquid being frozen through air convection. In this case, all the surfaces of the vial experience identical conditions, because the vials are immersed in air and no contact with the shelf occurs. The temperature and velocity of the surrounding air can theoretically be modulated in order to perform different freezing protocols. In this work, we used natural convection and, thus, the only processing parameter that could have been adjusted was the air/shelf temperature. As shown in Fig. 4.2b, the suspended-vial configuration was less efficient for a constant shelf-temperature, in terms of heat removed, that is, 0.24 vs. 0.15 W. However, it should be pointed out that these results are valid only as long as natural convection is the predominant heat transfer mechanism for the suspended-vial configuration. In Chapter 5, it will be shown that, if forced air is used, in place of natural convection, the results could be completely different. The freezing time can be reduced by as much as 1.5 h, or even more by further increasing the air velocity.

As can be seen in Fig. 4.2b, the average heat power removed as a result of adopting

59

suspended-vial freezing was not dependent on the vial-to-shelf clearance. As further confirmation of this result, Fig. 4.2a shows that the temperature of the product during freezing was independent of the vial-to-shelf clearance for the suspended-vial configuration, at least over the 3-28 mm range. A similar result was observed for the freezing time and for the product temperature that is reached at the end of freezing.

The influence of the two freezing configurations on the morphology of the lyophilized product was also investigated. SEM images were used to evaluate the impact of the two freezing configurations on the average size of the pores and their distribution, as well as on the vial-to-vial and intra-vial heterogeneity. An example of the results is shown in Fig. 4.3. The non-suspended freezing led to a compact structure, with pores of approximately 40 μm in diameter. Furthermore, the porous structure was not uniform as the pore size was in the 10-60 μm range, see Fig. 4.3a. On the other hand, the suspended-vial freezing produced a more uniform porous structure, with an average size of 70 μm. This result can be confirmed from the SEM images and the pore size distributions shown in Fig. 4.3b, which show that the pore size ranged from 65 to 80 μm. Our results suggest that suspended-vial freezing promoted crystal growth and led to a more homogeneous structure made up of pores with a narrow size distribution, see Fig. 4.3c.

4.3.2 Drying behavior

The heat transfer in conventional freeze-drying varies significantly according to the position of the vial within the batch, and a batch of vials is conventionally divided into five groups, Fig. 4.4a (Pisano et al., 2011). Vials at the edge of the batch receive more heat than those located in the center, due to the contribution of radiation from the chamber walls. Fig. 4.4b shows, as an example, the spatial distribution of heat power during primary drying, as observed experimentally. It can be observed that the heat power of the edge-vials is about 0.30 W, whereas that of central vials is approximately 0.15 W m^{-2}. This is typical batch freeze-drying behavior, which leads not only to remarkable differences in terms of drying time among the vials but is also a problem during the scale-up of a cycle or when there is a lack of control of the cycles.

On the other hand, when the configuration proposed in this work is adopted, the vials are subject to identical conditions (Fig. 4.4c), and, as a consequence, the variations in heat power between vials of the same lot are modest. It is possible to observe, in Fig. 4.4d, that the heat power during primary drying does not depend on the clearance between the shelf and the vial bottom. In the case of vials in contact with the shelf but completely irradiated, the heat power is about 0.35 W, and thus is much higher than that observed in the case of edge-vials processed in a batch freeze-dryer. In fact, the edge vials in a batch unit are partially shielded by the metallic frame or by the neighboring vials, whereas in our configuration, the vials are almost completely exposed to radiation from the chamber walls and the surrounding area. However, this configuration led to great vial-to-vial variability in the heat transfer, that is, from 0.3 to 0.4 W, because the contribution of the contact between the shelf and the vial is significant and is difficult to control. On the other hand, in the case of suspended vials, the heat power dropped to about 0.2 W, regardless of the clearance, and was surprisingly uniform, thus suggesting that if heat is transferred predominantly by radiation, vial-to-vial uniformity will be increased and the drying time can be controlled more precisely.
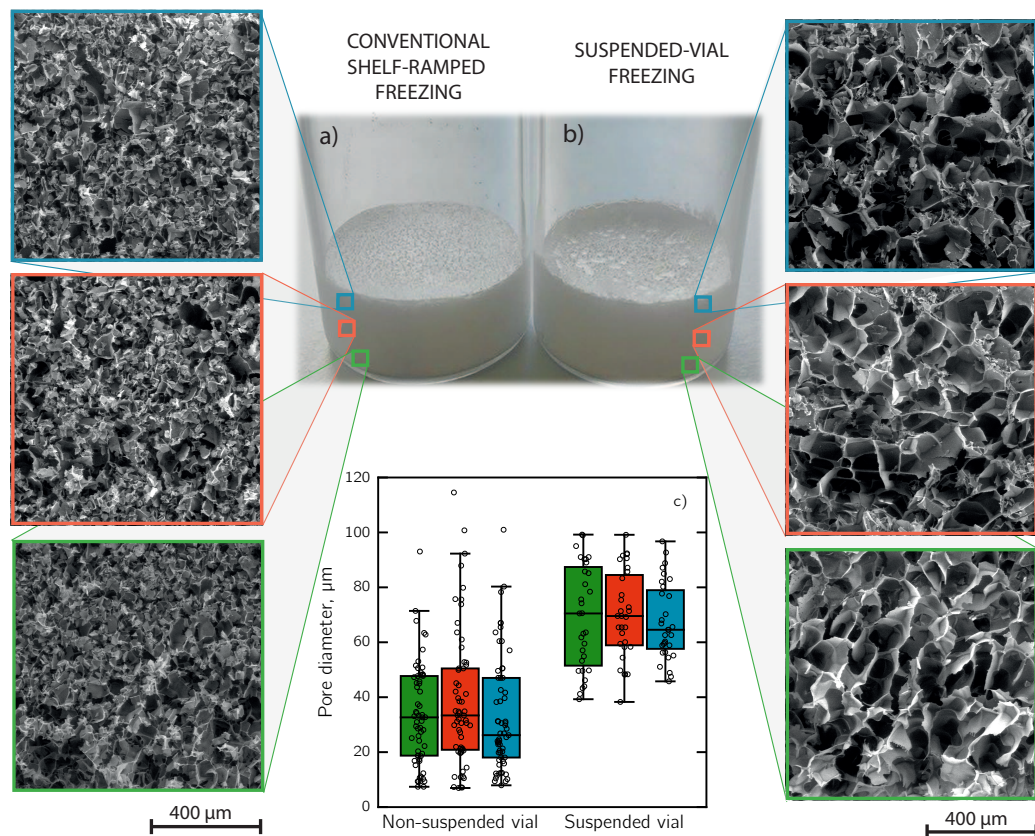
Figure 4.3 Lyophilized samples of mannitol as produced by (a) non-suspended and (b) suspended-vial freezing. (c) Comparison of the mean pore size of a dried product, obtained by means of SEM analysis, for the case of a non-suspended and a suspended vial configuration at different depths in the product, (■) bottom, (■) center and (■) top. The top bar in the box plot refers to the maximum observation while the lower bar refers to the minimum observation. The top of the box refers to the third quartile, the bottom to the first quartile, the middle bar is the median value and the bullets pertain to the original data.

The influence of the processing conditions, namely the shelf temperature and pressure, on the heat power transferred to the product was also investigated. As widely discussed in the literature, the heat power non-linearly increased with pressure, but only for the batch freeze-dryer, while it remained approximately unchanged for the suspended-vial configuration, see Fig. 4.5. This result was expected because the resistance to the heat transfer in a batch freeze-dryer is predominantly determined by conduction through the gas trapped within the gap at the bottom of the vial, which depends on the pressure.

On the other hand, in the case of the suspended-vial configuration, the heat power is almost completely independent of the pressure, because the main relevant heat transfer mechanism is radiation. Fig. 4.5a confirms, in fact, that the heat power remains approximately constant over the 5-20 Pa range. This means that it is possible to increase the sublimation rate by decreasing the pressure as much as possible; in fact, if the pressure is reduced, the driving force for mass transfer is greater and, since the heat power is not influenced by the pressure, the sublimation rate increases.

An example of the beneficial effect of lowering the chamber pressure, in the case of suspended-vial freeze-drying, is that the drying time for mannitol 5% (w/w) was

61
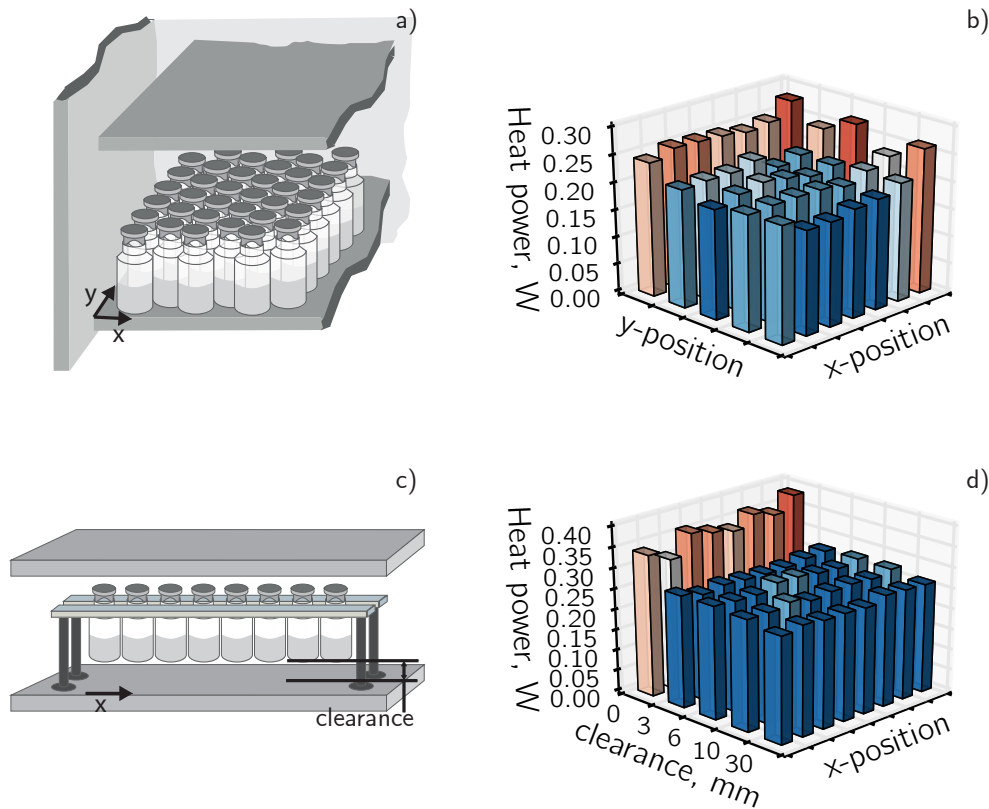
Figure 4.4 Comparison of the heat power in batch and suspended-vial freeze-drying mode. (a) Schematic of the vial positions in the chamber of a typical batch lyophilizer; (b) Spatial distribution of the heat power in a batch lyophilizer; (c) Schematic of the vial positions in a suspended-vial configuration; (d) Spatial distribution of the heat power as a function of the clearance for a suspended-vial configuration.

found to be approximately 14 h, if freeze-dried at 10 Pa and 263 K, while it was found to be 12 h at 5 Pa.

As shown in Fig. 4.5b, heat supplied to the product can be modulated by changing the shelf temperature, e.g., from 0.20 W at 248 K to 0.36 at 273 K. The influence of clearance was negligible in the range investigated here, i.e., from 3 to 28 mm (Fig. 4.5c).

The value of K_r^*/σ_{SB} was about 0.0026 m^2, which means that, since the total area of the product exposed to the heating surfaces is 0.0039 m^2, the overall view factor is about 0.66. A broader investigation on heat transfer will be presented in Chapter 6 using a computation approach.

4.3.3 Batch vs suspended-vial freeze-drying

Batch and suspended-vial lyophilization were compared as far as the processing time, vial-to-vial uniformity and the maximum product temperature excursion during drying are concerned. As a first step, we investigated three plant configurations: (A) vials were loaded on the shelf in a hexagonal arrangement, (B) vials were placed in line and in contact with the shelf, (C) vials were suspended and spontaneous nucleation was used. Configuration (C) can replicate the same heat transfer conditions as the
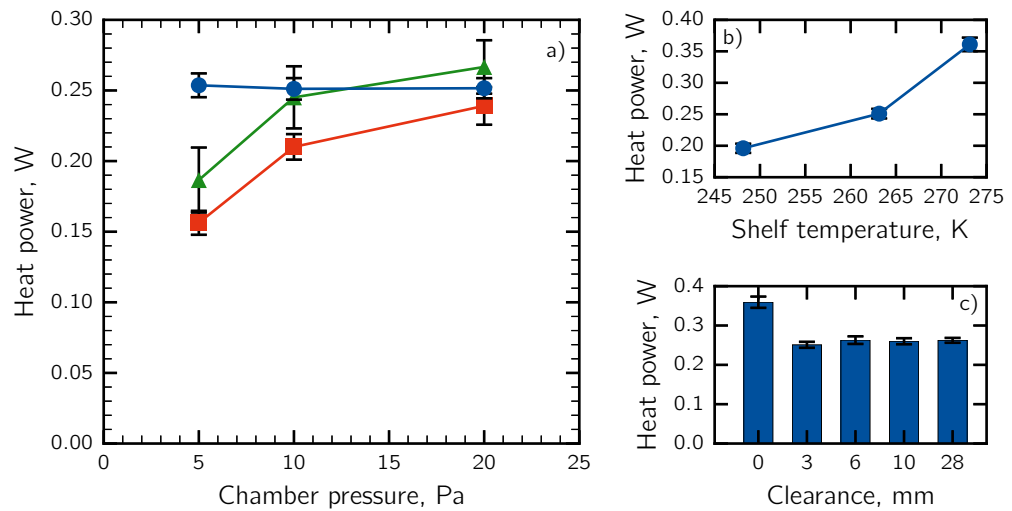
Figure 4.5 (a) Heat power during drying as a function of pressure in the case of (●) a suspended vial, (▲) edge-vials and (■) central vials in a batch lyophilizer; (b) heat power during drying as a function of shelf temperature; (c) heat power during drying as a function of the clearance.

continuous freeze-dryer proposed in this work. These tests were performed without controlling nucleation in the freezing phase. The results of this comparative analysis are shown in Table 4.2.

Table 4.2 Comparison of batch freeze-drying, radiative with vials in contact and suspended vial configurations using mannitol 5%w/w as the model solution.

Test case	Freeze-drying method	Nucleation type	Pressure, Pa	Drying, time, h	Onset/offset, h	$T_{p,max}$, K
1	(A) Batch	Spontaneous	10	22.0	5.2	257
2	(B) Contact+radiation	Spontaneous	10	13.2	1.8	256
3	(C) Suspended	Spontaneous	10	14.1	0.6	253
4	(C) Suspended	Spontaneous	4	10.0	0.7	256
5	(C) Suspended	Spontaneous	2	9.0	0.5	256

In the case of conventional batch freeze-drying (test 1), the drying time was found to be about 22 h, whereas this value dropped to about 14 h in the case of suspended vials performed at the same chamber pressure and shelf temperature (test 3). This occurred for two main reasons, i.e., the higher heat power and smaller mass transfer resistance to water vapor in the dried cake. As already pointed out, the heat power for the suspended vials was higher than that of the central vials in conventional freeze-drying, which represent 90 % of the vials in the batch configuration. Furthermore, the suspended vial configuration produced larger pores and, thus, a smaller mass transfer resistance to the vapor flow and, consequently, a higher rate of sublimation.

Fig. 4.6a compares the product temperature response observed for the three configurations for the constant shelf temperature and pressure. The product temperature represents an important variable that has to be controlled during the primary drying,

63

because it needs to be maintained below a critical temperature, e.g., the collapse temperature or the API deactivation temperature.

The edge-vials showed the highest temperature in the case of conventional batch freeze-drying. Although the central vials represent more than 90 % of the whole batch, the shelf temperature constraint is represented by the edge-vials, which could be overheated more easily.

When primary drying was performed at 263 K and 10 Pa, the maximum product temperature for the suspended vial configuration (test 3) was 4 K lower than that observed for the batch configuration (test 1). This means that a more aggressive cycle can be used considering a constant target for the product temperature.
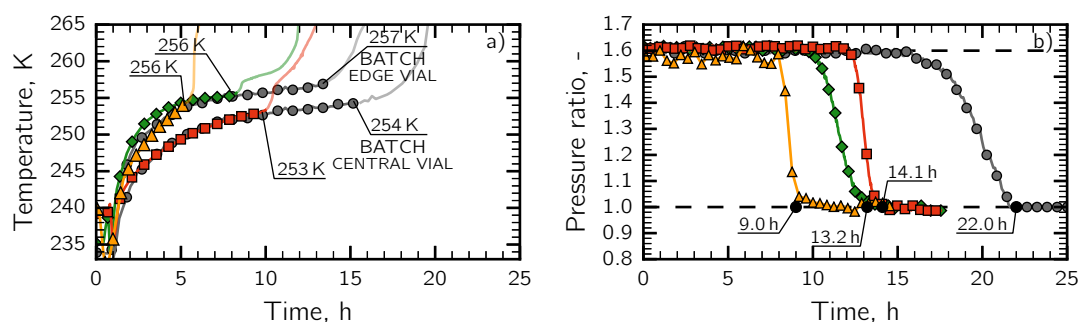
Figure 4.6 (a) Evaluation of the product temperature during primary drying and (b) the onset-offset time of the pressure ratio curve in the case of (●, test 1) conventional freeze-drying, (♦, test 2) conventional freezing followed by the drying of vials in contact and completely irradiated, and (■, test 3) the freezing and drying of suspended vials at T_{fluid}=263 K and P_c=10 Pa, and (▲, test 5) the freezing and drying of suspended vials at T_{fluid}=298 K and P_c=2 Pa,

The three configurations were then compared, in terms of drying time and vial-to-vial heterogeneity, considering a constant chamber pressure and shelf temperature. The drying time was determined as the time at which the pressure ratio signal reached a plateau level. Furthermore, the difference between the onset and offset times was related to the vial-to-vial variability of the drying time. As shown in Fig. 4.6b, the drying time of the batch configuration (test 1) was 22 h, and was found to be much higher than that observed for configurations (B) and (C), that is, 13 h for the test 2 and 14 h for test 3. Moreover, we observed that the batch configuration resulted in the largest vial-to-vial drying time variability. In order to provide a quantitative estimation, the onset-offset time was found to be 5 h for the batch configuration (test 1) and only 0.6 h for the suspended vial configuration (test 3). This was due to the fact that the heat power was supplied uniformly to the vials in the suspended vial configuration and, hence, all the vials were subjected to identical heat transfer conditions, whereas, in the case of conventional batch freeze-drying, the heat power supplied to the vials placed at the edge of the batch was much greater than that received by the central vials.

We compared the performances of the batch configuration and suspended-vial freeze-drying, considering that the maximum product temperature cannot exceed the target temperature, i.e., 257 K. In this case, the target temperature was chosen merely as an example of the possible target temperatures and it was only used to compare the performances of the two configurations. Suspended-vial freeze-drying was performed

at 293 K and 4 Pa in test 4, and this resulted in a primary drying time of 10 h. In test 5, the pressure was further reduced to 2 Pa, the shelf temperature increased to 298 K, and a further reduction in drying time, i.e., 9 h, was obtained. In both cases, the product remained below the target temperature.

4.3.4 VISF applied to the suspended-vial configuration in the case of a crystalline solute

Finally, we performed freeze-drying cycles using suspended vials coupled with VISF (configuration E). When using mannitol as the model formulation, and carrying out the primary drying at 263 K and 3 Pa (test 6), the drying time was about 14 h, while the maximum temperature reached by the product during drying was only 245 K. In tests 7 and 8, the shelf temperature increased to 283 K and 293 K, respectively, and the primary drying dropped to 11 h and 10 h. A further increase to 313 K in the shelf temperature (test 9) decreased the primary drying duration to about 7.5 h, and only in this case product temperature reached the target temperature of 257 K, see Fig. 4.7.

This sharp reduction in drying time was possible because (a) VISF produced larger pores, and as a result, the decreasing mass transfer resistance (R_p) and (b) the driving force to the mass transfer ($p_{w,i} - p_{w,c}$) increased as the chamber pressure decreased. Moreover, unlike the case of batch freeze-drying, lowering the chamber pressure did not affect the heat power supplied to the suspended vials, as the heat was essentially transferred by radiation, see Section 4.3.2.
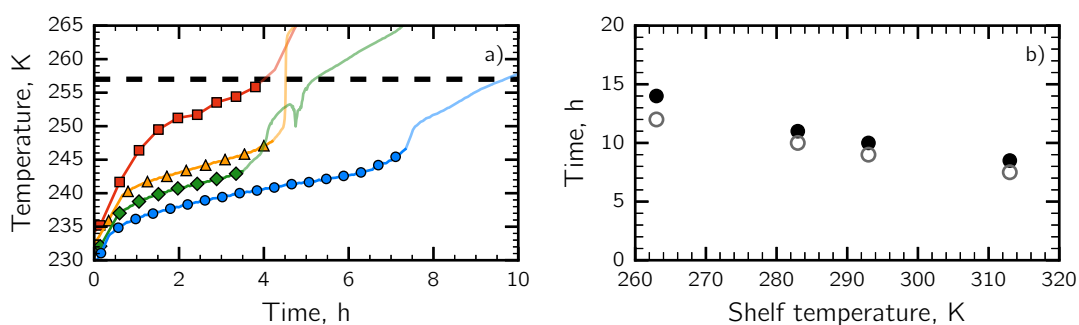
Figure 4.7 (a) Evolution of the product temperature during primary drying in the case of suspended-vial freeze-drying coupled with VISF, using (●, test 6) 263 K, (◆, test 7) 283 K, (▲, test 8) 293 K, (■, test 9) 313 K as the shelf temperature and 3 Pa. (b) Drying time in terms of (●) offset and (○) onset times.

VISF applied to a suspended-vial configuration was compared with the batch mode, in the case of spontaneous and controlled nucleation, see Fig. 4.8.

We used the LyoDriver control system for the batch cycles to optimize the cycles in-line, and set 247 K as the target temperature. Test 10 consisted of a batch cycle in which spontaneous nucleation occurred, whereas nucleation was induced at 269 K using VISF in test 11. The duration of the primary drying in test 10 was about 30 h, whereas it dropped to about 19 h when VISF was used. When VISF was applied to the suspended-vial configuration, which was not in-line optimized, the duration of the primary drying was about 10 h and the product temperature did not exceed the target temperature. This result demonstrated that the suspended-vial configuration, together with continuous freeze-drying, is able to reduce the duration of the primary
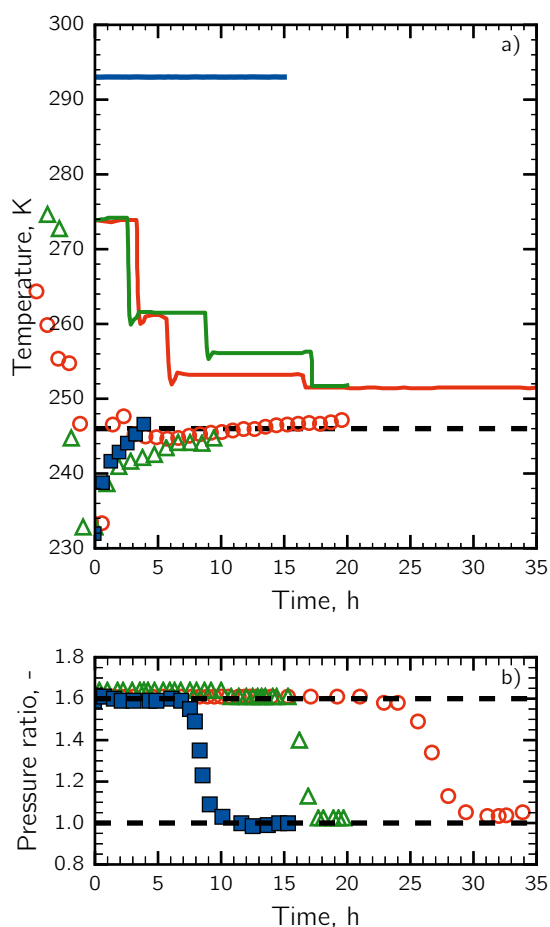
Figure 4.8 (a) Evolution of the shelf temperature (solid lines) and the product temperature (symbols); (b) Pirani/Baratron pressure ratio. ($\bigcirc$ and ——, test 10) batch and ($\triangle$ and ——, test 11) VISF applied to a batch optimised in-line using the LyoDriver control system; ($\blacksquare$ and ——, test 8) VISF coupled to a suspended-vial configuration ($T_{sh} = 293\,K$, $P_c = 3\,Pa$). The target temperature was set to 247 K.

drying compared to the optimized batch cycles.

Fig. 4.9 shows the resistance to water vapor for the three configurations, and it can be observed that VISF produces products with large open pores and, as a result, the mass transfer resistance decreases dramatically during drying. Oddone et al. (2016) has already demonstrated that VISF is able to reduce vial-to-vial variability in the product structure.

4.3.5 Suspended-vial configuration applied to an amorphous excipient

Another analysis was performed using a solution with an amorphous excipient, i.e., sucrose 5% w/w. The process conditions for the batch (test 12) and the suspended-vial configuration (test 13, 14) were chosen so that the product temperature did not exceed the target temperature, i.e., 240 K. In other words, tests 12 and 13 were carried out at 253 K and 10 Pa, and test 14 at 273 K and 2 Pa. As shown in Table 4.3, the primary drying was completed in about 18 h in the case of the batch cycle, whereas, under constant process conditions, the primary drying time was 13 h for the suspended-
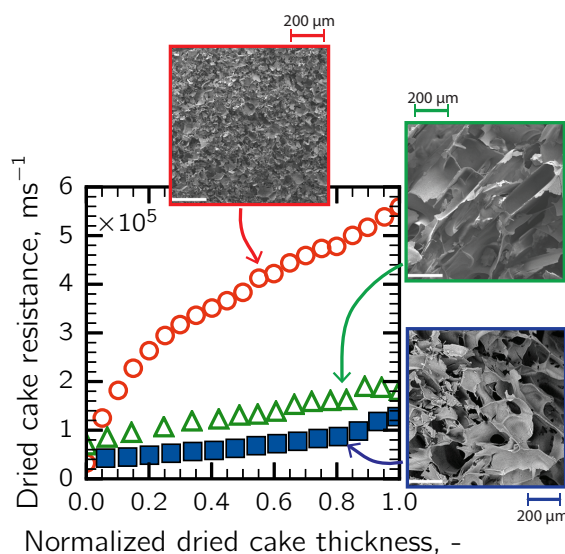
Figure 4.9 Resistance to water vapor in the case of (○, test 10) batch and (△, test 11) VISF applied to batch; (■, test 7) VISF coupled to a suspended-vial configuration (mannitol 5%).

vial freeze-drying case; in test 14, by lowering the pressure to 2 Pa, we were able to conclude the primary drying after only 8.8 h. Using a suspended-vial configuration, we obtained a substantial decrease in the primary drying as a result of several factors. First, the typical edge vial effect of the batch configuration was avoided and, as a result, sublimation occurred at the maximum rate in each vial. Moreover, it was possible to further increase the sublimation rate by lowering the chamber pressure; the chamber pressure and heat transfer are essentially independent in a suspended-vial configuration. The decrease in drying time was only partially due to the much larger pore structure in the dried cake; the R_p shown in Fig. 4.10 is very similar for tests 10 and 11.

Table 4.3 Comparison of batch and suspended-vial configurations in the case of the freeze-drying of sucrose 5% (w/w) in 10R vials.

Test case	Freeze-drying method	Nucleation type	Pressure, Pa	Drying, time, h	Onset/ offset, h	$T_{p,max}$, K
12	(A) Batch	Spontaneous	10	17.8	2.9	240
13	(E) Suspended	Spontaneous	10	13.0	1.1	240
14	(E) Suspended	Spontaneous	2	8.8	0.9	240
15	(E) Suspended	VISF (T_n=268 K)	2	5.5	0.5	239

Finally, we performed a test in which VISF was coupled to a suspended-vial configuration, and a sharp reduction of 5.5 h was obtained in the drying time (test 15). Therefore, using VISF coupled with a suspended-vial configuration, it was possible to substantially decrease the drying time while avoiding the usual batch constraint, and considerably increasing the sublimation rate as a result of the larger pores in the dried cake, see Fig. 4.10.
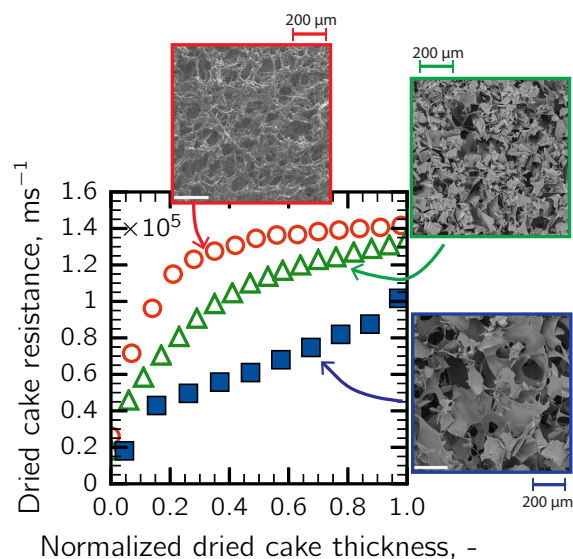
Figure 4.10 Resistance to the vapor flow in the case of (○, test 10) batch, (△, test 11) suspended-vial and (■, test 7) VISF coupled to a suspended-vial configuration (sucrose 5%).

4.3.6 Secondary drying

The residual moisture of the sucrose-based products was measured at the end of primary drying and after 2, 4 and 6 h of secondary drying for both batch (test 12) and suspended-vial configuration (test 14 and 15), see Fig. 4.11.
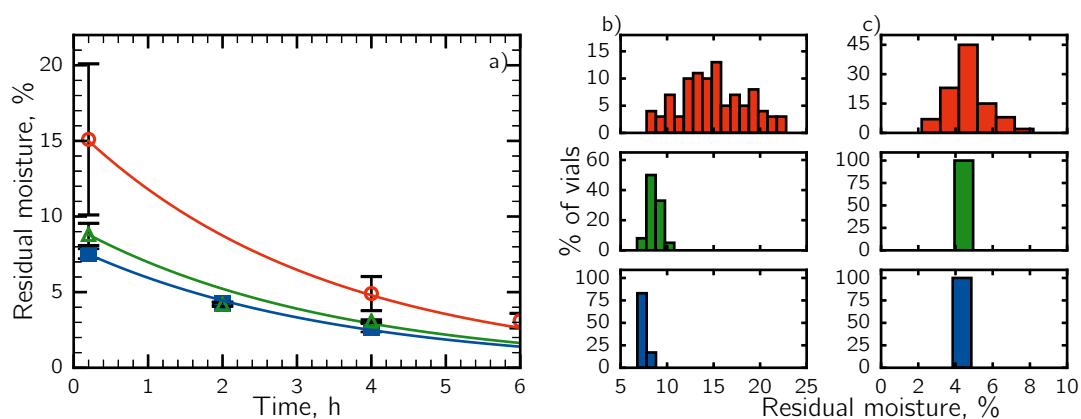
Figure 4.11 (a) Evolution of residual moisture during secondary drying; (b) residual moisture distribution within vials at the end of primary drying and (c) at the end of secondary drying. Data refers to sucrose solutions in the case of (○ and ——, test 12) batch, (△ and ——, test 14) suspended-vial and (■ and ——, test 15) VISF coupled to a suspended-vial configuration.

As shown in Fig. 4.11b, at the end of primary drying, the residual moisture observed in the central vials of the batch was 15.5 %, with a standard deviation of 5.2 %, whereas in the side vials was only about 10 %. On the other hand, the suspended-vial configuration led to a lower value of residual moisture and a substantial reduction of its variability, i.e., 8.8 ± 0.7 % for spontaneous nucleation and 7.5 ± 0.3 % for VISF. These results are somewhat counterintuitive since desorption rate depends on the specific surface area of the dried matrix, and, in particular, it increases as the

pore size decreases. In the case of suspended-vial configuration (test 14 and 15), pore size was much higher than in the batch configuration (test 12), but the residual moisture at the end of primary drying was still much lower. This sharp reduction was due to the fact that, in the case of suspended-vial configuration, the heating surfaces entirely irradiated the vials, increasing the temperature of the dried matrix and, finally, promoting desorption already during primary drying. Contrary, in the batch configuration, chamber walls partially irradiate only side vials and not central ones.

As shown in Fig. 4.11c, in the suspended-vial configuration, after 2 h of secondary drying carried out at 293 K and 2 Pa, the residual moisture was 4.2 ± 0.1 % for both spontaneous nucleation and VISF. The residual moisture after 2 h of secondary drying carried out at 313 K was 2.4 ± 0.2 % for spontaneous nucleation, and 1.8 ± 0.1 % for VISF. In the case of the batch configuration, after 4h of secondary drying at 293 K and 2 Pa, the residual moisture of central vials was 4.9 ± 1.1 % and 4.0 ± 0.4 % for side-vials. This result demonstrated that the suspended-vial configuration was able to reduce the secondary-drying duration and the vial-to-vial variability of the residual moisture content.

In the case of the mannitol-based products, the residual moisture observed within the central vials of the batch was 3.17 ± 1.63 % at the end of primary drying (test 1), whereas, for the suspended-vial configuration (test 9) was 1.01 ± 0.28 %. Assuming that the residual moisture target was 1 %, several hours of secondary drying is still needed in batch configuration (Oddone et al., 2017), whereas it can be skipped in the case of suspended-vial configuration, which makes it possible to further reduce the total cycle time.

4.3.7 Impact of suspended-vial configuration on the LDH activity

The activity recovery of LDH after freezing and freeze-drying have been studied for different formulations, i.e., sucrose 5%, trehalose 5%, sucrose/trehalose 2.5/2.5% and, finally, without excipients; these formulations were prepared in potassium phosphate buffer. Three different configurations were compared, i.e., (i) conventional shelf-ramped freezing followed by conventional batch drying, (ii) suspended-vial freezing and drying, (iii) suspended-vial VISF (T_n=268 K) and drying.

The first step of this analysis consisted of studying the effect of freezing on protein degradation, see Figure 4.12a. The analysis of the activity recovery of LDH in buffer solution without excipients showed that the conventional shelf-ramped freezing (configuration *i*) presented the lowest recovery, whereas there was a relative increase of about 15% in the case of suspended-vial spontaneous freezing (ii) and of 27% in the case of suspended-vial VISF. These results are perfectly in agreement with those published by Fang et al. (2018), in which the recovery in the case of VISF at T_n=269 K (performed in the batch configuration in that specific case) was about 20% higher than that found in the case of conventional shelf-ramped freezing. This trend is much more evident for the solutions with the excipients. For instance, sucrose/trehalose formulation presented the highest activity recovery in the case of suspended-vial freezing, whereas there was a relative decrease of about 55% in the case of suspended-vial uncontrolled freezing and of 69% for the batch configuration.

Figure 4.12b shows the recovery activity after drying for the three configurations. The suspended-vial VISF followed by drying presented the higher value of recovery
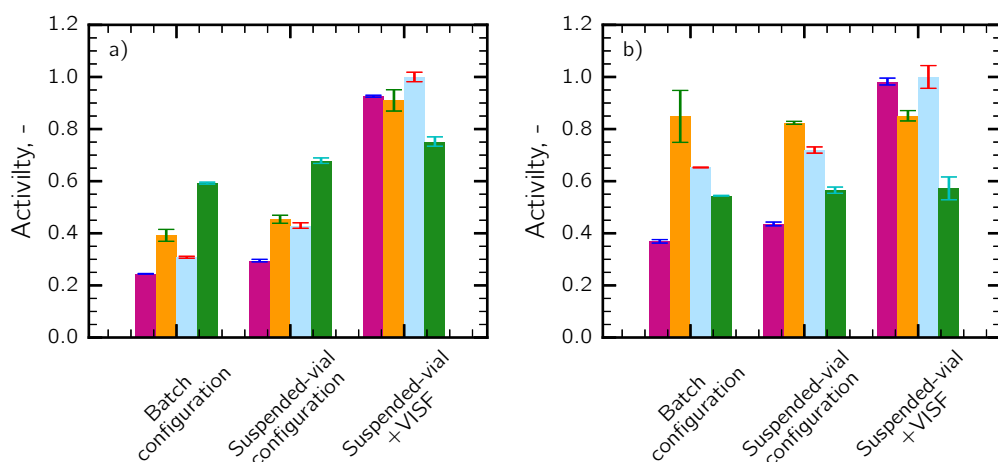
Figure 4.12 (a) Relative activity recovery after freezing and (b) after drying. Data refers to the following formulations (■) sucrose 5%, (■) trehalose 5%, (■) sucrose/trehalose 2.5/2.5% and (■) potassium phosphate buffer.

activity no matter which was the formulation. As expected, the solution without excipients showed lower recovery activity among the formulations. Compared to suspended-vial VISF, the activity loss in the case of suspended-vial without controlling freezing was about 2% and 5% in the case of the batch configuration without controlling freezing. As a matter of fact, Fang et al. (2018) reported that the difference in the activity recovery after drying between uncontrolled freezing and VISF at T_n=269 K was about 8%, whereas Cochran and Nail (2009) reported that there was a difference of 60% in recovery activity in a range of supercooling of 10 K. It should be pointed out that the value of the final RM can also be a cause of protein deactivation, especially in the case of long storage.

In the case of sucrose/trehalose formulation, the differences in the values of activity recovery among the three configurations were much more evident, i.e., 28% activity loss in the case of suspended-vial without controlling freezing and 35% in the case of the batch compared to the suspended-vial VISF.

The higher activity recovery showed by using the suspended-vial configuration was due to the reduced specific surface area (SSA). In fact, as shown in the previous sections, the suspended-vial configuration was able to increase ice crystals dimension (and so, reduce SSA), which is much more evident when VISF is used. Since LDH, like many other proteins (Xu et al., 2014; Fishbein and Winkert, 1977; Sarciaux et al., 1999; Jiang and Nail, 1998), can be denaturated at the ice/freeze-concentrate interface, lowering SSA by using suspended-vial configuration mitigated the activity loss. Moreover, since VISF allows perfect control of nucleation and, finally, of SSA, it can be possible to reduce the variability in the recovery activity within the production.

4.4 Conclusions

A preliminary analysis of the new pharmaceutical freeze-drying concept, which makes it possible to move from batch to continuous manufacturing, has been reported in this chapter. The continuous flow of vials is achieved by suspending them over a

moving track. The vials move through chambers which have different pressure and temperature conditions and are separated by a sluice-gate system.

In order to obtain a quantitative estimation of the advantages of the proposed continuous strategy, with respect to the batch one, a functional version of the continuous plant has been set up, adapting a batch freeze-dryer. This plant allowed us to simulate the same heat transfer conditions to which vials would be exposed in a continuous lyophilizer. The performances of the batch and continuous configurations were evaluated in terms of processing time and vial-to-vial variability.

We have demonstrated that suspended vial freezing leads to a final product which has a larger and more uniform pore structure than that obtained with conventional freezing, which makes the drying step faster.

The suspended vial configuration has allowed more accurate control of the heat input, which is transferred uniformly to all the vials being processed. The freeze-drying of suspended vials has led to a reduction in the drying time and in the onset-offset time.

The obtained results have demonstrated the feasibility of our concept as a valid alternative to conventional batch freeze-drying, which may open up new perspectives and opportunities to completely re-think the production of parenteral products, and make freeze-drying more efficient and versatile.

Acronyms

KF Karl Fischer Titration; **LDH** L-Lactic Dehydrogenase; **NAD** Nicotinamide denine dinucleotide; **NADH** Nicotinamide adenine dinucleotide reduced; **SEM** Scanning Electron Microscope; **SSA** Specific surface area.

List of symbols

A_{450} absorbance at 450 nm, -

A_p inner cross-sectional area of the vial, m^2

A_{tot} total area of the vial, m^2

A_v outer cross-sectional area of the vial, m^2

$c_{p,ice}$ specific heat capacity of ice, $J\,kg^{-1}$

F radiation view factor, -

ΔH_s enthalpy of sublimation, $J\,kg^{-1}$

K_r^* overall radiative heat transfer coefficient for the suspended vial configuration, $J\,s^{-1}\,K^{-4}$

K_v' heat transfer coefficient between the shelf and the vial bottom, $J\,s^{-1}\,m^{-2}\,K^{-1}$

m mass, kg

n_{NADH} nmol of NADH generated during the reaction time, -

$p_{w,c}$ partial pressure of water in the drying chamber, Pa

$p_{w,i}$ partial pressure of water at the sublimating interface, Pa

$\dot{Q}_d$ heat flow supplied to the product during drying, $J\,s^{-1}$

$\dot{Q}_f$ heat flow supplied to the product during freezing, $J\,s^{-1}$

R_p resistance of the dried layer to vapor flow, $m\,s^{-1}$

T_b product temperature at vial bottom, K

T_{sh} shelf temperature, K

$T_{sh,m}$ holding temperature after the induction of nucleation, K

$T_{sh,n}$ holding temperature before the induction of nucleation, K

V volume, m^3

Greek letters

ϵ emissivity, -

σ_{SB} Stefan–Boltz constant, $W\,m^{-2}\,K^{-4}$

Subscript

fin   radiative fin

ini initial

RXN   reaction

References

Bullich, R (2015). Continuous Freeze Drying. In: *PharmaProcess Forum, October 2–6, 2015, Barcelona, Spain*.

Cochran, T. and Nail, S. L. (2009). Ice nucleation temperature influences recovery of activity of a model protein after freeze drying. *Journal of Pharmaceutical Sciences* 98 (9), pp. 3495–3498.

Corver, J. A.W. M. (2012). Method and system for freeze-drying injectable compositions, in particular pharmaceutical compositions. U.S. pat. 20140215845 A1.

De Meyer, L, Van Bockstal, P.-J., Corver, J, Vervaet, C, Remon, J. P., and De Beer, T (2015). Evaluation of spin freezing versus conventional freezing as part of a continuous pharmaceutical freeze-drying concept for unit doses. *International Journal of Pharmaceutics* 496 (1), pp. 75–85.

Fang, R., Tanaka, K., Mudhivarthi, V., Bogner, R. H., and Pikal, M. J. (2018). Effect of controlled ice nucleation on stability of lactate dehydrogenase during freeze-drying. *Journal of Pharmaceutical Sciences* 107 (3), pp. 824–830.

Fishbein, W. and Winkert, J. (1977). Parameters of biological freezing damage in simple solutions: catalase. I. The characteristic pattern of intracellular freezing damage exhibited in a membraneless system. *Cryobiology* 14 (4), p. 389.

Fissore, D., Pisano, R., Velardi, S., Barresi, A., and Galan, M. (2009). PAT tools for the optimization of the freeze-drying process. *Pharmaceutical Engineering*.

Ganguly, A., Nail, S. L., and Alexeenko, A. (2013). Experimental determination of the key heat transfer mechanisms in pharmaceutical freeze-drying. *Journal of Pharmaceutical Sciences* 102 (5), pp. 1610–1625.

Jennings, T. A. (1999). *Lyophilization: introduction and basic principles*. New York: CRC Press.

Jiang, S. and Nail, S. L. (1998). Effect of process conditions on recovery of protein activity after freezing and freeze-drying. *European Journal of Pharmaceutics and Biopharmaceutics* 45 (3), pp. 249–257.

Oddone, I., Fulginiti, D., Barresi, A. A., Grassini, S., and Pisano, R. (2015). Non-invasive temperature monitoring in freeze drying: control of freezing as a case study. *Drying Technology* 33 (13), pp. 1621–1630.

Oddone, I., Van Bockstal, P.-J., De Beer, T., and Pisano, R. (2016). Impact of vacuum-induced surface freezing on inter-and intra-vial heterogeneity. *European Journal of Pharmaceutics and Biopharmaceutics* 103, pp. 167–178.

Oddone, I., Barresi, A. A., and Pisano, R. (2017). Influence of controlled ice nucleation on the freeze-drying of pharmaceutical products: the secondary drying step. *International Journal of Pharmaceutics* 524 (1-2), pp. 134–140.

Pikal, M., Roy, M., and Shah, S. (1984). Mass and heat transfer in vial freeze-drying of pharmaceuticals: Role of the vial. *Journal of Pharmaceutical Sciences* 73 (9), pp. 1224–1237.

Pisano, R., Fissore, D., Velardi, S. A., and Barresi, A. A. (2010). In-line optimization and control of an industrial freeze-drying process for pharmaceuticals. *Journal of Pharmaceutical Sciences* 99 (11), pp. 4691–4709.

Pisano, R., Fissore, D., and Barresi, A. A. (2011). Heat transfer in freeze-drying apparatus. In: *Developments in Heat Transfer*. Rijeka, Croatia: InTech, pp. 92–114.

Rey, L. (2016). *Freeze-Drying/Lyophilization of Pharmaceutical and Biological Products*. CRC Press, New York.

Rhian, M, Maister, H., and Hutton, R. (1957). A continuous freeze drier for laboratory studies. *Applied Microbiology* 5 (5), p. 323.

Sarciaux, J.-M., Mansour, S., Hageman, M. J., and Nail, S. L. (1999). Effects of buffer composition and processing conditions on aggregation of bovine IgG during freeze-drying. *Journal of Pharmaceutical Sciences* 88 (12), pp. 1354–1361.

Van der Wel, P. G. J. (2015). Active Freeze Drying. In: *Proceedings of 5th European Drying Conference*. Oct. 21–23, 2015. Budapest, Hungary.

Wang, W. (2000). Lyophilization and development of solid protein pharmaceuticals. *International Journal of Pharmaceutics* 203 (1-2), pp. 1–60.

Xu, Y., Grobelny, P., Von Allmen, A., Knudson, K., Pikal, M., Carpenter, J. F., and Randolph, T. W. (2014). Protein quantity on the air–solid interface determines degradation rates of human growth hormone in lyophilized samples. *Journal of Pharmaceutical Sciences* 103 (5), pp. 1356–1366.

PART III

Multi-scale modeling of continuous freeze-drying

5

Modeling freezing

Freezing represents is a key step in lyophilization as it determines the final characteristics of the dried product. The perfect control of freezing is fundamental to produce standardized products with the desired final attributes, to predict its variability within production and the losses due to undesired off-target products; this is particularly true in the perspective of moving to continuous freeze-drying. In this chapter, a mathematical model of freezing is developed for both batch and continuous freeze-drying, as well for spontaneous and controlled nucleation. This model was used to compare the batch and the continuous technology in terms of product structure, vial-to-vial and intra-vial variability[*].

5.1 Introduction

As discussed in Section 2.2.1, freezing is a key step in freeze-drying because it has a significant impact on such product characteristics as morphology, crystallinity and surface area, which depend on the nucleation temperature and freezing rate (Searles et al., 2001; Goshima et al., 2016). The product structure is a key factor for the production of stable and valuable dried products, because it affects the stability of APIs, determines the drying and desorption rate, the appearance of the product, its residual moisture and reconstitution time (Hottot et al., 2007). The number of scientific papers published over the last decade regarding the role of freezing and the method for controlling nucleation has increased parallel to the rise of requirements of quality, homogeneity, and standardization of freeze-dried products set by the regulatory authorities.

From the perspective of developing a continuous technology, the control of freezing is fundamental to obtain products with uniform and specific characteristics. To do that,

---

[*]Part of the work described in this chapter has been previously published in "Pisano, R. and Capozzi L.C. (2017) Prediction of product morphology of lyophilized drugs in the case of Vacuum Induced Surface Freezing. *Chemical Engineering Research and Design* 125, pp. 119-129" and "Capozzi, L.C. and Pisano, R. (2018) Looking inside the 'black box': Freezing engineering to ensure the quality of freeze-dried biopharmaceuticals. *European Journal of Pharmaceutics and Biopharmaceutics* 129, pp.58-65".

neither trial-and-error nor black box approaches, which are widely used to design freeze-drying cycles, are satisfactory to achieve the consistent product quality expected by using continuous manufacturing.

A mathematical model of freezing of pharmaceutical solutions in a vial was developed to estimate the average pore size and its distribution within the lyophilized product in the case of conventional, batch freezing, and the case of suspended-vial freezing. The latter represents the configuration used in the continuous apparatus proposed in this thesis. Moreover, the model was developed to study both spontaneous and controlled nucleation via vacuum-induced surface freezing (VISF). Summarizing, this chapter aims at,

  i. study heat transfer during freezing;

 ii. investigate the impact of freezing protocols on product structure, with particular regard to pore size distribution and its vial-to-vial variability;

iii. develop a modeling tool for designing freezing protocols in the continuous lyophilizer.

To make this chapter more readable, some details are reported in Appendix ref-freezing.

5.1.1   The fundamentals of freezing

During freezing, a pharmaceutical solution is cooled and its temperature is lowered below its freezing point to promote solidification. As shown in Figure 5.1, (A) the solution is first cooled down; during this first step, the liquid in the vial appears transparent and clear. Then, once the temperature is well below the equilibrium freezing point, nucleation occurs (B) and the solution becomes opaque because of the presence of ice crystals of sufficient size and in sufficient concentration to make it optically visible. The product temperature rises sharply from nucleation temperature T_n, which is stochastic, to the equilibrium freezing point. At this point, ice crystals start to grow (C) and the solution becomes lighter and lighter until the product becomes milky-white, which indicates that the product is completely frozen (D).

In the last decade, a certain number of methods have been proposed for controlling nucleation during freezing of pharmaceutical solutions. Among these, VISF has been chosen to control nucleation in the continuous lyophilizer, because it is relatively simple to perform, easy to replicate and flexible enough for producing lyophilized products with the desired characteristics.

VISF, as modified by Oddone et al. (2014), consists of (i) cooling down the product at given temperature (T_n), (ii) maintaining the product at T_n for 1 hour, (iii) decreasing chamber pressure for a short time to induce nucleation, (iv) cooling down the product until complete solidification occurs. By using this procedure, nucleation is induced by evaporation of water at the top of the solution and then propagates downwards. Once nucleation has occurred, ice crystals begin to grow until T'_g is reached. During this phase, the freezing front moves upwards, forming three different regions, an icy zone at the bottom and a liquid zone at the top, divided by a mushy zone where ice crystals are in suspension in the undercooled solution.
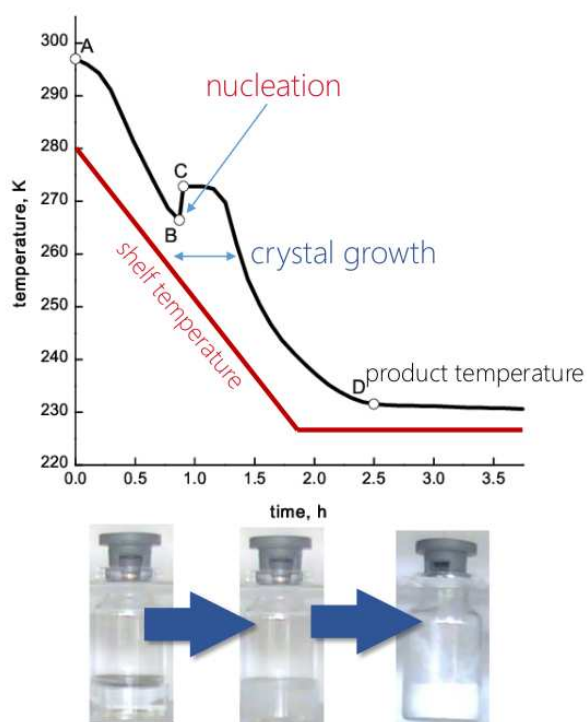
Figure 5.1 Example of evolution of product and shelf temperature during freezing of a pharmaceutical solution.

5.1.2 Batch vs. continuous configuration

In conventional freezing, as performed in a batch cycle, vials are loaded over the shelves into the chamber; in an industrial apparatus, the loading process requires a long time, up to 6 h, and represents an important issue for achieving the uniformity of products within a batch. Once the vials are loaded, shelf temperature is decreased according to the desired protocols; usually, these protocols do not include controlled nucleation as it is difficult to perform at the industrial scale. Heat transfer involves convection, conduction in the small gap between the vial and the shelf, contact with the shelf and radiation, see Figure 5.2.

Freezing as performed in the continuous apparatus proposed in this thesis is a continuous process that includes continuous loading of vials, to achieve the desired throughput. As described in Section 3.2.2, vials are equilibrated at a specific temperature and, then, frozen using a desired cooling rate; the apparatus can perform both uncontrolled nucleation and VISF. In the continuous apparatus, vials are suspended over a track and not in contact with the shelf, and the heat is removed mainly using a cryogenic gas; different protocols can be performed by adjusting the gas temperature and velocity. It should be pointed out that in this work, natural convection was used to perform freezing.

In the suspended-vial configuration, the contribution of conduction is small, as the gap between the vial and the shelf is much bigger than in conventional freezing; moreover, the contribution given by the contact between the vial and the shelf is completely absent, as the vials are suspended into the chamber.

77
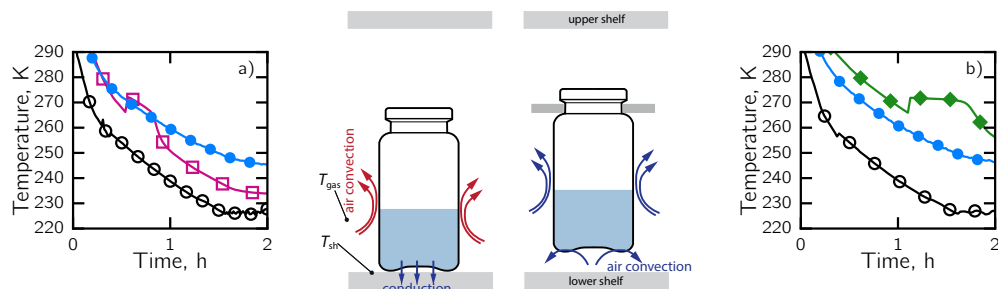
Figure 5.2 Schematic of the heat transfer mechanics between the shelf and the vial, and temperature profile in the case of (a, □) conventional, batch, freezing and (b, ◆) suspended-vial freezing. The (O) shelf temperature and (●) temperature of the air are also shown.

5.2 Materials and methods

The mathematical model for freezing of a pharmaceutical solution in vials presented in this section has been coupled with experimental measurements of nucleation temperatures to predict the structure of lyophilized products and their variability within a batch. A schematic of the workflow is shown in Figure 5.3. Such a procedure requires (i) the freezing conditions and (ii) the nucleation time as input. The process conditions, i.e., shelf temperature, heat transfer coefficients, cooling rate, vial filling, and vial geometry, as well as the properties of the solution, are determined a priori. However, for uncontrolled nucleation, the nucleation time cannot be known a priori, because nucleation is a stochastic event and therefore needs to be determined experimentally. Only once the distribution of the nucleation temperature has been determined, the mathematical model can be used to simulate the thermal behavior during freezing and predict the size of the ice crystals.
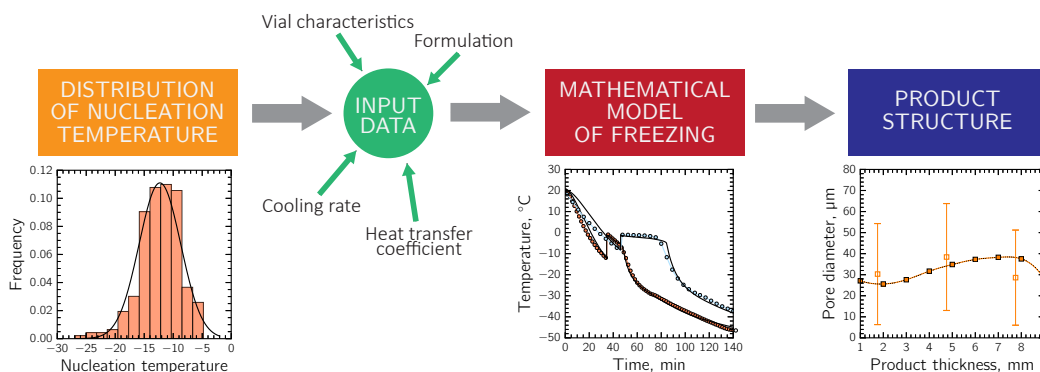
Figure 5.3 The workflow used to calculate the size of the ice crystals for a given distribution of the nucleation temperature.

The mathematical model developed by Nakagawa et al. (2007) and Pisano and Capozzi (2017) was used to simulate temperature profiles during the freezing of pharmaceutical solutions in vials and, hence, to determine the freezing front rate and the temperature gradient within the product. This model can describe the evolution of a temperature profile within a liquid being frozen, as shown in Figure 5.1.

Temperature profiles within the liquid being frozen were used in the model proposed by Arsiccio et al. (2017) to determine the ice crystal size. This first-principle model relates the crystal size to the velocity of the freezing front and temperature

gradients within the product. This model allows a quantitative assessment of the pore structure within a vial to be made while varying the freezing parameters, i.e., the nucleation temperature and the cooling rate.

The last step consisted of coupling the ice nucleation temperatures collected experimentally with the above mathematical model, and thus, correlating each nucleation temperature to the corresponding product morphology. In this manner, variations in the nucleation temperature can be related to the vial-to-vial heterogeneity within a batch. Moreover, this approach provides a statistical description of the structure of lyophilized products within a vial and also a quantitative evaluation of the intra-vial heterogeneity.

5.2.1 Mathematical model of freezing

The mathematical model used to describe the evolution of the product temperature during freezing is based on the following energy balance equation,

$$\rho c_p \frac{\partial T}{\partial t} = \boldsymbol{\nabla} \cdot \kappa \boldsymbol{\nabla} T + \dot{Q}_n + \dot{Q}_c \tag{5.1}$$

where $\dot{Q}_n$ represents the exothermic heat release due to the nucleation event, $\dot{Q}_c$ is the contribution due to the growth of ice crystals.

During cooling ($t < t_n$), $\dot{Q}_n$ and $\dot{Q}_c$ are equal to zero, $c_p = c_{p,\text{liq}}$, $\rho = \rho_{\text{liq}}$ and $\kappa = \kappa_{\text{liq}}$.

At a certain temperature T_n, which is stochastic if nucleation is not controlled, corresponding to $t = t_n$, nucleation occurs and, then, stable ice crystals start growing. During this period, the sample can be divided into several zones corresponding to different physical states, i.e., a clear liquid zone (Ω_{I}), a mushy zone (Ω_{II}), and a solid zone (Ω_{III}), see Figure 5.4a. The mushy zone is a suspension of ice in the liquid solution, with ice fraction X_{ice}.

The heat released due to nucleation is proportional to the degree of supercooling and reads,

$$\dot{Q}_n = \Delta H_f k_n (T_{eq} - T) \tag{5.2}$$

where k_n is a first-order reaction constant that describes the ice formation rate and which can be calculated from a theoretical consideration (Nakagawa et al., 2007). k_n was estimated to be equal to $430 \, \text{kg} \, \text{m}^{-3} \text{s}^{-1} \text{K}^{-1}$ (Nakagawa et al., 2007), $\Delta H_f = 333\,500.0 \, \text{J} \, \text{kg}^{-1}$ and $\kappa_{\text{sol}} = 2.5 \, \text{W} \, \text{m}^{-1} \, \text{K}^{-1}$.

The ice crystal growth is described as follows,

$$\dot{Q}_c = \Delta H_f \frac{\partial}{\partial t} (\rho X_{\text{ice}}) \tag{5.3}$$

Assuming that the crystal growth rate is entirely controlled by heat transfer, the source term $\dot{Q}_c$ can be expressed as,

$$\Delta H_f \frac{\partial}{\partial t} (\rho X_{\text{ice}}) = \Delta H_f \rho \frac{\partial X_{\text{ice}}}{\partial T} \frac{\partial T}{\partial t} \tag{5.4}$$

where $\frac{\partial X_{\text{ice}}}{\partial T}$ is approximated with $\Delta X_{\text{ice}}/\Delta T$, and ΔT represents the temperature difference through the mushy zone. This source term can be included in the accumulation term using the apparent specific heat capacity c_p^* defined by Lunardini (1981),

$$c_p^* = \begin{cases} c_{p,\text{liq}} & T > T_{eq} + \Delta T/2 \\ \frac{c_{p,\text{liq}}+c_{p,\text{sol}}}{2} + \frac{\Delta H_f}{\Delta T}\Delta X_{\text{ice}} & T_{eq} - \Delta T/2 < T < T_{eq} + \Delta T/2 \\ c_{p,\text{sol}} & T < T_{eq} - \Delta T/2 \end{cases} \tag{5.5}$$

These equations were solved using Comsol Multiphysics 5.0; the computation domain was discretized using a mapped grid for liquid domain and an unstructured triangular grid for the vial wall. The grid was sufficiently refined to obtain a grid-independent solution.
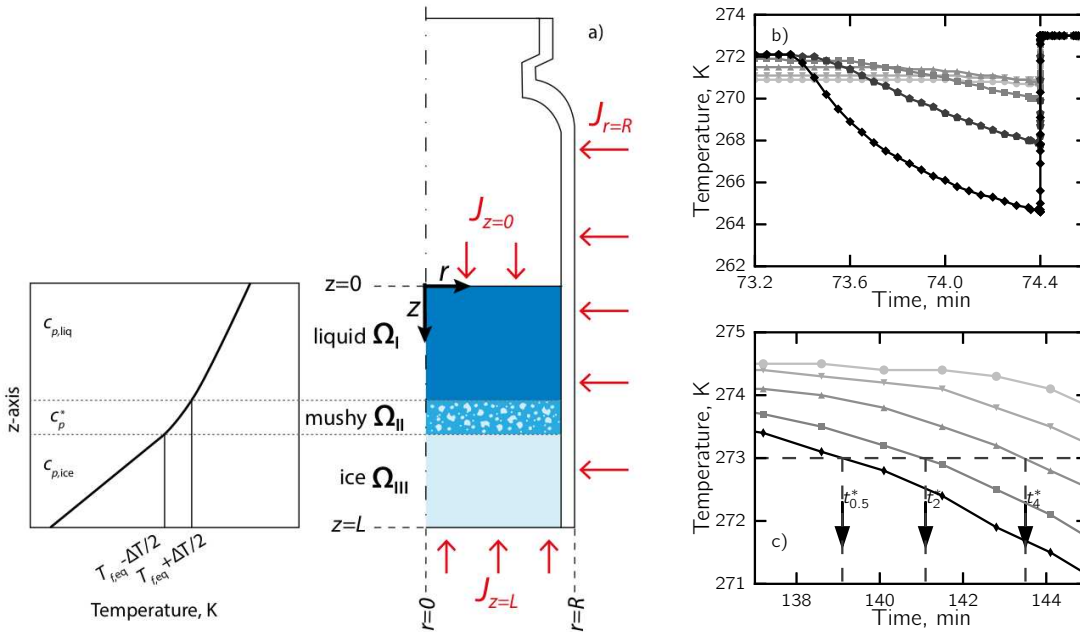
Figure 5.4 (a) Schematic of computational domain and representation of the three different regions presented in the product during freezing. (b) Model predictions of product temperature during vacuum, (c) evolution of the product temperature after nucleation. (◆) $z = 0\,\text{mm}$, (◆) $z = 0\,\text{mm}$, (⬥) $z = 1\,\text{mm}$, (■) $z = 2\,\text{mm}$, (▲) $z = 4\,\text{mm}$, (▼) $z = 6\,\text{mm}$, (●) $z = 8\,\text{mm}$ from the top surface. Data refer to VISF of mannitol 5%, T_n 268 K.

The model parameters are (i) the vial characteristics and geometry, (ii) the heat transfer in the chamber and (iii) the nucleation time to which T_n corresponds. During cooling and freezing, heat is supplied to the product through various mechanisms.

As shown in Figure 5.4, three heat fluxes have to be defined as boundary conditions, i.e., the heat flux to the vial bottom $J_{q,z=L}$, vial side $J_{q,r=R_{gl}}$, and the water surface $J_{q,z=0}$. The expressions of these terms depend on the specific configuration.

Boundary conditions for conventional shelf-ramped freezing

The heat flux at the bottom of the vial reads,

$$J_{q,z=L} = U(T_{sh} - T_{z=0}) \tag{5.6}$$

where U is the overall heat transfer coefficient at the bottom of the vial, which is defined as follows,

$$U = \left(\frac{s_{gl}}{\kappa_{gl}} + \frac{1}{\tilde{U}}\right)^{-1} \quad \text{where } \tilde{U} = K_c + K_g + K_r \tag{5.7}$$

K_c is the heat transfer coefficient related to the direct contact between the shelf, and it depends on vial geometry, which changes with the type of vial and supplier; here K_c was estimated to be $2.5\,\mathrm{W\,m^{-2}\,K^{-1}}$.

The heat transfer coefficient related to the air conduction in the small gap between the bottom surface of the vial and the shelf reads,

$$K_g = \frac{\kappa_{air}}{\ell_v} \tag{5.8}$$

where ℓ_v is the characteristic distance between the shelf and the vial, here estimated to be $0.0428\,\mathrm{cm}$. Here K_c was estimated to be $54\,\mathrm{W\,m^{-2}\,K^{-1}}$.

The radiative heat transfer coefficient K_r can be expressed as follows,

$$K_r = \frac{\sigma_{SB} e (T_{sh}^4 - T^4)}{T_{sh} - T} \approx 4\sigma_{SB} e \overline{T}^3 \tag{5.9}$$

where $\overline{T}$ is the average temperature and the effective emissivity is defined combining the emissivity of vial glass (ϵ_{gl}) and shelf surface (ϵ_{sh}) as follows,

$$e = \frac{1}{1 + (1/\epsilon_{gl} - 1) + (1/\epsilon_{sh} - 1)} \tag{5.10}$$

Here K_r was estimated to be equal to $4\,\mathrm{W\,m^{-2}\,K^{-1}}$.

The heat flux at the vial side reads,

$$J_{q,r=R_{gl}} = h_{vs}(T_{gas} - T) + \sigma_{SB} F_{vs,wall}(T_{wall}^4 - T^4) + \sigma_{SB} F_{vs,sh}(T_{sh}^4 - T^4) \tag{5.11}$$

where the first term refers to heat transferred by air convection, the second to radiation from the side-walls of the chamber and the last term to radiation from the shelf.

In the case of natural convection, the heat transfer coefficient h_{vs} towards the lateral surface of the vial was estimated by mean of the following formulas (Rohsenow et al., 1998),

$$
\begin{aligned}
\mathrm{Nu}^T &= 0.75 \frac{0.671}{[1+(0.492/\mathrm{Pr})^{9/16}]^{4/9}} (\mathrm{GrPr})^{0.25} \\
\mathrm{Nu}_l &= [(\mathrm{Nu}_{cond})^n + (\mathrm{Nu}^T)^n]^{1/n} \\
\mathrm{Nu}_t &= 0.096(\mathrm{GrPr})^{0.33} \\
\mathrm{Nu} &= [\mathrm{Nu}_l^{10} + \mathrm{Nu}_t^{10}]^{0.1} = \frac{h_{vs} 2 R_{gl}}{\kappa_{air}}
\end{aligned}
\tag{5.12}
$$

where $n = 1.075$ and $\mathrm{Nu}_{cond} = 1.3$.

Boundary conditions for the suspended-vial freezing

In the case of suspended-vial freezing, vials are not in contact with the shelf and the heat flux at the bottom of the vial reads,

$$J_{q,z=L} = U(T_{sh} - T_{z=0}) + h_b(T_{gas} - T_{z=0}) \tag{5.13}$$

where U is defined as,

$$U = \left(\frac{s_{gl}}{\kappa_{gl}} + \frac{1}{K_r} \right)^{-1} \tag{5.14}$$

where the term K_r related to the radiation from the shelf is evaluated using Eq. 5.9, and was estimated equal to $5\,\mathrm{W\,m^{-2}\,K^{-1}}$. The second term of Eq. 5.13 refers to convection at the bottom of the vial. In the case of natural convection, h_b was evaluated to be about about $8.8\,\mathrm{W\,m^{-2}\,K^{-1}}$ for a clearance equal to 10 mm, $10\,\mathrm{W\,m^{-2}\,K^{-1}}$ for a clearance of 6 mm and $13\,\mathrm{W\,m^{-2}\,K^{-1}}$ for a clearance of 3 mm.

In the case of forced convection, h_b was estimated from (Rathore and Kapuno, 2011),

$$\mathrm{Nu} = 0.6664\mathrm{Re}^{1/2}\mathrm{Pr}^{1/3} \tag{5.15}$$

The heat flux at the vial side reads,

$$J_{q,r=R_{gl}} = h_{vs}(T_{gas} - T) + \sigma_{SB}F_{vs,wall}(T_{wall}^4 - T^4) + \sigma_{SB}F_{vs,sh}(T_{sh}^4 - T^4) \tag{5.16}$$

In the case of natural convection, the h_{vs} coefficient has been evaluated using Eqs. 5.12 and estimated to be about $5\,\mathrm{W\,m^{-2}\,K^{-1}}$ (Rohsenow et al., 1998), whereas $F_{vs,wall}$ and $F_{vs,sh}$, in the specific configuration of vials in a row, has been found to be 0.18 and 0.45, respectively. In the case of forced convection, h_{vs} was estimated as follows (Rathore and Kapuno, 2011),

$$\mathrm{Nu} = 0.683\mathrm{Re}^{0.466}\mathrm{Pr}^{1/3} \tag{5.17}$$

As shown in Figure 5.5, heat transfer is rate-controlled by gas conduction in the case of batch freeze-drying, where radiation and conduction by direct contact of the vial onto the shelf represents only the 10% of the total heat supplied to the product. In the case of suspended-vial configuration, convection represents about the three-quarters of total heat supplied. The variation of clearance in the range of 3 to 10 mm showed differences of about 10%.

Boundary conditions in the case of VISF

In the case of controlled nucleation using VISF, once the liquid being frozen reached its target temperature, pressure is reduced and kept at approximately 1 mbar for 30 s, promoting ice nucleation. Then, vacuum is released as fast as possible.
These conditions promote the evaporation of water and, in its turn, a further cooling of the solution. The vapour flux is estimated as follows (Marek and Straub, 2001),

$$N_{w,z=0} = \sqrt{\frac{\eta^2}{2M_w\pi\kappa}} \left(\frac{p_w^{eq}}{T_{liq}^{1/2}} - \frac{p}{T_{vap}^{1/2}} \right) \tag{5.18}$$
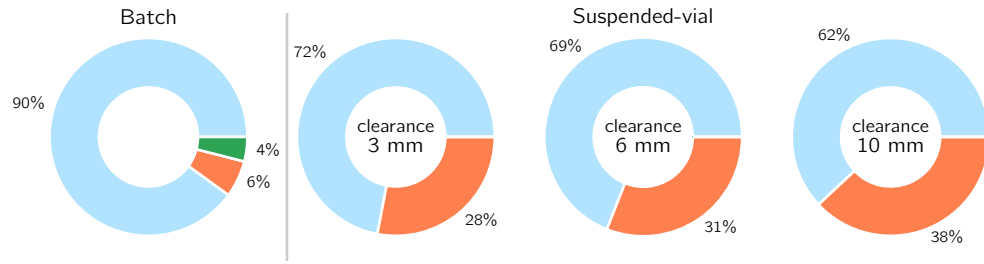
Figure 5.5 Contribution of the various mechanisms to heat transfer for the batch (central vial) and suspended-vial configuration; (■) gas conduction and convection, (■) radiation and (■) shelf/vial direct contact.

where η is the condensing/evaporating efficiency. This parameter ranges from 0.004 to 0.015 in the case of evaporation from a stagnant water surface in a glass vessel under vacuum (Marek and Straub, 2001). We may further write the heat flux of evaporation as,

$$J_{q,z=0} = \Delta H_e M_w N_{w,z=0} \tag{5.19}$$

As can be seen in Figure 5.4b, the decrease in pressure promoted the removal of heat, because of the evaporation of water, and hence the decrease in product temperature. As expected, the decrease in temperature varied with the position within the liquid; it was more relevant close to the top surface of the liquid where evaporation occurred, approximately 8 K, and very small at the bottom of the vial, less than 0.1 K. It follows that the impact of water evaporation on product temperature reduction was smaller and smaller moving towards the bottom of the vial. After nucleation occurred, the temperature increased, because of the latent heat released, and leveled off at the equilibrium freezing temperature.

5.2.2 Crystal sizing

Once the temperature profile within the product has been obtained, the size of the ice crystals can be established using either empirical correlations (Bomben and King, 1982; Kochs et al., 1991; Kurz and Fisher, 1998) or a first-principle model (Arsiccio et al., 2017). Here, crystal sizing along the product depth was calculated using the first-principle model (Arsiccio et al., 2017),

$$d_P = \frac{4\varepsilon\gamma a_s v}{\varepsilon\rho\Delta H_f v - \kappa\lambda} \tag{5.20}$$

where γa_s is equal to $\gamma b/\lambda^{2/3}$. The term γb is a fitting parameter, v is the freezing front rate and λ is the temperature gradient within the frozen layer. As a matter of fact, γa_s can be also estimated by using molecular dynamics (Arsiccio and Pisano, 2018).

The simulation results were used to estimate the freezing front rate v and temperature gradients within the liquid being frozen λ, and then the average size of ice crystals and hence of pores. To give you an example, Figure 5.4c shows the product

temperature evolution as predicted at various values of z, as well as the time at which the product reached its equilibrium freezing temperature, t_z^*. Knowledge of this time makes it possible to determine the position of the freezing front over time and thus its rate. Further details regarding the procedure to determine the pore size are reported in Appendix A.

The γb parameter does not depend on the cooling rate or on the nucleation temperature, but only on the formulation, and was determined by regression of experimental data. The procedure adopted to determine the crystal size within a product consisted in monitoring a vial and its nucleation temperature, and, after drying, in analyzing the sample sections using SEM, thus obtaining three different images of the top, center and bottom of the sample. The mean pore diameter was determined at different positions within the product using the procedure described in Section 5.2.5.

A simulation was then carried out using the same cooling rate and nucleation temperature as that of the experimental run, and the spatial evolution of the temperature within the product over the whole freezing step was thus obtained. These data were post-processed to determine the freezing front rate v and temperature gradient within the frozen zone λ (Nakagawa et al., 2007; Pisano and Capozzi, 2017; Arsiccio et al., 2017). At this point, γb was obtained by minimizing the mean square deviation of the model predictions, $d_P = d_P(\gamma b)$, and the observed values, $d_{P,i}^*$,

$$\min_{\gamma b} \frac{1}{3} \sum_i \left(d_{p,i}(\gamma b) - d_{p,i}^* \right)^2 \tag{5.21}$$

where i represents the top, center and bottom positions within the sample. The model has no restriction on the number of i locations that can be predicted in either the axial or radial positions since it depends on the space-discretization used to solve the equation that describes the temperature profile within the solution being frozen.

It should be pointed out that the model can be used to have an estimation of the pore size but was not tailored to predict throats, interconnectivity, tortuosity or the shape of pores.

5.2.3 Experimental determination of the nucleation temperature distribution

An experimental campaign was carried out to measure the nucleation temperature of a statistically significant number of samples for both the conventional and suspended-vial configuration. In the latter configuration, vials were suspended by means of a Plexiglass track and sustained by screw pillars, which allow the clearance between the shelf and vials to be adjusted. Unlike conventional freezing, the vials were not placed in contact with the shelf, and the heat was not removed through direct contact between the shelf and vials, but only by means of convection through air and radiation from the surroundings. In both protocols, tests were carried out using mannitol as the model formulation. However, the obtained results can be extended to other formulations.

A solution of 5% w/w of mannitol was prepared using water for injection (Fresenius Kabi Italia, Isola della Scala, Italy). The solution was then filtered using 0.2 µm filters and introduced into tubing vials (10R 24.0 x 45.0, Nuova Ompi, Piombino Dese, Italy). About 400 vials were filled with 3 ml of the solution and placed onto the shelves of a pilot-scale lyophilizer (LyoBeta 25, Telstar, Terrassa, Spain).

Multiple runs of 64 vials each were performed in order to obtain a statistically relevant number of samples. The vials were arranged in a line to allow them to be inspected visually and their freezing to be recorded via video cameras placed in front of the Plexiglas door of the freeze dryer. Nucleation was clearly detected, using a video camera, as the solution became opaque because of the presence of ice crystals. As an example, Figure 5.6 shows image sequences of the nucleation event in the case of suspended-vial freezing, as captured by the video camera; once the nucleation had started, the nucleation front propagated inside the solution in less than 1 second. In the case of the suspended-vial mode, nucleation started randomly from either the top surface, the bottom or from the vial wall side, whereas, in the case of conventional freezing, it generally started from the bottom or from the side of the vial wall. The product temperatures of some vials were monitored during freezing using T-type thermocouples, and these were considered as a reference to determine the nucleation temperature of the other products. The nucleation exothermicity profile was not taken into consideration, and the temperature values beyond the nucleation event were extrapolated from the previous point of that curve, creating a fictitious curve sub-cooling curve. Since it is well known that the presence of thermocouples can disturb a system and results in higher temperatures, their nucleation temperatures were not included in our statistics.
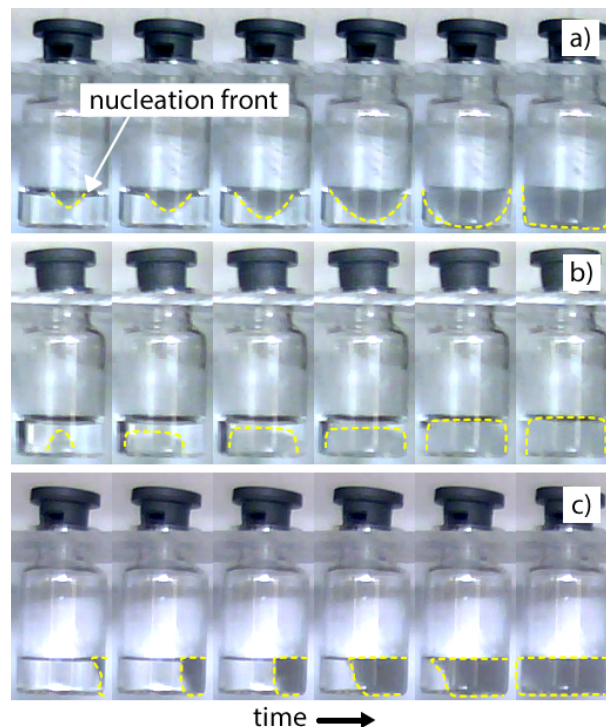
Figure 5.6 (a-c) The nucleation event in the case of suspended-vial freezing, as captured by the video camera. The nucleation front is pointed out with a yellow dashed line.

The procedure used to determine the distribution of the nucleation temperature within the batch included:

(i) observing nucleation in the samples using a video camera and collecting the time at which nucleation occurred;

(ii) monitoring the product temperature of a certain number of reference samples using thermocouples;

(iii) relating the nucleation time of the individual vials to an appropriate temperature value using the temperature profile observed for the references.

In the case of controlled nucleation via VISF, nucleation occurs in all the vials at the same time, triggered by dropping the pressure in the chamber. In this case, nucleation temperature is controlled, and there was no need of using the experimental procedure presented above for spontaneous nucleation.

5.2.4 Prediction of the product morphology

Once the nucleation time has been converted into the nucleation temperature, the statistical population can be divided into 7 equispaced classes, marked with T_n. The class interval was chosen as 2 °C, so that each class contained samples with a nucleation temperature of $T_n \pm 1$ °C. Each class was representative of a number of vials, and its frequency was calculated as the fraction of samples nucleated between $T_n - 1$ °C and $T_n + 1$ °C, with respect to the total samples. The nucleation temperature of each class was used in the mathematical model to predict the product morphology of that class.

5.2.5 Image analysis of the lyophilized product

After freeze-drying, the products were analyzed using a scanning electron microscope (SEM, FEI type, Quanta Inspect 200, Eindhoven, The Netherlands). Dried products were sliced at different positions along with their depth and, for each of them, SEM images were acquired. We analyzed samples that had different nucleation temperatures in order to cover the whole nucleation temperature distribution. The SEM image analysis was carried out by selecting up to hundreds of pores per image, approximating them with an ellipse and, finally, calculating d_P as the diameter of the circle with the same area-to-perimeter ratio as the ellipse. It has to be pointed out that here, as almost everywhere in literature, the analysis of the SEM images was handled manually. In chapter 7, the problem of determining product characteristics will be discussed in detail, and it will be shown that other methods, such as the image analysis of μ-CT scans, can be more accurate in the determination of pore size.

5.2.6 Resistance to vapor flow and its variability

As shown in Figure 5.7, the resistance of vapor and its variability is calculated by dividing the product into n equi-spaced slices along its depth, and each slice i is bound between L_{i-1} and L_i to have a thickness of s_i. The value of $d_{p,i}$ calculated with Eq. 5.20 is associated to each slice and its variability is expressed as the standard deviation $\sigma_{d_{p,i}}$. Then, the resistance to the vapor flow for each i slice reads (Rambhatla et al., 2004),

$$R_{\mathrm{P},i} = \frac{3}{2} \frac{\tau^2}{\varepsilon} \frac{s_i}{d_{\mathrm{p},i}} \sqrt{\frac{\pi R T}{2 M_{\mathrm{w}}}}; \qquad \sigma_{R_{\mathrm{P},i}} = \frac{3}{2} \frac{\tau^2}{\varepsilon} \frac{s_i}{d_{\mathrm{p},i}^2} \sqrt{\frac{\pi R T}{2 M_{\mathrm{w}}}} \sigma_{d_{\mathrm{p},i}} \qquad (5.22)$$

where ε/τ^2 is assumed equal to 0.225 (Nakagawa et al., 2007), RT refers to the gas constant and absolute temperature, while M_w is the molecular weight of water.

When the dried thickness is equal to $L_{d,i}$, which is the sum of the slice thicknesses from 1 to i ($L_{d,i} = \sum_i s_i$), the total resistance to the vapor flow reads,

$$R_p(L_{d,i}) = R_{p,0} + \sum_{i=1}^{n} R_{p,i} \pm \sigma_{R_{p,i}} \tag{5.23}$$
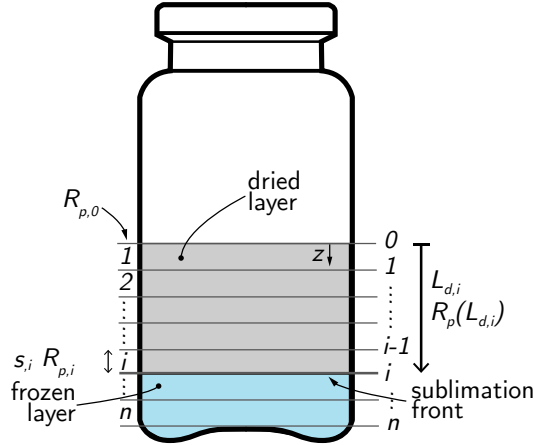
Figure 5.7 Schematic of the system used to calculate R_p and its variability as a function of the depth of the product.

5.3 Results

5.3.1 Batch vs. suspended-vial freezing: spontaneous nucleation

Variations in the nucleation temperature

As a first step, the nucleation temperature for a statistically significant number of samples was determined for the two configurations, i.e., conventional and suspended-vial freezing. As shown in the plots at the bottom of Figure 5.8, a camcorder was used, for each sample, to detect the time at which the solution became opaque, which corresponds to the time at which nucleation occurred. Once the nucleation times had been collected, they were correlated with the temperature of a reference sample (main plots in Figure 5.8), and the distribution of the nucleation temperatures was thus obtained (histograms in Figure 5.8).

In the case of conventional freezing, nucleation occurred over a range of temperature of -5 and $-27\,°C$, and showed a mean value of $-12.3\,°C$ and a standard deviation of $3.6\,°C$. The nucleation temperature in the case of suspended-vial freezing instead ranged between -6 and $-25\,°C$, with a mean value of $-12.9\,°C$ and a standard deviation of $4.1\,°C$. It is known that in GMP conditions these distributions are usually much broader because the environment is dust free, lowering the probability to a dust particle to be a nucleant.

The same analysis was performed by Florez Brun (2017) in her thesis work in collaboration between Politecnico di Torino and Ghent University, who compared the
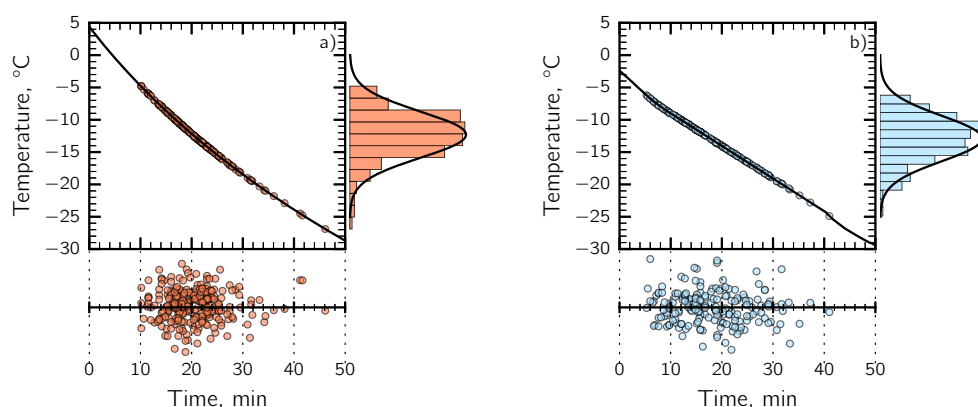
Figure 5.8 Nucleation times (dots in the plots at the bottom) and temperatures of the samples (dots in the main plots). The distribution curve of the nucleation temperature (bar plots) is also shown for (a) conventional and (b) suspended-vial freezing.

nucleation temperature distribution for a solution of 4% mannitol - 1% sucrose in buffer phosphate (pH 7.4, 0.05 M) using the conventional non-suspended configuration. Two different freezing protocols were compared having a cooling rate of (i) 1 K/min and (ii) 0.1 k/min respectively. In the case of the cooling rate of 1 K/min, the nucleation temperature ranged between -24.5 and -8.7 °C, with a mean value equal to -15.6 °C and a standard deviation of 2.7 °C. Similarly, in the case of the cooling rate of 0.1 K/min, the nucleation temperature ranged between -20.7 and -8.6 °C, with a mean value equal to -15.8 °C and a standard deviation of 2.0 °C.

It is important to point out that a systematic study of the nucleation event is beyond the scope of this work. In fact, a systematic study of the nucleation event would require a more controlled environment, e.g., GMP conditions, and a more reliable way of measuring nucleation temperature. Moreover, uncontrolled freezing in lyophilization is performed using cooling ramps, which means that the characterization of heterogeneous nucleation in such a system would involve constant-temperature experiments and non-isothermal experiments. The constant-temperature experiments would require the observation of the fraction of frozen samples within an identical population of samples during a time interval and at a fixed temperature, and so, relating the probability of nucleation event to temperature. The non-isothermal experiments would involve the observation of the fraction of frozen samples within an identical population of samples at different cooling rates (Vali, 2014). Intuitively, slowing the cooling rate might promote nucleation at higher freezing temperature because it would allow more time for unstable clusters to reach the critical state and to form stable nuclei. Vali and Stansbury (1966) found a shift towards higher mean freezing temperatures by lowering the cooling rate.

Effect of variations in the nucleation temperature on the mean pore diameter

The impact of nucleation temperature on the mean pore diameter of ice crystals is shown in Figure 5.9. An analysis of SEM images revealed that suspended-vial freezing produced lyophilized products with larger pores than conventional freezing, due to the slower freezing rate in suspended-vial freezing, that is, about 1.1 K/min vs. 0.5

K/min.

In the case of suspended-vial freezing, the mean pore diameter ranged from 80 to 100 μm, whereas it ranged from 28 to 45 μm for conventional freezing. As expected, for both conventional and suspended-vial freezing, the higher the nucleation temperature was, the larger the ice crystals, and, thus, the pores within the dried product. SEM images of the samples are shown in Figure 5.10 and 5.11.
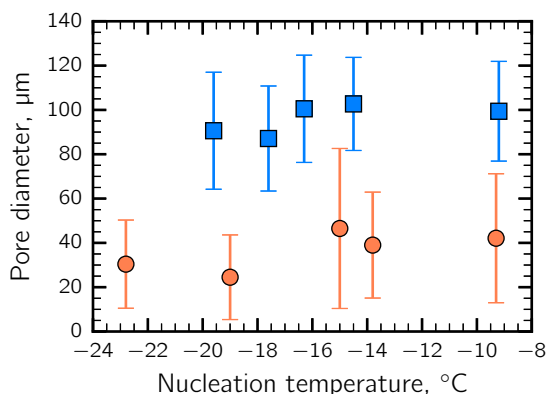
Figure 5.9 The mean pore diameter vs. the nucleation temperature in the case of (●) conventional and (■) suspended-vial freezing. The vertical bars refer to the standard deviation.

Validation of the mathematical model for freezing

The first step consisted in validating the model against the evolution of the product temperature during freezing. Figure 5.12a shows an example of product temperature predicted by means of the model and its experimental readings for the case of conventional and suspended-vial freezing; the model predictions were in a good agreement with the experimental data. In the case of suspended-vial freezing, the freezing rate was much slower than in the case of conventional freezing. These conditions promoted the formation of larger ice crystals, see Figure 5.12b. It must be remarked that experimental estimations of pore size, as obtained from SEM images, were characterized by very large error bars which are intrinsic of the methodology used for the morphological characterization.

Vial-to-vial variability in product morphology

Once the distributions of the nucleation temperature had been collected, the mathematical model was used to correlate each nucleation temperature to the corresponded mean pore diameter of the product. This value was calculated as the mean value of the pore diameters along with the entire depth of the product. In this manner, the distribution curve of the mean pore diameter for the entire production of lyophilized products was predicted, and an estimation of the vial-to-vial heterogeneity within the batch was obtained. The distribution of the pore size also considers that the nucleation temperatures were not all equally probable.

As shown in Figure 5.13a, in the case of conventional freezing, the lyophilized products presented a mean pore diameter of 39.8 μm and a standard deviation of

89
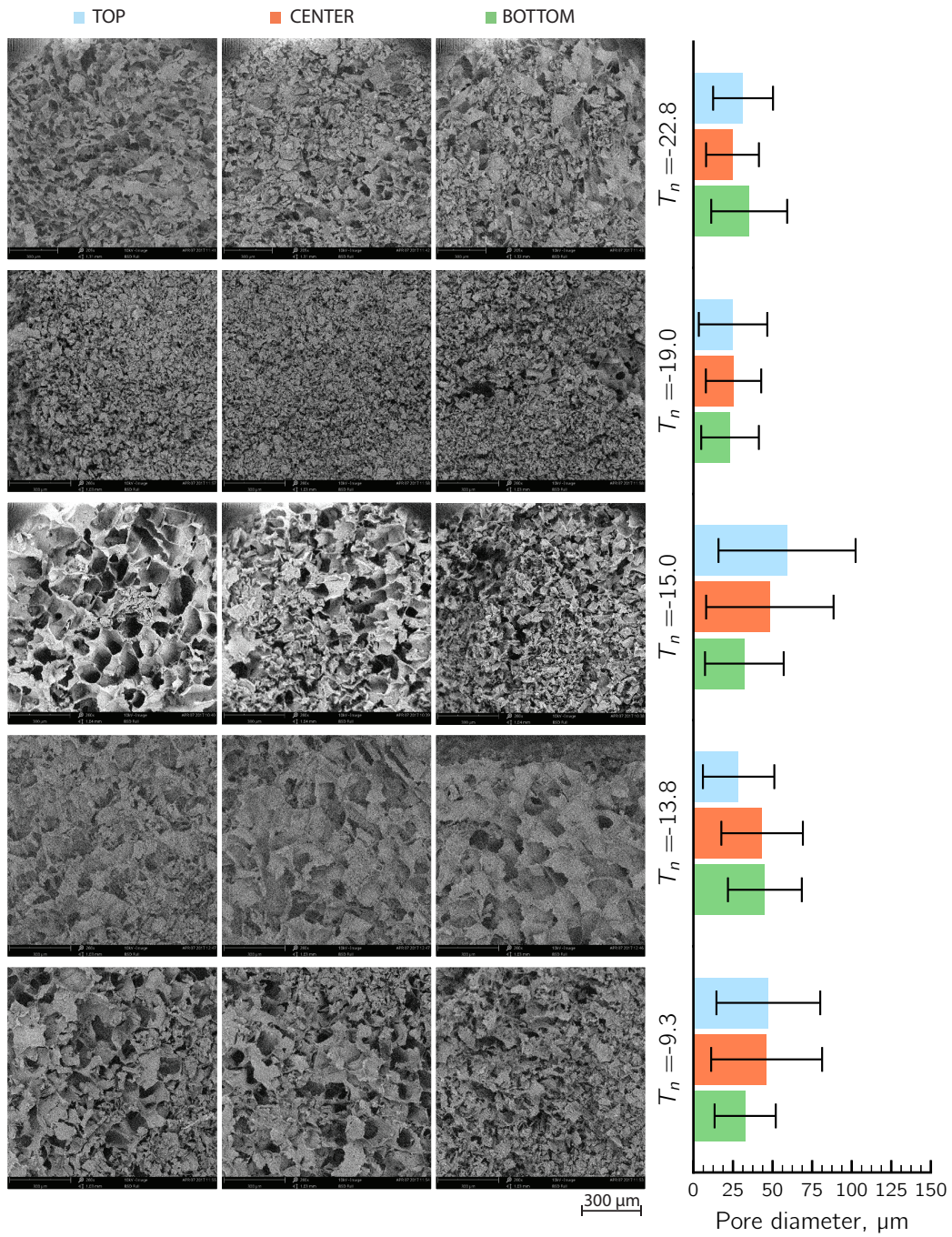
Figure 5.10 SEM images at the top (left column, ▪), center (central column, ▪) and bottom (right column, ▪) in the case of conventional freezing, uncontrolled nucleation. It is also reported the nucleation temperature of the samples and the mean pore diameter.
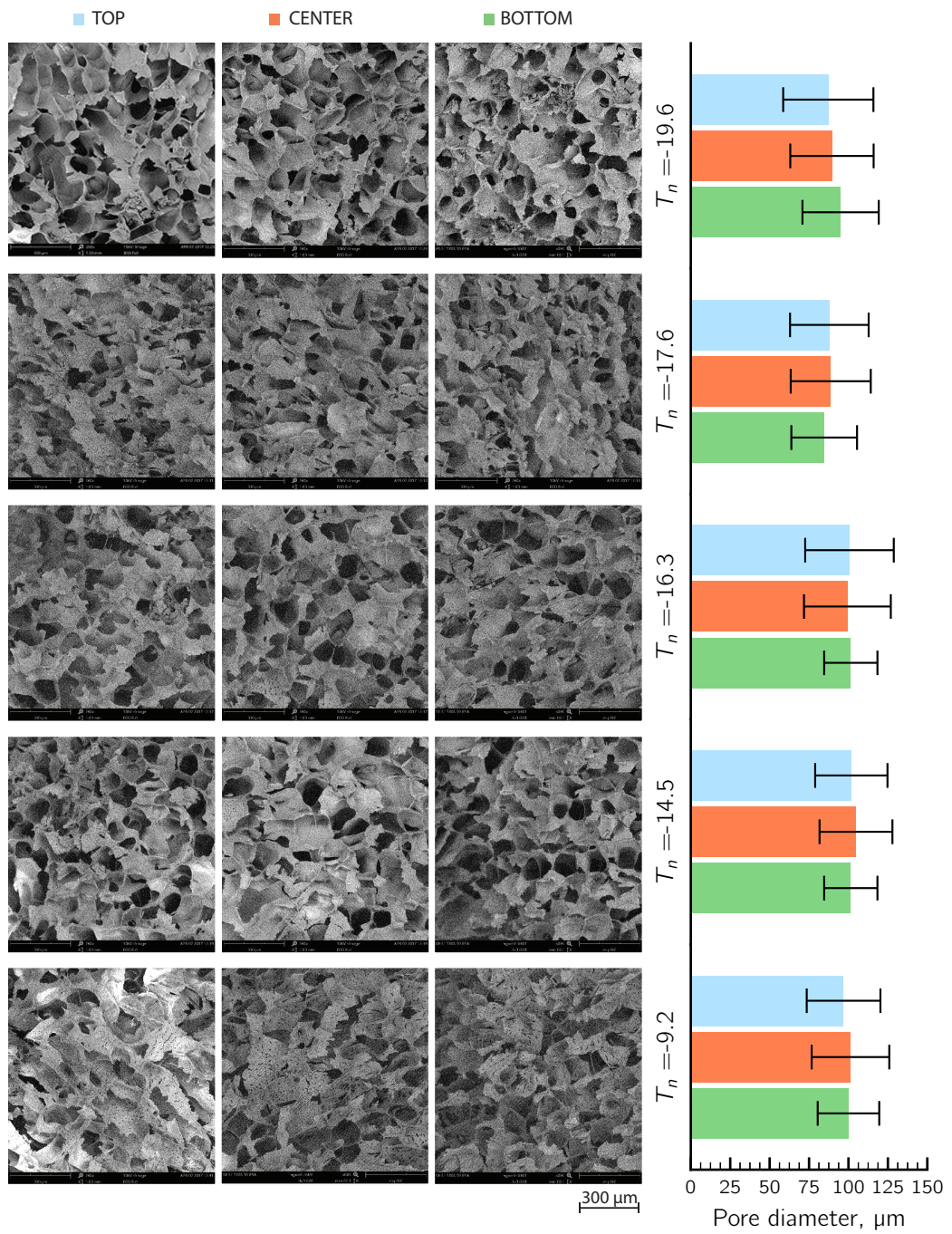
Figure 5.11 SEM images at the top (left column, ■), center (central column, ■) and bottom (right column, ■) in the case of suspended-vial freezing, uncontrolled nucleation. It is also reported the nucleation temperature of the samples
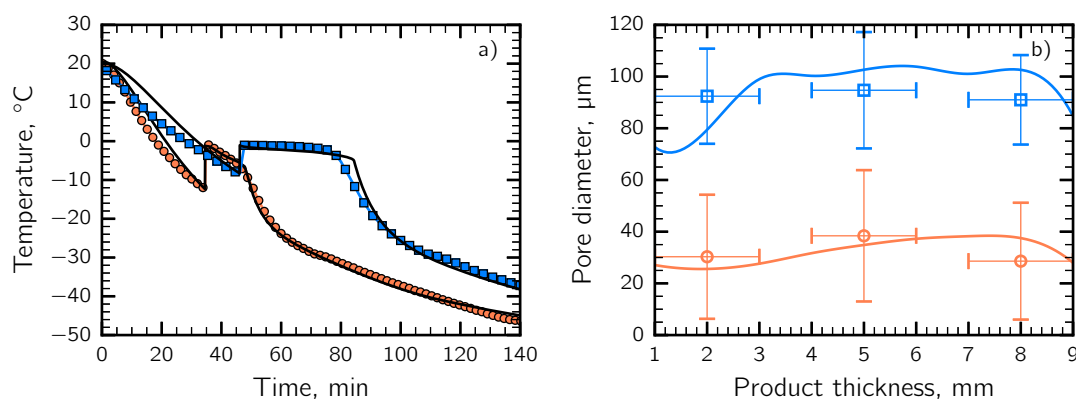
Figure 5.12 (a) Evolution of the product temperature during freezing, model predictions (solid line) vs. thermocouples readings (symbols). (b) The mean pore size, at different product depths, as (empty symbols) obtained from an analysis of SEM images and predicted by the model (solid line). The data refer to a 5% mannitol solution in the case of (●) conventional and (■) suspended-vial freezing. The vertical bars refer to the standard deviation, while the horizontal bars to the frame of the SEM images.

8.7 µm. On the other hand, the mean pore diameter in the samples produced using the suspended-vial freezing method was much larger, i.e., 93.4 µm, and the standard deviation was smaller, i.e., 5.1 µm.

Intra-vial variability

In addition to the mean pore size, the model can also predict its distribution within the dried product and, thus, provide information about the intra-vial heterogeneity. The pore diameter is shown as a function of the product thickness for both conventional and suspended-vial freezing in Figure 5.13b, see the solid lines. However, the model could also predict the vial-to-vial variations in the mean pore size. In fact, the band plots in Figure 5.13b correspond to the standard deviation of the pore diameter for different product depths.

The two freezing methods showed similar vial-to-vial variations in the pore size, in the range of 8-13 µm. However, if that variation is related to the mean pore size, the intra-vial heterogeneity was 10-20% for conventional freezing, and 8-12% for suspended-vial freezing.

Variability in cake resistance

This multi-step procedure can be used not only to predict the cake resistance to vapor flow (R_p), but also its variability within the batch. As pointed out in various works concerning the design space of a freeze-drying cycle (Pisano et al., 2013a; Van Bockstal et al., 2017; Mockus et al., 2011), the estimation of this parameter and its uncertainty is crucial for a robust design of the primary drying step.

The predictions of R_P are compared in Figure 5.14 with those determined experimentally via the thermocouple response method. R_P was much higher in the case of conventional freezing than in the case of suspended-vial freezing, because of the differences in the product morphology. The band plots in Figure 5.14 represent the standard deviation of R_P for the different products in the batch. The products that
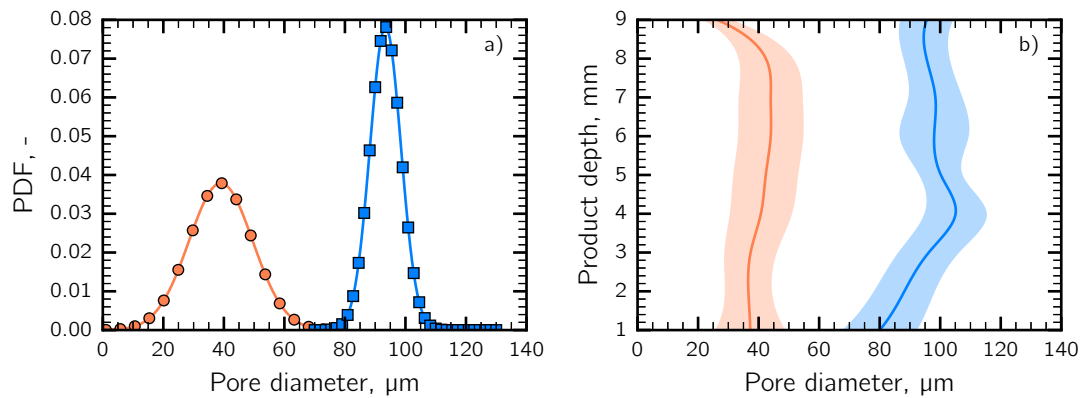
Figure 5.13 (a) Statistical distribution of the mean pore diameter of mannitol 5% in the case of (●) conventional and (■) suspended-vial freezing. (b) The mean pore diameter along the product depth and its variability within a batch of vials, containing mannitol 5%; the solid line refers to the mean value, while the band plot is the vial-to-vial variability.

were frozen using the conventional method exhibited a relative variability in R_p along with the product depth between 18% and 23%, whereas, the relative variability in R_p dropped to 5-8% when suspended-vial freezing was used.

The slight discrepancy between the experimental measurement of R_p and the predicted value might be related to the systematic error of the thermocouples, which is in the range of 1 K, but also to the fact that the particular vial that was monitored might not be completely representative of the whole batch or due to an overestimation of the tortuosity.
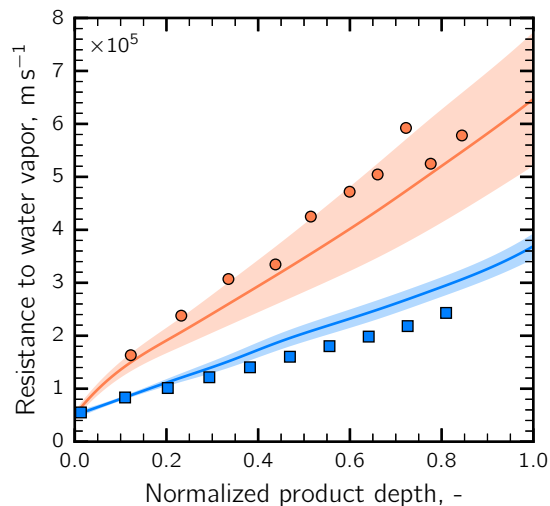
Figure 5.14 Simulation (line and band plot) and experimental data (solid marks) of the product resistance variability within a batch of vials in the case of a mannitol 5% w/w solution for (●) conventional and (■) suspended-vial freezing. The thickness of the frozen product was about 10 mm.

The estimation of the R_p variability is important for the design of a robust cycle (Giordano et al., 2011). To give you an example, this procedure was applied by

Florez Brun (2017) and Fornaro (2018) to determine the variability of R_p and used this value in the design space tool developed by Mortier et al. (2016); this model includes the uncertainty of input variables and calculates the design space on the bases of the desired level of 'risk of failure'.

5.3.2 Modeling VISF

Model simulations of VISF were experimentally validated by comparison with thermocouples readings. Two different cycles have been carried out using the same formulation, mannitol 5% (w/w), but varying the nucleation temperature, $T_n = 263$ K and $T_n = 268$ K. An example of results is given in Figure 5.15a,b, showing a fairly good agreement between model predictions of product temperature and its experimental measurements during both cooling and freezing. Results refer to product temperature close to the vial bottom. It must be pointed out that the model tended to underestimate the product temperature during cooling of the liquid slightly. This might be due to a computational error, which for a time-depending partial differential equation has two contributions, i.e., one from time discretization (ODE solver) and from another spatial discretization (FEM). Overall, the temperature predictions seemed accurate, in particular, the steady-state value at the end of cooling was very accurate.

The mathematical model was then used to predict the pore size distribution of such a production. An example of results is given in Figure 5.15c, showing a fairly good agreement between model predictions and SEM observations.

As expected, the higher the nucleation temperature, the bigger the ice crystals, and so the pores, in the product. For T_n of 263 K, pores range from 75 at the top of the product to 90 μm in the center. On the other hand, for T_n of 268, the pores range from 110 μm at the top to 120 μm in the center and bottom of the product. The results also confirmed that the morphology of a given formulation varied with T_n and demonstrated that the model can predict this behavior. This result was consistent with previous results published in Oddone et al. (2016).

5.3.3 Freezing in continuous

In the previous sections, natural convection was used to perform suspended-vial freezing. As a matter of fact, the continuous apparatus for performing continuous freeze-drying also includes the possibility to perform various freezing protocols, which means different cooling rates. The cooling rate can be modulated by changing T_{gas} and air velocity; T_{gas} affects heat driving force, and air velocity determines the heat transfer coefficient.

As proposed by Romano (2017), the convective heat transfer coefficient is reported as a function of air velocity (Figure 5.16a-b); h_{vs} and h_b increase as air velocity increases and, at the same time, freezing duration decreases, see Figure 5.16c. Of course, different freezing protocols produce products with a different structure, e.g., 41 μm as mean pore diameter using an air velocity of 0.5 m/s, 26 at 1 m/s and 15 at 10 m/s.
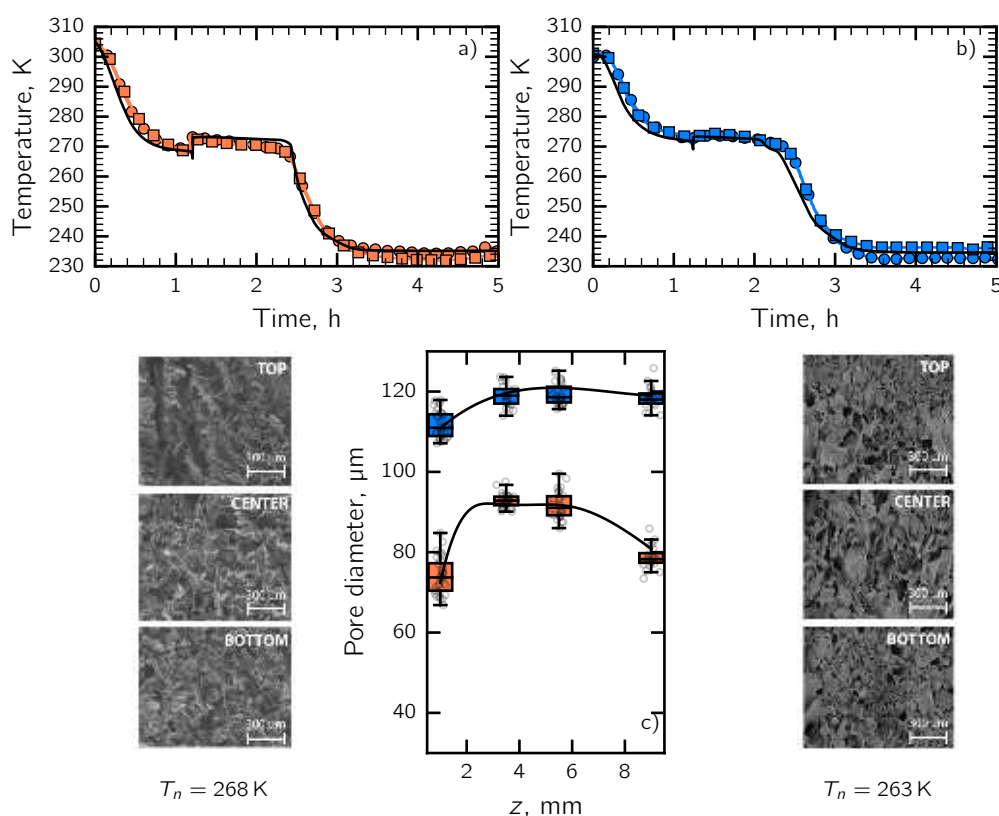
Figure 5.15 (a,b) Comparison between (solid line) model predictions and (symbols) observations for the temperature evolution of the liquid being frozen; (c) comparison between (solid line) model predictions and (box plots) SEM observations for the average pore size. Data refer to the freezing of mannitol 5% nucleated at (a, ■) 263 K and (b, ■) 268 K. For box plots, top bar is maximum observation, lower bar is minimum observation, top of box is third quartile, bottom of box is first quartile, middle bar is median value and bullets are original data.

5.4 Conclusions

In this chapter, a mathematical model of freezing was proposed for both conventional and suspended-vial freezing, and spontaneous and controlled nucleation via VISF.

Heat transferred in the two configurations has been studied, showing that the contribution of gas conduction and convection represents the main mode of heat transfer, i.e., 90% in the batch and 60-70% in the suspended configuration.

A multi-step procedure has been presented as a support to the development of a freeze-drying cycle in the case of batch and continuous configuration, and for both uncontrolled and controlled nucleation. This procedure combines the experimental determination of the nucleation time with a mechanistic model of freezing to produce a realistic evaluation of the morphology of lyophilized products. This method can be used to evaluate the vial-to-vial heterogeneity, in terms of pore diameter in the product within a batch, and the intra-vial variability along with the depth of the cake. From these data, it was possible to estimate the variability of product resistance to vapor flow and, finally, the drying time.

Conventional freezing and suspended-vial freezing produce lyophilized products
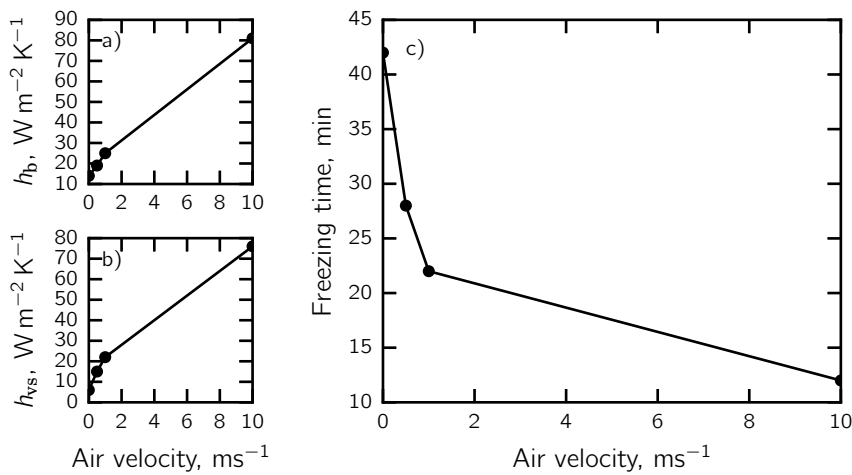
Figure 5.16 Heat transfer for forced air convection at (a) vial bottom and (b) vial side as a function of air velocity. (c) Freezing duration as a function of air velocity

that have different characteristics, and, thanks to the use of the proposed procedure, it was possible to obtain a quantitative estimation of the vial-to-vial and intra-vial variability. The suspended-vial freezing, in fact, showed a porous structure with larger pores, but also a smaller vial-to-vial and intra-vial variability than conventional freezing. As a consequence, the product resistance to vapor flow, in the case of suspended-vial freezing, presented a much smaller variability than that observed for the conventional freezing protocol.

It has been shown the effect of controlling nucleation by using VISF to the product structure; the simulations confirmed the experimental observations that VISF is able to produce products with bigger pores.

As a final step, it was shown the possibility of using forced convection to modulate heat transfer and, finally, the cooling rate.

Acronyms

μ-**CT** X-Ray Micro Computed Tomography; **GMP** Good Manufacturing Practice.

List of symbols

c_p	specific heat capacity, $\mathrm{J\,kg^{-1}\,K^{-1}}$
c_p^*	apparent specific heat capacity, $\mathrm{J\,kg^{-1.K^{-1}}}$
d_P	pore diameter within the bed, m
d_P^*	experimental value of the pore diameter, m
e	effective emissivity, -
h	heat transfer coefficient for air convection, $\mathrm{W\,m^{-2}\,K^{-1}}$
ΔH_e	enthalpy of evaporation, $\mathrm{J\,kg^{-1}}$
ΔH_f	latent heat of crystallization, $\mathrm{J\,kg^{-1}}$
J_q	heat flux, $\mathrm{W\,m^{-2}}$
k_n	rate constant of nucleation, $\mathrm{kg\,s^{-1}\,m^{-3}\,K^{-1}}$

K_r	heat transfer coefficient between the shelf and the vial due to radiation, $\mathrm{J\,s^{-1}\,m^{-2}\,K^{-1}}$
L_d	dried thickness, m
ℓ_v	characteristic distance between the shelf and the vial,, m
M	molecular weight, $\mathrm{kg\,kmol^{-1}}$
N	molar flux, $\mathrm{mol\,m^{-2}\,s^{-1}}$
p_w^{eq}	vapor equilibrium pressure, Pa
$\dot{Q}_c$	heat of crystallization, $\mathrm{W\,m^{-3}}$
$\dot{Q}_n$	heat of nucleation, $\mathrm{W\,m^{-3}}$
r	radial coordinate, m
R_{gl}	Outer vial diameter, m

s	thickness, m		ρ	density, $\mathrm{kg\,m^{-3}}$
T_{eq}	equilibrium freezing temperature, K		σ	standard deviation
T'_g	glass transition temperature, K		Ω_I	liquid zone
T_n	nucleation temperature, K		Ω_II	mushy zone
t_n	nucleation time, s		Ω_III	solid zone

U — heat transfer coefficient at the bottom of the vial, $\mathrm{W\,m^{-2}\,K^{-1}}$

$\tilde{U}$ — heat transfer coefficient between the heating shelf and the bottom of the vial, $\mathrm{W\,m^{-2}\,K^{-1}}$

X_ice — mass fraction of ice, $\mathrm{kg\,m^{-3}}$

z — axial coordinate, m

Adimensional numbers

Gr	Grashof number
Nu	Nusselt number
Re	Reynolds number

Greek letters

Subscript

γb	fitting constant of the first-principle empirical correlation for crystal sizing, $\mathrm{m\,K^{1/2}s^{-1/2}}$		air	air
			b	vial bottom
			gl	vial glass
ϵ	emissivity, -		liq	liquid
ε	porosity, -		sh	shelf
η	condensing/evaporating efficiency, -		sol	solid
κ	thermal conductivity, $\mathrm{W\,m^{-1}\,K^{-1}}$		vap	vapor
λ	temperature gradient, $\mathrm{k\,m^{-1}}$		vs	vial sidewall
ν	freezing front rate, $\mathrm{m\,s^{-1}}$		w	wall

References

Arsiccio, A. and Pisano, R. (2018). Application of the Quality by Design Approach to the Freezing Step of Freeze-Drying: Building the Design Space. *Journal of Pharmaceutical Sciences* 107 (6), pp. 1586–1596.

Arsiccio, A., Barresi, A. A., and Pisano, R. (2017). Prediction of ice crystal size distribution after freezing of pharmaceutical solutions. *Crystal Growth & Design* 17 (9), pp. 4573–4581.

Bomben, J. L. and King, C. J. (1982). Heat and mass transport in the freezing of apple tissue. *International Journal of Food Science and Technology* 17 (5), pp. 615–632.

Florez Brun, E. C. (2017). "Development of freeze-drying cycles and evaluation of uncertainty on heat and mass transfer". MA thesis. Italy: Politecnico di Torino.

Fornaro, M. V. (2018). "Impact of freezing on the activity of an active pharmaceutical ingredient". MA thesis. Italy: Politecnico di Torino.

Giordano, A., Barresi, A. A., and Fissore, D. (2011). On the use of mathematical models to build the design space for the primary drying phase of a pharmaceutical lyophilization process. *Journal of Pharmaceutical Sciences* 100 (1), pp. 311–324.

Goshima, H., Do, G., and Nakagawa, K. (2016). Impact of ice morphology on design space of pharmaceutical freeze-drying. *Journal of Pharmaceutical Sciences* 105 (6), pp. 1920–1933.

Hottot, A., Vessot, S., and Andrieu, J. (2007). Freeze drying of pharmaceuticals in vials: Influence of freezing protocol and sample configuration on ice morphology and freeze-dried cake texture. *Chemical Engineering and Processing: Process Intensification* 46 (7), pp. 666–674.

Kochs, M., Körber, C., Nunner, B., and Heschel, I. (1991). The influence of the freezing process on vapour transport during sublimation in vacuum-freeze-drying. *International Journal of Food Science and Technology* 34 (9), pp. 2395–2408.

Kurz, W. and Fisher, D. (1998). *Fundamentals of Solidification*. Uetikon-Zuerich, Switzerland: Trans Tech Publications. ISBN: 0878498044.

Lunardini, V. J. (1981). *Heat Transfer in Cold Climates*. New York, USA: Van Nostrand Reinhold Company.

Marek, R. and Straub, J. (2001). Analysis of the evaporation coefficient and the condensation coefficient of water. *International Journal of Heat and Mass Transfer* 44 (1), pp. 39–53.

Mockus, L. N., Paul, T. W., Pease, N. A., Harper, N. J., Basu, P. K., Oslos, E. A., Sacha, G. A., Kuu, W. Y., Hardwick, L. M., Karty, J. J., et al. (2011). Quality by design in formulation and process development for a freeze-dried, small molecule parenteral product: a case study. *Pharmaceutical Development and Technology* 16 (6), pp. 549–576.

Mortier, S. T. F., Van Bockstal, P.-J., Corver, J., Nopens, I., Gernaey, K. V., and De Beer, T. (2016). Uncertainty analysis as essential step in the establishment of the dynamic Design Space of primary drying during freeze-drying. *European Journal of Pharmaceutics and Biopharmaceutics* 103, pp. 71–83.

Nakagawa, K., Hottot, A., Vessot, S., and Andrieu, J. (2007). Modeling of freezing step during freeze-drying of drugs in vials. *AIChE Journal* 53 (5), pp. 1362–1372.

Oddone, I., Pisano, R., Bullich, R., and Stewart, P. (2014). Vacuum-Induced nucleation as a method for freeze-drying cycle optimization. *Industrial & Engineering Chemistry Research* 53 (47), pp. 18236–18244.

Oddone, I., Van Bockstal, P.-J., De Beer, T., and Pisano, R. (2016). Impact of vacuum-induced surface freezing on inter-and intra-vial heterogeneity. *European Journal of Pharmaceutics and Biopharmaceutics* 103, pp. 167–178.

Pisano, R. and Capozzi, L. C. (2017). Prediction of product morphology of lyophilized drugs in the case of Vacuum Induced Surface Freezing. *Chemical Engineering Research and Design* 125, pp. 119–129.

Pisano, R., Fissore, D., Barresi, A. A., Brayard, P., Chouvenc, P., and Woinet, B. (2013a). Quality by design: optimization of a freeze-drying cycle via design space in case of heterogeneous drying behavior and influence of the freezing protocol. *Pharmaceutical Development and Technology* 18 (1), pp. 280–295.

Rambhatla, S., Ramot, R., Bhugra, C., and Pikal, M. J. (2004). Heat and mass transfer scale-up issues during freeze drying: II. Control and characterization of the degree of supercooling. *AAPS Pharmscitech* 5 (4), pp. 54–62.

Rathore, M. M. and Kapuno, R (2011). *Engineering heat transfer*. Jones & Bartlett Publishers.

Rohsenow, W., Hartnett, J., and Cho, Y. (1998). *Handbook of Heat Transfer*. New York, USA: McGraw-Hill.

Romano, A (2017). "Applicazione del quality by design paradigma al congelamento di preparati farmaceutici". MA thesis. Italy: Politecnico di Torino.

Searles, J. A., Carpenter, J. F., and Randolph, T. W. (2001). The ice nucleation temperature determines the primary drying rate of lyophilization for samples frozen on a temperature-controlled shelf. *Journal of Pharmaceutical Sciences* 90 (7), pp. 860–871.

Vali, G. (2014). Interpretation of freezing nucleation experiments: singular and stochastic; sites and surfaces. *Atmospheric Chemistry and Physics* 14 (11), pp. 5271–5294.

Vali, G. and Stansbury, E. (1966). Time-dependent characteristics of the heterogeneous nucleation of ice. *Canadian Journal of Physics* 44 (3), pp. 477–502.

Van Bockstal, P.-J., Mortier, S. T. F., Corver, J., Nopens, I., Gernaey, K. V., and De Beer, T. (2017). Quantitative risk assessment via uncertainty analysis in combination with error propagation for the determination of the dynamic Design Space of the primary drying step during freeze-drying. *European Journal of Pharmaceutics and Biopharmaceutics* 121, pp. 32–41.

6
Modeling drying

In this chapter, a detailed mathematical model for primary drying is presented and used to make a comparison between the batch and continuous technology in terms of primary drying duration, and better understand the impact of process conditions on process performances. A 2D model is first used to understand the various contribution of heat transfer. This model takes into account mass and energy balances in the dried layer, at the sublimating interface, in the frozen layer, and along the vial wall. Moreover, a simplified mono-dimensional model for primary drying is presented and used to simulate batch and continuous freeze-drying by taking into account process and product variability.

6.1   Introduction

Primary drying is the longest step of the whole process, and its control is so fundamental that many efforts have been made by researchers and professionals to design robust cycles, and recently to apply QbD approaches.

The main process variables are shelf temperature and chamber pressure, but drying behavior also depends on product characteristics, vial characteristics and features of the apparatus.

Since the early stage, many authors have understood the importance of modeling the drying stage to understand the process, but also as a tool for designing robust cycles.

Among the earliest models of the drying stage, there are to mention the "uniformly retreating ice front" model (URIF model) (King, 1971), the "desorption-sublimation model" by Litchfield and Liapis (1979) and the monodimensional pseudo-steady state model by Pikal (1985). Sadikoglu and Liapis (1997) proposed a detailed one-dimensional model of the primary and secondary drying stages, and Mascarenhas et al. (1997) the first two-dimensional axisymmetric model by using the finite element method; an analogous model was developed by Sheehan and Liapis (1998). Among the earliest simplified models, there could be mentioned those developed by Velardi and

Barresi (2008) having in mind their application in optimization and in-line monitoring.

The number of publications on this topic is dramatically increased in the last years, as modeling of primary drying was proposed having in mind different aspects, i.e., gaining new insight into the heat/mass transfer (Scutellà et al., 2017; Scutellà et al., 2018), monitoring and control (Fissore et al., 2010; Fissore et al., 2018), understand both process and equipment (Barresi et al., 2018; Marchisio et al., 2018; Zhu et al., 2018), and develop tools for designing cycles by applying the QbD approach.

The success of modeling and simulation in freeze-drying is due to the requests of scientists and professionals of having a deeper understanding of the process and, at the same time, reducing the number of experiments in the laboratory, which are usually long and expensive. Also in this thesis, modeling and simulations have been extensively used and successfully benchmarked with experiments.

This chapter aims to present a bidimensional axisymmetric model of primary drying (2D-model, from now on) in the case of the continuous freeze-drying process, and compare it with the batch process. This model was used to understand the influence of process parameters on drying behavior. Besides, a simplified 1D pseudo-steady state model (1D-model, from now on) is also presented and used to simulate drying by taking into account the variability or the uncertainty of process parameters and product structure. Summarizing, this chapter aims at,

i. present mathematical models of primary drying used as a support for designing continuous freeze-drying process;

ii. study heat transfer during primary drying with particular regard to the suspended-vial configuration;

iii. compare primary drying performances of the batch and continuous process.

The 2D model is used to understand the various contribution of heat transfer for both the batch and the continuous configuration. The 1D model is specifically used to simulate entire productions of thousands of vials, taking into account process variability and parameters uncertainty.

To make this chapter more readable, a brief introduction to transport phenomena under vacuum is presented in Appendix B. Moreover, some details of the models are reported in Appendix C.

6.2 Batch vs. continuous configuration

As already explained in Section 2.2.2, batch freeze-drying is carried out in apparatus constituted of a chamber with a certain number of shelves where vials are placed over; this chamber is connected to a condenser and vacuum pumps. After the freezing step is completed, the chamber pressure is decreased in a range of 5 to 20 Pa, and shelf temperature is increased to promote sublimation. As shown in Figure 6.1a, heat is supplied to the product from the shelf by direct contact between shelf and vial, gas conduction in the gap between the vial and the shelf and radiation from the shelf and the environment. The heat supplied to the product strongly depends on chamber pressure because of the gas conduction in the gap; it has to be pointed out that gas in the gap is rarefied. A crucial issue in performing freeze-drying in batch resides in the fact that the heat supplied to the vials also depends on their position over the

shelf. In fact, it is possible to distinguish at least five different classes if vials are arranged in hexagonal arrays: central vials (C), peripheral vials (L, M, N) and corner vials (P) (Pisano et al., 2011); vials can also be arranged in square arrays. Central vials receive heat mostly from the bottom shelf; peripheral vials receive heat also from chamber walls and the band surrounding the shelf (if present). This extra heat impacts the most on the variability of heat supplied.
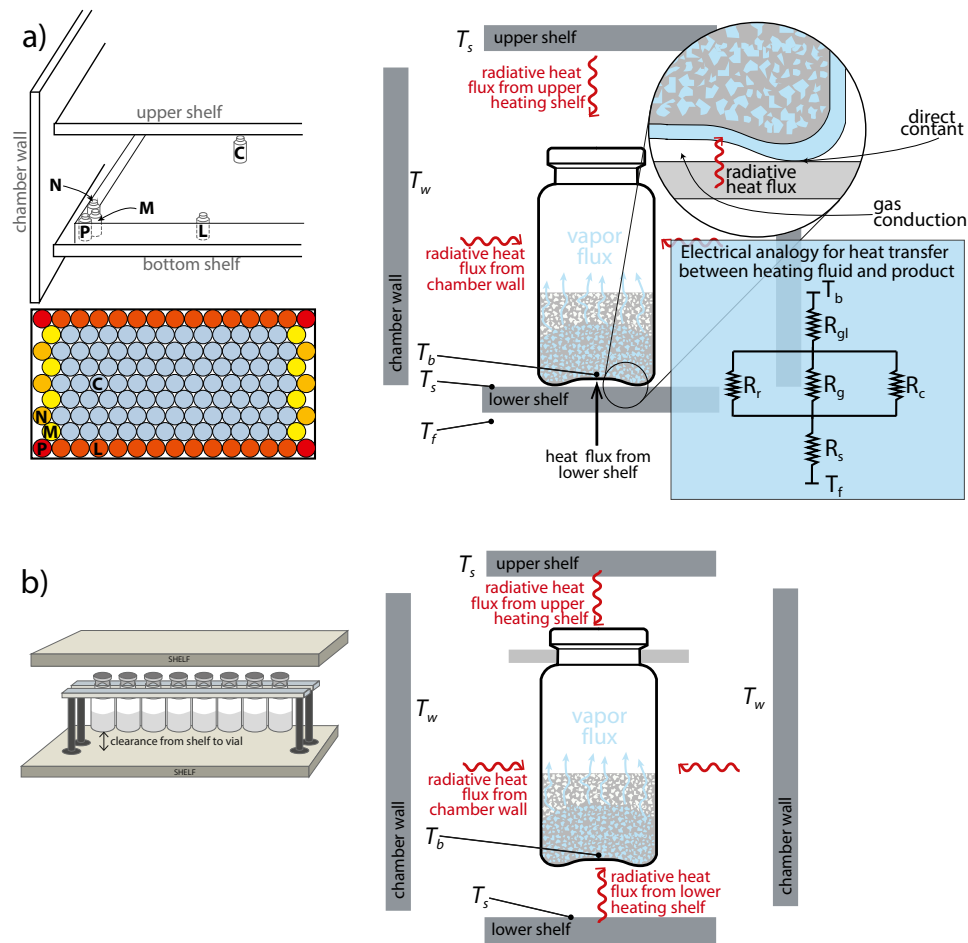
Figure 6.1 (a) Vial position over the shelf and main heat transfer mechanisms in the batch freeze-drying of unit doses in vials. (b) Suspended-vial configuration and its main heat transfer mechanisms.

In the case of the suspended-vial configuration, vials receive heat essentially by radiation from the temperature-controlled surfaces. A small contribution can also be attributed to the gas conduction between the bottom shelf and the vial bottom, although this contribution becomes less important as the shelf/vial clearance increases. In the configuration proposed in this thesis for performing continuous freeze-drying, vials follow the same, identical, path, so that no edge-vial effect is present anymore.

6.3 Mathematical formulation

6.3.1 Detailed 2D model

A mathematical model that describes the behavior of frozen solutions during the primary drying stage was developed for both conventional, batch, freeze-drying and suspended vial freeze-drying. As shown in Figure 6.2, heat and mass transfer equations were solved using a two-dimensional and axisymmetric geometry. The product is divided into two distinct subdomains, a dried layer (Ω_I), in which the free water has been removed via sublimation, and a frozen layer (Ω_{II}) below the dried layer. The dried and frozen layers are divided by the sublimation interface $H(r,t)$, that, as sublimation occurs, recedes from the upper product surface ($z = L_p$) to the bottom of the product ($z = 0$). Once sublimated, the water vapor flows in the dried layer, moving from the sublimation interface to the upper product surface and experiencing resistance to mass flow due to the small, interconnected, pores of the dried layer. Furthermore, this model takes into account the vial side wall (Ω_{III}).
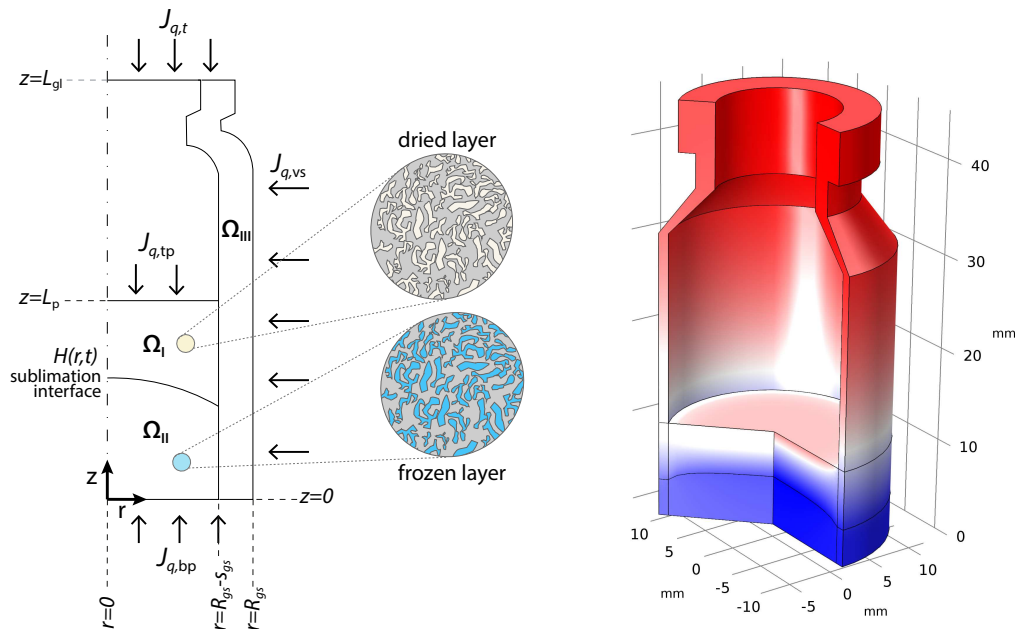
Figure 6.2 (a) Schematic illustration of freeze-drying of a frozen liquid solution in a vial. L_p is the filling height, L_{gl} is the glass vial height, R_{gl} is the outer radius of the glass vial and s_{gl} its thickness. The dried layer Ω_I and the frozen layer Ω_{II} are separate by the sublimation interface $H(r,t)$. (b) An example of temperature profile obtained from simulations.

The 2D model was developed using the software Comsol Multiphysics 5.1, coupling the transport of diluted species module, heat transport in porous media module and the deformed geometry module. The vial wall was meshed using an unstructured triangular grid and the product domain a mapped grid.

During primary drying, the heat necessary to sublimate ice is supplied from the heating shelves and the chamber walls. Heat transfer contributions are quantified using the heat fluxes $J_{q,bp}$, $J_{q,tp}$, that take into account respectively the heat transferred from the surrounding to the bottom and top of the product, and $J_{q,vs}$, that considers the heat input to the side of the vial. The heat is then transmitted to the sublimation

interface by conduction through the dried and frozen layers. Heat transferred via convection is not considered, since, as reported by Rambhatla et al. (2004), this contribution is negligible in the vacuum condition that occurs during primary drying. In the case of suspended-vial configuration, the conduction through the gas in the clearance between the bottom shelf and vial is also considered although this contribution loses importance as the clearance increases.

The dried and frozen layers are considered as a pseudo-homogeneous medium, and their properties are calculated weighting the properties of the phases of the solution. Ice fraction characterizes the frozen solution and, once dried, corresponds to the porosity of the product ε. Moreover, the product is characterized by the mean pore diameter (d_P) and tortuosity (τ).

Heat transfer

The heat balance in the dried layer can be expressed as follows,

$$\rho_\mathrm{I} c_{p,\mathrm{I}} \frac{\partial T_\mathrm{I}}{\partial t} = \boldsymbol{\nabla} \cdot (\kappa_\mathrm{I} \boldsymbol{\nabla} T_\mathrm{I}) - c_{p,\mathrm{gas}} \mathbf{M} \cdot \boldsymbol{\nabla} T_\mathrm{I} \qquad \text{in} \quad \Omega_\mathrm{I} \tag{6.1}$$

where $c_{p,\mathrm{gas}}$ is the specific heat capacity of the gas mixture, and $\mathbf{M}$ is the total mass flux. The actual density of dried layer is calculated as $\rho_\mathrm{I} = \rho_\mathrm{ice}\varepsilon + \rho_\mathrm{sol}(1 - \varepsilon)$, the specific heat capacity $c_{p,\mathrm{I}} = c_{p,\mathrm{ice}}\varepsilon + c_{p,\mathrm{sol}}(1 - \varepsilon)$ and the thermal conductivity following the Maxwell-Eucken relation $\kappa_\mathrm{I} = \kappa_\mathrm{sol}(2\kappa_\mathrm{sol} + \kappa_\mathrm{gas} - 2\varepsilon(\kappa_\mathrm{sol} - \kappa_\mathrm{gas}))/(2\kappa_\mathrm{sol} + \kappa_\mathrm{gas} + \varepsilon(\kappa_\mathrm{sol} - \kappa_\mathrm{gas}))$.

The heat balance in the frozen layer is give by,

$$\rho_\mathrm{II} c_{p,\mathrm{II}} \frac{\partial T_\mathrm{II}}{\partial t} = \boldsymbol{\nabla} \cdot (\kappa_\mathrm{II} \boldsymbol{\nabla} T_\mathrm{II}) \qquad \text{in} \quad \Omega_\mathrm{II} \tag{6.2}$$

where the actual density of frozen layer is calculated as $\rho_\mathrm{II} = \rho_\mathrm{gas}\varepsilon + \rho_\mathrm{sol}(1 - \varepsilon)$, the specific heat capacity $c_{p,\mathrm{II}} = c_{p,\mathrm{gas}}\varepsilon + c_{p,\mathrm{sol}}(1 - \varepsilon)$ and the thermal conductivity $\kappa_\mathrm{II} = \kappa_\mathrm{gas}\varepsilon + \kappa_\mathrm{sol}(1 - \varepsilon)$.

The heat balance for the vial wall side reads,

$$\rho_\mathrm{III} c_{p,\mathrm{III}} \frac{\partial T_\mathrm{III}}{\partial t} = \boldsymbol{\nabla} \cdot (\kappa_\mathrm{III} \boldsymbol{\nabla} T_\mathrm{III}) \qquad \text{in} \quad \Omega_\mathrm{III} \tag{6.3}$$

where ρ_III, $c_{p,\mathrm{III}}$ and κ_III are the density, the specific heat capacity and the thermal conductivity of the glass vial.

Considering T_0 the temperature of the product at the end of the freezing step, the heat transfer initial conditions can be expressed as follows,

$$T_\mathrm{I} = T_\mathrm{II} = T_\mathrm{III} = T_0 \qquad \text{for } t = 0, \quad \forall r, z \tag{6.4}$$

The boundary conditions to solve the heat balance are represented by the heat fluxes $J_\mathrm{q,bp}$, $J_\mathrm{q,tp}$ and $J_\mathrm{q,vs}$. The expression of these fluxes depends on the heat transfer mechanisms occurring during primary drying.

The heat transferred from the heating shelf and chamber walls to the vial side ($J_\mathrm{q,vs}$) is given by,

$$J_\mathrm{q,vs} = -\mathbf{n} \cdot (-\kappa \boldsymbol{\nabla} T)_{r=R_\mathrm{gl}} = \sigma_\mathrm{SB} F_\mathrm{vs,sh}(T_\mathrm{sh}^4 - T^4) + \sigma_\mathrm{SB} F_\mathrm{vs,wall}(T_\mathrm{wall}^4 - T^4)$$
$$\text{for } t > 0, \quad r = R_\mathrm{gl}, \quad \forall z \tag{6.5}$$

where $F_{vs,sh}$ and $F_{vs,wall}$ are the view factors for the radiative heat transfer respectively from shelves and chamber walls to vial side.

The heat transferred from the heating shelf and chamber walls to the top boundary of product ($J_{q,tp}$) reads,

$$J_{q,tp} = -\mathbf{n} \cdot (-\kappa \boldsymbol{\nabla} T)_{z=L_p} = \sigma_{SB} F_{tp,sh}(T_{sh}^4 - T^4) + \sigma_{SB} F_{tp,wall}(T_{wall}^4 - T^4)$$
$$\text{for } t > 0, \quad \forall r, \quad z = H(r,t)$$
(6.6)

where $F_{tp,sh}$ and $F_{tp,wall}$ are the view factors for the radiative heat transfer respectively from shelves and chamber walls to the top surface of the product.

The view factors for the batch and suspended-vial configuration were estimated by using Comsol 5.0 and are reported in Appendix C.

Heat flux from bottom - batch configuration In the case of batch freeze-drying (Figure 6.1a), the heat flux reads,

$$J_{q,bp} = -\mathbf{n} \cdot (-\kappa \boldsymbol{\nabla} T)_{z=0} = \left(\frac{1}{K_v'} + \frac{s_{gl}}{\kappa_{gl}} \right)^{-1} (T_{sh} - T_{z=0})$$
$$\text{for } t > 0, \quad \forall r, \quad z = 0$$
(6.7)

where K_v' is a the overall heat transfer coefficient between shelf and the bottom of the vial. As reported by Pisano et al. (2011), this coefficient reads,

$$K_v' = C_1 + \frac{C_2 P_c}{1 + C_3 P_c}$$
(6.8)

where,

$$C_1 = K_c + 4\sigma_{SB} e \bar{T}^3$$
$$C_2 = \frac{\alpha}{2 - \alpha} \sqrt{\frac{273.15}{T}} \Lambda_0$$
$$C_3 = \ell_V \left(\frac{\Lambda_0}{\kappa_0} \frac{\alpha}{2 - \alpha} \sqrt{\frac{273.15}{T}} \right)$$
(6.9)

C_1 takes into account the direct conduction from the shelf to the glass at the points of contact and the radiation from the lower shelf; this term is independent on chamber pressure. K_c is the term related to heat transfer through direct contact and it is a experimentally-determined parameter. C_2 and C_3 take into account the conduction through the gas in the narrow gap between the shelf surface and the vial bottom. The conduction through the gas in rarefied conditions depends on total pressure and the effective distance between shelf and vial bottom (ℓ_V).

Heat flux from bottom - suspended-vial configuration In the case of suspended-vial freeze-drying, vials are not in contact with the shelf, and the expression of the overall heat transfer coefficient from the shelf to the vial bottom is,

$$J_{q,bp} = -\mathbf{n} \cdot (-\kappa \boldsymbol{\nabla} T)_{z=0} = \sigma_{SB} F_{bp,sh}(T_{sh}^4 - T^4)$$
$$+ \sigma_{SB} F_{bp,wall}(T_{wall}^4 - T^4) + K_g(T_{sh} - T)$$
(6.10)
$$\text{for } t > 0, \quad \forall r, \quad z = 0$$

where $F_{bp,sh}$ and $F_{bp,wall}$ are the view factors for the radiative heat transfer respectively from shelves and chamber walls to the bottom surface of the product, and K_g is the gas conduction between the shelf and the vial, which is a function of the vial to shelf clearance ($\ell_{b/s}$),

$$K_g = \frac{\dfrac{\alpha}{2-\alpha}\sqrt{\dfrac{273.15}{T}}\Lambda_0 P_c}{1 + \ell_{b/s}\dfrac{\Lambda_0}{\kappa_0}\dfrac{\alpha}{2-\alpha}\sqrt{\dfrac{273.15}{T}}P_c} \qquad (6.11)$$

In this case the main relevant heat transfer mechanism is the radiation from the lower shelf to the vial bottom, and gas conduction is often negligible.

The main physical properties used in the model are reported in Table C.6 in Appendix C.

Mass transfer

During primary drying, the vapor sublimated from the sublimation interface flows through the dried layer to the product surface. In the dried layer, vapor encounters resistance to flow due to the porous matrix. This porous matrix consists of a network of pores in the range from few microns up to about a hundred microns which varies depending on the freezing protocol and formulation employed, see Chapter 5. In the model used in this work, the dried layer is described using the mean pore diameter d_P, the tortuosity τ and the porosity ε as the parameters of the model.

Under the low-pressure conditions employed during primary drying, i.e., 10- 20 Pa, the continuum approach fails to describe the flows of vapor through the dried layer. In this condition, the Knudsen or transition flow takes place, and a proper expression for the mass flux has to be used. Appendix B is dedicated to introducing some basic aspects of the mass transport under vacuum. In the model here presented, the molar fluxes of vapor and inert gas are expressed with the dusty gas-model (Mason and Malinauskas, 1983), which combines the expression of the flux of a multicomponent mixture in Knudsen and continuous regimes in porous media. The expression of the flux of the i-component obtained from the dusty-gas model (DGM) reads,

$$\mathbf{N}_i = -\frac{1}{R_g T}\left(D_i' \boldsymbol{\nabla} p_i + D_i'' p_i \boldsymbol{\nabla} p\right) \qquad i = w, in \qquad (6.12)$$

where p_i is the partial pressure of the i-component, p the total pressure and D_i' and D_i'' ($i = w, in$) are the transport coefficients depending on concentration and pressure gradients respectively, see Appendix B.1.2.

The equation of conservation of species expressed on a molar basis for the i-component in the dried layer Ω_I can be expressed as follows,

$$\varepsilon\frac{\partial c_i}{\partial t} = -\boldsymbol{\nabla}\cdot\mathbf{N}_i \qquad i = w, in \qquad (6.13)$$

where the flux of the i-component is expressed using the Eq. 6.12.

The initial conditions for the mass balance equations are given by the following expressions,

$$c_w(t_0) = \frac{p_w^{eq}(T_0)}{R_g T_0} \qquad c_{in}(t_0) = \frac{P_c - p_w^{eq}(T_0)}{R_g T_0} \qquad \text{for } t = 0, \quad \forall r, z \qquad (6.14)$$

where T_0 is the temperature of the product after freezing, P_c the chamber pressure and $p_w^{eq}(T_0)$ the equilibrium pressure of vapour over ice at the corresponding temperature T_0, determined following the Goff-Gratch relation (Goff and Gratch, 1946).

The boundary conditions are determined by the condition in the chamber, and can be expressed as follows,

$$c_w = \frac{0.95 P_c}{R_g T_c} \qquad c_{in} = \frac{0.05 P_c}{R_g T_c} \qquad t > 0, \quad \forall r, \quad z = L \qquad (6.15)$$

Mass and heat balance at the sublimating interface

The drying (Ω_I) and the frozen (Ω_{II}) layers are divided by the sublimation interface $H(r,t)$, that recedes from the surface ($z = L$) to the bottom of the product ($z = 0$). In order to determine the position of moving interface $H(r,t)$, mass and heat balances across the interface are solved.

The mass balance across the interface reads,

$$-\mathbf{n} \cdot M_w \mathbf{N}_w \Big|_{\mathbf{z}=H(r,t)} = -v_s(\rho_I - \rho_{II}) \qquad (6.16)$$

The heat balance across the interface is given by,

$$\mathbf{n} \cdot (\kappa_I \boldsymbol{\nabla} T_I - \kappa_{II} \boldsymbol{\nabla} T_{II}) \Big|_{z=H(r,t)} + (\rho_I c_{p,I} - \rho_{II} c_{p,II}) v_s T_{int} =$$

$$= \mathbf{n} \cdot (c_{p,gas} T_{int} + \Delta H_s) M_w \mathbf{N}_w \Big|_{z=H(r,t)} \qquad (6.17)$$

The velocity of interface is obtained by combining Eqs. 8.22 and 8.23,

$$v_s = \frac{\mathbf{n} \cdot (\kappa_I \boldsymbol{\nabla} T_I - \kappa_{II} \boldsymbol{\nabla} T_{II})}{(\Delta c_p T_{int} + \Delta H_s)(\rho_I - \rho_{II})} \qquad (6.18)$$

where $\Delta c_p = c_{p,gas} - (\rho_{II} c_{p,II} - \rho_I c_{p,I})/(\rho_{II} - \rho_I)$.

6.3.2 Simplified 1D pseudo-steady state model

A simplified pseudo-steady state model of primary drying has been developed to obtain fast outcomes and, potentially, simulate the behavior of an entire batch, and not only a single specific vial. This model was inspired to the one proposed by Pikal (1985) and Pikal et al. (2016), and was adapted to take into account vials in different positions on the shelf and the variability of process parameters (shelf temperature and chamber pressure), vial characteristics (filling volume, heat transfer coefficients) and in product characteristics (mass transfer resistance). This model was also adapted to simulate continuous freeze-drying as proposed in this thesis.

As shown in Figure 6.3a, product height is divided $n-1$ equal slices, and the following equations are solved for each slice i,

$$\frac{dm}{dt} = \frac{A_p(p_{w,int} - P_c)}{R_p} = J_q \Delta H_s \qquad (6.19)$$

$$R_p = R_p(L_{d,i}) \qquad (6.20)$$

$$p_{w,int} = p_{w,int}(T_{int}) \qquad (6.21)$$

$$T_p = \dot{Q}_d \left(\frac{L_p - L_{d,i}}{\kappa_f A_p} \right) T_{int} \qquad (6.22)$$
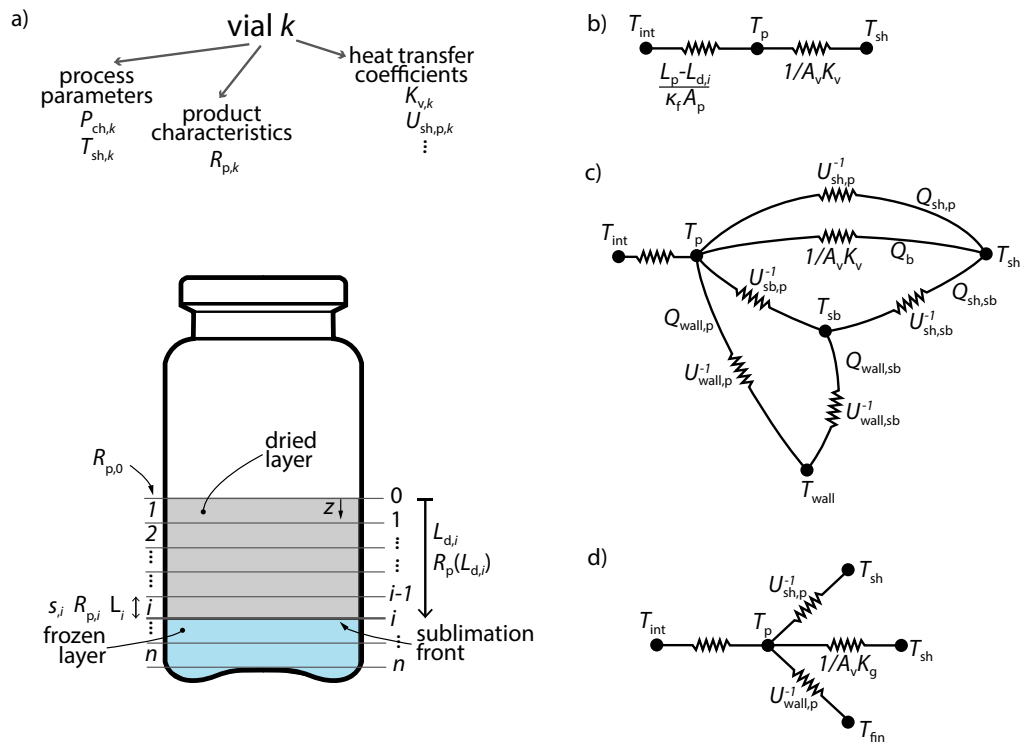
Figure 6.3 (a) Schematic of the domain of the simplified 1D pseudo-steady state model; electrical analogy of the heat transfer in the case of (b) central vials and (c) peripheral vials in a batch freeze-drier, and in the case of (d) suspended-vial freeze-drying.

This model was used to simulate an entire batch by taking into account the variability of process parameters and product characteristics. The variability and uncertainty of the input parameters were taken into account by assigning to each vial i the input parameters of its specific class, increased or decreased of a contribution due to the variability of the parameters; this contribution is chosen following a Gaussian distribution. The process parameters taken into account are the chamber pressure, shelf temperature, filling volume, mass transfer resistance, and heat transfer coefficients.

In the case fo batch, vials were divided into 5 classes, i.e., central (C), edge vials (L, M, N) and corner vials (P). In the case of continuous freeze-drying of suspended-vial, only one class was considered as all the vials follow the same path in the lyophilizer and, so, no edge-vial effect is present.

The 1D model was implemented in Python 3 using the Numpy and Scipy modules.

Heat and mass transfer equations

Resistance to water vapor (R_p) can be equivalently expressed using different equations according to the data available. R_p can be expressed as a function of mean pore diameter d_P (Rambhatla et al., 2004),

$$R_\mathrm{p}(L_{\mathrm{d},i}) = R_{\mathrm{p},0} + \sum_{i=1}^{L_{\mathrm{d},i}} R_{\mathrm{p},i}, \qquad \text{where } R_{\mathrm{p},i} = \frac{3}{2}\frac{\tau^2}{\epsilon}\frac{s_i}{d_{\mathrm{p},i}}\sqrt{\frac{\pi RT}{2M_w}} \tag{6.23}$$

or using the fitting parameters $R_{p,0}$, Γ_1 and Γ_2,

$$R_p(L_{d,i}) = R_{p,0} + \frac{\Gamma_1 L_{d,i}}{1 + \Gamma_2 L_{d,i}} \tag{6.24}$$

The heat flow $\dot{Q}_d$ represents the sum of different contributions, i.e., heat supplied from the shelf and heat provided from the surroundings. As shown in Figure 6.3b, in the case of central vials in the batch freeze-drier, the heat supplied from the shelf is usually the only contribution considered,

$$\dot{Q}_d = A_v \left(\frac{1}{K_v'} + \frac{s_{gl}}{\kappa_{gl}} \right)^{-1} (T_{sh} - T_p) \tag{6.25}$$

In the case of peripheral vials in the batch freeze-drier, the expression for the heat transferred to the product is much complicated, see Figure 6.3c. The details of the model are reported in Appendix C.

On the other hand, in the case of continuous freeze-drying here proposed (Figure 6.3), the heat is supplied from the heating sources, which for the functional prototype used in this thesis are the shelves and the chamber walls, here indicated as fins. For the functional prototype, the heat power reads,

$$\dot{Q}_d = U_{sh,p}(T_{sh}^4 - T_b^4) + U_{fin,p}(T_{fin}^4 - T_b^4) + K_g A_v (T_{sh} - T_b) \tag{6.26}$$

where the first term is related to the heat supplied from the upper and bottom shelf, the second from the chamber wall and the third through gas conduction from shelf to vial. The determination of the heat transfer coefficients is reported in Appendix C.

6.4 Results

6.4.1 Validation

The 2D-model and the 1D-model, have been validated for both batch and suspended-vial configuration.

Those models were validated by comparing the numerical output of the simulations with the experimental results obtained using a water solution of mannitol 5% w/w as model formulation. The experimental runs were carried out in the pilot-scale lyophilizer LyoBeta 25 (Telstar, Terrassa, Spain). Product temperature was measured using thin thermocouples (T type, Tersid, Milano, Italy) placed in different vials; vials (10R 24.0 x 45.0, Nuova Ompi, Piombino Dese, Italy) were filled in with 3 ml of liquid solution. Drying time was estimated from the Pirani/Baratron pressure ratio curve, taking its midpoint as the average drying time and the onset-offset as the variability of drying times within the central vial, in the case of the batch, and within the entire lot in the case of suspended-vial configuration. The simulation test cases and the parameters used to simulate them are shown in Table 6.1.

Figure 6.4a shows the curves of product temperature in the central vial and peripheral vial (vial L) within the batch. The 2D- and 1D-model are in good agreement with the experimental data, as they are both able to catch the dynamics of temperature rise and the maximum product temperature reached during drying. As shown in Figure 6.4b, the sublimation rate was at its maximum rate at the beginning and, then,

Table 6.1 Simulation test cases.

Test	Configuration	Cycle parameters		Product parameters	
		T_{sh}, K	P_c, Pa	D_p, μm	ε/τ^2
1	Batch, vial C	263	10	40	0.225
2	Batch, vial L	263	10	40	0.225
3	Suspended-vial (uncontrolled nucleation)	263	10	93	0.225
4	Suspended-vial (uncontrolled nucleation)	298	2	93	0.225

decreased as the resistance to vapor flow increased. The position of the sublimation interface is shown in Figure 6.4c. It is clear that the central vial exhibited a lower sublimation rate, about 30 % lower than the vial L, but also lower product temperature, about 3-4 K lower than the vial L. The higher sublimation rate and product temperature of the peripheral vial L is due to the extra heat received from the chamber wall and the surroundings; this effect is usually called edge-vial effect. As a consequence of this variability in the heat supplied to vials in different positions on the shelf, the central vial was dried after about 20 h, whereas vial L was already dried only after 13 h, see Table 6.2.
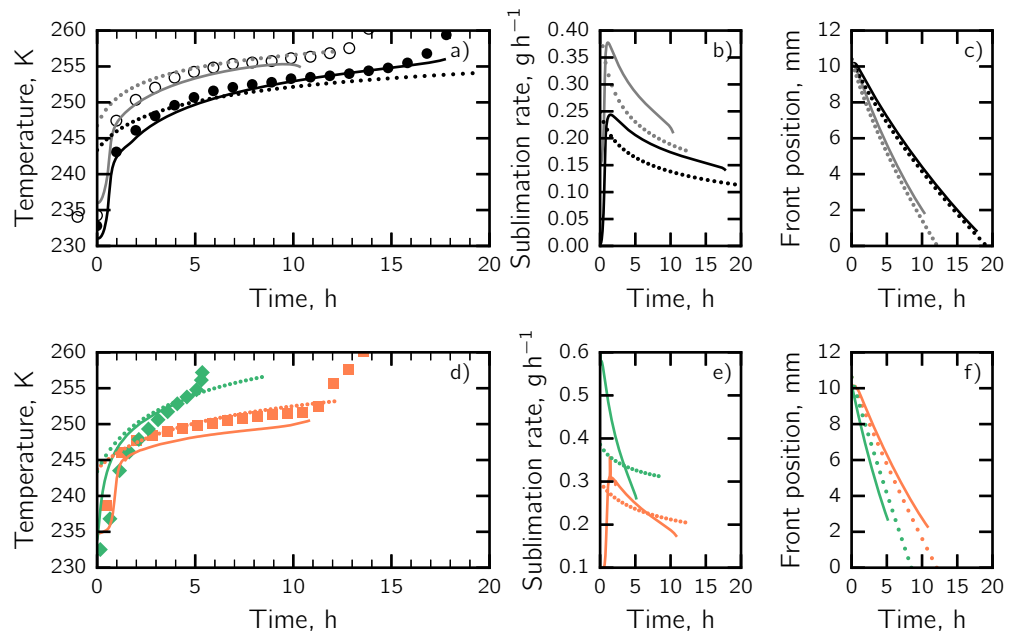
Figure 6.4 (a,d) Experimental and simulated temperature profile during primary drying, (b,e) sublimation rate and (c,f) position of the sublimation interface. (a,b,c) refer to conventional freeze-drying (T_{sh} = 263 K, P_c = 10 Pa): experimental value obtained for (●) central vials and (○) peripheral vials; (b,e,f) refer to suspended-vial freeze-drying: experimental value obtained at (■) T_{sh} = 263 K, P_c = 10 Pa and (◆) T_{sh} = 298 K, P_c = 2 Pa. Continuous lines refer to simulation using 2D model, dotted lines to 1D model.

Figure 6.4d-f shows the comparison between suspended-vial freeze-drying performed at different process conditions, i.e., 263 K and 10 Pa vs. 298 K and 2 Pa. In the first case, the maximum product temperature reached during drying was about 253 K, whereas in the second case about 256 K. As a consequence drying duration

decreased from about 14 h to 9 h. This result is impressive as, considering 256 K as the constraint for the maximum temperature that the product can reach during drying, the suspended-vial configuration was able to halve drying duration. That is possible for two reasons mainly, (i) all the vials received the maximum possible heat and (ii) the product presented a much smaller resistance to mass transfer.

Table 6.2 Comparison of primary drying times predicted with the 2D and 1D mathematical models.

Configuration	T_{sh}, K	P_c, Pa	Drying time, h		
			experimental	simulation 2D	simulation 1D
Conventional FD	263	10	19.5 ± 2.5	vial C: 20 vial L: 13	vial C: 19.1 vial L: 12.2
Suspended-vial FD	263	10	13.7 ± 0.3	14	12.2
Suspended-vial FD	298	2	8.8 ± 0.2	8	8.5

It should be pointed out that the computational times of the two models differed of orders of magnitude. Using a machine equipped with an Intel Core i7-4700MQ (2.40 GHz) a running Linux X86-64 operating system, the 2D model required hours to complete the simulation, whereas the 1D model required less than one second for each simulation. The 1D model was, so, fast enough to be used to simulate a high number of vials, e.g., the production of 100,000 vials.

Product temperature during primary drying

Further interesting results obtained from the 2D-model simulations are the contour plots of product temperature during drying shown in Figure 6.5. It is possible to distinguish the upper, dried, layer divided from the lower frozen layer by the sublimation interface, represented with the tick line. For a product being dried by using the suspended-vial configuration, the temperature in the dried layer was much higher than in the case of the batch configuration because it received much more heat by radiation from the heating surfaces. Moreover, the heating surfaces were at a much higher temperature in the suspended-vial configuration. This difference was sharper comparing suspended vial with a central vial of the batch, where radiation from the chamber wall is almost negligible. The extra radiative heat supplied in the suspended-vial configuration triggered water desorption from the dried layer already during primary drying, whereas it is usually negligible in the batch (except for peripheral vials). As a result, at the end of primary drying, the residual moisture in the case of suspended-vial was much lower than in the batch, e.g., 3.17% vs. 1.01%, see Section 4.3.6.

6.4.2 2D-model

The 2D-model was used to better understand the role of the different heat transfer mechanisms in the batch and suspended-vial configuration. Here, heat transfer has been studied by simulating the sublimation of pure ice, and so, replicating the gravimetric tests that are usually performed in the laboratory, see Section 4.2.2. Experimental runs and simulations referred to vials 10R ($K_c = 2.776\,\mathrm{W\,m^{-2}\,K^{-1}}$,
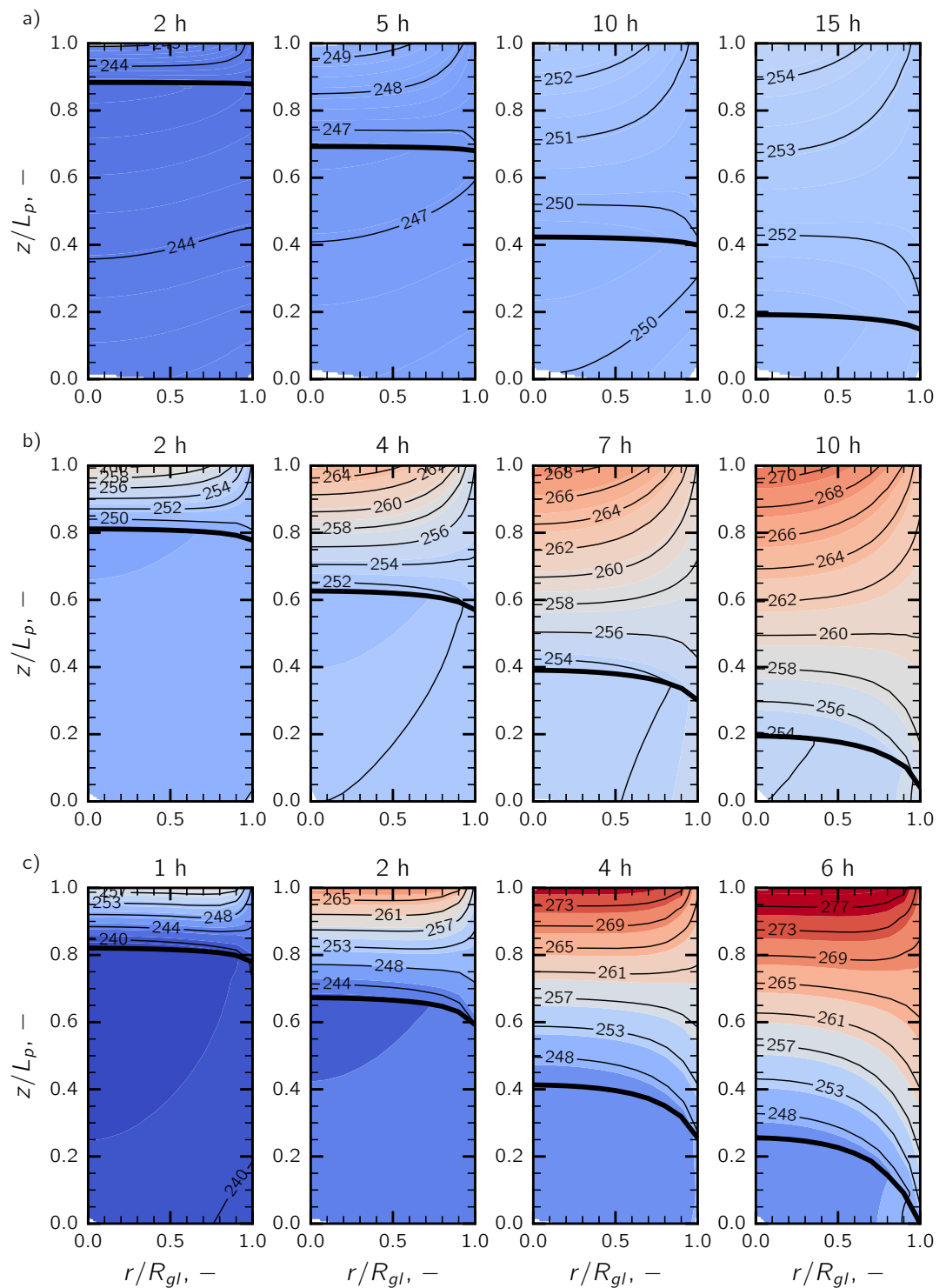
Figure 6.5 Contour plot of product temperature during primary drying. (a) Central vial and (b) peripheral vial in a batch; (c) suspended-vial configuration. The thick lines represent the sublimation interface, thin lines represent the isolines and the numbers the corresponding temperatures.

111

$\ell_V = 2.25 \times 10^{-4}$ m) filled with 3 ml of pure ice. Moreover, the experimental runs were performed in the pilot-scale lyophilizer LyoBeta 25 (Telstar, Terrassa, Spain).

Batch freeze-drying

The first step of this analysis consisted of analyzing the effect of shelf temperature, chamber pressure and vial position on the heat power supplied to the product during the primary drying, see Figure 6.6.

As shown in Figure 6.6a, the heat provided to the product can be modulated by varying shelf temperature. The most important contribution is related to the gas conduction in the gap between the vial bottom and the shelf (about 55 %); radiation and the direct contact contribute respectively for about 30% and 15% of the total heat supplied to the product.

Chamber pressure also plays a central role in heat transfer because it influences the heat transfer coefficient K_v, but is also connected to mass transfer. As shown in Figure 6.6b, heat supplied to the product increases as chamber pressure increases in the range of 1 to about 20 Pa, but decreases for higher values. This seems counterintuitive as K_v always increases as chamber pressure increases. On the other hand, the driving force for heat transfer $(T_{sh} - T_p)$ sharply decreases as chamber pressure increased; a more in-deep discussion on these aspects are reported in Capozzi (2014).

A fundamental aspect that should be taken into account is the position of vials over the shelf, which represents a serious cause of variability in the heat flow rate transferred to the product during the primary drying. As shown in Figure 6.6d, peripheral vials receive much more heat than central ones, because of radiation from chamber walls. Although only 10-15 % of the whole batch is constituted by peripheral vials, they have to be taken into consideration during the cycle design; shelf temperature, in fact, is chosen so that the product in peripheral vials does not exceed its target temperature.
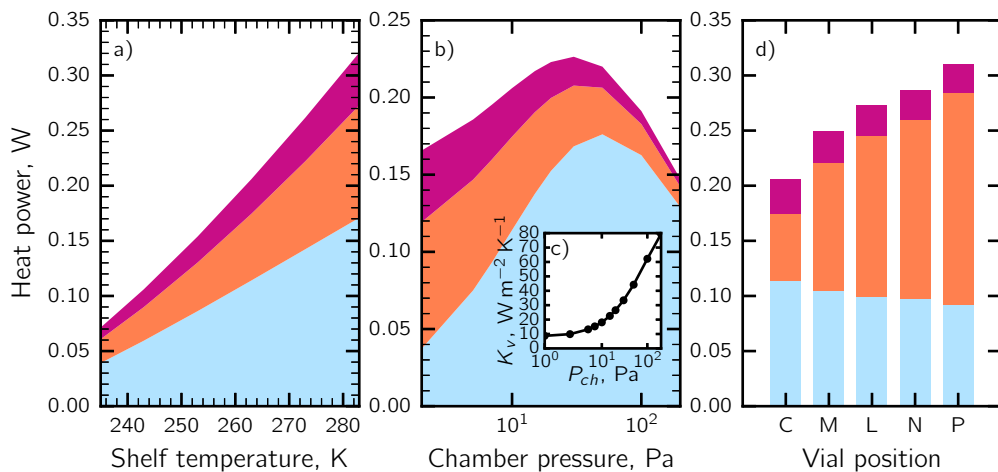
Figure 6.6 Heat power supplied to the product in a batch lyophilizer by varing (a) shelf temperature, (b) chamber pressure and (d) for vial placed in different position in the chamber; (c) K_v as a function of chamber pressure. The heat transfer mechanisms are (▨) gas conduction, (▨) radiation and (▨) direct contact.

The effect of process conditions on drying time and the maximum temperature reached during primary drying have been simulated by varying the shelf temperature in the range 235-283 K and the chamber pressure between 2 and 200 Pa, see Figure 6.7. From these results, it is clear that shelf temperature and chamber pressure affect both product temperature and drying time, and have to be carefully chosen in the design of lyophilization cycles. In fact, in the optimization framework, chamber pressure and shelf temperature have to be chosen so that i) the maximum product temperature is several degrees below the collapse temperature, ii) the primary drying duration is the lowest as possible.
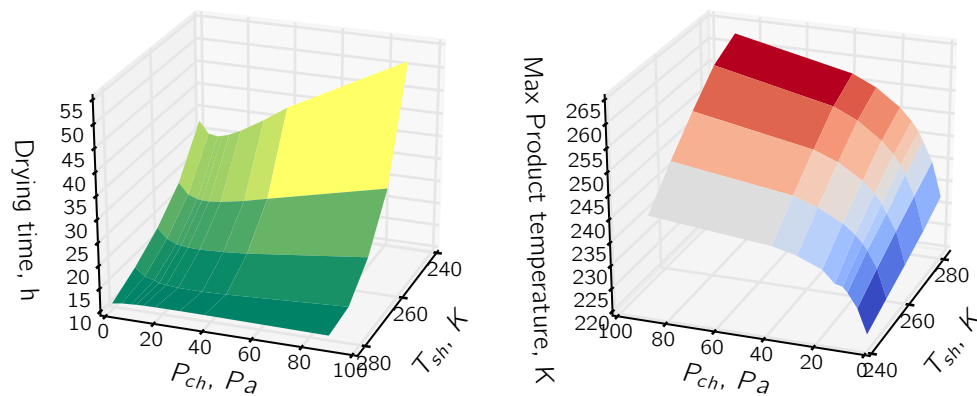
Figure 6.7 Overview of the effect of shelf temperature and chamber pressure on (a) drying time and (b) maximum ice temperature during sublimation.

Suspended-vial freeze-drying

Figure 6.8 shows the effect of shelf temperature, chamber pressure and vial-to-shelf clearance on the heat power supplied to the product during primary drying for the suspended-vial configuration.

Heat supplied to the product can be changed by varying shelf temperature as shown in Figure 6.8a. Radiation is the most relevant heat transfer contribution in the range of shelf temperature 235-295K and represents from 96 to 94 % of the whole heat supplied during primary drying. Contrary to conventional, batch freeze-drying, the effect of chamber pressure on heat power supplied to the product in the case of suspended-vial configuration is modest because the relative contribution of gas conduction is also modest, and ranges from 4 to 6% of the whole heat supplied to the product, see Figure 6.8b. As shown in Figure 6.8c, the contribution of the gas conduction decreases as the vial-to-shelf clearance increases. In the range of 3-30 mm, the relative contribution of gas conduction to the total heat power decreases from 14% to 2%.

Heat transfer in batch and suspended-vial configuration

Figure 6.9 compares the heat power supplied to the vials in three different scenarios, i.e., (i) conventional batch for central (C) and peripheral (M and P) vial, (ii) vial in
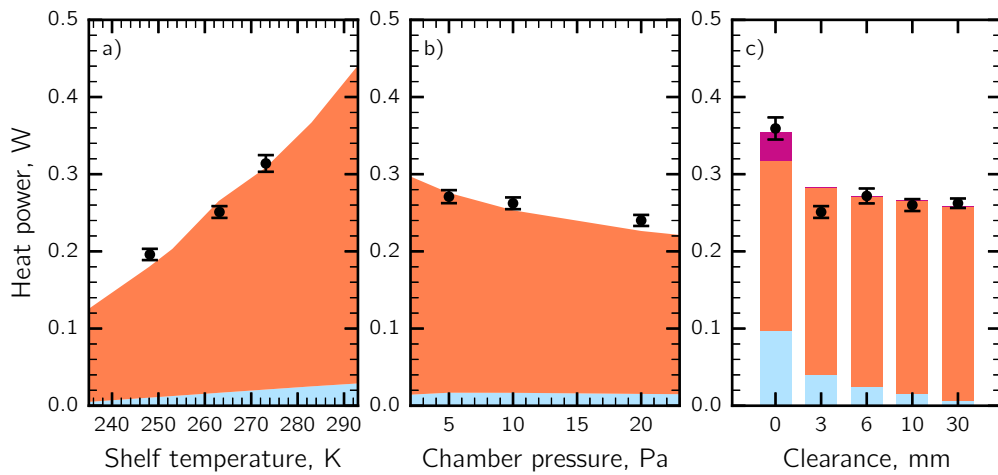
Figure 6.8 Heat power supplied to the product in the suspended-vial configuration by varing (a) shelf temperature, (b) chamber pressure and (c) vial-to-shelf clearance. The heat transfer mechanisms are (▪) gas conduction, (▪) radiation and (▪) direct contact; the experimental values (●) and standard deviationss are also reported.

contact with the shelf but wholly irradiated and (iii) suspended-vial configuration. The heat contributions are divided into (a) conduction by vial/shelf direct contact, (b) gas conduction through the shelf-to-vial clearance, and (c) radiation to vial bottom, top and side.
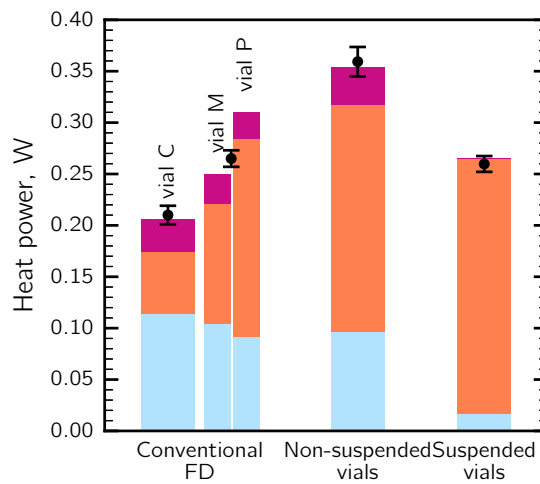
Figure 6.9 Heat power during primary drying in the case of conventional freeze-drying (for both central and edge vials), freeze-drying of non-suspended and suspended vials (clearance of 10 mm). Total heat power, as obtained from simulation, is divided into three terms: (▪), (▪) conduction through direct contact of vial and shelf, gas conduction in the small gap between vial and (▪) shelf and radiation from shelf and the environment. Experimental value of heat flux (●) and standard deviation are also reported. Freeze-drying runs were carried out at $P_c = 10$ Pa and $T_{sh} = 263$ K.

As concern batch freeze-drying, gas conduction, and direct contact accounted for more than 65% of the total heat supplied to the product, whereas the radiative heat is almost supplied from the bottom shelf as vials are mutually shielded. On the other

hand, the peripheral vials receive almost the same heat because of the direct contact and gas conduction but, at the same time, radiative heat is more than doubled; this extra heat is supplied mostly from chamber walls. Vials in contact with the shelf and completely exposed to chamber walls, but also to bottom and upper shelves, receive almost three times the radiative heat received by central vials in the batch. In the case of suspended-vial configuration, heat is mainly supplied by radiation and the contribution of gas conduction is usually lower than 6%.

6.4.3 1D-model

The 1D-model was used to better understand the effect of process conditions in the case of batch and suspended-vial configuration. The 1D-model is enough computational inexpensive to be used for parametric analysis and to simulate a high number of vials. The simulation referred to 5% mannitol in 8R vials (filling volume of 3 ml). In the case of batch freeze-drying, the variation on the heat transfer (Eq. C.4) coefficient C_1, C_2 e C_3 has been set to $7.8\,\mathrm{W\,m^{-2}\,K^{-1}}$, $1.6\,\mathrm{W\,m^{-2}\,K^{-1}\,Pa^{-1}}$ and $0.015\,\mathrm{Pa^{-1}}$. The coefficients of Eq. 6.24 were set to $R_{p,0} = 7.0 \times 10^4$, $\Gamma_1 = 6.0 \times 10^7$ and $\Gamma_2 = 0$ in the case of batch cycle (uncontrolle nucleation), $R_{p,0} = 7.0 \times 10^4$, $\Gamma_1 = 3.0 \times 10^7$ and $\Gamma_2 = 0$ in the case of suspended-vial freeze-drying (uncontrolled nucleation), and $R_{p,0} = 7.0 \times 10^4$, $\Gamma_1 = 1.2 \times 10^7$ and $\Gamma_2 = 0$ in the case of suspended-vial freeze-drying and VISF ($T_n = 2268\,\mathrm{K}$).

Effect of process conditions on batch freeze-drying

The effect of process conditions on drying behavior in a batch lyophilizer is reported in Figure 6.10 for a central vial; simulations refer to 5% mannitol.

Figure 6.10a-f shows the combined effect of chamber pressure and shelf temperature on drying time and maximum product temperature reached during drying. The effect of shelf temperature on drying time was evaluated for T_{sh} in the range 243 - 283 K (Figure 6.10b,e) and P_c from 1 to 20 Pa (Figure 6.10c,f). To give you an example, at 10 Pa drying duration decreases from 35 h to 21 h by increasing shelf temperature from 253 to 263 K; on the other hand, maximum product temperature increases from about 248 to 253 K. At the same time, the peripheral vials L are completely drying after 26 h at 253 K and 15 h at 263 K, and reaches a maximum product temperature of 250 K and 256 K respectively, which are several degrees higher than that shown by central vials.

The effect of chamber pressure on drying time was studied in a range of 1 - 20 Pa, Figure 6.10c-d. Chamber pressure plays a double role, it affects the driving force for mass transfer within the dried product, but also the heat transfer coefficient for the heat transferred from the shelf to the vial bottom. In fact, the pressure difference between the sublimation interface and the upper surface of the product increased if chamber pressure decreased, see Eq. 2.1. In contrast, the value of K_v decreased as well by decreasing chamber pressure, and the heat flux to the bottom of the vial felt down, see Eq. 6.8.

The effect known as *edge-vial effect* is due to the extra heat supplied by radiation from the chamber wall and the surroundings. It represents a severe cause of vial-to-vial heterogeneity in the drying behavior and makes freeze-drying challenging to design, optimize and control. Figure 6.11 shows the effect of vial position on drying
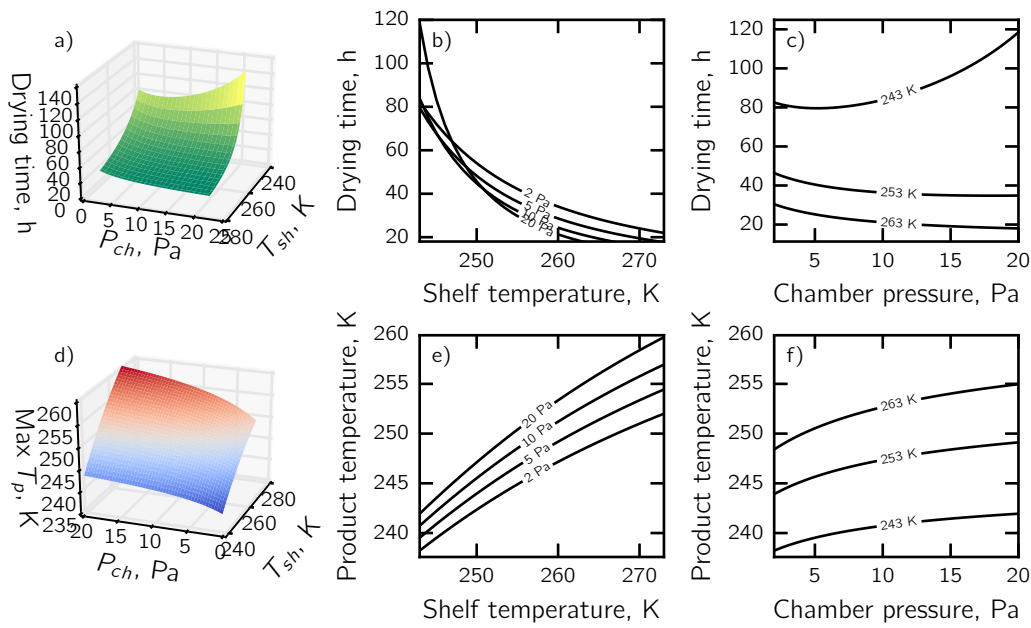
Figure 6.10 Drying time and maximum product temperature as a function of chamber pressure and shelf temperature in the central vial of a batch lyophilizer.

time and product temperature as obtained by the 1D model for a cycle carried out at 263 K and 10 Pa; each class of vial presents a different drying behavior, with about 8 h of difference in drying duration between the corner and the central vials, and more than 4 K in the product temperature.
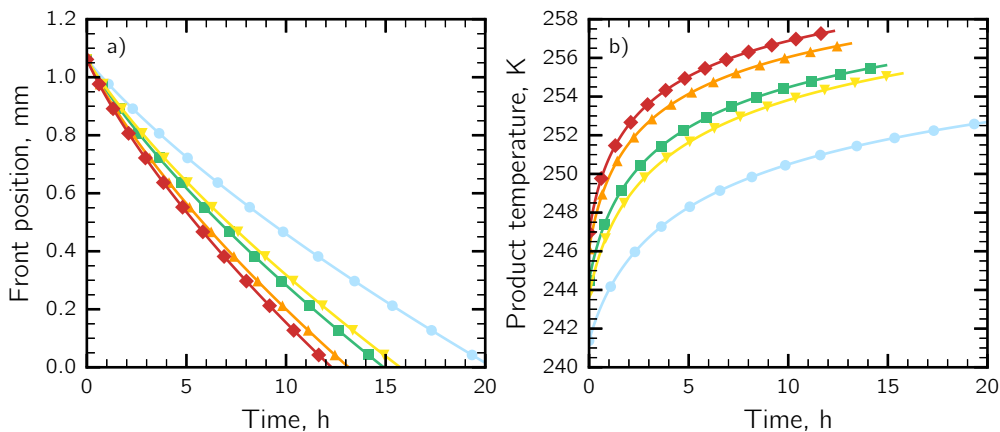
Figure 6.11 (a) Position of the sublimation front and (b) product temperature evolution during primary drying divided by classes of vials: (—●— C) central, (—■— L, —▽— M, —△— N) peripheral and (—◆— P) corner vials. The simulation refers to batch cycle at 263 K and 10 Pa.

Effect of process conditions on suspended-vial freeze-drying

The effect of process conditions on drying behavior in the case of suspended-vial freeze-drying is reported in Figure 6.12 in the case of uncontrolled nucleation and Figure 6.13 in the case of controlled nucleation via VISF; simulations refer to 5% w/w mannitol.

Similarly to batch freeze-drying, the drying duration for the suspended-vials configuration decreases as shelf temperature increases. In the case of uncontrolled nucleation, drying duration decreases from 14 h to 8 h as shelf temperature increases from 280 to 300 K ($P_c = 2\,\text{Pa}$); at the same time, maximum product temperature increases from 251 to 256 K. In the case of controlled nucleation, drying duration is reduced from 16 to 7 h as shelf temperature is increased from 280 to 300 K ($P_c = 2\,\text{Pa}$); at the same time, product temperature is much lower than that observed in the case of uncontrolled nucleation, i.e., respectively, 243 and 248 K.

Controlling nucleation via VISF is an essential feature of the concept of continuous freeze-drying studied in this thesis because it reduces the variability of product characteristics but also promotes the formation of bigger ice crystals (and pores in the dried layer) and, finally, speeds-up the drying process. Supposing 250 K as the target temperature, a cycle without controlling nucleation can be carried out at about 275 K and 2 Pa, resulting in a drying duration of about 15 h. On the other hand, the cycle can be carried out at 308 K and 2 Pa, resulting in a drying duration of about 7 h if VISF is applied.
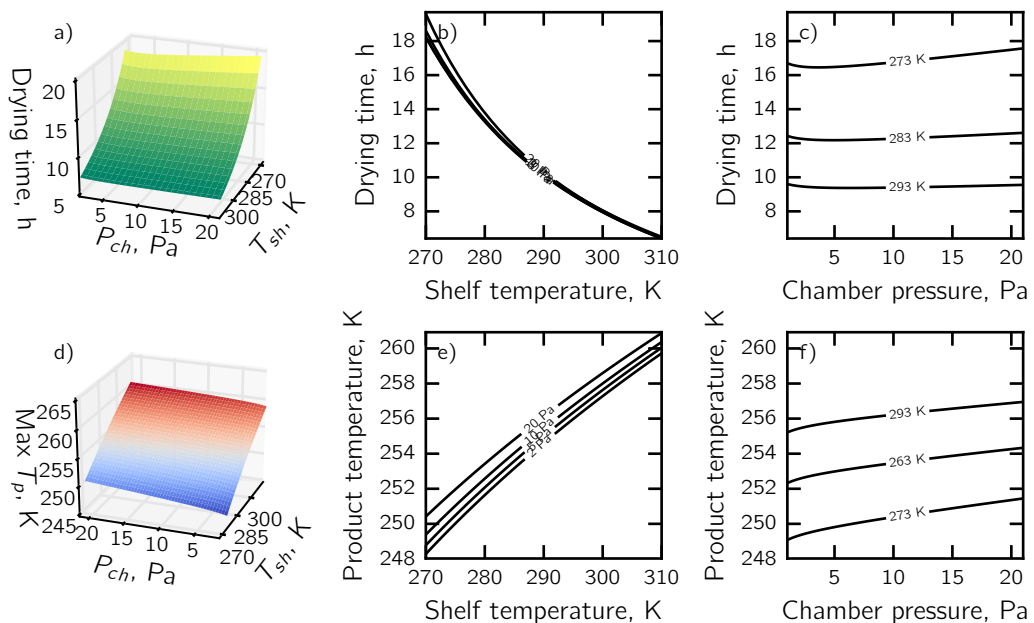
Figure 6.12 Drying time and maximum product temperature as a function of chamber pressure and shelf temperature in suspended-vial configuration (uncontrolled nucleation).
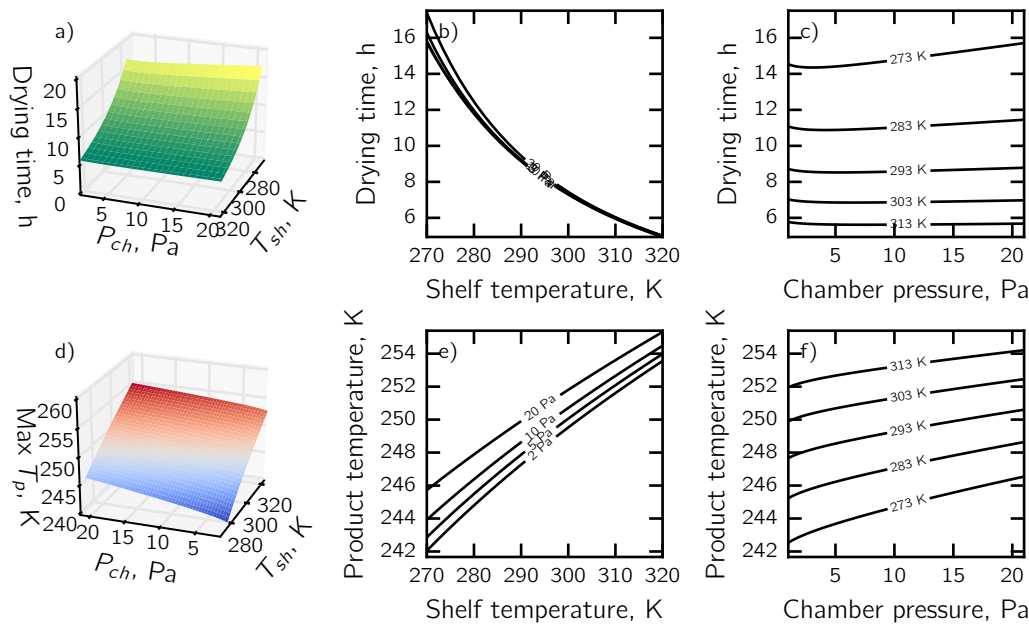
Figure 6.13 Drying time and maximum product temperature as a function of chamber pressure and shelf temperature in suspended-vial configuration (controlled nucleation using VISF).

6.4.4   Batch vs. continuous freeze-drying

In this last section, a comparison between batch freeze-drying and continuous freeze-drying of suspended vials is performed by taking into account the variability of the input parameters; the variability is here expressed in terms of standard deviation.

The primary drying of 100,000 samples containing a frozen solution of 5% mannitol was simulated in three different scenarios,

1. spontaneous nucleation, batch freeze-drying;

2. spontaneous nucleation, continuous freeze-drying;

3. VISF, continuous freeze-drying.

In the case of batch freeze-drying, 90.9% vials were identified as central vials (C), 5% vials as edge vials L, 2% as N and M, and 0.1% as the corner vials P. 100,000 vials were also simulated in the case of continuous freeze-drying, but, since they followed the same path and experienced the same process conditions, they were not divided into different classes.

Filling volume accuracy has been supposed to be 0.5% on nominal dosing volume, accordingly to the technical data declared by the pharmaceutical manufacturer IMA on its website for the in-line filling machine *SMART* (IMA, 2018).

Variations of shelf temperature have been supposed to be 2.5 K (Rambhatla et al., 2006) and the chamber pressure of 2 Pa. It is important to point out that this simulation was only carried out for purposes of illustration. As a matter of fact, variations in shelf temperature and chamber pressure strongly depend on the freeze-dryer geometry, as extensively studied in the literature (Barresi et al., 2018; Rasetto et al., 2010; Alexeenko et al., 2009; Ganguly et al., 2017).

In the case of batch freeze-drying, the variation on the heat transfer (Eq. C.4) coefficient C_1, C_2 e C_3 has been set to $7.8\,\mathrm{W\,m^{-2}\,K^{-1}}$, $1.6\,\mathrm{W\,m^{-2}\,K^{-1}\,Pa^{-1}}$ and $0.015\,\mathrm{Pa^{-1}}$.

The variability of product structure has also been considered; for the case (1) the coefficients of Eq. 6.24 were $R_{p,0} = 7.0 \times 10^4 \pm 10\%$, $\Gamma_1 = 6.0 \times 10^7 \pm 18\%$ and $\Gamma_2 = 0$, for the case (2) $R_{p,0} = 7.0 \times 10^4 \pm 10\%$, $\Gamma_1 = 3.0 \times 10^7 \pm 10\%$ and $\Gamma_2 = 0$, for the case (3) $R_{p,0} = 7.0 \times 10^4 \pm 7\%$, $\Gamma_1 = 1.2 \times 10^7 \pm 5\%$ and $\Gamma_2 = 0$

As the first step, many simulations were performed by varying T_{sh} until the 99 % of products did not exceed the target temperature, which was set to 254 K; the final outcomes are shown in Figure 6.14. Figure 6.14a-b shows the distribution of drying times and maximum product temperature within the batch divided per vial class, whereas Figure 6.14c shows the complementary cumulative distribution of the fraction of dried products during primary drying in the case of batch freeze-drying; Figure 6.14d-f refers to continuous freeze-drying.
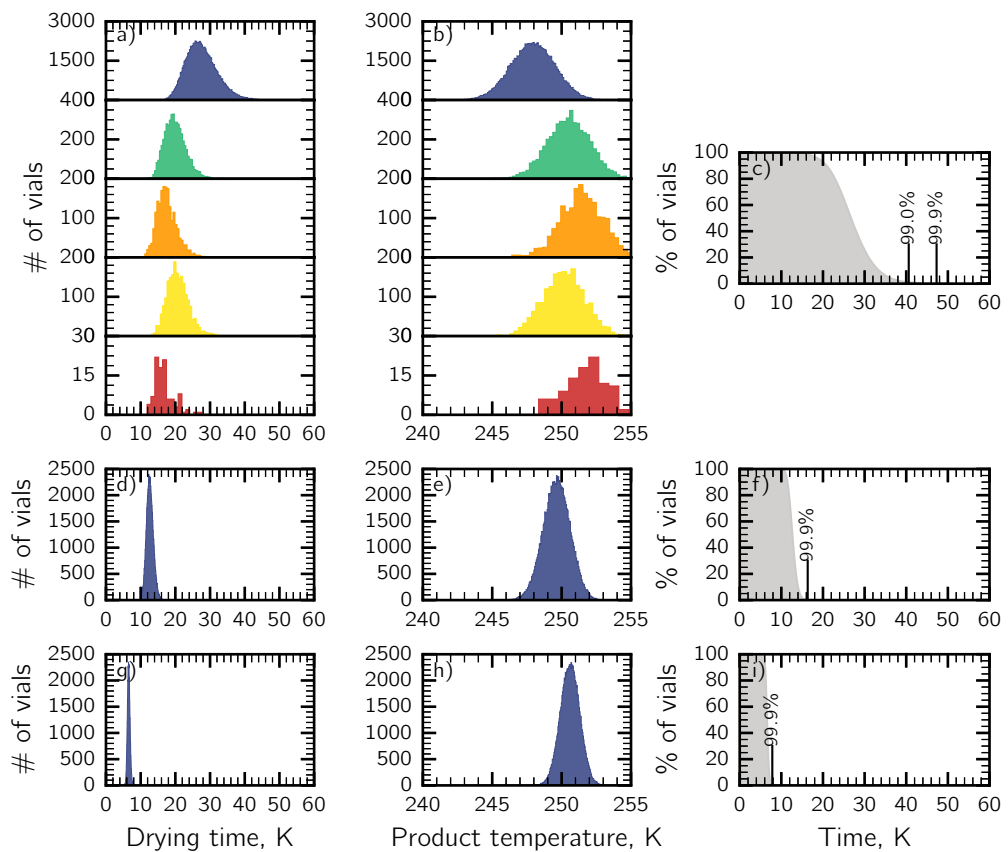
Figure 6.14 Distribution curves of (a,d,g) drying time, (b,e,h) maximum product temperature and (c,f,i) the complement of the cumulative distribution of drying time in the case of (a,b,c - case 1) batch/uncontrolled nucleation, (d,e,f - case 2) continuous/uncontrolled nucleation and (d,e,f - case 2) continuous/VISF. In the case 1, vials are divided into five classes, i.e., (■)C, (■)L, (■)M, (■)N, (■)P.

In the case of the batch configuration, shelf temperature can be set to 258 K. The vast majority of products reached a maximum product temperature well below the target temperature, i.e., 248 K, whereas a relatively small fraction of products, especially among peripheral vials, reached temperatures close to the target temperature, see Figure 6.14b. The drying behavior of these samples decreased the efficiency of the

119

process so that the 99% of samples were dried after 41 h and the 99.9% only after 47 h, see Figure 6.14c.

It can be noted that in batch freeze-drying, samples show very different behavior mainly due to the differences in the heat supplied but also because of the vial-to-vial variability of the product structure. Unfortunately, the differences in heat transfer are intrinsic to the batch process, and can not be eliminated. On the other hand, the vial-to-vial variability of the product structure can be mitigated by using controlled nucleation, although most of these techniques are difficult to perform at the industrial scale.

Figure 6.14d,e shows the distribution of drying times and maximum product temperature in the case 2, i.e., continuous freeze-drying without controlling nucleation during freezing. This cycle was performed using 270 K as shelf temperature and 2 Pa; the 99.9 % of vials were completely dried after 16 h, see Figure 6.14f.

Case 3 (Figure 6.14g,h) refers to continuous freeze-drying coupled with VISF; here cycle was performed at 286 K and 2 Pa, and the drying duration fell down to 8 h, see Figure 6.14i.

Contrary to batch, continuous freeze-drying of suspended vials showed narrower distributions in drying time because the edge-vial effect is not present and heat is supplied uniformly among vials. Moreover, product structure can accurately be controlled by using VISF.

6.5 Conclusions

In this chapter, a detailed bidimensional model and a simplified monodimensional model of primary drying were developed to understand the suspended-vial configuration better and, then, compare it with the conventional, batch, freeze-drying. Moreover, these models were used as practical tools to understand the potentiality of the continuous process.

As a first step, heat transfer mechanisms have been studied, showing that in the case of batch gas conduction represents the main mode of heat transfer for central vials, whereas radiation and gas conduction are equally important for peripheral vials. Peripheral vials receive much more heat than central vials due to the extra heat supplied from chamber walls; this effect is commonly known as the edge-vial effect. In the case of suspended-vial configuration, heat is supplied mainly by radiation, and gas conduction contributes only for less than 6%. The suspended-vial configuration allows avoiding important sources of heat transfer variability, such as the direct contact between shelf and vial and the edge-vial effect due to the different position of vials within the shelf.

The 2D- and 1D-model were used to simulate the drying behavior of a model formulation, showing a good agreement with the experimental results. These models were used to quantify the impact of process and product variability on the drying behavior and process efficiency, showing that continuous freeze-drying can reduce drying duration of 2-4 times with respect to batch lyophilization.

Acronyms

DGM Dusty-Gas Model; **QbD** Quality by Design.

List of symbols

A_p inner cross-sectional area of the vial, m^2

A_v outer cross-sectional area of the vial, m^2

C_1 parameter expressing the dependence of K_v' from radiation and the contact between vial bottom and tray surface, $J\,s^{-1}\,m^{-2}\,K^{-1}$

C_2 parameter expressing the pressure dependence of K_v', $J\,s^{-1}\,m^{-2}\,K^{-1}\,Pa^{-1}$

C_3 parameter expressing the pressure dependence of K_v', Pa^{-1}

c_i molar concentration of the i-component, $mol\,m^{-3}$

c_p specific heat capacity, $J\,kg^{-1}\,K^{-1}$

D_i',D_i'' transport coefficients of DGM equation for molar flux of specie-i, $m^2\,s^{-1}$

d_P pore diameter within the dried layer, m

e effective emissivity, -

F radiation view factor, -

$H(r,t)$ position of the sublimation interface, m

J_q heat flux, $W\,m^{-2}$

K_c heat transfer coefficient due to direct conduction from the shelf to the glass at the points of contact, $J\,s^{-1}\,m^{-2}\,K^{-1}$

K_g heat transfer coefficient due to conduction in the gas between the shelf and the vial bottom, $J\,s^{-1}\,m^{-2}\,K^{-1}$

K_v' heat transfer coefficient between the shelf and the vial bottom, $J\,s^{-1}\,m^{-2}\,K^{-1}$

$\ell_{b/s}$ vial/shelf clearance, m

L_d dried thickness, m

L_{gl} Vial height, m

L_P Product height, m

ℓ_v characteristic distance between the shelf and the vial,, m

m mass, kg

N molar flux, $mol\,m^{-2}\,s^{-1}$

$\mathbf{n}$ normal versor

p total pressure, Pa

P_c chamber pressure, Pa

p_i partial pressure of the i-component, Pa

p_w^{eq} vapor equilibrium pressure, Pa

$\dot{Q}_d$ heat flow supplied to the product during drying, $J\,s^{-1}$

r radial coordinate, m

R_g universal gas constant, $J\,mol^{-1}\,K^{-1}$

R_{gl} Outer vial diameter, m

R_p resistance of the dried layer to vapor flow, $m\,s^{-1}$

s_{gl} thickness of the glass at the bottom of the vial, m

T temperature, K

t time, s

$U_{fin,p}$ radiative fin to product extra heat transfer coefficient, $W\,K^{-4}$

$U_{sh,p}$ Shelf to product extra heat transfer coefficient, $W\,K^{-4}$

$U_{wall,p}$ wall to product extra heat transfer coefficient, $W\,K^{-4}$

v_s velocity of sublimation front, $m\,s^{-1}$

z axial coordinate, m

Greek letters

κ_0 heat conductivity of the water vapor at ambient pressure, $J\,s^{-1}\,m^{-1}\,K^{-1}$

ε porosity, -

κ thermal conductivity, $W\,m^{-1}\,K^{-1}$

Λ_0 free molecular heat conductivity at $0\,°C$, $J\,s^{-1}\,m^{-1}\,K^{-1}$

ρ density, $kg\,m^{-3}$

σ_{SB} Stefan–Boltz constant, $W\,m^{-2}\,K^{-4}$

τ tortuosity, -

Ω computational domain

Subscript

0   initial condition

bp   vial bottom

f   frozen

fin   radiative fin

I   dried layer

ice   ice

II   frozen layer

III   vial wall

i,j,k saturation index

in   inert gas

int   sublimation interface

sol   solid

tp   product top surface

vs   vial sidewall

water   water vapor

References

Alexeenko, A. A., Ganguly, A, and Nail, S. L. (2009). Computational analysis of fluid dynamics in pharmaceutical freeze-drying. *Journal of Pharmaceutical Sciences* 98 (9), pp. 3483–3494.

Barresi, A. A., Rasetto, V., and Marchisio, D. L. (2018). Use of computational fluid dynamics for improving freeze-dryers design and process understanding. Part 1: Modelling the lyophilisation chamber. *European Journal of Pharmaceutics and Biopharmaceutics* 129, pp. 30–44.

Capozzi, L. C. (2014). "Modellazione matematica del processo di liofilizzazione di granuli". MA thesis. Italy: Politecnico di Torino.

Fissore, D., Pisano, R., and Barresi, A. A. (2010). On the methods based on the Pressure Rise Test for monitoring a freeze-drying process. *Drying Technology* 29 (1), pp. 73–90.

Fissore, D., Pisano, R., and Barresi, A. A. (2018). Process analytical technology for monitoring pharmaceuticals freeze-drying–A comprehensive review. *Drying Technology*, pp. 1–27.

Ganguly, A., Varma, N., Sane, P., Bogner, R., Pikal, M., and Alexeenko, A. (2017). Spatial variation of pressure in the lyophilization product chamber part 1: computational modeling. *AAPS PharmSciTech* 18 (3), pp. 577–585.

Goff, J. A. and Gratch, S. (1946). Low-pressure properties of water from -160 to 212 F. *Transactions of the American Society of Heating and Ventilating Engineers* 51, pp. 125–164.

IMA (2018). *In-line filling, stoppering and capping machine: SMART*. URL: http://imacare.it/Product/EN/Products-F575/Aseptic_Processing_and_Freeze_Drying-S633/Aseptic_Processing-T638/Liquid_filling_and_stoppering-Q640/In_line_filling%2C_stoppering_and_capping_machine%3A_SMART-M64.html (visited on 09/02/2018).

King, C. J. et al. (1971). *Freeze-drying of foods.* London: Butterworth & Co. Ltd.

Litchfield, R. and Liapis, A. (1979). An adsorption-sublimation model for a freeze dryer. *Chemical Engineering Science* 34 (9), pp. 1085–1090.

Marchisio, D. L., Galan, M., and Barresi, A. A. (2018). Use of computational fluid dynamics for improving freeze-dryers design and process understanding. Part 2: Condenser duct and valve modelling. *European Journal of Pharmaceutics and Biopharmaceutics* 129, pp. 45–57.

Mascarenhas, W., Akay, H., and Pikal, M. (1997). A computational model for finite element analysis of the freeze-drying process. *Computer Methods in Applied Mechanics and Engineering* 148 (1), pp. 105–124.

Mason, E. A. and Malinauskas, A. (1983). *Gas Transport in Porous Media: The Dusty-Gas Model*. Amsterdam: Elsevier, Amsterdam.

Pikal, M. J., Bogner, R., Mudhivarthi, V., Sharma, P., and Sane, P. (2016). Freeze-drying process development and scale-up: scale-up of edge vial versus center vial heat transfer coefficients, Kv. *Journal of Pharmaceutical Sciences* 105 (11), pp. 3333–3343.

Pikal, M. (1985). Use of laboratory data in freeze drying process design: heat and mass transfer coefficients and the computer simulation of freeze drying. *PDA Journal of Pharmaceutical Science and Technology* 39 (3), pp. 115–139.

Pisano, R., Fissore, D., and Barresi, A. A. (2011). Heat transfer in freeze-drying apparatus. In: *Developments in Heat Transfer*. Rijeka, Croatia: InTech, pp. 92–114.

Rambhatla, S, Tchessalov, S, and Pikal, M. J. (2006). Heat and mass transfer scale-up issues during freeze-drying, III: control and characterization of dryer differences via operational qualification tests. *AAPS PharmSciTech* 7 (2), E61–E70.

Rambhatla, S., Ramot, R., Bhugra, C., and Pikal, M. J. (2004). Heat and mass transfer scale-up issues during freeze drying: II. Control and characterization of the degree of supercooling. *AAPS Pharmscitech* 5 (4), pp. 54–62.

Rasetto, V., Marchisio, D. L., Fissore, D., and Barresi, A. A. (2010). On the use of a dual-scale model to improve understanding of a pharmaceutical freeze-drying process. *Journal of Pharmaceutical Sciences* 99 (10), pp. 4337–4350.

Sadikoglu, H and Liapis, A. (1997). Mathematical modelling of the primary and secondary drying stages of bulk solution freeze-drying in trays: Parameter estimation and model discrimination by comparison of theoretical results with experimental data. *Drying Technology* 15 (3-4), pp. 791–810.

Scutellà, B., Passot, S., Bourlés, E., Fonseca, F., and Tréléa, I. C. (2017). How vial geometry variability influences heat transfer and product temperature during freeze-drying. *Journal of Pharmaceutical Sciences* 106 (3), pp. 770–778.

Scutellà, B., Bourlès, E., Plana-Fattori, A., Fonseca, F., Flick, D., Trelea, I.-C., and Passot, S. (2018). Effect of Freeze Dryer Design on Heat Transfer Variability Investigated Using a 3D Mathematical Model. *Journal of Pharmaceutical Sciences* 107 (8), pp. 2098–2106.

Sheehan, P and Liapis, A. (1998). Modeling of the primary and secondary drying stages of the freeze drying of pharmaceutical products in vials: Numerical results obtained from the solution of a dynamic and spatially multi-dimensional lyophilization model for different operational policies. *Biotechnology and Bioengineering* 60 (6), pp. 712–728.

Velardi, S. and Barresi, A. (2008). Development of simplified models for the freeze-drying process and investigation of the optimal operating conditions. *Chemical Engineering Research and Design* 86 (1), pp. 9–22.

Zhu, T., Moussa, E. M., Witting, M., Zhou, D., Sinha, K., Hirth, M., Gastens, M., Shang, S., Nere, N., Somashekar, S. C., et al. (2018). Predictive models of lyophilization process for development, scale-up/tech transfer and manufacturing. *European Journal of Pharmaceutics and Biopharmaceutics* 128, pp. 363–378.

7

Modeling lyophilized products at the micro-scale

This chapter deals with the problem of estimate the morphological characteristics of lyophilized products. X-ray microcomputed tomography (μ-CT) is used to analyze and reconstruct the structure of the porous product. The computational methods were used to determine the structural parameters that impact on mass transport of vapor during drying, i.e., pore size, tortuosity, and permeability. These methods included (i) slice-by-slice 2D image analysis, (ii) 3D image analysis and (iii) CFD simulations. Moreover, μ-CT is proposed as an alternative for the visual inspection of lyophilized products as it is able to catch small defects such as structural micro-collapse.

7.1 Introduction

As extensively described in the previous chapters, the product structure influences sublimation and desorption rates, but it has also implications in the long-term stability, the final reconstitution ability of the dried products, and in the activity recovery of many APIs.

Traditionally, the final morphology of a lyophilized product has been investigated using Brunauer-Emmett-Teller specific surface area analysis (BET) or, more commonly, SEM imaging (Rey, 1999; Zhang, 2018; Bosca et al., 2013; Hottot et al., 2004); the product can also be characterized somehow through indirect measurements of the resistance to vapor flow and correlating that to its pore diameter and tortuosity (Rambhatla et al., 2004).

In the last few years, the lyophilization community has put many efforts on trying to better understand the relationship between freezing protocols and product structure, such as to predict product morphology (Nakagawa et al., 2006; Nakagawa et al., 2007; Pisano and Capozzi, 2017; Arsiccio et al., 2017; Oddone et al., 2017). At the same time, the community is also moving towards new imaging techniques, such as X-Ray micro-computed tomography (μ-CT) (Mousavi et al., 2007; Izutsu et al., 2014; Nygaard et al., 2008; Parker et al., 2010; Xiao et al., 2007; Pisano et al., 2017b; Izutsu et al., 2014;

Goshima et al., 2016; Haeuser et al., 2018). New approaches have been implemented to extrapolate information from images, i.e., image segmentation (Arsiccio et al., 2018a; Capozzi et al., 2018), frequency domain image analysis, and artificial neural network (Grassini et al., 2016). These imaging techniques can be used to estimate morphology parameters of the product, i.e., pore diameter and tortuosity, and, in turn, estimate the cake resistance to vapor flow during drying.

In this chapter, μ-CT analysis is used as a non-destructive method to analyze the structure of the sample. The outcomes from μ-CT analysis of the samples were analyzed using various approaches with the aim of estimating the structural parameters of the product. In particular, the analysis will consist of the following,

1. Slice-by-slice 2D image analysis of the entire sample;

2. 3D image analysis of small portions of the product (the so-called representative elementary volume, REV) sampled at different heights along with the product;

3. CFD simulations applied to REVs at different heights in the products.

7.2 Methods

3D non-destructive X-ray μ-CT tomography is used to analyze and reconstruct the internal structure of lyophilized samples, whereas various computational methods are used for calculating their structural properties, i.e., porosity, pore diameter, tortuosity, and permeability.

7.2.1 Micro-CT and product reconstruction

The first step of this procedure consists of analyzing the dried sample using the non-destructive X-ray micro-CT tomography. Computed tomography is a non-destructive imaging technique for producing 3D 'virtual' structure of a sample. Nano-CT (SkyScan 1272, Bruker microCT, Kontich, Belgium) was used to analyze freeze-dried samples; X-ray beams were generated by a tungsten filament at 50 kV and 200 μA. Samples were analyzed over a rotation range of 180°, with a step of 0.1°, an exposure time of 200 ms per projection and a pixel size of 3 μm. The samples were not analyzed completely but their lateral portions were cut in order to increase the resolution of the images obtained from the analysis. The analyses were performed in the laboratory of Prof. Chiara Vitale Brovarone with the help of Giorgia Novaira and Giorgia Montalbano.

7.2.2 Computational methods for quantitative analysis of product structure

2D Image Analysis

The output of the μ-CT analysis consisted of an image for each layer of the product; to give you an example, for a typical lyophilized product these images were about 3000. The central portion of these images was analyzed using the open-source image processing library `scikit-image`, which implements the most common image processing algorithms and is perfectly integrated into the Python ecosystem (Walt et al., 2014; Gouillart et al., 2017).

The first step consisted of filtering the raw data using a thresholding algorithm and binarize the image; after that, small objects below 70 px were removed. The binarization divides the foreground, which represents the voids in the pores, from the background, which represents the pore walls.

The equivalent pore diameter can be calculated from the binarization of the image as follows,

$$d_{\mathrm{P}} = \frac{4A_{\mathrm{void}}}{P_{\mathrm{wetted}}} \approx \frac{4A_{\mathrm{BKGD}}}{P_{\mathrm{FGND}}} \tag{7.1}$$

where A_{BKGD} is the area of the background and P_{FGND} is the overall perimeter of the foreground.

As a second step, a more refined algorithm was used to identify the pores and calculate their properties, i.e., the random walker segmentation algorithm. The random walker segmentation algorithm is a semi-supervised segmentation algorithm which requires a set of user-defined labels (or seeds) to identify the regions that belong to different segments, i.e., the voids. After that, the algorithm determines the probability that a random walk from each unlabeled pixel first arrives at user-defined seeds (Grady, 2006). As shown in Figure 7.1, the procedure used in this work consisted of the following,

(a) identify the seeds using a binary erosion algorithm;

(b) apply the random walker algorithm;

(c) calculate the properties of each labeled pore i (A_i, P_i).

The equivalent pore diameter can be calculated as follows,

$$\langle d_{\mathrm{P}} \rangle = \frac{1}{n} \sum_i^n \frac{4A_i}{P_i} \tag{7.2}$$

where n is the number of pores identified in the image.

A further way to characterize the pore size is to calculate the distance from pore walls and its medial axis; this procedure is also known as topological skeletonization. It was then possible to estimate the local width of the objects, which in the case of pores represents a 'local' pore diameter (d_{Ploc}).

Image analysis can also be used to estimate the permeability by considering the pores in each slice as parallel pores so that the total viscous flow is the sum of the flow rates through the pores. The general expression for average permeability of parallel pores reads,

$$\langle B_0 \rangle_{\|} = \frac{\sum_i^n B_{0,i} A_i}{\sum_i^n A_i}, \qquad B_{0,i} = \frac{d_{\mathrm{P},i}^2}{32} \tag{7.3}$$

where $B_{0,i}$ is the permeability coefficient of pore i and A_i its sectional area.

A number-weight permeability coefficient has also been evaluated,

$$\langle B_0 \rangle_{\mathrm{nw}} = \frac{1}{n} \sum_i^n \frac{d_{\mathrm{P},i}^2}{32} \tag{7.4}$$
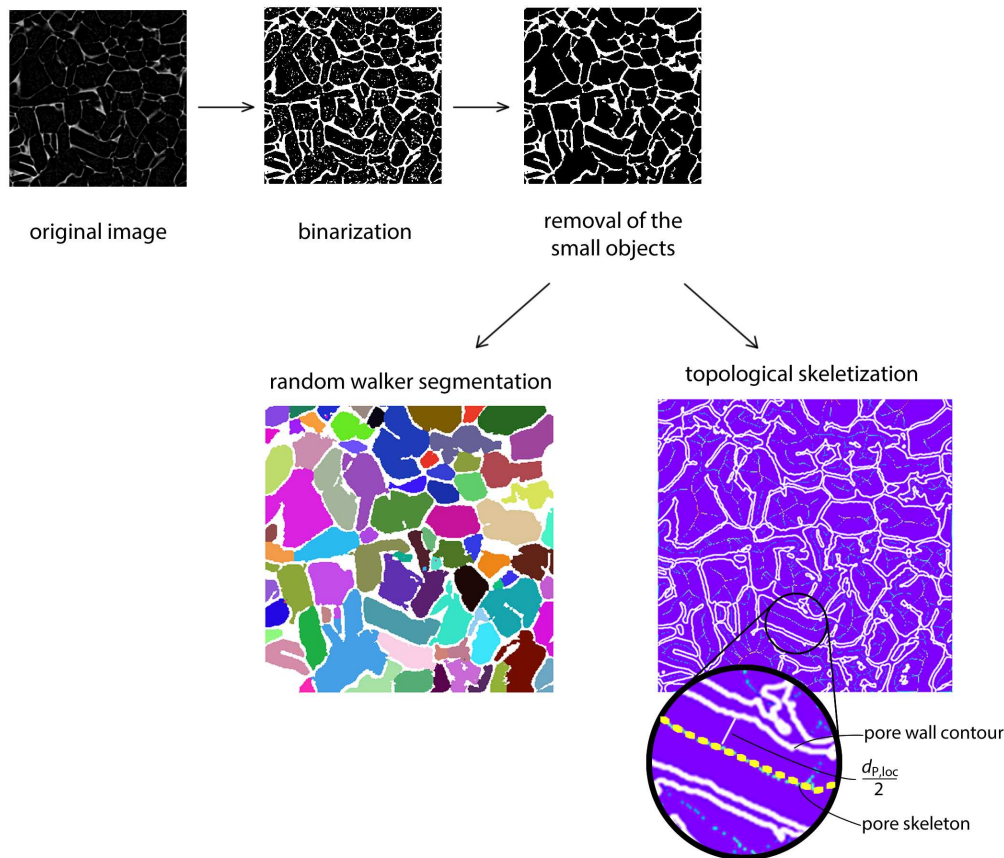
Figure 7.1 Image analysis workflow.

3D Image Analysis

The pores in the lyophilized cake are constituted of the voids left by the ice crystals after the sublimation has occurred. In the case of the pharmaceutical product, the concentration of the solutes is usually lower than 10%, which means that the porosity of the cake is usually high, i.e., 90-95%. As a consequence, the lyophilized cake is constituted of a dense network of pores, highly interconnected each other and difficult to separate. In the literature, image analysis has been used for single SEM images; this means that only the cross-sections of the cake have been analyzed.

In this work, the software BLOB3D developed by Ketcham (2005) was used to isolate pores and calculate their characteristics. This software has been specifically designed for geological applications, but it has also been used for engineering applications. The workflow consisted of three main stages (Figure 7.2),

(a) segmentation of the images from μ-CT by setting the criteria to select the voxels that belong to the voids or the pore walls;

(b) separation of the contiguous set of voxels so as to divide interconnected or touching objects;

(c) extraction of the data.
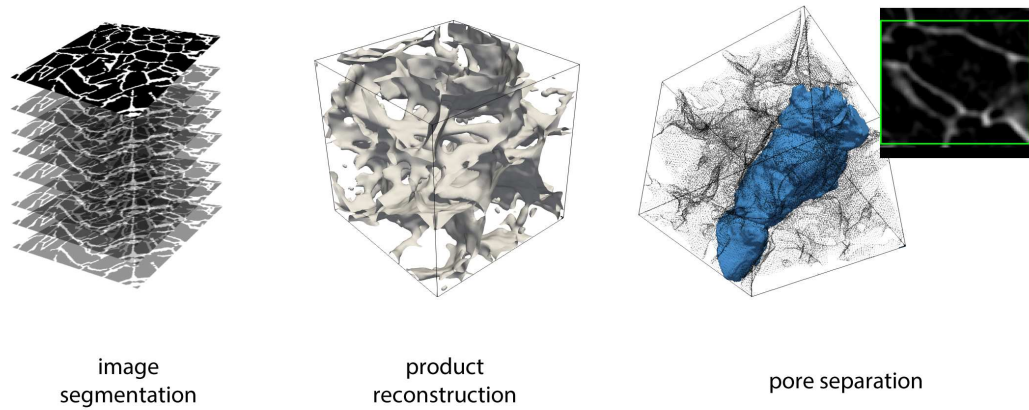
Figure 7.2   Workflow of the software BLOB3D.

The difficulty in this procedure is to identify what is a single pore and separate it from the rest of the structure. The structure within the cake is usually much more complicated than how a porous medium is usually depicted, e.g., as made of parallel cylindrical pores with a certain pore diameter, porosity, and tortuosity. At any rate, although the procedure here used to identify and separate the pores has a certain degree of arbitrariness, it might be used to have a different look to the product structure and appreciate its complexity. Figure 7.3 shows some of these complex structures isolated in the dried cake.
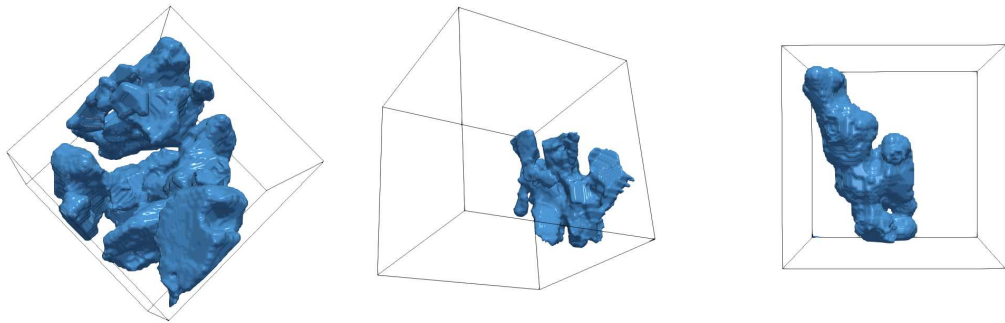
Figure 7.3   Examples of pore structure in the dried cake.

The equivalent pore diameter can be calculated as follows,

$$\langle d_\mathrm{P} \rangle = \frac{1}{n} \sum_i^n \frac{4V_i}{S_i} \tag{7.5}$$

where n is the number of pores identified within the sample, and V_i and S_i are the volume and the surface of the pore i.

CFD simulations

The images collected from the μ-CT analysis were reconstructed using a filtered back-projection algorithm (NRecon, Bruker, Bruker microCT, Kontich, Belgium), and then converted into STL file using the software Bruker CTvox software (Mannheim,

Germany). Once the REV has been created, CFD simulations were performed to estimate the structural properties of the sample. The simulation was performed using OpenFOAM 5.0. The cubic sample represents the solid matrix of the sample, whereas the computational domain for a CFD simulation is constituted by the voids where the fluid flows. The utilities *blockMesh* and *snappyHexMesh* were used to generate the computational domain; the grid independence of the solution was obtained by successive refinements of the mesh as shown in Figure 7.4. Full 3-D Navier-Stokes equations under Stokes flow conditions is solved within the REV, so that, both turbulence and inertial contributions can be neglected. It is important to underline that these simulations are not representative of the flow condition during freeze-drying, but are only used to predict the dusty-gas model parameters which depend only on the structure of the porous cake.
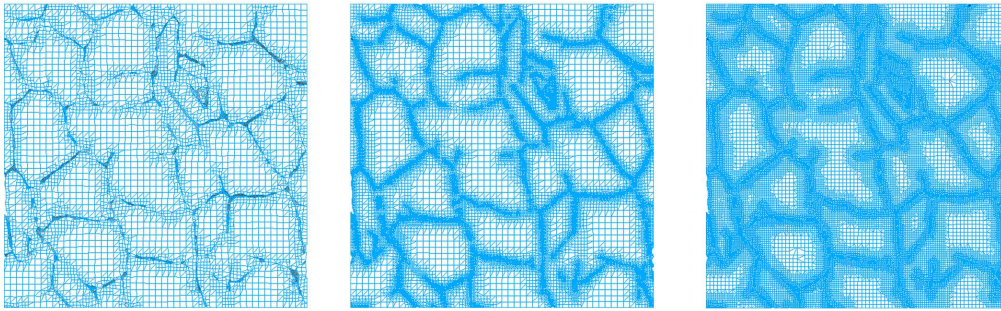
Figure 7.4 Example of mesh refinement of the computational domain.

Tortuosity τ, based on a purely geometrical definition, is the ratio of the actual distance traveled by the fluid in the REV to the shortest distance between the REV inlet and outlet. The tortuosity was calculated by integrating the velocity field in the REV as follows (Icardi et al., 2014):

$$\tau = \frac{\int_{\text{REV}} |\mathbf{u}| dV}{\int_{\text{REV}} u_z dV} \tag{7.6}$$

where $\mathbf{u}$ is the magnitude of the velocity field and u_z is velocity in the z-direction, that in our case is the prevalent flow direction. In principle, this method is equivalent to the experimental observations made by Carman in his works, where he evaluated the tortuosity from the average angle between the direction of the flow and the streamlines formed by a colored tracer through a bed of spheres (Carman, 1956), see Figure 7.5.

At low values of Reynolds number, the flow of Newtonian fluids in a porous medium is governed by Darcy's law. The permeability coefficient of the (B_0) can be evaluated by solving the Navier-Stokes equations, and imposing as boundary conditions the pressure drop through the REV (Δp_z), whereas the velocity vector field $\mathbf{u}$ is known from the solution at every point in the flow field. In this work, the z-direction was used as the main flow direction, and the pressure drop in this direction was set sufficiently low to simulate laminar Stokes flow. In this case, the Reynolds number was much lower than one, and both inertial and turbulence effects were not present. The mean velocity in the z-direction $\langle u_z \rangle$ can be evaluated by integrating u_z

Mesh generation   Velocity field   Streamlines
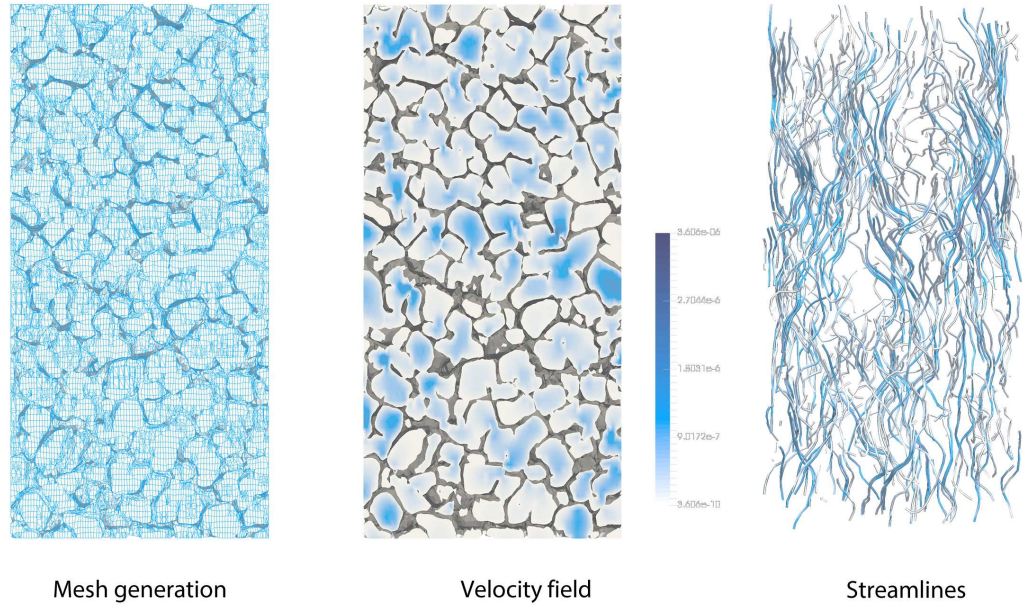
Figure 7.5 Example of the computationa domain and its mesh, and the outcomes of the simulation, i.e., the velocity field and streamlines.

over the REV (Fig. 7.5). Thus, the permeability coefficient reads,

$$B_0 = \mu \left(\frac{\Delta p_z}{L_z} \right)^{-1} \frac{1}{V_{\text{REV}}} \int_{\text{REV}} u_z \mathrm{d}V \qquad (7.7)$$

7.3   Results

7.3.1   Preliminary consideration about the role of product characteristics on the mass transfer resistance to vapor flow

To better understand the influence of the product structure on mass transport during primary drying, as a first step, a parametric analysis was performed using the 2D-model presented in Section 6.3.1, which uses the dusty-gas model (DGM) presented in Appendix B to describe the vapor flow in the product being dried. This analysis was carried out by simulating the drying of a product for various mean pore diameters d_{P} and tortuosity τ. Pore diameter and tortuosity play a central role in determining the resistance to vapor flow, as they influence the permeability coefficient B_0 (Eq. B.3) and the D_i^{Kn} diffusion coefficient (Eq. B.3). Moreover, the pore diameter, together with gas pressure, strongly affects the flow regime that occurs in the medium, see Eq. B.1.

As shown in Figure 7.6a, resistance to vapor flow has a strong dependence on the pore diameter; the predictions of the model have been compared to the experimental data referring to 5% mannitol and various freezing protocols, i.e., vacuum-induced surface freezing (VISF), suspended-vial freezing, shelf-ramped freezing and quench freezing in liquid nitrogen. The effect of pore size on drying duration is reported in Figure 7.6b; simulations refer to batch freeze-drying performed using T_{sh} of 253 K and P_{c} of 10 Pa.
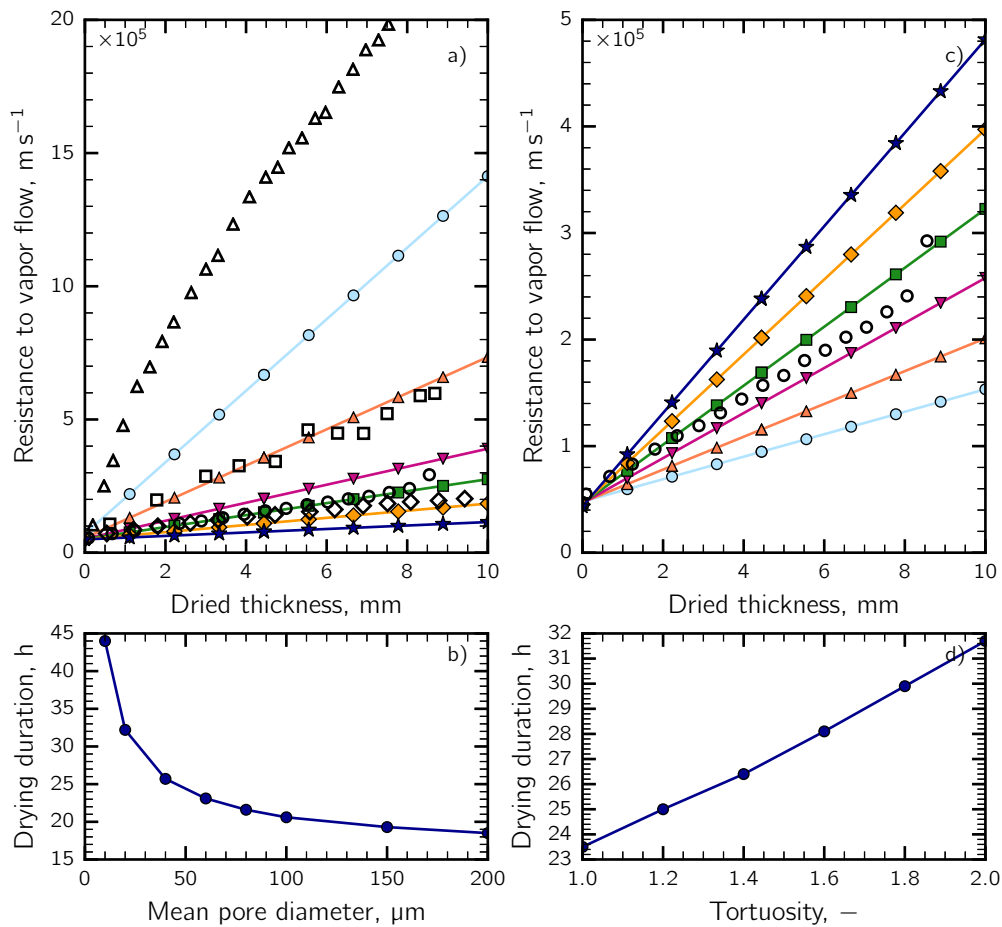
Figure 7.6 (a) Resistance to vapor flow as obtained from the 2D-model for products having (—○—) 10 μm, (—△—) 20 μm, (—▽—) 40 μm, (—■—) 60 μm, (—◇—) 100 μm and (—★—) 200 μm as mean pore diameter, and the experimental values referring to a 5% mannitol solution frozen using (△) quench in liquid nitrogen, (□) shelf-ramped freezing, (○) suspended-vial configuration and (◇) VISF ($T_n = 268$ K). (b) Drying duration as a function of the mean pore diameter ($T_{sh} = 253$ K, $P_c = 10$ Pa). (c) Resistance to vapor flow as obtained from the 2D-model for products having a mean pore diameter of 60 μm and a tortuosity equal to (—○—) 1, (—△—) 1.2, (—▽—) 1.4, (—■—) 1.6, (—◇—) 1.8 and (—★—) 2. (d) Drying duration as a function of tortuosity ($T_{sh} = 253$ K, $P_c = 10$ Pa).

Tortuosity is a further fundamental parameter that influences the drying behavior; it has to be pointed out that in the framework of DGM, Mason and Malinauskas (1983) defined tortuosity on purely geometrical bases, whereas this parameter can be generally defined in many different ways. Figure 7.6c shows the effect of tortuosity in a range of 1 to 2 on the resistance to vapor flow, whereas Figure 7.6d shows the drying time as a function of the tortuosity; simulations refer to a product having mean pore diameter equal to 60 μm

In the range of pore diameter studied, i.e., 10 to 200 μm, diffusive flow is the prevalent mechanism of mass transport within the dried cake. To give you an example, in the case of pores of 10 μm, viscous flow contributed only for 0.5% of the total flux; in that conditions, the time-volume averaged Kn was about 48, which indicated

that mass transport occurred in the Knudsen flow regime. The contribution of the viscous flow increased as the pore diameter increased; in the case of pores of 200 μm viscous flow contributed for about 5% and the time-volume averaged Kn was about 4.5, indicating that mass transport occurred in the transition regime.

7.3.2 Product characteristics: pore size, tortuosity and permeability

The second step of this investigation consisted of estimating product characteristics, and in particular pore size, tortuosity and permeability, starting from the μ-CT analysis of the samples.

There exists a strong correlation between freezing protocol and pore dimension. Figure 7.7 shows the diameter of pores within the porous cake along with the product height. Pore diameter was calculated using both the 2D and 3D image analysis in the case of products obtained from a batch cycle and suspended vial configuration, in which nucleation was uncontrolled, and in the case of suspended-vial configuration where nucleation was controlled via VISF. VISF was able to produce a product with pores in the range of 90-100 μm, with a thin crust at the top surface made of small pores. These small pores are formed because of the local supercooling due to fast evaporation that triggers nucleation, see Section 5. In the case of uncontrolled nucleation, suspended-vial configuration led to a cake with bigger pores than those obtained in the conventional, batch, shelf-ramped freezing.
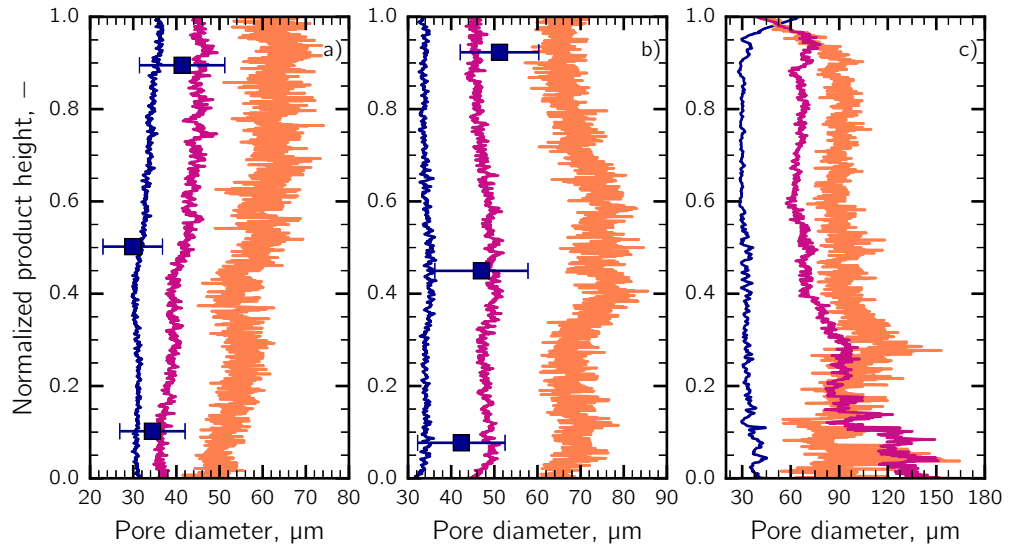
Figure 7.7 Mean pore diameter along the product height in the case of the (a) batch and uncontrolled nucleation, (b) suspended-vial configuration and uncontrolled nucleation (c) suspended-vial configuration and VISF. Data refer to 5% mannitol; 2D image analysis: (———) d_P defined in Eq. 7.1, (———) $\langle d_P \rangle$ defined in Eq. 7.2, (———) $d_{P,loc}$; (—■—) 3D image analysis.

From Figure 7.7 it is clear that there are differences in the values of pore diameter depending on the definition of pore diameter itself. The evaluation of the pore diameter as defined in Eq. 7.1 seemed not to be consistent as that method predicted almost the same mean pore diameter for the three cases, whereas direct and indirect observation of the products clearly state that these three products possessed very

different pore size. The values of pore diameter defined from the medial axis of the topological skeleton were lower compared to those obtained by defining pore diameter on the area to perimeter ratio (Eq. 7.2). However, the pore diameter defined on the area to perimeter ratio, also called hydraulic diameter $\langle d_P \rangle$, is based on a purely fluid-dynamics definition, as it represents the diameter of an equivalent circular conduit which maintains the same conservation of momentum of the pristine pore. On the other hand, $d_{P,loc}$ seemed to be more coherent with the values found by using the 3D image analysis.

The second parameter which in the framework of DGM affects mass transfer is tortuosity. As shown in Figure 7.8, the tortuosity, as evaluated by using CFD simulations, ranged between 1.2 and 1.4. These values are smaller than those obtained by (Goshima et al., 2016), where tortuosity was found to be a 2-3; it has to be pointed out that the approach of Goshima et al. (2016) is based on the image analysis of longitudinal sections of the lyophilized cake, and so on pure geometrical bases.
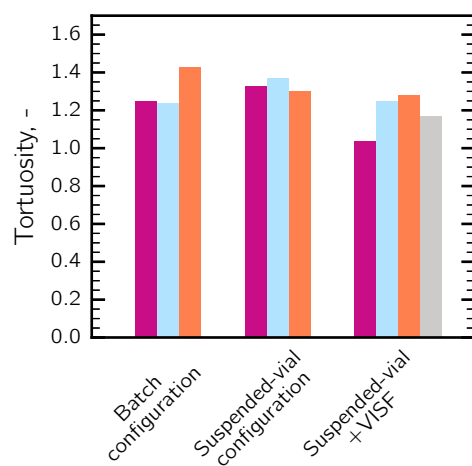
Figure 7.8 Tortuosity evaluated using CFD simualtions in the case of batch and suspended-vial configuration (uncontrolled nuclation) and in the case of VISF applied to suspended-vial configuration. Bars refers to different height in the product structure: (■) bottom, (■) center, (■) top, (■) top crust.

Finally, the permeability coefficient of the porous cake was evaluated using the image analysis or CFD simulations, see Figure 7.9. The evaluation of permeability from image analysis and Eq. 7.3, supposes that each slice in the porous cake is constituted of parallel pores of different size, whereas Eq. 7.4 is based on a pure arithmetic average. On the other hand, the permeability as calculated from CFD simulations takes into account the real structure of the pore medium. Anyway, Figure 7.9 shows that the two approaches result in comparable values.

7.3.3 Product morphologies

The further step of this investigation consisted of exploring the potential application of μ-CT to look the inside of product structures. This analysis can give information not only on pore size and shape but also on defects in the product.

In Figure 7.10, the reconstruction of the morphology is shown for a sample of 5% mannitol obtained using a conventional freeze-drying cycle, where the product
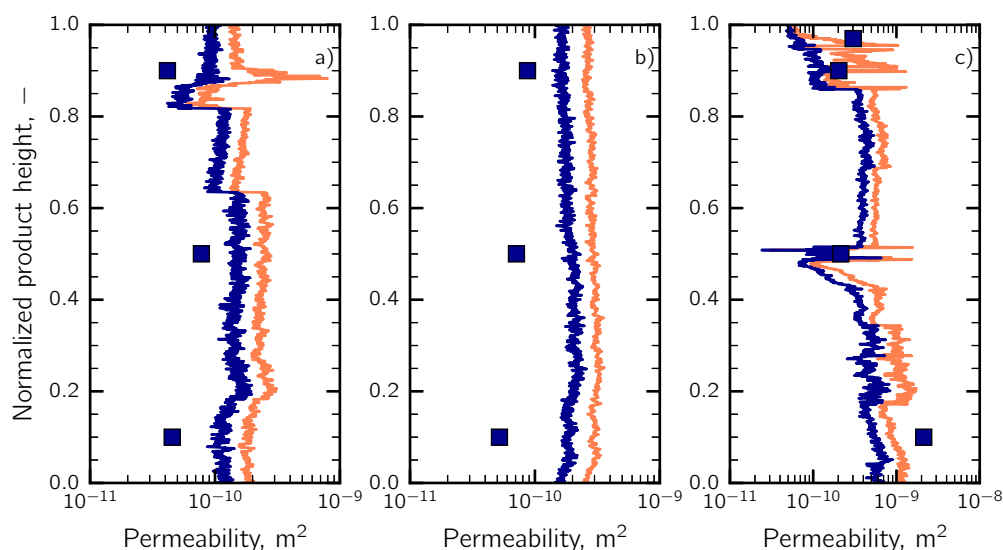
Figure 7.9 Permeability along the product height in the case of the (a) batch and uncontrolled nucleation, (b) suspended-vial configuration and uncontrolled nucleation (c) suspended-vial configuration and VISF. Data refer to 5% mannitol; 2D image analysis: (——) $\langle B_0 \rangle_\parallel$, (——) $\langle B_0 \rangle_{nw}$; (■) 3D image analysis.

was frozen using the shelf-ramped freezing protocol. The structure appears irregular and constituted by pore of different size and shape. The same analysis is shown for the same formulation obtained using the suspended-vial configuration for both uncontrolled and controlled nucleation.

The resolution of the instrument allowed to reconstruct some critical details, such as the presence of a crust in the top product surface, see Figure 7.11. The sample analyzed showed a crust about 500 μm thick, which are straight in the z-direction, and appeared like elongated narrow cracks. The solid upper surface appeared pitted and constituted of tiny pores which are presumably the voids due to small ice crystals; these pores seems to be isolated and not interconnected with each other.

A further interesting phenomenon that is possible to reveal with μ-CT is the presence of micro-collapse in the structure. Micro-collapse is the collapse of small domains over product surfaces when the temperature is below T'_g, and the amorphous phase is subject to viscous flow, without losing the macroscopic structure (MacKenzie, 1975). This phenomenon does not affect the general appearance of the product, that does not show the collapse of its macroscopic structure and appears intact. The small holes over the surface were in the order of few micrometers, see Figure 7.12.

7.4   Conclusions

In this chapter, various computational techniques for the estimation of morphological characteristics have been presented and compared. X-ray μ-CT tomography was used to analyze the structure of the product, obtaining a stack of images of the cross-section of the product along with its height. Some computational methods were used to determine the structural parameters that impact on mass transport during drying. These methods included (i) slice-by-slice 2D image analysis, (ii) 3D image analysis
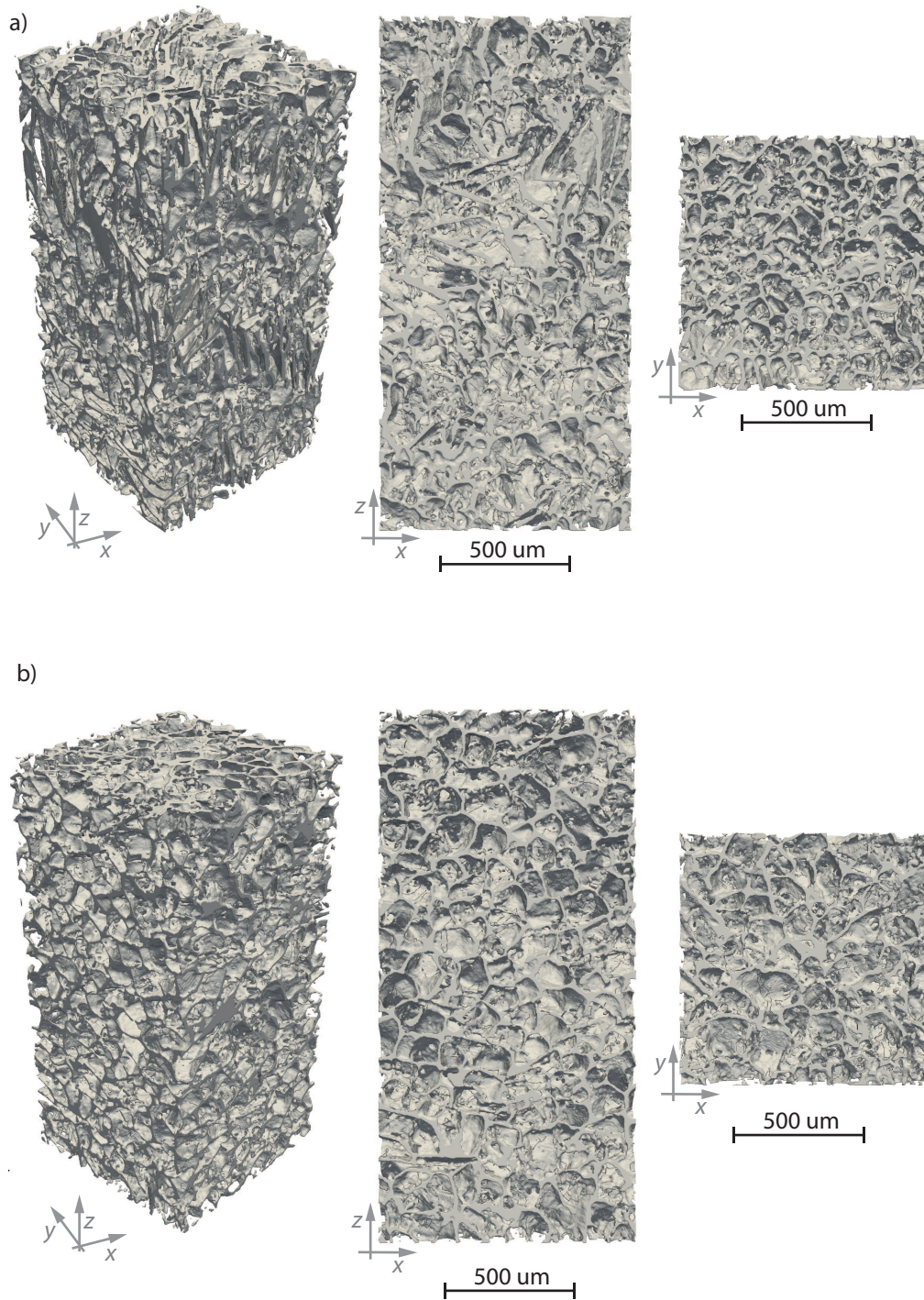
Figure 7.10 Morphology of the central portion of a mannitol 5% sample obtained from (a) batch configuration and (b) suspended-vial configuration, in the case of spontaneous nucleation.
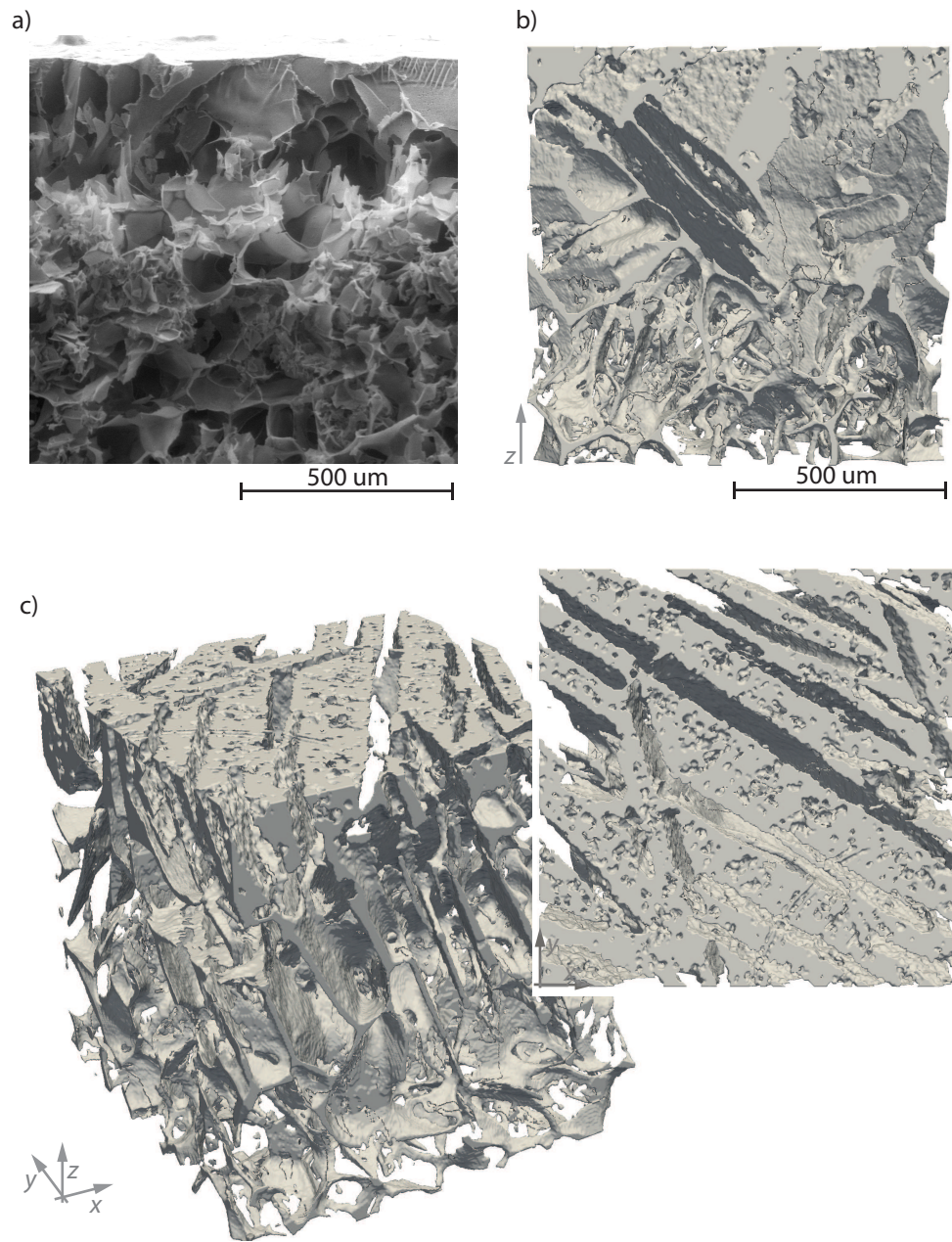
Figure 7.11 Morphology of upper product surface showing the typical crust produced using VISF: (a) SEM image, (b) 3D reconstruction in the xy-plane, (c) isometric and top view of the product (5% mannitol)

a)

500 um

b)

500 um

Figure 7.12 Morphology of 5% sucrose showing microcollapse: (a) SEM image, (b) 3D reconstruction in isometric and top view.

and (iii) CFD simulations for REVs at different heights within the product. It has been shown that these methods can give different results according to the definition of the structural parameters. Far from providing a definitive answer, these results highlight the complexity of modeling such complex systems and call for further research on this topic.

Acronyms

API Active Pharmaceutical Ingredient; **BET** Brunauer, Emmett and Teller analysis; μ**-CT** X-Ray Micro Computed Tomography; **REV** Relevant Element Volume; **STL** Stereolithography file format; **VISF** Vacuum-Induced Surface Freezing.

List of symbols

A	area, m^2
B_0	permeability coefficient, m^2
$d_{P,loc}$	local pore diameter, m
L_z	REV size, m
P	perimeter, m
p_z	pressure drop in z-direction through the REV, Pa
T_n	nucleation temperature, K
$\mathbf{u}$	velocity vector, m s^{-1}
$\mathbf{u}_{in}$	inlet velocity vector, m s^{-1}
$\mathbf{u}_{out}$	outlet velocity vector, m s^{-1}
u_z	vector in the z-direction, m s^{-1}

Greek letters

μ	viscosity of gas mixture, kg m^{-1} s^{-1}

Subscript

$\parallel$	parallel model
BKGD	background
FGND	foreground
nw	number weight

Adimensional numbers

Kn	Knudsen number

References

Arsiccio, A, Sparavigna, A., Pisano, R, and Barresi, A. (2018a). Measuring and predicting pore size distribution of freeze-dried solutions. *Drying Technology*, pp. 1–13.

Arsiccio, A., Barresi, A. A., and Pisano, R. (2017). Prediction of ice crystal size distribution after freezing of pharmaceutical solutions. *Crystal Growth & Design* 17 (9), pp. 4573–4581.

Bosca, S., Barresi, A. A., and Fissore, D. (2013). Use of a soft sensor for the fast estimation of dried cake resistance during a freeze-drying cycle. *International journal of pharmaceutics* 451 (1-2), pp. 23–33.

Capozzi, L. C., Arsiccio, A., Sparavigna, A. C., Pisano, R., and Barresi, A. A. (2018). Image Segmentation and 3D reconstruction for improved prediction of the sublimation rate during freeze drying. In: *IDS2018–21st International Drying Symposium*.

Carman, P. C. (1956). *Flow of Gases through Porous Media*. London: Butterworths Scientific Publications.

Goshima, H., Do, G., and Nakagawa, K. (2016). Impact of ice morphology on design space of pharmaceutical freeze-drying. *Journal of Pharmaceutical Sciences* 105 (6), pp. 1920–1933.

Gouillart, E., Nunez-Iglesias, J., and Van Der Walt, S. (2017). Analyzing microtomography data with Python and the scikit-image library. *Advanced Structural and Chemical Imaging* 2 (1), p. 18.

Grady, L. (2006). Random walks for image segmentation. *IEEE transactions on pattern analysis and machine intelligence* 28 (11), pp. 1768–1783.

Grassini, S, Pisano, R, Barresi, A., Angelini, E, and Parvis, M (2016). Frequency domain image analysis for the characterization of porous products. *Measurement* 94, pp. 515–522.

Haeuser, C., Goldbach, P., Huwyler, J., Friess, W., and Allmendinger, A. (2018). Imaging techniques to characterize cake appearance of freeze-dried products. *Journal of Pharmaceutical Sciences* 107 (11), pp. 2810–2822.

Hottot, A., Vessot, S., and Andrieu, J. (2004). A direct characterization method of the ice morphology. Relationship between mean crystals size and primary drying times of freeze-drying processes. *Drying Technology* 22 (8), pp. 2009–2021.

Icardi, M., Boccardo, G., Marchisio, D. L., Tosco, T., and Sethi, R. (2014). Pore-scale simulation of fluid flow and solute dispersion in three-dimensional porous media. *Physical Review E* 90 (1), p. 013032.

Izutsu, K.-i., Yonemochi, E., Yomota, C., Goda, Y., and Okuda, H. (2014). Studying the morphology of lyophilized protein solids using X-ray micro-CT: effect of post-freeze annealing and controlled nucleation. *AAPS PharmSciTech* 15 (5), pp. 1181–1188.

Ketcham, R. A. (2005). Computational methods for quantitative analysis of three-dimensional features in geological specimens. *Geosphere* 1 (1), pp. 32–41.

MacKenzie, A. (1975). Collapse during freeze drying–qualitative and quantitative aspects. In: *Freeze Drying and Advanced Food Technology*. Ed. by S. A. Goldblith, R. L, and R. W. W. New York: Academic Press, pp. 277–307.

Mason, E. A. and Malinauskas, A. (1983). *Gas Transport in Porous Media: The Dusty-Gas Model*. Amsterdam: Elsevier, Amsterdam.

Mousavi, R., Miri, T., Cox, P. W., and Fryer, P. J. (2007). Imaging food freezing using X-ray microtomography. *International journal of food science & technology* 42 (6), pp. 714–727.

Nakagawa, K., Hottot, A., Vessot, S., and Andrieu, J. (2006). Influence of controlled nucleation by ultrasounds on ice morphology of frozen formulations for pharmaceutical proteins freeze-drying. *Chemical Engineering and Processing: Process Intensification* 45 (9), pp. 783–791.

Nakagawa, K., Hottot, A., Vessot, S., and Andrieu, J. (2007). Modeling of freezing step during freeze-drying of drugs in vials. *AIChE Journal* 53 (5), pp. 1362–1372.

Nygaard, J., Andersen, M., Howard, K., Foss, M, Bünger, C., Kjems, J, and Besenbacher, F (2008). Investigation of particle-functionalized tissue engineering scaffolds using X-ray tomographic microscopy. *Biotechnology and bioengineering* 100 (4), pp. 820–829.

Oddone, I., Barresi, A. A., and Pisano, R. (2017). Influence of controlled ice nucleation on the freeze-drying of pharmaceutical products: the secondary drying step. *International Journal of Pharmaceutics* 524 (1-2), pp. 134–140.

Parker, A., Rigby-Singleton, S., Perkins, M., Bates, D., Le Roux, D., Roberts, C. J., Madden-Smith, C., Lewis, L., Teagarden, D. L., Johnson, R. E., et al. (2010). Determination of the influence of primary drying rates on the microscale structural attributes and physicochemical properties of protein containing lyophilized products. *Journal of pharmaceutical sciences* 99 (11), pp. 4616–4629.

Pisano, R. and Capozzi, L. C. (2017). Prediction of product morphology of lyophilized drugs in the case of Vacuum Induced Surface Freezing. *Chemical Engineering Research and Design* 125, pp. 119–129.

Pisano, R., Barresi, A. A., Capozzi, L. C., Novajra, G., Oddone, I., and Vitale-Brovarone, C. (2017b). Characterization of the mass transfer of lyophilized products based on X-ray micro-computed tomography images. *Drying Technology* 35 (8), pp. 933–938.

Rambhatla, S., Ramot, R., Bhugra, C., and Pikal, M. J. (2004). Heat and mass transfer scale-up issues during freeze drying: II. Control and characterization of the degree of supercooling. *AAPS Pharmscitech* 5 (4), pp. 54–62.

Rey, L. (1999). Glimpses into the realm of freeze-drying: classical issues and new ventures. In: *Freeze-Drying/Lyophilization of Pharmaceutical and Biological Products*. Ed. by L Rey and J. C. May. 3rd. New York: Marcel Dekker Inc.: New York. Chap. 1, pp. 1–30.

Walt, S. Van der, Schönberger, J. L., Nunez-Iglesias, J., Boulogne, F., Warner, J. D., Yager, N., Gouillart, E., and Yu, T. (2014). scikit-image: image processing in Python. *PeerJ* 2, e453.

Xiao, X., Tao, L.-R., and Hua, T.-C. (2007). Micro-computed tomography observation of sublimation interface and image analysis on sublimation process during freeze-drying. *CryoLetters* 28 (4), pp. 253–260.

Zhang, H. (2018). *Ice Templating and Freeze-Drying for Porous Materials and Their Applications*. John Wiley & Sons.

8

Modelling the freeze-drying of microparticles in packed-bed

This chapter discusses the problem of mass transfer within the products during primary drying of microparticle-based materials in a vial. In the framework of the multi-scale approach used in this thesis, this chapter is dedicated to investigating the product at pore-scale. More specifically, structural parameters of lyophilized products have been estimated to describe mass transfer during primary drying. The procedure consists in generating realistic packings of microparticles using DEM simulations, coupled to CFD simulations at pore scale*.

8.1   Introduction

In this thesis, it has been pointed out the importance of converting batch processes into continuous productions to improve control over quality and process safety, reduce processing costs and enhance process flexibility (Baxendale et al., 2015; Byrn et al., 2015). It has also been proposed a new technology for converting freeze-drying to a continuous process.

In this chapter, it will be shown an alternative to freeze-drying of liquid solutions in bulk, which includes the combination of spray freezing and vacuum drying, and fits perfectly in the continuous process proposed in this thesis.

The idea of using particle-based drugs to perform freeze-drying in continuous, to our best knowledge, belongs to Rey, and consists of freezing droplets, drying

---

*Part of the work described in this chapter has been previously published in "Capozzi, L.C., Barresi, A.A., Pisano, R. (2019) A multi-scale computational framework for modeling the freeze-drying of microparticles in packed-beds. *Powder Technology* 343, pp. 834-846" and "Capozzi, L.C., Barresi, A.A., Pisano, R. (2019) Supporting data and methods for the multi-scale modelling of freeze-drying of microparticles in packed-beds. *Data in Brief*, 22, pp. 722-755". Part of the macro-scale model here presented has been developed by the author in his master thesis "Capozzi, L. C. (2014). Modellazione matematica del processo di liofilizzazione di granuli (en: Mathematical modelling of freeze-drying of particle-based materials). MA thesis. Italy: Politecnico di Torino".

the frozen particles in a heated vibrating tray and, finally, filling vials with the dried particles (Rey, 2016). An alternative to this consists of performing freeze-drying of microparticles directly into vials, avoiding the possible contamination of the product or the dispersion of powders into the environment. From a processing point of view, using microparticles, as an alternative to bulk dosage form, potentially allows saving the processing time needed for freezing the solution, and, if the spray freezing is well designed, to control better product characteristics and vial-to-vial heterogeneity. Regarding the final applications, microparticle-based drugs can be used for pulmunary (Ye et al., 2017) and epidermal delivery (Chen et al., 2002) because of their ability to improve drug solubility, dissolution, bioavailability and stability of many APIs (Khadka et al., 2014).

While freeze-drying in bulk has been widely investigated in the past, concerning freezing (Nakagawa et al., 2007; Pisano and Capozzi, 2017; Capozzi and Pisano, 2018) and drying behavior (Sadikoglu and Liapis, 1997; Mascarenhas et al., 1997; Velardi and Barresi, 2008), but also in terms of product structurep (Pisano et al., 2017b; Haeuser et al., 2018), little is known about the behavior of spray freeze-drying. Here, spray freeze-drying will be studied using a multi-scale computational framework. Spray-freeze drying consists of atomizing a solution via a nozzle to form droplets that are frozen in a cryogenic fluid, dosed in a vessel (vial or tray) and, finally, placed in the lyophilizer, where the sublimation of ice occurs.

Although various mono- and two-dimensional models for the freeze-drying of particle-based material have been proposed in the literature (Liapis and Bruttini, 2009; Kim and Lee, 2008; Bruttini and Liapis, 2015), none of them investigate the role of packed-bed structure and its impact on mass transfer phenomena. In fact, once the frozen microparticles are filled in a vial, they form a randomly packed structure characterized by several parameters, i.e., bed porosity, tortuosity factor, permeability and mean pore diameter, which are essential for describing the drying behavior. Determining packing characteristics is particularly complicated and, essentially, case-specific because atomized microparticles can have different physical properties, i.e., shape and particle-size distribution width, that depend on atomization conditions (Maa et al., 1999).

The investigation of the properties of randomly packed beds has been widely studied in various fields and using different methods, e.g., discrete element method (DEM) (Tangri et al., 2017; Jiang et al., 2017; Linsong et al., 2018), rigid-body simulations (Boccardo et al., 2015), generation algorithms (Icardi et al., 2016), X-Ray micro-computed tomography (Suzuki et al., 2008), but not in relation to the freeze-drying process.

In this chapter, the structural properties of different packings will be studied by coupling the DEM for generating packing of microparticles, CFD for estimating their properties, and, finally, a mathematical model at the macro-scale for studying their behavior during freeze-drying. DEM is a robust technique by which it is possible to generate packings starting from an adequate number of particles, i.e., 100,000 particles, and so reproduce realistically the remarkable polydispersity in size shown by the microparticles produced via spray freezing.

8.2 Multiscale procedure

The aim of this chapter is to study the impact of different particle size distributions on the drying behavior of microparticles in packed-bed. We propose a multi-scale approach, which consists of generating realistic random packings, estimating the properties of packings through CFD simulations at the pore-scale and finally using these properties to simulate the freeze-drying process at the macro-scale (Figure 8.1).
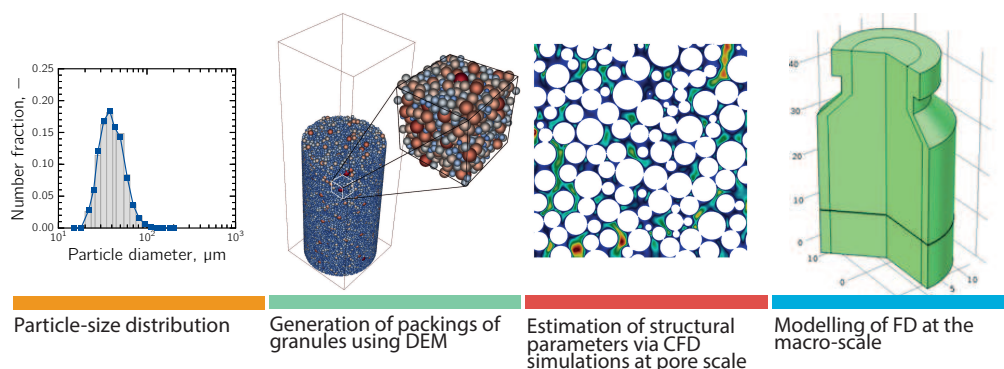
Figure 8.1   Workflow used in this work to estimate the properties and the freeze-drying behaviour of packed-beds of uniform and non-uniform microparticles within a vial.

Packings were generated using DEM simulations, considering both uniform and non-uniform distributions of spherical particles. Once the packing has been created, a cubic-shaped portion of it was selected to generate the computational domain used by the CFD simulation. This portion of the packed-bed was chosen to be representative of the entire packing of microparticles within the vial, and we refer to it as the representative elementary volume of the packing (REV).

Similarly to Chapter 7, once the REV has been extracted, the packed-bed porosity and the mean pore diameter are obtained from the grid-mesh, while its tortuosity and permeability result from CFD simulations. The last step of this multi-scale approach consists of simulating the freeze-drying process at the macro-scale, using the structural parameters found previously. A two-dimensional, axisymmetric, unsteady-state model was developed to simulate the heat and mass transport in the freeze-drying of granular beds within a vial. The dusty-gas model (DGM) (Mason and Malinauskas, 1983), which is detailed in Appendix B was used to describe the mass transport in the packed-bed.

8.2.1 Packing generation

As shown in Figure 8.1, the first step of this approach is to generate random packings of spherical particles. The generation of packings was made by letting the microparticles to fall down into a cylindrical container, see Figure 8.2.

In this work, the generation of packed-beds of frozen microparticles was performed by DEM, which is a powerful numerical technique used to simulate granular media (Cundall and Strack, 1979). The numerical simulations of falling of the frozen particles into a vial were performed varying particle size and its distributions.

Particle diameter, μm
20   45   70   95   120
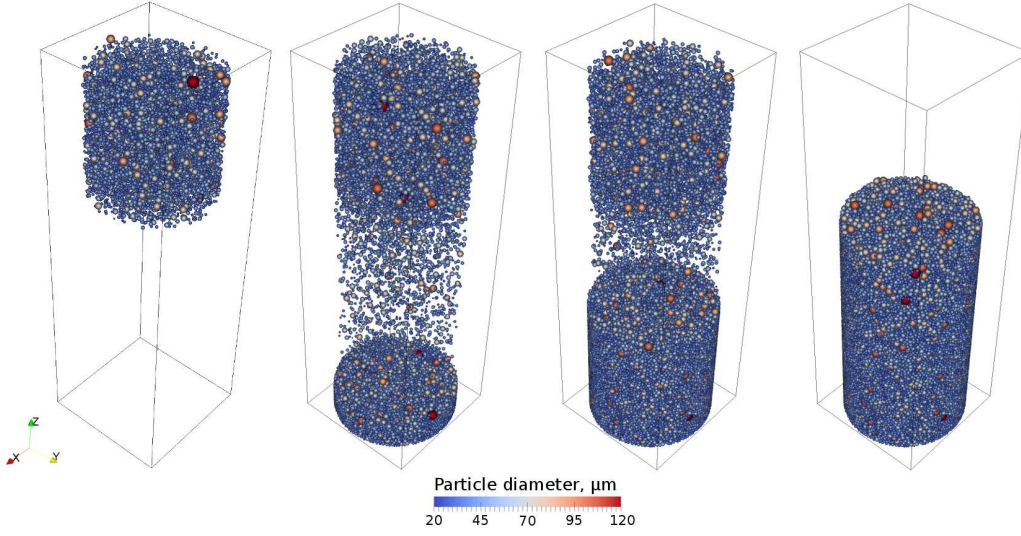
Figure 8.2   Generation of random packings by simulation of particles falling into a cylinder.

In DEM simulations, Newton's second law of motion for translation and rotation is applied to any particle i at any time t as follows:

$$m_i \frac{d^2 \mathbf{r}_i}{dt^2} = \sum_c \mathbf{F}_{c,i} + m_i \mathbf{g} \qquad (8.1)$$

$$I_i \frac{d\boldsymbol{\omega}_i}{dt} = \mathbf{t}_i \qquad (8.2)$$

where m_i is the mass of particle i, $\mathbf{r}_i$ its position, $\mathbf{F}_{c,i}$ the total force acting on it. I_i is the moment of inertia, $\boldsymbol{\omega}_i$ the angular velocity, and $\mathbf{t}_i$ the total torque.

Hertz-Mindlin contact model was used to describe the particle-to-particle and the particle-to-wall contacts. Both normal and tangential forces are modeled as a combination of springs, dashpots and a slider (Tsuji et al., 1992). The total force acting on each particle reads:

$$\mathbf{F}_{c,i} = \mathbf{F}_{n,i} + \mathbf{F}_{t,i} \qquad (8.3)$$

$$\mathbf{F}_{n,i} = \left(\frac{4}{3} Y^* \sqrt{R^*} \delta_n^{1.5} - 2\sqrt{\frac{5}{6}} \beta \sqrt{S_n m^*} v_{n,r} \right) \mathbf{n}_{ij} \qquad (8.4)$$

$$\mathbf{F}_{t,i} = \left(S_t \delta_t - 2\sqrt{\frac{5}{6}} \beta \sqrt{S_t m^*} v_{t,r} \right) \mathbf{t}_{ij} \qquad (8.5)$$

in which $v_{n,r}$ and $v_{t,r}$ are the normal and the tangential component of relative velocity, Y^* is the equivalent Young's modulus, R^* is the equivalent radius, δ_n and δ_t are the normal and tangetial dispacement, β is a coefficient related to restitution coefficient. S_n and S_t are the normal and tangential stiffness, see Appendix E for details.

The simulations of packings were performed with the open source DEM simulation software LIGGGHTS 3.3.1; see Appendix E for computational details, particles properties and the interaction parameters used in the DEM simulations.

144

8.2.2 Estimation of packing properties

The second step of our procedure is to perform CFD simulations at the pore scale to estimate the structural properties of packings, see Figure 8.3. These simulations were carried out using OpenFOAM 3.0.1. The computational domain was built sampling a cubic portion from the packing previously generated. The cube sample was chosen in the center of the vial to avoid border effects, and the particles which were into this cube were extracted to generate the REV. Each REV contained thousands of spheres and was seen to be representative of the starting distribution (Figure 8.3a).
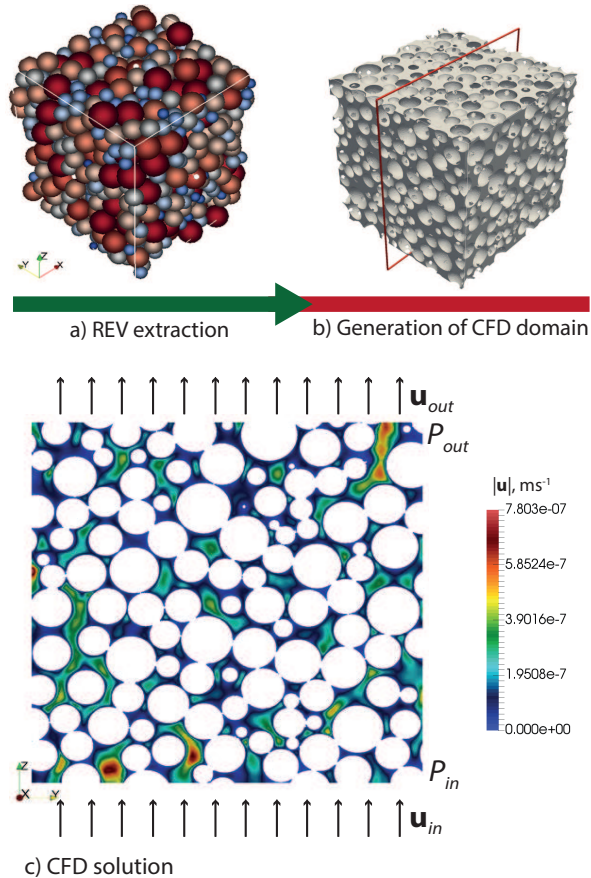
Figure 8.3 (a) Microparticles are extracted from the bed to generate the REV, (b) CFD domain is generated meshing the voids between the microparticles, (c) example of solution given by CFD simulation.

At this point, the computational domain was generated using the meshing utilities *blockMesh* and *snappyHexMesh* (included in OpenFOAM 3.0.1) (Boccardo et al., 2015). The interstitial void space between the particles was meshed mostly with hexahedral elements and with varying degrees of refinement to model the geometry properly. The number of mesh cells, i.e., 30 million for each packing, was sufficiently large to achieve grid independence of the solution (Figure 8.3b); for further details, see Appendix E.

The voids between particles determine a net of tortuous and interconnected pores, which are distributed in sizes and shapes. This net of pores can be sufficiently described with three parameters: bed porosity ε_b, tortuosity τ_b and mean pore diameter d_P.

The bed porosity ε_b was estimated from the volume of mesh as follows:

$$\varepsilon_b = \frac{V_{\text{void}}}{V_{\text{tot}}} \approx \frac{V_{\text{mesh}}}{V_{\text{REV}}} \tag{8.6}$$

where the volume of voids is estimated from the volume of mesh V_{mesh}, and V_{REV} is the volume of the REV.

The equivalent pore diameter of the packed-bed d_P was estimated as (Dullien, 2012):

$$d_P = \frac{4V_{\text{void}}}{S_{\text{wetted}}} \approx \frac{4V_{\text{mesh}}}{S_{\text{mesh}}} \tag{8.7}$$

where S_{mesh} is the area of the particles in the REV, which is equivalent to the wetted surface. Eq. 8.7 is the mean hydraulic diameter of a porous medium and is widely used in the Carman-Kozeny equation of permeability. The hydraulic pore diameter obtained from the simulation was compared with the following expression (Dullien, 2012):

$$d_P = \frac{2}{3}\left(\frac{\varepsilon_b}{1-\varepsilon_b}\right)D_P \tag{8.8}$$

where ε_b and D_p were obtained by using the DEM-CFD procedure previously described.

As detailed in Chapter 7, tortuosity τ_b, based on a purely geometrical definition, is the ratio of the actual distance traveled by the fluid in the REV to the shortest distance between the REV inlet and outlet. The tortuosity was calculated by integrating the velocity field in the REV as follows (Icardi et al., 2014):

$$\tau_b = \frac{\int_{\text{REV}} |\mathbf{u}|dV}{\int_{\text{REV}} u_z dV} \tag{8.9}$$

where $\mathbf{u}$ is the magnitude of the velocity field and u_z is velocity in the z-direction, that in our case is the prevalent flow direction. In principle, this method is equivalent to the experimental observations made by Carman in his works, where he evaluated the tortuosity from the average angle between the direction of the flow and the streamlines formed by a colored tracer through a bed of spheres (Carman, 1956).

At low values of Reynolds number, the flow of Newtonian fluids in a porous medium is governed by Darcy's law. The permeability coefficient of the packed bed (B_0) can be evaluated by solving the Navier-Stokes equations, and imposing as boundary conditions the pressure drop through the REV (Δp_z), whereas the velocity vector field $\mathbf{u}$ is known from the solution at every point in the flow field. In this work, the z-direction was used as the main flow direction, and the pressure drop in this direction was set sufficiently low to simulate laminar Stokes flow. In this case, Reynolds number was much lower than one, and both inertial and turbulence effects were not present. The mean velocity in the z-direction $\langle u_z \rangle$ can be evaluated by integrating u_z over the REV (Figure 8.3c). Thus, the permeability coefficient reads:

$$B_0 = \mu\left(\frac{\Delta p_z}{L_z}\right)^{-1}\frac{1}{V_{\text{REV}}}\int_{\text{REV}} u_z dV \tag{8.10}$$

The permeability coefficient as obtained from CFD simulation was compared to the Carman-Kozeny expression,

$$B_0 = \frac{D_{\mathrm{P}}^2}{180} \frac{\varepsilon_{\mathrm{b}}^3}{(1 - \varepsilon_{\mathrm{b}})^2} \tag{8.11}$$

where ε_{b} and D_{P} were obtained by using the DEM-CFD procedure previously described.

Material handling and vial filling can cause particles segregation because of differences in the size and physical properties of the particles. The main segregation mechanisms are (a) sifting, (b) fluidization, (c) entrainment of particles in the airstream, (d) flotation due to vibration and (e) agglomeration (Carson, 1988). The particles segregation that occurs in the granules filler upstream was not considered in this work, whereas particles segregation due to the filling itself was studied by simulating the generation of packings of 100k, 200k, and 500k microparticles, and evaluating packing characteristics along with the height of those packings.

8.2.3   Macro-scale modelling

The last step of our workflow consists of simulating the freeze-drying of microparticles within vials; in Appendix E a model for the freeze-drying of microparticles in a tray and of a single microgranule is also presented. For this reason, a two-dimensional, axisymmetric, unsteady-state model that describes the behavior of a packed bed of frozen microparticles that undergoes primary drying has been developed and is shown schematically in Figure 8.4. Heat and mass transport equations were solved numerically using the commercial finite element solver *Comsol Multiphysics 5.0*. The computational domain was divided into three subdomains: the dried region Ω_{I}, in which the particles are completely dried, the frozen region Ω_{II}, where the particles can be completely or partially frozen, and the vial side wall (Ω_{III}). Our model describes each layer as a pseudo-homogeneous medium so that each cell in the domain represents a significant number of particles. In this description, the properties are volume-averaged as detailed in Appendix E. The packed bed can be considered a bidisperse porous medium, as it is characterized by particle porosity ε_{p} and bed porosity ε_{b}.

In the subdomain Ω_{II} particle behaviour can be described with a *frozen fraction* function ϕ_{S} defined as follows:

$$\phi_{\mathrm{S}} = \begin{cases} \dfrac{\frac{4}{3}\varepsilon_{\mathrm{p}}\pi D_{\mathrm{P}}^{*3}}{\frac{4}{3}\varepsilon_{\mathrm{p}}\pi D_{\mathrm{P}}^{3}} = \left(\dfrac{D_{\mathrm{P}}^{*}}{D_{\mathrm{P}}}\right)^{3}, & \text{for } D_{\mathrm{P}}^{*} \leq D_{\mathrm{P}}, \\[3ex] \dfrac{\frac{4}{3}\varepsilon_{\mathrm{p}}\pi D_{\mathrm{P}}^{3} + \frac{4}{3}\pi(D_{\mathrm{P}}^{*3} - D_{\mathrm{P}}^{3})}{\frac{4}{3}\varepsilon_{\mathrm{p}}\pi D_{\mathrm{P}}^{3}}, & \text{for } D_{\mathrm{P}}^{*} > D_{\mathrm{P}}. \end{cases} \tag{8.12}$$

where D_{P} and D_{P}^{*} are the total particle diameter and the diameter of the frozen core, respectively. As shown in Figure 8.4, if $\phi_{\mathrm{S}} = 1$ particles are completely frozen, $\phi_{\mathrm{S}} < 1$ are partially dried and $\phi_{\mathrm{S}} > 1$ an ice layer is condensed over the particle surface. The value of the derivative of the ϕ_{S} function indicates the phenomena occurring in the particle. In particular, if vapor pressure is lower than vapor equilibrium pressure,
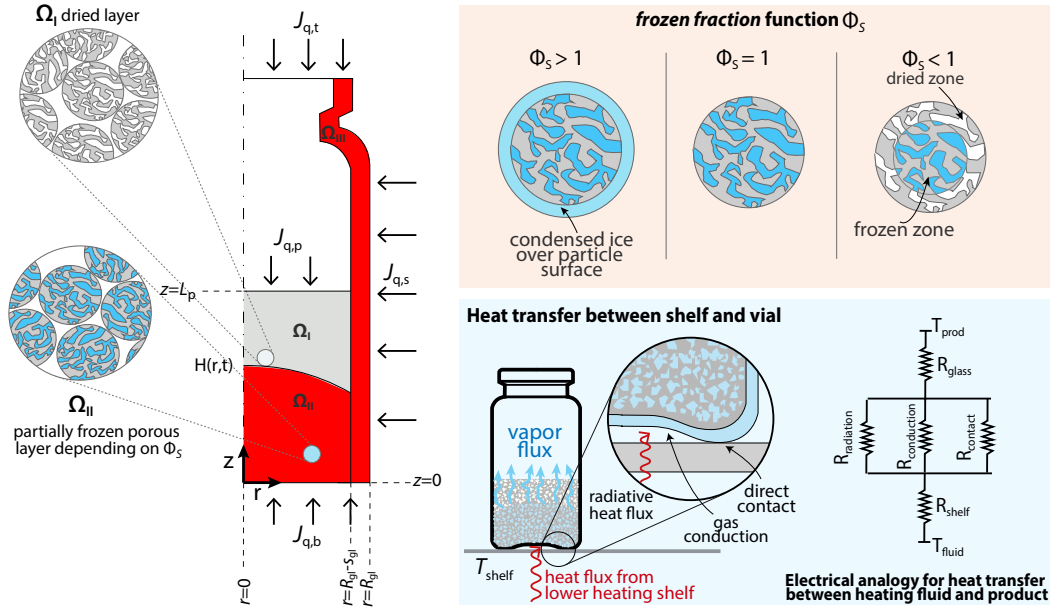
Figure 8.4 Schematic illustration of the freeze-drying process of a particle-based material within a vial. Subdomain Ω_I is the dried layer of particles, Ω_II is the layer of particles that can be completely or partially frozen, and described by the function ϕ_S, Ω_III is the vial side wall.

sublimation of ice into vapor occurs and $\frac{\partial \phi_\mathrm{S}}{\partial t} < 1$. On the other hand, if vapor pressure is higher than vapor equilibrium pressure, condensation of ice over the particle occurs and $\frac{\partial \phi_\mathrm{S}}{\partial t} > 1$.

Heat transfer

The energy balances in both dried and frozen subdomains consider the particle packed-bed and the gas flowing through the interstitial pores as a pseudo-homogeneous system and the effective properties are calculated. The contribution of the vial wall to the heat transfer is also considered.

The energy balance in the subdomain Ω_I is given by:

$$\rho_\mathrm{I} c_{p,\mathrm{I}} \frac{\partial T_\mathrm{I}}{\partial t} = \boldsymbol{\nabla} \cdot (\kappa_\mathrm{I} \boldsymbol{\nabla} T_\mathrm{I}) - c_{p,\mathrm{gas}} \mathbf{M} \cdot \boldsymbol{\nabla} T_\mathrm{I} \qquad \text{in} \quad \Omega_\mathrm{I} \tag{8.13}$$

The energy balance in the subdomain Ω_II reads:

$$\rho_\mathrm{II} c_{p,\mathrm{II}} \frac{\partial T_\mathrm{II}}{\partial t} = \boldsymbol{\nabla} \cdot (\kappa_\mathrm{II} \boldsymbol{\nabla} T_\mathrm{II}) - c_{p,\mathrm{gas}} \mathbf{M} \cdot \boldsymbol{\nabla} T_\mathrm{II} + \Delta H_s (\rho_\mathrm{f} - \rho_\mathrm{d}) \frac{\partial \phi_\mathrm{S}}{\partial t} \qquad \text{in} \quad \Omega_\mathrm{II} \tag{8.14}$$

where $\mathbf{M} = M_\mathrm{w} \mathbf{N}_\mathrm{w} + M_\mathrm{in} \mathbf{N}_\mathrm{in}$ is the total mass flux, ΔH_s is the heat of sublimation, and the last term on the right-hand side of Eq. 8.14 denotes the heat contribution due to the sublimation of ice from the inside of the particles.

The heat balance for the vial wall can be expressed as:

$$\rho_\mathrm{III} c_{p,\mathrm{III}} \frac{\partial T_\mathrm{III}}{\partial t} = \boldsymbol{\nabla} \cdot (\kappa_\mathrm{III} \boldsymbol{\nabla} T_\mathrm{III}) \qquad \text{in} \quad \Omega_\mathrm{III} \tag{8.15}$$

where ρ_III, $c_{p,\mathrm{III}}$ and κ_III are respectively the density, heat capacity and thermal conductivity of the glass vial.

The heat transfer initial and boundary conditions are the same used in Section 6.

Mass transfer

The conservation of species expressed on a molar basis for water vapor and inert gas in the dried subdomain Ω_I can be expressed as:

$$\frac{\partial \varepsilon_{tot,I} c_{w,I}}{\partial t} = -\boldsymbol{\nabla} \cdot \mathbf{N}_{w,I}$$
$$\frac{\partial \varepsilon_{tot,I} c_{in,I}}{\partial t} = -\boldsymbol{\nabla} \cdot \mathbf{N}_{in,I} \qquad \text{in } \Omega_I \tag{8.16}$$

and in the frozen subdomain Ω_{II} as:

$$\frac{\partial \varepsilon_{tot,II} c_{w,II}}{\partial t} = -\boldsymbol{\nabla} \cdot \mathbf{N}_{w,II} - \frac{(\rho_f - \rho_d)}{M_w} \frac{\partial \phi_s}{\partial t}$$
$$\frac{\partial \varepsilon_{tot,II} c_{in,II}}{\partial t} = -\boldsymbol{\nabla} \cdot \mathbf{N}_{in,II} \qquad \text{in } \Omega_{II} \tag{8.17}$$

The typical rarified conditions at which freeze-drying is performed leads to the transition regime ($0.1 < \mathrm{Kn} < 10$), in which mass flux manifests aspects of both gas continuum, i.e., molecule-molecule collisions, and free-molecular Knudsen regimes, i.e., molecule-wall collisions. In this case, the expression of flux of the i-component can be obtained from the dusty-gas model as follows:

$$\mathbf{N}_i = -\frac{1}{R_g T} \left(D_i' \boldsymbol{\nabla} p_i + D_i'' y_i \boldsymbol{\nabla} p + \frac{B_0}{\mu} p_i \boldsymbol{\nabla} p \right) \tag{8.18}$$

where the first term represents the contribution of concentration-dependent diffusive flux, the second term the pressure contribution to molecular diffusion, and the last one the pressure contribution to viscous flow, expressed with the Darcy's law (Thorstenson and Pollock, 1989). The coefficients D_i' and D_i'' ($i = \mathrm{w, in}$) represent the transport coefficients as defined in Section 7.

As shown in the previous chapter, once the structural parameters of the porous media are known, DGM can describe mass flux in the transitional regime by combining ordinary diffusion (D_{ij}^{eff}), Knudsen diffusion (D_i^{Kn}), and Darcy's flow (B_0/μ). In particular, the effective binary diffusion D_{ij}^{eff} reads:

$$D_{ij}^{eff} = \frac{\varepsilon_b}{\tau_b^2} \mathscr{D}_{ij} \tag{8.19}$$

where ε_b and τ_b are the bed porosity and tortuosity respectively, and $\mathscr{D}_{ij}$ the binary diffusion coefficient. The effective Knudsen diffusivity for the i-component is given as:

$$D_i^{Kn} = \frac{\varepsilon_b}{\tau_b^2} \frac{d_P}{3} \sqrt{\frac{8 R_g T}{\pi M_i}} \tag{8.20}$$

If particles are sufficiently small compared to the dimension of the whole packing, mass transfer resistance into the particle can be considered negligible compared to that of the interparticle voids. Moreover, also temperature gradient into the particle is so small to be considered negligible. Under these assumptions, the concentration of water

vapor in Ω_{II} can be directly determined from the local thermodynamic equilibrium between particles and the vapor within the interstitial voids of the bed as follows:

$$c_{w,II} = \frac{p_w^{eq}(T_{II})}{R_g T_{II}} \qquad \text{in} \quad \Omega_{II} \tag{8.21}$$

where $p_w^{eq}(T_{II})$ is determined from Marti-Mauersberger correlation (Marti and Mauersberger, 1993).

The mass transfer initial and boundary conditions are the same used in Section 6.

Mass and heat balance at the moving interface

A moving interface separates the dried ($\phi_s = 0$) and the frozen subdomines ($\phi_s \geq 0$). The mass balance across the interface gives:

$$-\mathbf{n} \cdot M_w \mathbf{N}_w \Big|_{z=H(r,t)} = -v_s(\rho_I - \rho_{II}) \tag{8.22}$$

while the heat balance can be written as follows:

$$\mathbf{n} \cdot (\kappa_I \boldsymbol{\nabla} T_I - \kappa_{II} \boldsymbol{\nabla} T_{II}) \Big|_{z=H(r,t)} + (\rho_I c_{p,I} - \rho_{II} c_{p,II}) v_s T_{int} +$$
$$- \mathbf{n} \cdot (c_{p,gas} T_{int} + \Delta H_s) M_w \mathbf{N}_w \Big|_{z=H(r,t)} = 0 \tag{8.23}$$

Combining Eqs. 8.22 and 8.23 the velocity of the interface is:

$$v_s = \frac{\mathbf{n} \cdot (\kappa_I \nabla T_I - \kappa_{II} \nabla T_{II})}{(\Delta c_p T_{int} + \Delta H_s)(\rho_I - \rho_{II})} \tag{8.24}$$

where $\Delta c_p = c_{p,gas} - (\rho_{II} c_{p,II} - \rho_I c_{p,I})/(\rho_{II} - \rho_I)$.

8.3 Model validation

The freeze-drying of frozen microparticles consisting of a water mixture 35% w/w of trehalose, mannitol, dextran (10 kDa) and dextran (150 kDa) (TMDD) in a ratio of 3:3:3:1 has been simulated and compared to experimental results obtained by Schiffter et al. (2010). The solution was atomized at (a) 48 kHz or (b) 25 kHz using an ultrasound nozzle, quench frozen in liquid nitrogen and then filled in tubing vials with a maximum capacity of 20 ml; the total amount of product filled into each vial was 3 g. Primary drying was performed using a shelf temperature of 253 K and 13.3 Pa as chamber pressure. In this work, we generated the packings using the droplet size distributions obtained from Schiffer et al. (Schiffter et al., 2010) and measured by laser light diffraction, determining the four parameters of the mathematical model, i.e., bed porosity, equivalent pore diameter, tortuosity, and permeability coefficient. After that, we compared our simulation results with experimental data of product temperature as measured placing a thermocouple in a vial filled in with the spray-frozen product; the water content and sublimation rate during drying were measured using a microbalance inside the drying chamber.

The thickness of the packed-bed that these frozen microparticles form into the vial (L_p) mainly depends on the porosity of the packed-bed (ε_b) and the total water content m_w:

$$L_p = \frac{m_w}{\pi R_{gl}^2 \rho_{ice} \varepsilon_p (1 - \varepsilon_b)} \tag{8.25}$$

where R_{gl} is the internal radius of the vial, ρ_{ice} is the density of ice, ε_p the internal porosity of the particles. All the simulations in this work refer to the same amount of m_w. The physical properties and parameters adopted for the simulation of primary drying cycles are shown in Appendix E.

The dried cake resistance was calculated as follows:

$$R_p = \frac{p_{w,int} - p_{w,c}}{|\mathbf{N}_w| M_w} \tag{8.26}$$

where $p_{w,int}$ and $p_{w,c}$ are the partial pressure at sublimation interface and in the chamber, and $\mathbf{N}_w$ the vapor flux from the product. The overall mass transfer resistance R_p is here used to compare different packings in terms of drying behavior.

As the second step of this analysis, we studied the impact of particle size and their distribution on packing characteristics, and, finally on drying time. The freeze-drying behavior of the packed-bed of microparticles was, in this case, investigated using an aqueous solution of mannitol (21.5% w/w) as a model product, and, so, the ice fraction of particles after the spray and the freezing process was estimated to be about 0.785. In the spray freeze-drying process, once the solution is sprayed, and the particles are frozen in a cryogenic fluid, each vial is filled with a certain amount of product. Firstly, packings were generated from DEM simulations of monodisperse microparticles with a diameter in the range 10-90 μm. Afterward, we generated packings from Gaussian-polydisperse microparticles with an average diameter of 50 μm and standard deviations from 0 to 5 μm. We will refer to the number-mean diameter of microparticles $D_p = \sum n_i D_{p,i} / \sum n_i$, where n_i is the number of particle with $D_{p,i}$ as diameter. Packings were generated using 100,000 microparticles to cover a wide size range, and REVs were constituted of a large number of particles, i.e., more than 1500.

8.4 Results

8.4.1 Preliminary considerations about freeze-drying of a single granule and granules in packed-beds

Results concerning the behavior of a single particle during freeze-drying are reported for an aqueous solution of mannitol (21.5% w/w) used as a model product. Primary drying was performed at 10 Pa and has been supposed that the particle is completely irradiated from a surface at 253 K. Particles from 10 to 100 μm and having pore diameters from 0.5 to 10 μm have been considered. As shown in Figure 8.5a, drying time for a single micro-particle depends on both particle diameter and pore diameter within the particle. In the case of a particle of 10 μm, drying time is below one minute, no matter the dimension of pores within it. On the other hand, in the case of bigger particles, the dimension of pores is relevant. In fact, particles of 100 μm and having

pores of 10 μm showed drying time of 78 min, whereas the same particles with pores of 2 μm were completely dried in about 380 min. The data in Figure 8.5b refer to the drying time of a particle with a diameter of 50 μm and having pores of 5 μm; drying time is plotted as a function of the temperature of the radiant surface.
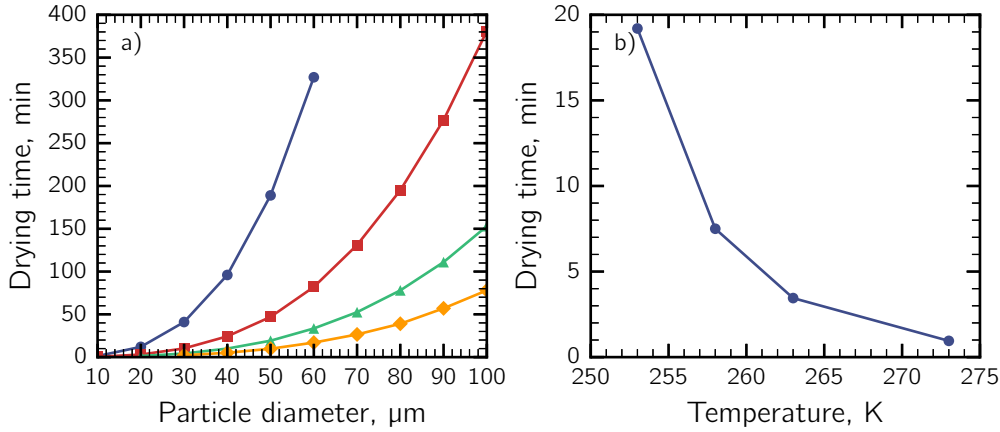
Figure 8.5 (a) Drying time of a single micro-particle as a function of particle diameter D_p and for different d_P^*: 0.5 μm (●), 2.0 μm (■), 5.0 μm (▲) and 10.0 μm (◆). Primary drying was carried out at 10 Pa and supplying heat by radiation from a surface at 253 K. (b) Drying time of a single micro-particle ($D_p = 50$ μm, $d_P^* = 5$ μm) as a function of the temperature of the radiative surface.

The effect of bed porosity on drying time was evaluated taking into account monodisperse particles of 30 μm packed according to four regular arrangements, i.e., rhombohedric ($\varepsilon_b = 0.260$), tetragonal ($\varepsilon_b = 0.302$), orthorhombic ($\varepsilon_b = 0.395$) and cubic ($\varepsilon_b = 0.746$). We also compared these regular arrangements and the random packing as obtained from DEM-CFD simulations, that showed a porosity of 0.375. As shown in Figure 8.6, drying time was extremely affected by bed porosity, and, in general, by the structure formed by the particles packed into a vial. That result gave us the motivation to deeply investigate the role of structure on the behavior of microparticle-based product during primary drying.

8.4.2 Packing generation

At first, the number-weighted distribution of particle size has been taken from Schiffter et al. (2010) and its packing has been simulated using the procedure shown in Figure 8.1.

The two packings, corresponding to the two atomization conditions, were generated by DEM, starting from the particle distribution discretized into several classes and having same D_p and span. Once the packing has been created, a cube containing 1451 particles for the case (a) and 1872 for the case (b) was extracted from the center of the packed bed. Figure 8.7 shows that there was a good agreement between the experimental particle distribution and that in the REV for the two tests considered.

As shown in Tab. 8.1, in the case (a), the packed-bed was made of microparticles with a mean diameter of 38.6 μm, its porosity was 0.3382 and the average size of the inter-particle voids was 14.0 μm. In the case (b), mean particle diameter was 54.2 μm, porosity 0.3429 and the average size of the inter-particle voids was 19.3 μm.
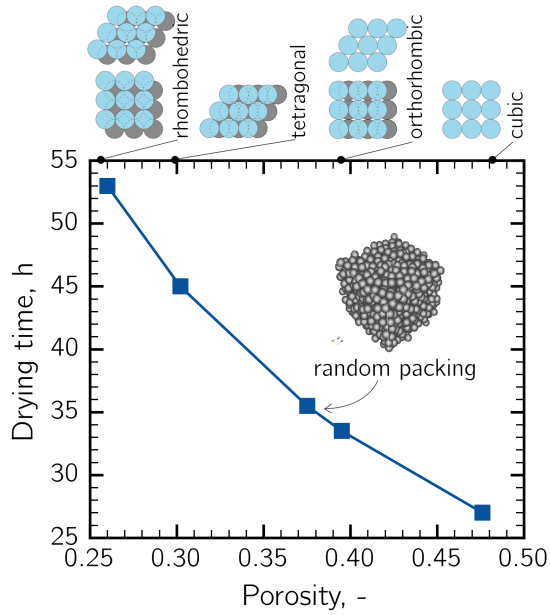
Figure 8.6 Effect of bed porosity on drying time of packing of monodisperse microparticles (30 μm)
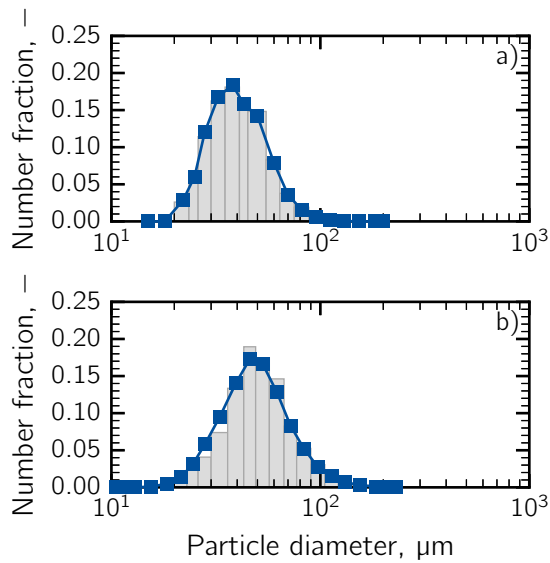
Figure 8.7 Comparison between the particle distribution as observed experimentally by Schiffter et al. (2010) (gray bins) and in the REV generated by DEM simulation (■) in the case of water-TMDD solutions atomized at (a) 48 kHz and (b) 25 kHz.

Table 8.1 Characteristics of the packing generated by simulations in the case of 35 % w/w water-TMDD (3:3:3:1).

Frequency	D_P, μm	span	ε_b	τ_b	d_P, μm	B_0, m^2
25 kHz	54.2	0.908	0.3429	1.256	19.3	2.907×10^{-12}
48 kHz	38.6	0.758	0.3328	1.263	14.0	1.415×10^{-12}

153

8.4.3 Drying simulation

The mathematical model described in section 8.2.3 is here used to simulate the drying behavior of the two packed-bed defined in Tab. 8.1. The model simulations were then compared to experimental results by Schiffer et al. (Schiffter et al., 2010). In our simulations, we have assumed that freeze-drying was performed using Schott-20T vials, having $3.6474\,\text{W}\,\text{m}^{-1}\,\text{K}^{-1}$ as K_V and $0.0249\,\text{cm}$ as ℓ_V (Kuu et al., 2009), and the vials were completely irradiated by the chamber walls.

For the case study (a), Figure 8.8a shows a good agreement between the product temperature at the vial bottom as obtained by our simulations and the experimental results. Figure 8.8b shows the evolution of the residual water content within the product as measured using a microbalance inside the drying chamber. Furthermore, experimental data showed that primary drying was completed after approximately 38 h, similarly to the drying time predicted by the model. A similar good agreement was observed for the evolution of the rate of sublimation (Fig. 8.8c).
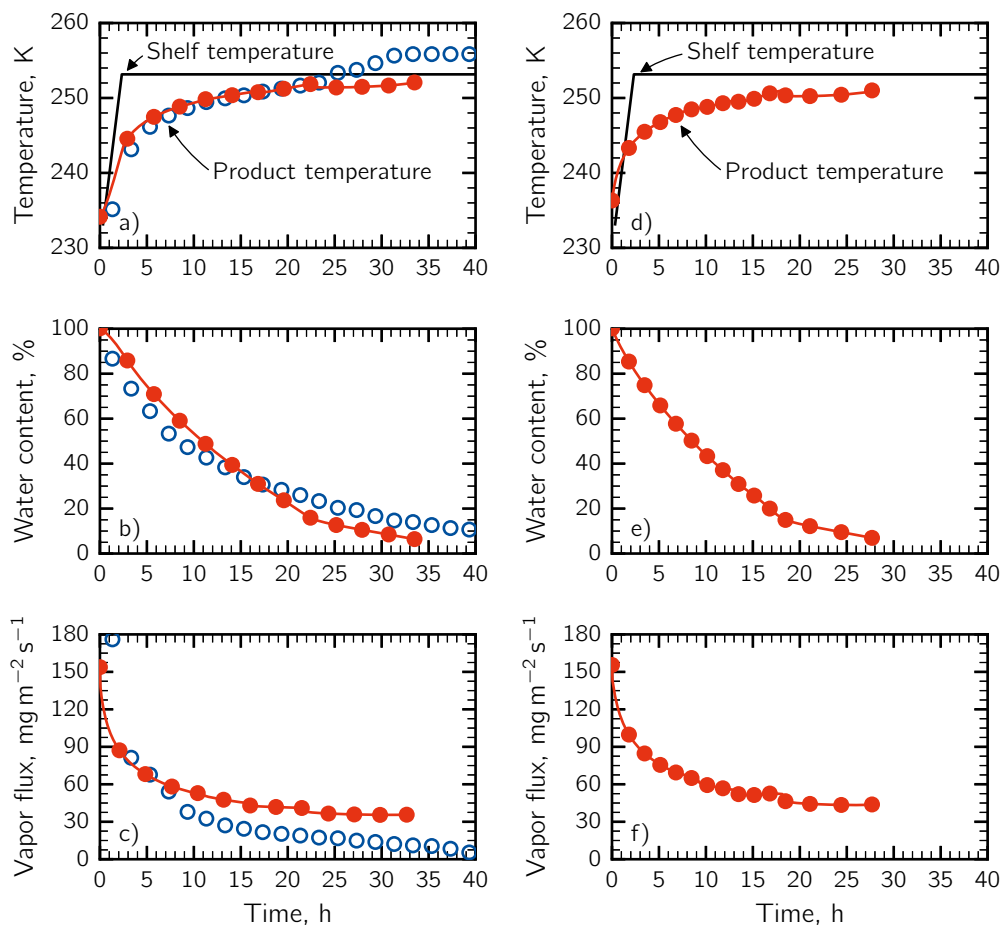
Figure 8.8 Comparison between simulations (●) and experimental (○) results for spray-freeze-drying of TMDD solutions atomized at (a-c) 48 kHz and (d-f) 24 kHz. Experimental data are obtained from Schiffter et al. (Schiffter et al., 2010), who carried out the primary drying at 253 K and 13.3 Pa.

The same analysis was performed for the case study (b) to evaluate the impact of packing characteristics on drying behavior, see Figure 8.8(d-e). In this case, the

primary drying time was approximately 8 h less than that found for the case (a). In fact, the packing structure generated from the particle distribution (b) showed a lower mass transfer resistance to water vapor (Figure 8.9), because of a higher bed porosity, mean pore diameter, and permeability.
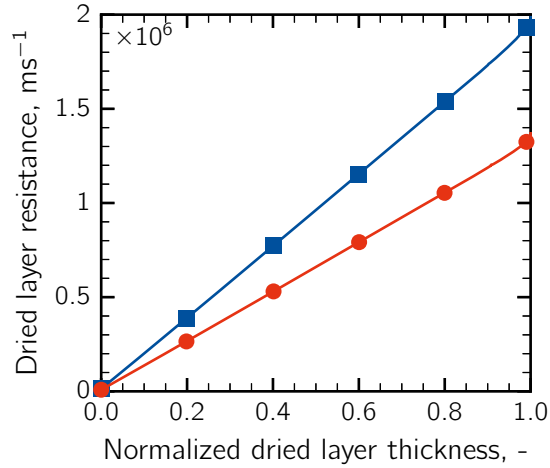
Figure 8.9 Mass transfer resistance to water vapor as a function of thickness of dried packed-bed in the case of solution atomized at (a, ■) 48 kHz and (b, ●) 24 kHz.

8.4.4 Effect of the average size of particles and of its distribution on structural characteristics of packings

In the case of freeze-drying of microparticles in packed-bed, the particle size and particle size distribution significantly affect the structural characteristics of packings of microparticles within a vial, and, finally, the drying time.

To elucidate this aspect, packings of monodisperse microparticles having diameters from 10 to 90 μm were generated using DEM and their structural parameters obtained from CFD simulations; the properties of these packings are shown in Tab. 8.2. Bed porosity and tortuosity were not dramatically affected by the particle diameter; in particular, bed porosity was in the range 0.371-0.375 and tortuosity between 1.26 and 1.24. The values of tortuosity obtained in our packings of monodisperse particles were slightly lower than those found by Carman, i.e., 1.44 (Carman, 1956).

Table 8.2 Characteristics of packings formed by monodisperse particles having a different diameter as predicted by CFD simulations.

D_p, μm	ε_b	τ_b	d_P, μm		B_0, m^2	
			Eq. 8	Simulation	Eq. 11	Simulation
10	0.375	1.253	4.0	3.1	9.000×10^{-14}	8.605×10^{-14}
30	0.375	1.252	12.0	10.9	6.750×10^{-13}	9.143×10^{-13}
50	0.375	1.262	20.0	18.2	1.875×10^{-12}	2.552×10^{-12}
70	0.372	1.245	28.0	25.0	3.675×10^{-12}	3.941×10^{-12}
90	0.371	1.247	35.4	32.2	5.808×10^{-12}	8.315×10^{-12}

155

On the other hand, the pores formed in the packing, and consequently the permeability coefficient, were dramatically influenced by the particle diameter. In the case of microparticles having $D_p = 10\,\mu m$, d_P was approximately of $3.1\,\mu m$ and its permeability coefficient $8.605 \times 10^{-14}\,m^2$. On the other hand, in the case of $D_p = 90\,\mu m$, d_P was approximately $32.2\,\mu m$ and its permeability coefficient increased up to $8.315 \times 10^{-12}\,m^2$. Both mean pore diameter and permeability coefficient were in good agreement with the theoretical expression for evaluating d_P from porosity and particle diameter (Eq. 8.8) and with the semi-empirical equation derived by Carman and Kozney for estimating the permeability coefficient of a packed-bed of spheres B_0 (Eq. 8.11), see Tab 8.2.
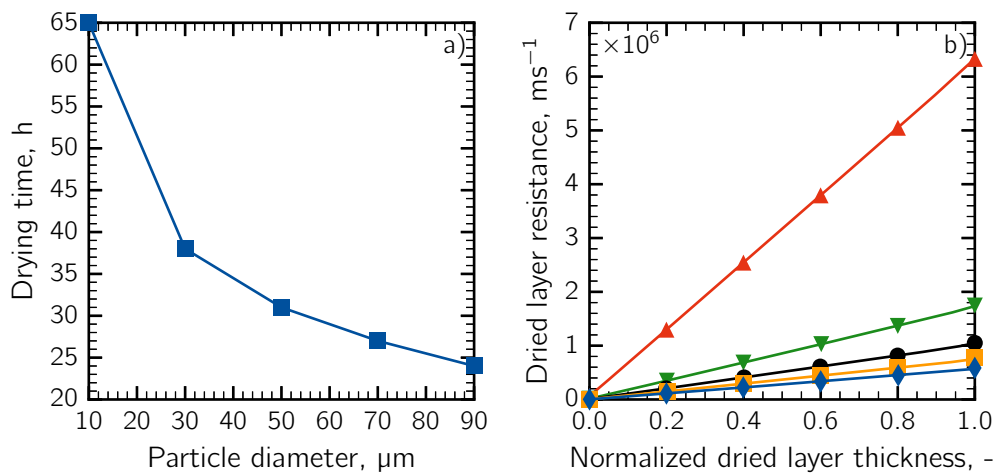
Figure 8.10 (a) Drying time for packings of monodisperse particles of several diameters ($L_p = 10\,mm$). Primary drying was simulated by setting the chamber pressure at 10 Pa and shelf temperature at 253 K. (b) Dried cake resistance to water vapor as a function of dried thickness for packing of monodisperse particles of (—▲—) $10\,\mu m$, (—▼—) $30\,\mu m$, (—●—) $50\,\mu m$, (—■—) $70\,\mu m$ and (—◆—) $90\,\mu m$.

These differences in the structural parameters dramatically affect mass transfer during primary drying and, in its turn, its time. As shown in Figure 8.10a, it is clear that an increase in the particle diameter resulted in a nonlinear decrease in drying time, i.e., 65 h in the case of microparticles having $10\,\mu m$ as diameter and 24 h for microparticles of $90\,\mu m$. In fact, increasing the particle diameter, the pores formed by the particles within the bed increased in dimension, causing a decrease of R_p and, consequently, a sharp increase in the rate of sublimation.

As shown in Section 8.2.3, DGM equations describe mass transport in the packed-bed in the transition regime by taking into account Darcy's flow and diffusional transport, i.e., ordinary and Knudsen diffusion. The relative contribution of Darcy's and diffusional transport depends on pressure and characteristic length of the medium in which mass flux occurs, i.e., the pore diameter. In our simulations, we have found that the contribution of the diffusional transport mechanisms was usually much higher with respect to that of the viscous flow at the conditions occurring during primary drying. In particular, our simulations showed that in the case of microparticles of $10\,\mu m$, vapor flux due to diffusion contributed more than 99% of the total flux. Increasing the size of microparticles, the contribution of viscous flow, which we has been modeled by Darcy's Law, increased as well. Viscous flux contributed to the

1.5% of the total vapor flux in the dried bed of microparticles of 50 μm, and 4% for microparticles of 90 μm. The contribution of viscous flow was modest because, in the scenarios considered in this work, Kn is slightly smaller than 10 and, so, at the lower limit of the transition regime and close to the pure molecular regime. However, DGM was used to describe at macroscale level and with relatively simple equations the complex phenomena of mass transfer in the transition regime, and, in this framework, some relevant physical aspects could be missed.

The effect of particle diameter on the overall mass transfer resistance within the bed is shown in Figure 8.10b.

As a second step, we compared packings of monodisperse microparticles with packings made of Gaussian-polydisperse microparticles with a mean particle diameter of 50 μm and varying standard deviation in the range 0-5 μm. The number of particles within the REV (i) has to be representative of the original particle distribution and (ii) sufficiently large to avoid fluctuation in the value of properties, i.e., porosity. In fact, if the REV was not sufficiently large, the simulations cannot catch the global properties but only local ones.

As shown in Tab. 8.3, there was a decrease in porosity with increasing particle size-distribution width. This can be explained by the ability of small particles to fill the voids around larger particles and create an overall more dense packing structure. As a consequence, as polydispersity increased, the mean pore diameter decreased from 18.2 to 17 μm and permeability decreased from 2.552×10^{-12} m^2 to 2.041×10^{-12} m^2. On the other hand, tortuosity did not seem to be affected by the polydispersity of microparticles, as its value remained constant at about 1.25-1.26.

Table 8.3 Packing characteristics for a packed-bed made of microparticles having 50 μm as mean diameter.

σ	ε_b	τ_b	d_P, μm	B_0, m^2
0.0	0.375	1.262	18.2	2.552×10^{-12}
0.5	0.373	1.253	18.0	2.505×10^{-12}
1.0	0.369	1.252	17.8	2.434×10^{-12}
2.0	0.367	1.253	17.6	2.389×10^{-12}
5.0	0.359	1.254	17.2	2.041×10^{-12}

The effect of polydispersity of microparticles on the drying behavior of the packed-bed is shown in Figure 8.11. In the case of monodisperse microparticles, the drying time was about 29 h if primary drying was carried out at 253 K and 10 Pa. At the same process conditions, drying time increased as polydispersity increased, i.e., 32 h for microparticles of 50 μm as mean diameter and a standard deviation of 5 μm. These differences in drying time were a direct consequence of the different structural parameters of the two packings, which affect the cake resistance to vapor as shown in Figure 8.11b.

8.4.5   Clarifying the role of REV size and particles segregation

Moving from the pore-scale to the macro-scale implicates that the parameters estimated at the smaller scales are used at the larger scales. In this work, DEM and CFD describe the packing of granules at the smaller scales; from these simulations, some parameters
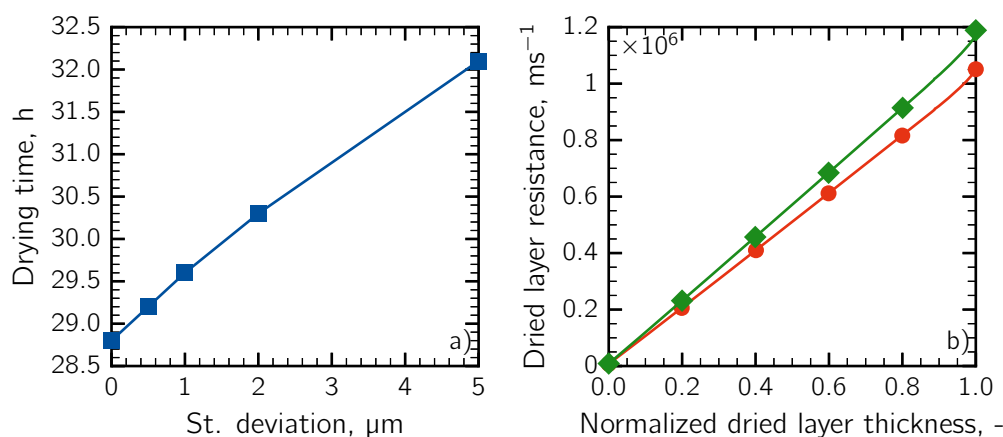
Figure 8.11 (a) Drying time vs. polydisperity of the particle-size distribution for particles of 50 μm as mean diameters. Primary drying was carried out at 10 Pa and 253 K. (b) Dried cake resistance to vapor flow as a function of the dried thickness of the packing for (—●—) monodisperse and (—◆—) Guassian-polydisperse microparticles with a standard deviation of 5 μm.

are estimated and used at the larger scale, which is represented by the mathematical model of the freeze-drying of a packed-bed of micro-particles. In that context, the product in the vial, which is constituted of the whole packing of micro-granules, is described only by four parameters, i.e., porosity, pore diameter, tortuosity, and permeability.

The problem of coupling pore-scale and macro-scale by using the approach here described consisted, as a first step, in choosing the size and location of the REV which is the smallest volume whose properties are 'representative' of the whole packing. Three elements have to be taken into account: (a) REV dimension, (b) wall effects and (c) particles segregation.

The concern about REV dimension resides in the fact that product characteristics in the pore/particle-scale simulation framework change point by point, as shown in Figure 8.12a. The porosity of small REVs, containing 10 to 100 particles, strongly fluctuated as the REV position was slightly moved from the center of the packing; in that case, the properties estimated are the local properties of the packing. These fluctuations decreased as the REV size increased and became insignificant if REVs contain more than 1,000 particles.

The second concern relates to the effect of the wall on the properties of the packed bed generated by DEM and those simulated at the macro-scale. In this study, simulations were carried out using a cylindrical container of 0.2 cm as diameter (Figure 8.12b), whereas a vial is usually in the order of 1-2 cm. For this reason, the REVs were always selected in the central part of the packing, carefully avoiding the peripheral parts, where the wall effects predominated. However, as a rule of thumb, wall effects are negligible if the ratio of the vial to particle diameter is higher than 15 - 50 (Mehta and Hawley, 1969; Delgado, 2006). In the case of a lyophilization vial filled with micro-particles, this ratio is usually higher than 100, thus the wall effects can be neglected.

The third concern deals with the effect of particles segregation. As shown by many authors, packings of granules show size-based segregation because of material
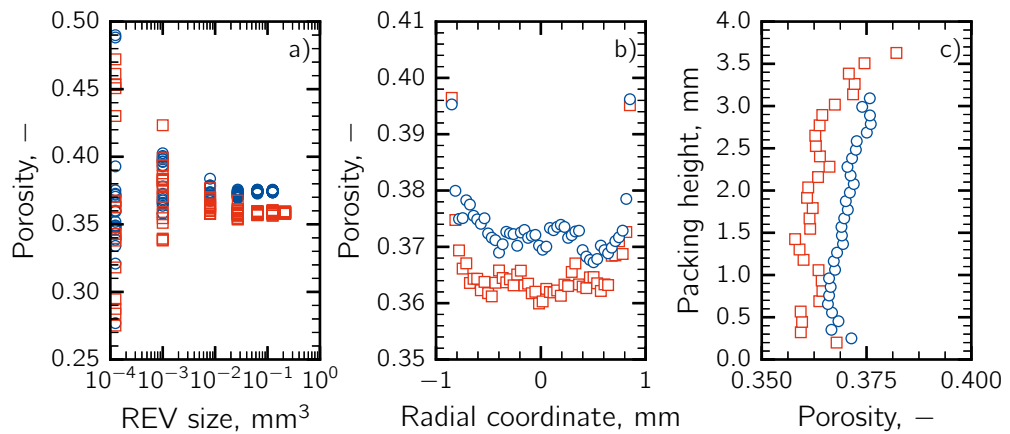
Figure 8.12 (a) Packing porosity as a function of REV volume and (b) radial porosity distribution and (c) porosity along the packing height in the case of (O) monodisperse and (□) polydisperse microparticles ($\sigma = 5\,\mu m$) with a mean diameter of $50\,\mu m$.

handling and vial filling (Jaklič et al., 2015). To elucidate this aspect, DEM simulations of 100k, 200k, and 500k microparticles have been carried out using monodisperse particles having $50\,\mu m$ as particle diameter, and polydisperse particles having the same average particle diameter and a standard deviation of $5\,\mu m$. Mean pore diameter and mean particle diameter were estimated at different heights in the packings. As shown in Figure 8.12c, the properties of the packed-bed did not change dramatically along the vertical direction. Moreover, from these simulations, it can be seen that the characteristics of the packing made of 100k particles were slightly different from those observed for the 200k and 500k configuration, see Figure 8.13. The porosity in the packings of 200k and 500k was slightly smaller than the one found for the packing of 100k, maybe because of a rearrangement of the particles. These results call for further research to confirm the outcomes of the model and better understand the factors that influence particles segregation.
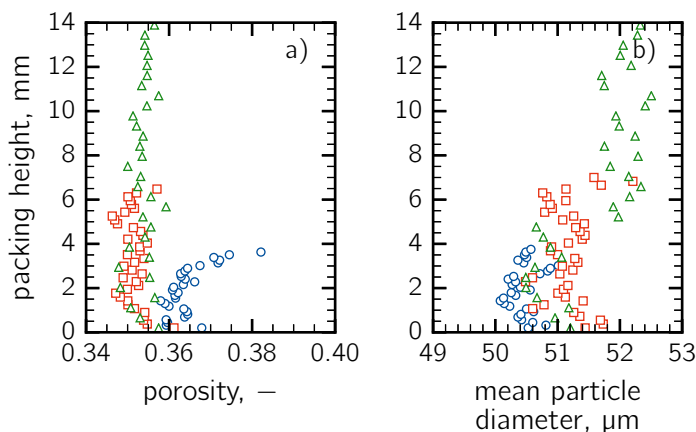
Figure 8.13 Distribution of the (a) porosity (b) mean particle diameter along the packing height in the case of polydisperse microparticles ($\sigma = 5\,\mu m$) with a mean diameter of $50\,\mu m$. Dara refer to packings of (O) 100k, (□) 200k and (△) 500k particles.

8.5 Conclusions

The main goal of the current study was to design a novel method to evaluate the structural properties and the behavior of a packed-bed of microparticles to be freeze-dried. DEM, CFD and a mechanistic model of freeze-drying process at the macro-scale were used to achieve this objective, studying the process at different scales. DEM simulations allowed a detailed description of particle-particle interactions and, thus, a more realistic generation of random packings of microparticles, even of a large number of particles, i.e., 100,000. CFD simulations at pore scale provided an estimation of structural parameters of these packings, i.e., mean pore diameter, porosity, tortuosity, and permeability. At last, these parameters were used in the DGM equations for describing mass transfer in the mechanistic model of freeze-drying at the macro-scale.

This multi-scale procedure was found to describe realistically some case studies published in the literature and evaluate drying time and product temperature during drying. We also investigated the role of packing structure on freeze-drying by generating packings from monodisperse and Gaussian-polydisperse microparticles. Polydisperse microparticles generated packings with higher mass transfer resistance, because small particles can fill the voids among the larger particles, and, so, reducing the size of interstitial voids, the porosity and the permeability of the packed-bed. By contrast, the values of tortuosity of packed beds appeared to be almost constant for different particle size distributions.

The main advantage of using this multi-scale procedure is that, once the particle distribution resulted from certain spray conditions is known, one can evaluate the structural properties of the packing, and, so, the mass transfer resistance and drying time. This is particularly important because different particle distributions can lead to very different behavior during drying, as shown in this work.

Acronyms

CFD Computational Fluid Dynamics; **DGM** Dusty-Gas Model.

List of symbols

B_0 permeability coefficient, m^2

c_i molar concentration of the i-component, $mol\,m^{-3}$

c_p specific heat capacity, $J\,kg^{-1}\,K^{-1}$

D_i', D_i'' transport coefficients of DGM equation for molar flux of specie-i, $m^2\,s^{-1}$

D_{ij}^{eff} effective binary diffusion coefficient, $m^2\,s^{-1}$

D_i^{Kn} Knudsen diffusion coefficient, $m^2\,s^{-1}$

D_p particle diameter, m

D_p^* diameter of frozen core in the particle, m

d_P pore diameter within the bed, m

$\mathbf{F}_{c,i}$ vector of total force contact acting on particle i, N

$\mathbf{F}_{n,i}$ vector of normal force contact acting on particle i, N

$\mathbf{F}_{t,i}$ vector of tangential force contact acting on particle i, N

$\mathbf{g}$ gravity vector, $m\,s^{-2}$

ΔH_s enthalpy of sublimation, $J\,kg^{-1}$

I_i momentum of inertia of particle i, $kg\,m^{-2}$

L_z REV size, m

M molecular weight, $kg\,kmol^{-1}$

m^* equivalent mass, kg

m_i mass of particle i, kg

N molar flux, $mol\,m^{-2}\,s^{-1}$

$\mathbf{n}_{ij}$ normal vector, -

p total pressure, Pa

p_i partial pressure of the i-component, Pa

p_w^{eq} vapor equilibrium pressure, Pa

p_z pressure drop in z-direction through the REV, Pa

R^* equivalent radius, m

R_g universal gas constant, $\mathrm{J\,mol^{-1}\,K^{-1}}$

$\mathbf{r}_i$ vector position of particle i, m

S surface area, $\mathrm{m^2}$

S_n normal stiffness, $\mathrm{N\,m^{-1}}$

S_t tangential stiffness, $\mathrm{N\,m^{-1}}$

T temperature, K

t time, s

$\mathbf{t}_i$ vector of total torque acting on particle i, $\mathrm{N\,m}$

$\mathbf{t}_{ij}$ tangential vector, -

$\mathbf{u}$ velocity vector, $\mathrm{m\,s^{-1}}$

$\mathbf{u}_{in}$ inlet velocity vector, $\mathrm{m\,s^{-1}}$

$\mathbf{u}_{out}$ outlet velocity vector, $\mathrm{m\,s^{-1}}$

u_z vector in the z-direction, $\mathrm{m\,s^{-1}}$

V volume, $\mathrm{m^3}$

$v_{n,r}$ normal component of relative velocity, $\mathrm{m\,s^{-1}}$

v_s velocity of sublimation front, $\mathrm{m\,s^{-1}}$

$v_{t,r}$ tangential component of relative velocity, $\mathrm{m\,s^{-1}}$

Y^* equivalent Youngs modulus, $\mathrm{N\,m^{-2}}$

Greek letters

β constant related to the restitution coefficient, -

δ_n normal displacement, m

δ_t tangential displacement, m

ε_b bed porosity, -

ε_p particle porosity

ε porosity, -

κ thermal conductivity, $\mathrm{W\,m^{-1}\,K^{-1}}$

μ viscosity of gas mixture, $\mathrm{kg\,m^{-1}\,s^{-1}}$

ϕ_S frozen fraction function, see Eq. 8.12

ρ density, $\mathrm{kg\,m^{-3}}$

τ tortuosity, -

Ω computational domain

$\boldsymbol{\omega}_i$ angular velocity vector, $\mathrm{rad\,s^{-1}}$

Subscript

d   dried

f   frozen

gas   gas

i, j, k saturation index

in   inert gas

int   sublimation interface

mesh   computational mesh

I   layer of completely dried microparticles

II   layer of completely or partially frozen microparticles

III   vial wall side

REV   relevant element volume

tot   total

void   void within the product

water   water vapor

wetted   wetted surface

References

Baxendale, I. R., Braatz, R. D., Hodnett, B. K., Jensen, K. F., Johnson, M. D., Sharratt, P., Sherlock, J.-P., and Florence, A. J. (2015). Achieving Continuous Manufacturing: Technologies and Approaches for Synthesis, Workup, and Isolation of Drug Substance. May 20-21, 2014 Continuous Manufacturing Symposium. *Journal of Pharmaceutical Sciences* 104 (3), pp. 781–791.

Boccardo, G., Augier, F., Haroun, Y., Ferre, D., and Marchisio, D. L. (2015). Validation of a novel open-source work-flow for the simulation of packed-bed reactors. *Chemical Engineering Journal* 279, pp. 809–820.

Bruttini, R. and Liapis, A. I. (2015). The drying rates of spray freeze drying systems increase through the use of stratified packed bed structures. *International Journal of Heat and Mass Transfer* 90, pp. 515–522.

Byrn, S., Futran, M., Thomas, H., Jayjock, E., Maron, N., Meyer, R. F., Myerson, A. S., Thien, M. P., and Trout, B. L. (2015). Achieving continuous manufacturing for final dosage formation: Challenges and how to meet them. May 20–21, 2014 Continuous Manufacturing Symposium. *Journal of Pharmaceutical Sciences* 104 (3), pp. 792–802.

Capozzi, L. C. and Pisano, R. (2018). Looking inside the black box: Freezing engineering to ensure the quality of freeze-dried biopharmaceuticals. *European Journal of Pharmaceutics and Biopharmaceutics* 129, pp. 58–65.

Carman, P. C. (1956). *Flow of Gases through Porous Media*. London: Butterworths Scientific Publications.

Carson, J. W. (1988). Overcoming particle segregation in the pharmaceutical and cosmetics industries. *Drug Development and Industrial Pharmacy* 14 (18), pp. 2749–2758.

Chen, D., Maa, Y.-F., and Haynes, J. R. (2002). Needle-free epidermal powder immunization. *Expert Review of Vaccines* 1 (3), pp. 265–276.

Cundall, P. A. and Strack, O. D. (1979). A discrete numerical model for granular assemblies. *Geotechnique* 29 (1), pp. 47–65.

Delgado, J. (2006). A critical review of dispersion in packed beds. *Heat and Mass Transfer* 42 (4), pp. 279–310.

Dullien, F. A. (2012). *Porous Media: Fluid Transport and Pore Structure*. New York, NY, USA: Academic press, New York.

Haeuser, C., Goldbach, P., Huwyler, J., Friess, W., and Allmendinger, A. (2018). Imaging techniques to characterize cake appearance of freeze-dried products. *Journal of Pharmaceutical Sciences* 107 (11), pp. 2810–2822.

Icardi, M., Boccardo, G., Marchisio, D. L., Tosco, T., and Sethi, R. (2014). Pore-scale simulation of fluid flow and solute dispersion in three-dimensional porous media. *Physical Review E* 90 (1), p. 013032.

Icardi, M., Boccardo, G., and Tempone, R. (2016). On the predictivity of pore-scale simulations: Estimating uncertainties with multilevel Monte Carlo. *Advances in Water Resources* 95, pp. 46–60.

Jaklič, M, Kočevar, K, Srčič, S, and Dreu, R (2015). Particle size-based segregation of pharmaceutical powders in a vertical chute with a closed bottom: An experimental evaluation. *Powder Technology* 278, pp. 171–180.

Jiang, L., Liu, H., Wu, D., Wang, J., Xie, M.-Z., and Bai, M. (2017). Pore-scale simulation of hydrogen–air premixed combustion process in randomly packed beds. *Energy & Fuels* 31 (11), pp. 12791–12803.

Khadka, P., Ro, J., Kim, H., Kim, I., Kim, J. T., Kim, H., Cho, J. M., Yun, G., and Lee, J. (2014). Pharmaceutical particle technologies: An approach to improve drug solubility, dissolution and bioavailability. *Asian Journal of Pharmaceutical Sciences* 9 (6), pp. 304–316.

Kim, Y.-Y. and Lee, K.-S. (2008). Comparative numerical study of freeze drying of solution and spray-frozen particles in trays and vials. *Numerical Heat Transfer, Part A: Applications* 54 (4), pp. 406–425.

Kuu, W. Y., Nail, S. L., and Sacha, G. (2009). Rapid determination of vial heat transfer parameters using tunable diode laser absorption spectroscopy (TDLAS) in response to step-changes in pressure set-point during freeze-drying. *Journal of Pharmaceutical Sciences* 98 (3), pp. 1136–1154.

Liapis, A. and Bruttini, R (2009). A mathematical model for the spray freeze drying process: The drying of frozen particles in trays and in vials on trays. *International Journal of Heat and Mass Transfer* 52 (1), pp. 100–111.

Linsong, J., Hongsheng, L., Shaoyi, S., Maozhao, X., Dan, W., and Minli, B. (2018). Pore-scale simulation of flow and turbulence characteristics in three-dimensional randomly packed beds. *Powder Technology* 338, pp. 197–210.

Maa, Y.-F., Nguyen, P.-A., Sweeney, T., Shire, S. J., and Hsu, C. C. (1999). Protein inhalation powders: spray drying vs spray freeze drying. *Pharmaceutical Research* 16 (2), pp. 249–254.

Marti, J. and Mauersberger, K. (1993). A survey and new measurements of ice vapor pressure at temperatures between 170 and 250 K. *Geophysical Research Letters* 20 (5), pp. 363–366.

Mascarenhas, W., Akay, H., and Pikal, M. (1997). A computational model for finite element analysis of the freeze-drying process. *Computer Methods in Applied Mechanics and Engineering* 148 (1), pp. 105–124.

Mason, E. A. and Malinauskas, A. (1983). *Gas Transport in Porous Media: The Dusty-Gas Model*. Amsterdam: Elsevier, Amsterdam.

Mehta, D. and Hawley, M. (1969). Wall effect in packed columns. *Industrial & Engineering Chemistry Process Design and Development* 8 (2), pp. 280–282.

Nakagawa, K., Hottot, A., Vessot, S., and Andrieu, J. (2007). Modeling of freezing step during freeze-drying of drugs in vials. *AIChE Journal* 53 (5), pp. 1362–1372.

Pisano, R. and Capozzi, L. C. (2017). Prediction of product morphology of lyophilized drugs in the case of Vacuum Induced Surface Freezing. *Chemical Engineering Research and Design* 125, pp. 119–129.

Pisano, R., Barresi, A. A., Capozzi, L. C., Novajra, G., Oddone, I., and Vitale-Brovarone, C. (2017b). Characterization of the mass transfer of lyophilized products based on X-ray micro-computed tomography images. *Drying Technology* 35 (8), pp. 933–938.

Rey, L. (2016). *Freeze-Drying/Lyophilization of Pharmaceutical and Biological Products*. CRC Press, New York.

Sadikoglu, H and Liapis, A. (1997). Mathematical modelling of the primary and secondary drying stages of bulk solution freeze-drying in trays: Parameter estimation and model discrimination by comparison of theoretical results with experimental data. *Drying Technology* 15 (3-4), pp. 791–810.

Schiffter, H., Condliffe, J., and Vonhoff, S. (2010). Spray-freeze-drying of nanosuspensions: the manufacture of insulin particles for needle-free ballistic powder delivery. *Journal of the Royal Society Interface* 7 (4), S483–S500.

Suzuki, M, Shinmura, T, Iimura, K, and Hirota, M (2008). Study of the wall effect on particle packing structure using X-ray micro computed tomography. *Advanced Powder Technology* 19 (2), pp. 183–195.

Tangri, H., Guo, Y., and Curtis, J. S. (2017). Packing of cylindrical particles: DEM simulations and experimental measurements. *Powder Technology* 317, pp. 72–82.

Thorstenson, D. C. and Pollock, D. W. (1989). Gas transport in unsaturated zones: Multicomponent systems and the adequacy of Fick's laws. *Water Resources Research* 25 (3), pp. 477–507.

Tsuji, Y., Tanaka, T., and Ishida, T (1992). Lagrangian numerical simulation of plug flow of cohesionless particles in a horizontal pipe. *Powder Technology* 71 (3), pp. 239–250.

Velardi, S. and Barresi, A. (2008). Development of simplified models for the freeze-drying process and investigation of the optimal operating conditions. *Chemical Engineering Research and Design* 86 (1), pp. 9–22.

Ye, T., Yu, J., Luo, Q., Wang, S., and Chan, H.-K. (2017). Inhalable clarithromycin liposomal dry powders using ultrasonic spray freeze drying. *Powder Technology* 305, pp. 63–70.

PART IV

Batch vs. continuous: an economical perspective

9

Note on the industrial perspective of continuous freeze-drying

This chapter is a final note on the industrial perspective of the continuous freeze-drying process. Three case studies were used to illustrate the advantages of continuous freeze-drying in terms of reduction of processing duration and equipment volume; some considerations were given concerning the production cost of a unit dose. Finally, continuous freeze-drying as proposed in this thesis will be compared to other emerging processes that aim to replace the conventional batch freeze-drying.

9.1 Introduction

This last chapter is dedicated to depicting the continuous freeze-drying process as proposed in this thesis into the realm of the industrial production of pharmaceuticals and biopharmaceuticals. It will explore the advantages and the disadvantages of continuous freeze-drying process, and make a comparison with the conventional batch process.

Although this chapter is not intended to be a cost analysis of the process, it will provide a quick glimpse of the production costs in the case of batch and continuous freeze-drying. It is quite difficult to find data in the literature on the economics of the process as these data are usually hidden by the pharmaceutical companies. Millman et al. (1985) published a note on the economics of batch freeze dryers and proposed a way to evaluate the costs of the process on the basis of some simple variables. A comprehensive report on cost projections for producing freeze-dried foodstuff was published by Bird (1964), based on data from the industry. The cost breakdown presented by Ratti (2001) for the freeze-drying of high and low-value foods shows that freeze-drying impacts to the final cost about 4-9% because of the energy cost and 16-25% because of the investment costs. Although a direct comparison can not be done between food and pharmaceutical processes, those data demonstrated that freeze-drying should not be regarded as a prohibitively expensive process. This is

particularly true for freeze-drying of pharmaceuticals, where the cost of raw materials and upstream processes might be orders of magnitude higher than the freeze-drying process itself.

In this chapter, emphasis will be put on the process throughput and equipment volume, as they have a tremendous impact on the profitability of the process.

This chapter ends with a comparison between the continuous freeze-drying concept as proposed in this thesis and other emerging processes that aim to replace the conventional batch freeze-drying.

9.2 Methodology

In this section, the following three case studies are analyzed and compared,

I. mannitol-based formulation (5% w/w), 3 ml in 10R vials,
objectives: $T_{p,max} = 257$ K, final RM = 1%.

    a. batch - uncontrolled nucleation;
       PD: $T_{sh} = 257$ K, $P_c = 10$ Pa; SD: $T_{sh} = 313$ K, $P_c = 2$ Pa

    b. continuous - uncontrolled nucleation;
       PD: $T_{sh} = 298$ K, $P_c = 2$ Pa; SD: $T_{sh} = 313$ K, $P_c = 2$ Pa

II. mannitol-based formulation (5% w/w), 3 ml in 10R vials,
$T_{p,max} = 247$ K, final RM = 1%.

    a. batch - uncontrolled nucleation;
       PD: $T_{sh} = 255$ K, $P_c = 10$ Pa; SD: $T_{sh} = 293$ K, $P_c = 2$ Pa

    b. batch - controlled nucleation;
       PD: $T_{sh} = 260$ K, $P_c = 10$ Pa; SD: $T_{sh} = 293$ K, $P_c = 2$ Pa

    c. continuous - controlled nucleation;
       PD: $T_{sh} = 285$ K, $P_c = 2$ Pa; SD: $T_{sh} = 293$ K, $P_c = 2$ Pa

III. sucrose-based formulation (5% w/w), 2 ml in 10R vials,
$T_{p,max} = 240$ K, final RM = 3%.

    a. batch - uncontrolled nucleation;
       PD: $T_{sh} = 253$ K, $P_c = 10$ Pa; SD: $T_{sh} = 293$ K, $P_c = 2$ Pa

    b. continuous - uncontrolled nucleation;
       PD: $T_{sh} = 273$ K, $P_c = 10$ Pa; SD: $T_{sh} = 293$ K, $P_c = 2$ Pa

    c. continuous - controlled nucleation;
       PD: $T_{sh} = 293$ K, $P_c = 2$ Pa; SD: $T_{sh} = 293$ K, $P_c = 2$ Pa

The duration of these cycles refers to those obtained in Section 4.

9.2.1 Apparatus

Batch lyophilizer

A typical industrial batch lyophilizer has been considered having the following specifications (Figure 9.1): chamber volume of 13 m^3, 17 shelves (and a further radiative
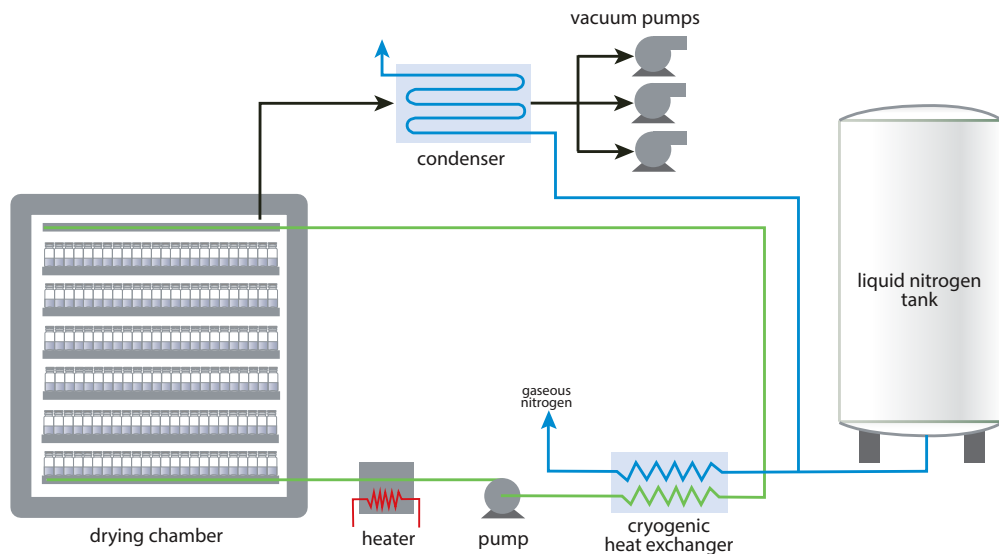
Figure 9.1 Schematic of the batch lyophilizer

plate) for a total shelf area of about $29\,\text{m}^2$ ($27\,\text{m}^2$ available), a condenser of $6\,\text{m}^3$ and a surface of $24\,\text{m}^2$ refrigerating with liquid nitrogen and defrosted in vacuum with steam. The apparatus is equipped with vacuum pumps which work in parallel having an overall average power consumption of 6.7 kW. Silicone oil is used as the heat-transfer fluid and it is refrigerated by a cryogenic cooling system based on the use of liquid nitrogen and electrical resistance.

Continuous lyophilizer

The continuous apparatus has been considered having a single freezing module and a number of drying modules so that its productivity is the same as the batch lyophilizer (Figure 9.2). Each module has a surface of $1.44\,\text{m}^2$ and a volume of $0.12\,\text{m}^3$; the vials move through channels of $0.06\,\text{m}$ that form a path extended for $20\,\text{m}$ within the module. The apparatus is equipped with a vacuum pump dedicated to the nucleation chamber having an overall average power consumption of 0.3 kW and three vacuum pumps which work in parallel having an overall average power consumption of 3.1 kW. Freezing is performed by using sterilized liquid nitrogen; the vial comes into contact with the countercurrent flow of sterilized nitrogen gas which extracts heat, cooling down and partially freeze the product, then passes below a spray of liquid nitrogen that completes the freezing. Silicone oil is used as the heat-transfer fluid in the drying modules and it is refrigerated by a cryogenic cooling system based on the use of liquid nitrogen and electrical resistance.

9.2.2 Energy consumption and costs

A basic model to calculate energy consumption during freeze-drying is reported in Appendix D. The model takes into account the energy requirements for freezing and drying the product, the vacuum pumps, condenser, and the energy losses.
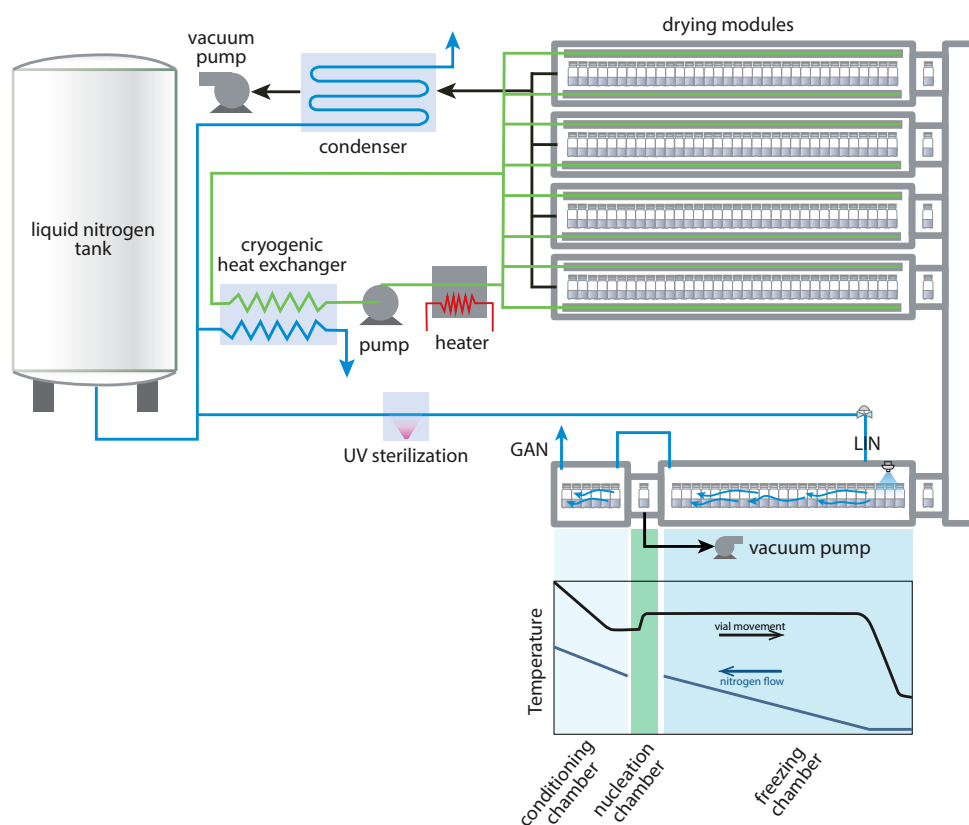
Figure 9.2   Schematic of the continuous lyophilizer

9.3   Results

9.3.1   Processing time, equipment volume and processing costs

One of the advantages of continuous freeze-drying consists in the reduction of process duration as a result of the reduction of cycle duration and the absence of dead times. Figure 9.3a shows the processing time for batch and continuous freeze-drying production of about 50,000 doses of a mannitol-based formulation ($T_{p,max}$ = 257 K, RM = 1%); no controlled nucleation technique is used in this scenario. In this case, cycle duration is reduced by about 4 times mainly because of the reduction of primary drying duration (27 vs 10h) and the elimination of dead times due to loading and unloading (12 h) and the other ancillary operations (15 h).

Similar results were obtained in the case study II ($T_{p,max}$ = 247 K, RM = 1%), where batch freeze-drying in the case of controlled and uncontrolled nucleation was compared to continuous freeze-drying coupled with controlled nucleation. Oddone et al. (2014) had already shown that VISF is able to reduce the cycle duration of about 20-40%; aside from the technical difficulty of performing VISF in an industrial lyophilizer, VISF applied to batch has no influence on dead time. As shown in Figure 9.3b, VISF applied to the batch process resulted in an overall reduction of process duration of about 12 h. On the other hand, VISF applied to continuous resulted in a reduction of cycle duration of 31 h (20 h compared to batch + VISF) and an overall reduction of the processing time of about 58 h (47 h compared to batch +

VISF).

In case study III, the freeze-drying of a sucrose-based formulation ($T_{p,max} = 240$ K, RM = 3%) was compared in the case of a batch (uncontrolled nucleation) and a continuous process for both controlled and uncontrolled nucleation. These results confirm the sharp reduction of processing time in the case of continuous.
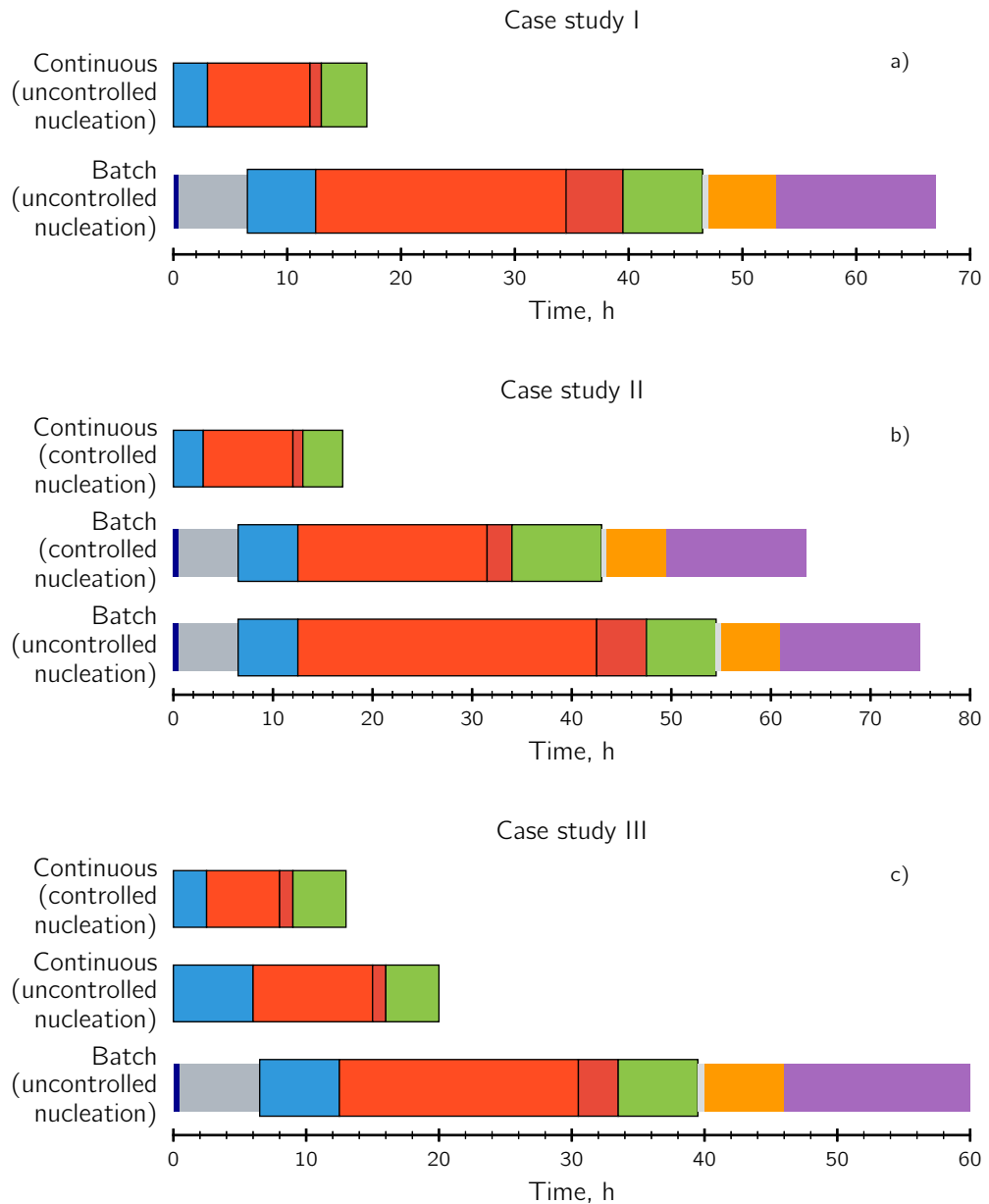
Figure 9.3 Processing time. a) Case study I: mannitol 5%, $T_{p,max} = 257$ K, RM = 1%; b) Case study II: mannitol 5%, $T_{p,max} = 247$ K, RM = 1%; c) Case study III: sucrose 5%, $T_{p,max} = 240$ K, RM = 3%. The following step are considered: (■) leak test, (■) loading, (■) freezing, (■) primary drying, (■) soak time, (■) secondary drying, (■) stoppering, (■) unloading, (■) SIP/CIP.

This sharp reduction in processing time has a strong impact on the dimension of the continuous lyophilizer. At constant productivity, the total volume of the modules

in the case of the continuous apparatus is reduced of about 6 times with respect to the batch apparatus in all the case studies presented in this chapter, see Figure 9.4.
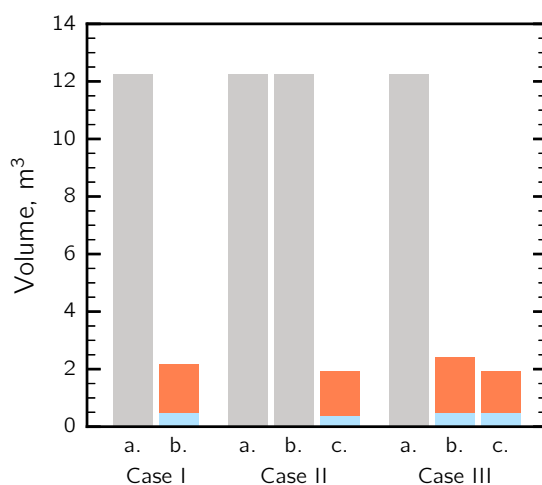
Figure 9.4 Chamber volume in the case of (■) batch and continuous apparatus: (■) freezing module and (■) drying module.

Although lyophilization is usually seen as an expensive method for dehydration compared to other techniques, in the case of pharmaceuticals, the production cost is not a real issue. We have estimated that in the case studied here presented, the energy cost for the batch production was about 0.0012 EUR/vial, whereas it was about 0.0009 EUR/vial in the case of continuous freeze-drying, see details in Appendix D. It should be kept in mind that the cost of the apparatus or the costs for SIP/CIP can impact more than energy cost. To give you an example, an industrial freeze-drier requires 1-2 million investment, which means that if the apparatus has the productivity of 2 cycles/week (50,000 vials/cycle), works for 52 weeks/year and depreciates in 10 years, the depreciation cost per vial is about 0.02-0.04 EUR/vial. These numbers should be compared to the selling price of a unit dose in the market which can be up to thousands of euros.

9.4 Comparison of alternative technologies to conventional batch freeze-drying

In Table 9.1 a comparison has been reported between batch lyophilization and three different concepts of the continuous process,

1. the Hosokawa Micron BV lyophilization concept (Touzet et al., 2018)

2. continuous lyophilization in unit doses proposed by RheaVita - Ghent University based on spin-frozen product (Corver, 2012)

3. continuous lyophilization in unit doses proposed by Politecnico di Torino-MIT (Capozzi et al., 2019)

These three technologies are presented in details in Chapter 2.

Table 9.1 Comparison of batch freeze-drying with some continuous technologies.

	Batch	Hosokawa Micron BV	ReaVita-Ghent University concept	Politecnico di Torino-MIT concept
Technology status	Roboust and well established	Continuous equipment not already commercialized	Prototype phase	Proof of concept
Dosage form	Bulk, Unit dose (liquid frozen solution, particle based products), Cartridge	Particles	Unit doses (Spin-frozen product)	Unit doses (VISF-frozen product, particle-based products)
Filling volume/vial dimension	Almost everything	-	Almost everything	Almost everything
Dead time	Very long	No	No	No
Processing time	Very long	Shorter	Very short	Shorter
Equipment footprint	Large	Smaller	Smaller	Smaller
Control of product structure	Possible	No	No	Yes
Scale-up	Yes	Yes	No	No
Batch-to-batch variability	Yes	No	No	No
Vial-to-vial variability	Yes	-	Limited	No
In-line control	Lose	No	Yes	Yes
Process and product knowledge	Wide literature and long experience	No	Limited literature	Wide literature on VISF-based products but limited on process

Batch lyophilization is certainly a robust and established process, with extensive literature and long industrial experience. Although it still remains inefficient and expensive, with long dead time and limited throughput. Batch lyophilization has its weakness in the loose control of product quality, resulting in an unavoidable vial-to-vial and batch-to-batch variability of product characteristics.

The continuous technology proposed by Hosokawa Micron BV, does not produce end-to-use products, but only bulk materials in the form of fine particles. Handling this type of materials, the lack of knowledge on the impact of this technology on product quality, and the lack in controlling product temperature and final moisture within the product might be, in the opinion of this author, a further weakness of this technology. Besides that, this technology is almost already developed and it is expected to see new data and publications in the near future.

The two technologies proposed by Rhea Vita - Ghent University and Politecnico di Torino - MIT are designed to produce end-to-use products, avoiding the drawbacks of batch lyophilization in vials. Processing time and equipment footprint result dramatically reduced, no manual operation or breaks are necessary, in-line control is naturally implemented, and scale-up simply consists of adding parallel modules.

Rhea Vita - Ghent University proposed spin-freezing for shortening cycle time, even though it is almost impossible to control product structure. On the other hand, this process can reduce dramatically drying time.

Politecnico di Torino - MIT proposed a concept based on VISF protocols, but can also be extended to particle-based products in vials. Using VISF, product structure is completely controlled and can be designed modulating the freezing rate. A great advantage of VISF is the deep knowledge that the scientific community has gained in recent years. Moreover, there is no limitation in the vessel dimension or filling volume.

9.5   Discussion and conclusion

Continuous manufacturing is becoming increasingly important in pharmaceutical manufacturing, and lyophilization, as a downstream process, also needs to move from batch to continuous. In this chapter, the continuous technology proposed in this thesis has been depicted with the framework of the industrial production of pharmaceuticals and biopharmaceuticals.

Some real case studies have been used to project processing time, costs and volume equipment of real pharmaceutical production. It has been demonstrated that continuous freeze-drying can reduce the overall processing time 3 - 4 times, as well as equipment volume. The energetic costs do not seem dramatically influenced by the continuous process, although the revenues can increase dramatically because of the higher throughput generated by using continuous freeze-drying. There are further aspects which are difficult to monetize, such as the perfect control of the process and product quality. Product quality will be the challenge that the pharmaceutical industry has to address in the next years to respond to the more stringent quality requirements set by regulatory authorities.

The last chapter summarizes the drawbacks of batch lyophilization and their impact on the production of drugs and biotech drugs. Some continuous technologies currently under development have been presented and compared, i.e., active freeze-drying by Hosokawa Micron BV, continuous lyophilization of spin-frozen unit-doses by RheaVita - Ghent University and continuous lyophilization of VISF-based unit-doses proposed by Politecnico di Torino - MIT. It is the opinion of this author that these technologies are equally relevant and effective in the framework of continuous lyophilization of pharmaceuticals, and can potentially cover the broad spectrum of pharmaceutical products already in the market and the new ones under development. All of these technologies have their inherent advantages and limitations, and can fit the best only a market segment. The strength of the Hosokawa Micron BV lies in the ability to process large quantities of the product although the control of the process is loose. For such a process, prebiotics and probiotics seem particularly well-suited as they are usually lyophilized in bulk and they are much stable than the usual APIs produced in solid doses. The RheaVita - Ghent concept draws its strength from the ability to produce lyophilized drugs in unit doses in continuous, reducing dramatically drying

time; on the other hand, the lyophilized cake presents tiny pores (similar to quench freezing) and some doubts on the perfect control of some critical quality attributes (product structure and residual moisture) still remain. This technology is mainly fit for those products which are not affected by the surface-induced denaturation. On the other hand, although the continuous freeze-drying proposed by Politecnico di Torino - MIT and discussed in this thesis is not able to reduce processing time so much like the RheaVita - Ghent concept, its strength lies in the perfect control of critical quality attributes (product structure, residual moisture, APIs activity) so as in the ability to manage a wide spectrum of formulations and dosage forms.

References

Bird, K. (1964). *Freeze-drying of foods: cost projections*. 639. Marketing Economics Division, Economic Research Service, US Department of Agriculture.

Capozzi, L. C., Trout, B. L., and Pisano, R. (2019). From batch to continuous: freeze-drying of suspended vials for pharmaceuticals in unit-doses. *Industrial & Engineering Chemistry Research* 58 (4), pp. 1635–1649.

Corver, J. A.W. M. (2012). Method and system for freeze-drying injectable compositions, in particular pharmaceutical compositions. U.S. pat. 20140215845 A1.

Millman, M., Liapis, A., and Marchello, J. (1985). Note on the economics of batch freeze dryers. *International Journal of Food Science & Technology* 20 (5), pp. 541–551.

Oddone, I., Pisano, R., Bullich, R., and Stewart, P. (2014). Vacuum-Induced nucleation as a method for freeze-drying cycle optimization. *Industrial & Engineering Chemistry Research* 53 (47), pp. 18236–18244.

Ratti, C. (2001). Hot air and freeze-drying of high-value foods: a review. *Journal of Food Engineering* 49 (4), pp. 311–319.

Touzet, A., Pfefferlé, F., Wel, P. van der, Lamprecht, A., and Pellequer, Y. (2018). Active freeze drying for production of nanocrystal-based powder: A pilot study. *International Journal of Pharmaceutics* 536 (1), pp. 222–230.

Final discussion and conclusions

This work presented a new concept for freeze-drying of pharmaceuticals in unit-doses in response to the current trends in the pharmaceutical industry. There are some crucial questions to be answered to demonstrate the feasibility of the new concept of continuous lyophilization. This thesis responded to some of these questions using both experimental methods and simulation techniques. This final discussion merges the main results obtained by answering the questions that follow.

1. Is continuous manufacturing really useful and necessary in the pharmaceutical industry and, specifically, in freeze-drying?

As extensively explained in Chapter 1 and 2, the pharmaceutical industry is going through a period of important changes: (i) the opening of new markets in the emerging countries; (ii) the patent expiration of many 'blockbuster' drugs and the challenge of a more competitive market; (iii) the scrutiny and the new stringent requirements set by regulatory authorities; (iv) the emergence of new drugs such as the biopharmaceuticals. In this perspective, continuous manufacturing may represent an effective technology for producing drugs. The main advantages of the continuous processes are the operational flexibility, the shorter processing time, the absence of the scale-up, product quality monitored in real time, higher throughput and, at the same time, the reduction of the footprint and lower production costs. There are still few examples of commercialized drugs which are produced by using a continuous technology, and many other initiatives are ongoing in this sense. Also, regulatory authorities are encouraging the pharmaceutical community to move toward continuous processing to improve efficiency and manage variability.

As specifically concerns freeze-drying, the batch configuration currently used in industry presents many drawbacks: (i) long processing and dead time; (ii) poor control of the freezing step and, consequently, of product characteristics; (iii) non-uniformity of heat transferred during primary drying, which have important implications on the final quality of the products such as in the robustness and efficiency of the process; (iv) site-to-site, batch-to-batch and vial-to-vial variability are difficult to manage; (v) long and expensive scale-up from R&D to commercial productions. Much attention of lyophilization community was placed on improving batch robustness, control, monitoring, optimization and scale-up such as to enhance and manage quality and the uniformity of the product. Nonetheless, variability and product quality in the batch freeze-drying still remain difficult to control and manage.

In the last years, many technologies are emerging which aim to address the problems connected to batch lyophilization by using continuous or semi-continuous configurations. It is the opinion of this author that continuous can be an effective way to address the drawbacks associated to batch lyophilization and, at the same time, to manage product quality, increase its quality and throughput.

2. What are the solutions proposed for performing freeze-drying in continuous or semi-continuous modes? What the pros and cons of these technologies?

The idea of continuous lyophilization dates back to at least the 1940s, but only in the 1970s a fully continuous line, the Conrad freeze-dryer, was successfully introduced in the food industry. Until now, many ideas regarding continuous lyophilization of pharmaceuticals have been proposed, but none of them has been successfully applied in the industry because of their complexity, the difficulty of guarantee product sterility or handling safety problems.

As discussed in Chapter 2, some continuous technologies are emerging, which used the most various configurations and dosage forms.

The continuous technology proposed by Hosokawa Micron BV, can be used in semi-continuous modes. The solution is fed into a conical chamber, continuously stirred until completely frozen in the form of macroscopic blocks of nano/micro-crystals. During drying, the frozen material is continuously stirred, so that dried small fragments break away from the remaining frozen material; these fragments are collected into a filter cartridge. This technology does not produce end-to-use products, but only bulk materials in the form of fine particles. Handling this type of materials, the lack of knowledge on the impact of this technology on product quality, and the lack in controlling product temperature and final moisture within the product might be, in the opinion of this author, a further weakness of this technology. Besides that, this technology is almost already developed and new data are expected to be published in the near future.

A further technology which is emerging is the last years is the one proposed by RheaVita and Ghent University, which coupled spin-freezing and radiative drying. This technology is designed to produce end-to-use products, avoiding the drawbacks of batch lyophilization in vials. Processing time and equipment footprint result dramatically reduced, no manual operation or breaks are necessary, in-line control is naturally implemented, and scale-up simply consists of adding parallel modules. Although spin-freezing can shorter cycle time up to 20 times, it is almost impossible to control product structure. It is the opinion of this author that spin-freezing can be a promising technology for such products which contains robust APIs, whereas it might be not applied for those APIs which are very sensitive to denaturation or deactivation related to surface adsorption.

3. In what consists the continuous technology proposed in this thesis? What are the main problems that it aims to solve?

The concept proposed and studied in this thesis is the result of a collaboration between Politecnico di Torino and the Massachusetts Institute of Technology. As discussed in Chapter 3, the main idea behind this process is that a constant flow of vials enters and leaves the apparatus, passing through different, specialized, chambers. The process starts from the continuous filling of vials, which, at that point, are suspended and move over a track and into the conditioning module. Here, the flow of a cryogenic gas cools down the vial, bringing the product to the desired temperature. At the end of this module, the vial moves into a special chamber, the nucleation chamber, where the pressure is low enough to induce nucleation; many authors extensively studied VISF for the batch configuration and here applied to continuous lyophilization. After that, the vial moves in the freezing module, where, again, a

cryogenic gas cools down the vial, achieving the complete solidification of the product. It is possible to create customizable freezing protocols by changing the gas velocity, and so, modulating the freezing rate. The vial is then transferred to the drying module by mean of a load-lock system, which allows the passage of the vial from a module at a higher pressure to another at lower pressure without breaking the vacuum. In the drying module, vials are suspended over a track and move in the module following "snake"-type path. The module is constituted of temperature-controlled fins that supply heat to the product via radiation. It is possible to modulate heat transferred to the product by changing the temperature of surfaces, and, hence, to carry out both gentle and aggressive cycles. The last step of this process consists of the backfilling and vial stoppering. The entire process is carried out in continuous, without breaks between phase or manually intervention.

This technology aims to control product characteristics and, at the same time, eliminate scale-up and increase throughput. Product structure is controlled by using VISF, whereas the radiation is used to control heat supplied during primary and secondary drying. In fact, using VISF, nucleation temperature is the same for every sample, avoiding any differences in freezing history of the product, and, thus, in the final product structure. This technique allows the production of freeze-dried products with the desired morphological attributes by changing the cooling rate after nucleation has occurred. In recent year, VISF has become increasingly popular among researchers, and a wide literature already exists, making VISF a ready-to-use technique also in continuous. A further advantage is the perfect control and uniformity of heat supplied to products during primary and secondary drying. In fact, no edge-vial effect can be identified any longer because every vial follows the same path and experiences identical conditions. Moreover, contrary to batch lyophilization, small variations in the geometry of the vials have no significant effect on the heat supplied by radiation. Heat by radiation is largely independent of chamber pressure, allowing to further reduce pressure and, hence, increasing the sublimation rate. This method draws its strength from producing very uniform products, with the same characteristics because they undergo the same process conditions. It is extremely flexible because can also treat particle-based materials in vials, and it does not have a limitation in the shape of vessels.

4. Is continuous freeze-drying of suspended-vial able to control heat transferred to the product and reduce its variability?

In Chapter 4, it has been investigated the heat transfer of the suspended-vial configuration and compared to batch freeze-drying; the role of pressure, shelf temperature, and clearance between shelf and vials have been evaluated using an experimental set up similar to the one that will be used in the final apparatus.

In the batch freeze-drying, vials are placed in direct contact with the shelf, and heat is supplied by (i) direct conduction from the shelf to the glass at the points of contact, (ii) conduction through the gas in the gap at the bottom of the vial, (iii) radiation from the lower and upper shelves, and from the surroundings, i.e., the chamber walls and door, and (iv) by convection. The heat supplied by direct contact and radiation is independent of the chamber pressure, whereas convection and conduction both depend on the pressure. Convection plays a role only during freezing, whereas during drying it becomes negligible because the gas is rarefied. As shown in Chapter 4, during conventional shelf-ramped freezing, heat is removed from the bottom, as a

result of the direct contact between the shelf and the vial, but, at the same time, it is supplied to the vial side by air conduction and convection, thus creating a relatively large temperature gradient within the solution. The contribution of gas conduction has been estimated to be around 90% in the batch configuration, whereas radiation accounted for 5% and shelf/vial contact only for 4%, see Chapter 5. As concerns drying stage, the heat transferred in conventional freeze-drying varies significantly according to the position of the vial within the batch, and vials at the edge of the batch receive more heat than those located in the center (side-vial effect). These differences in heat transferred leads not only to remarkable differences, in terms of drying time among the vials, but is also a problem during the scale-up of a cycle or when there is a lack of control of the cycles.

In the case of the suspended-vial configuration, heat is supplied by radiation from the temperature-controlled surfaces, gas conduction and convection. Similarly to batch, convection plays a role only during freezing. On the other hand, gas conduction can play a role both in freezing and drying, but in the rarefied condition such as that occurs during drying, according to Smoluchowski, gas conduction depends on both vial-to-shelf clearance and chamber pressure. In the case of suspended-vial configuration, gas conduction and convection accounted for 60 to 75 % over a vial-to-shelf clearance of 3 to 10 mm range; the other contribution was related to radiation. The experimental results showed in Chapter 4 suggest that the average heat power removed from the product and, consequently, the temperature profiles were not dependent on the vial-to-shelf clearance, at least over the 3-28 mm range. Continuous freezing allows the cooling rate to be modulated by changing the temperature of the cryogenic gas and its velocity, and, finally, produce products with a different product structure. As concerns drying stage, Chapter 4 shows that, using suspended-vial configuration, vials are subject to identical conditions and the variations in heat power between vials of the same lot are modest. The experimental results suggest that the clearance between the shelf and the vial bottom does not influence significantly the heat supplied to the product. These results have been confirmed by the modeling simulations presented in Chapter 6 which state that gas conduction accounts for about 5% with a shelf-to-vial clearance of 10 mm and a chamber pressure of 10 Pa, but this value falls dramatically at lower pressures or higher shelf-to-vial clearance. Contrary to batch freeze-drying, as gas conduction is almost negligible in our configuration, heat transfer is essentially independent of chamber pressure and can be lowered much more than in the batch to increase mass transfer, without affecting the heat transferred.

5. Is continuous freeze-drying of suspended-vial able to reduce the vial-to-vial variability of product structure? Is it able to design products with specific characteristics?

The control of product quality is one of the most challenging requests in the production of pharmaceutical products, and, since many years, regulatory authorities are pushing in the direction of more reliable and safe processes which are able to manage product quality and variability.

For lyophilized product, product structure is one of these fundamental characteristics that one would control and design. From this point of view, batch freeze-drying has poor or no control of product structure. Of course, different freezing protocols can be used to increase or decrease pore diameter, and some protocols, such as annealing, can be used to slightly reduce vial-to-vial variability. For many years, it was well

understood that product structure has a fundamental impact not only on process performances but also on the activity of many APIs. Since then, many techniques have been introduced to control product structuring by controlling nucleation; many of them are presented in Chapter 2. The main drawbacks of these technologies are that, although they work quite well in the laboratory scales, they are not perfectly scalable at the industrial scale. Many vendors declare that their equipment is able to perform controlled nucleation in GMP conditions also in the industrial apparatus, but from the best knowledge of this author, there are no published data on the failure of this technique at a such a scale. In fact, the risk of using this technique at such a large scale is that the process conditions are different enough within the chamber so that nucleation might not be induced in a significant number of sample. From the direct experience of this author in performing VISF, there is a significant improvement in terms of duration, efficacy and failures (blow-up, missed nucleation, detachment of the frozen cake from the vial bottom) when controlled nucleation is performed in a small pilot lyophilizer, such as Martin Christ Epsilon 2-6D LSCplus, instead of using a medium-size lyophilizer, such as Telstar LyoBeta 25. The continuous technology proposed in this thesis overcome these drawbacks as the control of nucleation is performed for an individual or small group of vials, within a small chamber. Vials can be accepted or rejected before entering the drying modules.

As a first step, we have explored the possibility of using spontaneous nucleation coupled to the suspended-vial configuration. As shown in Chapter 4, suspended-vial configuration led to a product structure with larger pores that decreases the resistance to vapor flow during primary drying. In Chapter 5, we have developed a multi-step procedure to evaluate the impact of freezing protocols on product structure. As concerns nucleation temperature, batch and suspended-vial configuration did not show significant differences, but we have seen important differences in terms of the product structure. In the case of suspended-vial freezing, the mean pore diameter ranged from 80 to 100 μm, whereas it ranged from 28 to 45 μm for conventional freezing. As expected, for both conventional and suspended-vial freezing, the higher the nucleation temperature was, the larger the ice crystals, and, thus, the pores within the dried product. We have also seen a sharp reduction of the vial-to-vial variability of mean pore diameter.

Although suspended-vial configuration seemed to reduce vial-to-vial variability, continuous technology requires to produce products with a much narrow variability. For this purpose, we have used VISF for controlling nucleation. In this case, products nucleated at the same temperature and had the same thermal history. Using VISF, pores size is much bigger, and the resistance to vapor flow decreased dramatically. As the control of product structure is a key feature of this continuous technology, we looked inside the dried products using X-ray microtomography, obtaining a surprisingly detailed reconstruction of the product structures. For example, it was possible to observe the typical crust formed at the upper product surface when VISF is used to induce nucleation. But it was also possible to observe micro-collapse in an amorphous product lyophilized at a temperature close to the glass transition temperature. CFD simulations and other computational techniques were used to estimate important structural parameters of the products, such as pore diameter, and permeability. It is the opinion of this author that X-ray microtomography may be a useful technique for better understand the relation between freezing conditions and product structure, but also for monitoring product quality.

As already mentioned, the continuous technology is also designed to process particle-based material. For this reason, Chapter 8 studies the impact of different particle size distributions on the drying behavior of microparticles in vials. A multi-scale approach was used, which consists of generating realistic random packings, estimating the properties of packings through CFD simulations at the pore-scale and finally using these properties to simulate the freeze-drying process at the macro-scale.

6. Is continuous freeze-drying of suspended-vial able to reduce drying time and the variability of sublimation rates? Is also able to reduce variability in final residual moisture?

In Chapter 4, different scenarios have been taken into account, i.e., batch vs suspended-vial configuration, spontaneous nucleation vs VISF; these tests have been done using both crystalline and amorphous excipients, i.e., mannitol and sucrose. We have seen that for mannitol 5% (uncontrolled nucleation, filling volume of 3 ml), the drying duration decreased from 22 h obtained using obtained batch system to 9 h with the suspended-vial configuration; these tests were done at a constant maximum product temperature of 257 K. Using VISF coupled to suspended vial-configuration, drying duration felt down to 7 h. Similar results were obtained at a constant maximum product temperature of 247 K; in this case, the duration of the batch configuration and uncontrolled nucleation was 30 h, batch configuration and controlled nucleation 18 h, and suspended-vial configuration and controlled nucleation only 9 h. In the last example, batch cycles were optimized using the LyoDriver control system.

In the case of sucrose-based products (filling volume of 2 ml), at a constant target temperature of 240 K, the duration of the primary drying using the batch configuration and spontaneous nucleation was 18 h, suspended-vial configuration and spontaneous nucleation was 9 h, whereas controlling nucleation drying duration felt down to 6 h.

The experimental tests showed that the onset/offset time was always dramatically reduced in the case of suspended-vial configuration, and further reduced when VISF is applied. This is certainly due to two factors, i.e., uniformity in the heat transferred to the product in the case of suspended-vial configuration, but also the uniformity of product structure, especially when VISF is applied. To better understand the role of the non-uniformity of the batch configuration, Chapter 6 uses a mathematical model to simulate the behavior of an entire batch cycle or the equivalent continuous one, by taking into account the variability of the process parameters (heat transfer and product structure). These results state that the variability in the sublimation rate is more pronounced than suggested by the indirect experimental measurements.

As shown in Chapter 4, the suspended-vial configuration was able to dramatically reduce the vial-to-vial variability of residual moisture, but also to reduce secondary drying time. The reduction of vial-to-vial variability is due to the uniformity in the heat transferred to the product in the case of the suspended-vial configuration but also to the uniformity of product structure when VISF is applied.

These results regarding the reduction of drying duration in the case of suspended-vial configuration are somewhat counterintuitive. In fact, the desorption rate depends on the specific surface area of the dried matrix, and, in particular, it increases as the pore size decreases. This should be disadvantages for the samples produced using VISF and, as shown by other authors, extend the secondary drying duration of about 20-40%. The sharp reduction of the secondary drying duration in the case of suspended-vial configuration was due to the fact that the heating surfaces entirely irra-

diated the vials, increasing the temperature of the dried matrix and, finally, promoting desorption already during primary drying. Contrary, in the batch configuration, chamber walls partially irradiate only side vials and not central ones. The simulations in Chapter 6 confirmed that in the case of suspended-vial configuration, the temperature of the dried layer in the product being dried is much higher than in the case of central vials in the batch.

7. Is continuous freeze-drying of suspended-vial beneficial for sensitive APIs?

The activity recovery of LDH after freezing and freeze-drying was studied for different formulations, i.e., sucrose 5%, trehalose 5%, sucrose/trehalose 2.5/2.5% and, finally, without excipients. Three different configurations were compared, i.e., (i) conventional shelf-ramped freezing followed by conventional batch drying, (ii) suspended-vial freezing and drying, (iii) suspended-vial VISF (T_n=268 K) and drying. The suspended-vial VISF followed by drying presented the higher value of recovery activity no matter which was the formulation. The higher activity recovery showed by using the suspended-vial configuration was due to the reduced specific surface area. In fact, the suspended-vial configuration was able to increase ice crystals dimension (and so, reduce the specific surface area), which it is much more evident when VISF is used for controlling nucleation. Since LDH, like many other proteins, can be denatured at the ice/freeze-concentrate interface, lowering the specific surface area by using suspended-vial configuration mitigated the activity loss. Moreover, since VISF allows perfect control of nucleation and, finally, of the specific surface area, it can possibly reduce the variability in the recovery activity within the production.

8. Can continuous freeze-drying of suspended-vial respond to the request of flexibility and modularity of the pharmaceutical industry? Is it possible to reduce the footprint and increase the throughput?

This method draws its strength from producing very uniform products, with the same characteristics because they undergo the same process conditions. It is extremely flexible because it can also treat particle-based materials in vials, and it does not have a limitation in the shape of vessels. Besides, scale-up simply consists of adding parallel modules.

Our results suggested that the cycle duration is shortened by 2 to 4 times, including the elimination of dead times. This sharp reduction in processing time has a strong impact also on the dimension of the continuous lyophilizer. At constant productivity, the total volume of the modules in the case of continuous apparatus is reduced of about 4-6 times with respect to batch apparatus. The energetic costs do not seem dramatically influenced by the continuous process, although the revenues can increase dramatically because of the higher throughput generating by using continuous freeze-drying. There are further aspects which are difficult to monetize, such as the perfect control of the process and product quality. Product quality will be the challenge that the the pharmaceutical industry has to be addressed in the next years to respond to the more stringent quality requirements set by regulatory authorities.

Conclusions and future perspectives
This thesis has been dedicated to exploring the possibility of moving from the well-known long-used batch freeze-drying to a continuous process. The technology here proposed was designed with these characteristics in mind: (i) produce final products

in the dosage form identical to that already in the market; (ii) control of product quality, increase standardization and decrease variability; (iii) increase throughput and eliminate batch drawbacks.

Experiments and simulations have been used to demonstrate the feasibility of this new concept and its advantages, and try to answer the many questions that came up from lyophilization professionals. This thesis gives, at this point, a general picture of the process and the expectation from the realization of a prototype. Of course, many technical issues are expected especially in the realization of reliable components for the load-lock systems and the nucleation chamber. A further aspect that needs a deep understanding is to guarantee the sterility in the modules so that the process can be conducted in GMP conditions.

It is the opinion of this author that continuous freeze-drying will be increasingly important parallel to the realization of new upstream continuous processes. This is a long-term goal in the pharmaceutical industry and will be the result of the development of all the pieces of a complicated puzzle that includes equipment, control strategies, reaction pathways, but also production organization, storage, and transport systems, regulations, knowledge updating.

Appendices and supplemental materials

A

Freezing of pharmaceutical solutions: simulation set-up

A.1   Computational set-up

Comsol Multiphysics 5.0 (*Heat Transfer in Solids* module) was used to solve the heat balance equations for the liquid being frozen and the vial glass wall. The liquid being frozen has meshed with a mapped grid constituted from 600 to 2600 cells whereas the vial glass was with a triangular unstructured triangular grid constituted from 300 to 3500 cells (see Figure A.1); usually, the coarser mesh was sufficient to reach the grid-independency of the solution. The direct solver PARDISO based on the LU decomposition was used; the implicit time-depended solver BDF (Backward Differentiation Formula) was used with an order of accuracy from 1 to 3, with a conservative step solver and a relative tolerance of 0.01. The values of temperature were acquired by placing probes every 1 mm along with the product height.
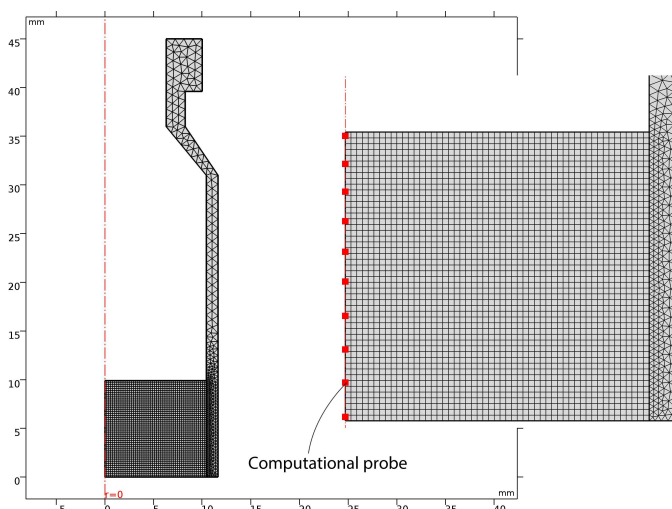
Figure A.1   Computational domain used

A.2 Determination of model parameters

A.2.1 Convective heat transfer coefficient

The model presented in Section 5.2.1 was preliminarily tuned and validate against experiments performed in the lyophilizer LyoBeta 25 (Azbil-Telstar, Terrassa, Spain). Tubing vials (10R 24.0 x 45.0, Nuova Ompi, Piombino Dese, Italy) were used, having the geometric characteristics shown in Table A.1; vials were filled in with 6 ml of distilled water.

Table A.1 Geometric characteristics of the vial 10 R.

External diameter	24 mm
Internal diameter	20 mm
Height	45 mm
Side glass thichness	1.0 mm
Bottom glass thichness	1.1 mm

T-type thermocouples were placed in different position in different positions in the drying chamber: TC1-TC2 within two vials to monitor water temperature during freezing, TC3-TC4 to the walls of the drying chamber, TC5-TC6 were used to monitor air temperature within the chamber (TC6 was shielded to partially protect it from the radiative heat from chamber walls and the surrounding. The convective heat transport coefficient related to the side surface of the vials was calculated using the readings of the thermocouples shown in Figure A.2. Gr was estimated to range from 60,000 to 130,000 (ΔT ranges from 5 to 10 K), Pr was about 0.69, and so, Nu ranges from 8.6 to 10.2. The heat transfer coefficient due to natural convection was then estimated to be 4-6 $\mathrm{W\,m^{-2}\,K^{-1}}$.
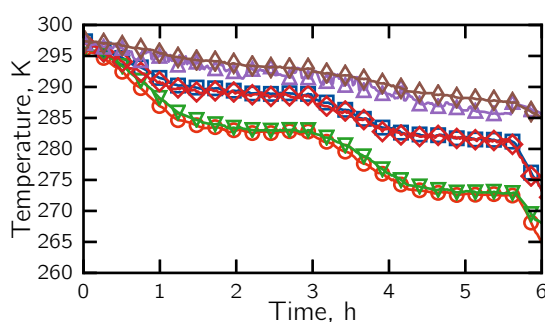
Figure A.2 Evolution of temperature for (TC1 ○, TC2 ▽) the liquid being frozen, (TC3 △, TC4 ◇)chamber side-walls, (TC5 □, TC6 ◇) the gas inside the drying chamber with and without shielding.

A.2.2 Modeling validation of the cooling phase

Once the heat transfer parameters were determined, the ability of the model to predict the product temperature during the cooling phase was tested for two cycles at different cooling rates, i.e., (a) 0.8 K/min and (b) 0.2 K/min. The results are shown in Figure A.3a-b.
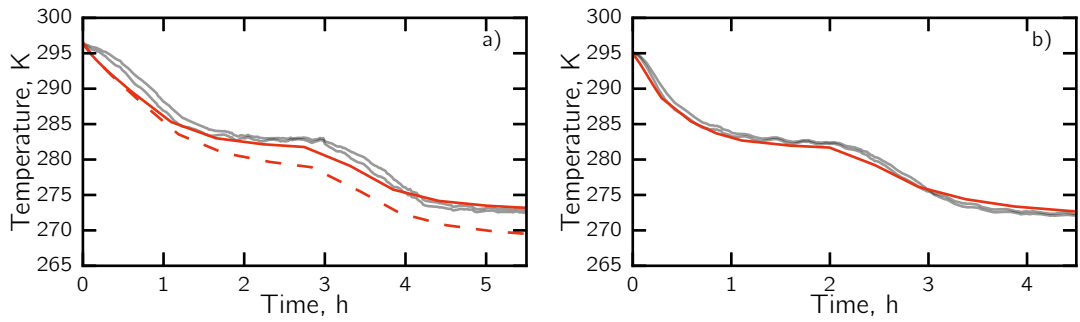
Figure A.3 Evolution of temperature for the liquid being cooled down using a cooling rate of (a) 0.8 K/min and (b) 0.2 K/min. (——) refers to the thermocouples readings and (——) simulation outcomes; (- - -) refers to the simulation outcomes when air convection is neglected.

A.2.3 Modeling validation of the freezing phase

The nucleation exothermicity profile is due to the heat released during the phase change from liquid to solid. The nucleation and growth terms were described by Eq. 5.2 ($\dot{Q}_n$) and 5.3 ($\dot{Q}_c$); the last term is included in the apparent specific heat capacity c_p^* defined by Lunardini (1981) (Eq. 5.5). The model requires two parameters, the nucleation rate constant k_n and the temperature extension of the mushy zone ΔT. In this work, the value of k_n and ΔT where those obtained experimentally by Nakagawa et al. (2007): $k_n = 430 \, \text{kg m}^{-3}\text{s}^{-1}\text{K}^{-1}$ and $\Delta T = 0.98 K$.

The model depictures the liquid being frozen into three zones, i.e., liquid, mushy and solid zone. The properties of the mushy zone depend on the ice crystal fraction that in turn, in this model, depends linearly on temperature, see Figure A.4.
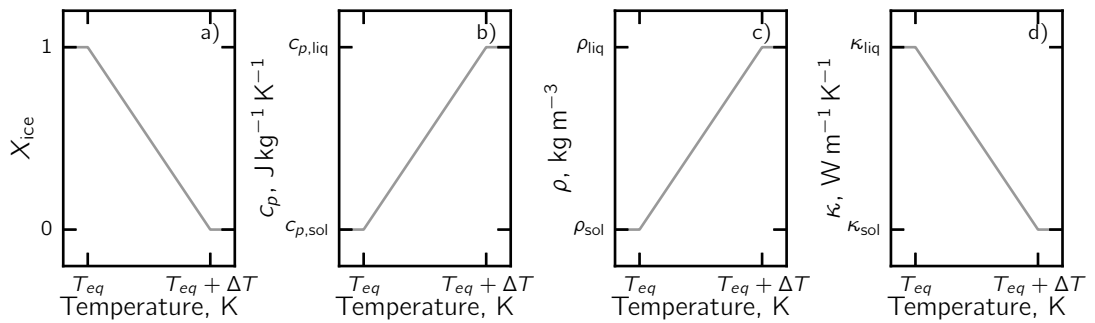
Figure A.4 Temperature dependence of (a) ice crystal fraction, (b) specific heat, (c) density and (d) thermal conductivity.

The physical properties of the liquid, solid zones, and of the vial glass are reported in Table A.2.

The ability of the model to predict the product temperature during the freezing was tested for two cycles at different cooling rates, i.e., (a) 0.8 K/min (vial 10R, 3 ml, 5% mannitol) and (b) 0.3 K/min (vial 10R, 3 ml, 5% sucrose). Simulation outcomes and experimental data are shown in Figure A.5.

Table A.2 Values of physical properties and parameters.

Parameter	Value	Unit
ρ_{sol}	920	$\mathrm{kg\,m^{-3}}$
ρ_{liq}	1000	$\mathrm{kg\,m^{-3}}$
ρ_{gl}	2600	$\mathrm{kg\,m^{-3}}$
κ_{sol}	2.56	$\mathrm{W\,m^{-1}\,k^{-1}}$
κ_{liq}	0.6	$\mathrm{W\,m^{-1}\,k^{-1}}$
κ_{gl}	1.0014	$\mathrm{W\,m^{-1}\,k^{-1}}$
$c_{p,sol}$	2100	$\mathrm{J\,kg^{-1}\,k^{-1}}$
$c_{p,liq}$	4186	$\mathrm{J\,kg^{-1}\,k^{-1}}$
$c_{p,gl}$	840	$\mathrm{J\,kg^{-1}\,k^{-1}}$
M_w	18	$\mathrm{kg\,kmol^{-1}}$
ΔH_f	333.5	$\mathrm{kJ\,kg^{-1}}$
ΔH_e	2500	$\mathrm{kJ\,kg^{-1}}$
R_g	8.314	$\mathrm{J\,kmol^{-1}\,K^{-1}}$
σ_{SB}	5.67×10^{-8}	$\mathrm{W\,m^{-2}\,K^{-4}}$
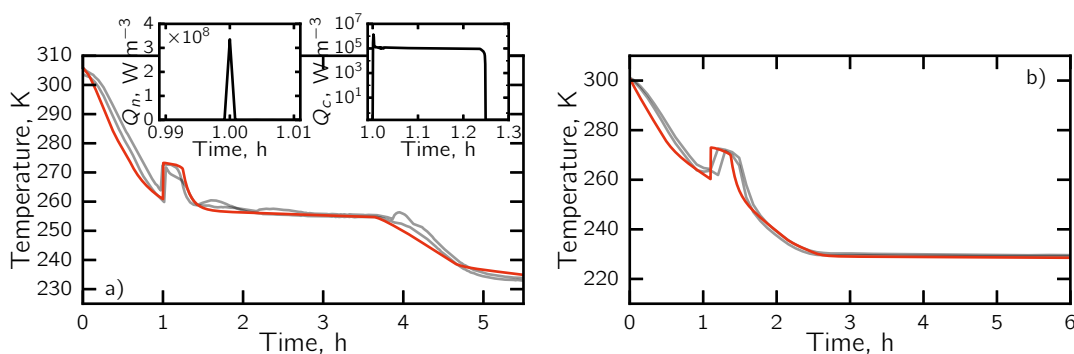
Figure A.5 Evolution of temperature for the liquid being cooled down using a cooling rate of (a) 5% mannitol cooled down at 0.8 K/min and (b) 5% sucrose cooled down at 0.2 K/min. (——) refers to the thermocouples readings and (——) simulation outcomes. The inserts refer respectively to the value of $\dot{Q}_n$ and $\dot{Q}_c$.

A.2.4 Prediction of product structure

The mathematical model developed in Comsol only gives product temperature evolution in time and space. The crystal size model requires two parameters, i.e., the freezing front rate ν and temperature gradient in the frozen zone λ.

Figure A.6 shows the procedure to calculate ν and λ from the temperature outcomes of a simulation. The first step requires the determination of the freezing front evolution. As shown in Figure A.6a, freezing front evolution is obtained by determining the time t_z^* at which product temperature at a certain z coordinate reaches the equilibrium freezing temperature. The freezing front position as a function of time is determined by collecting the t_z^* along with the product height, see Figure A.6b. The freezing front rate ν is the first derivative of the curve in Figure Xb, here approximated to the ratio between Δz and Δt_z^*. Moreover, at each t_z^* it is possible to collect the temperature profile along with the product height (see Figure A.6c), and finally, determine

the temperature gradient in the frozen zone λ. An example of the calculation of the mean pore diameter is shown in Figure A.7.
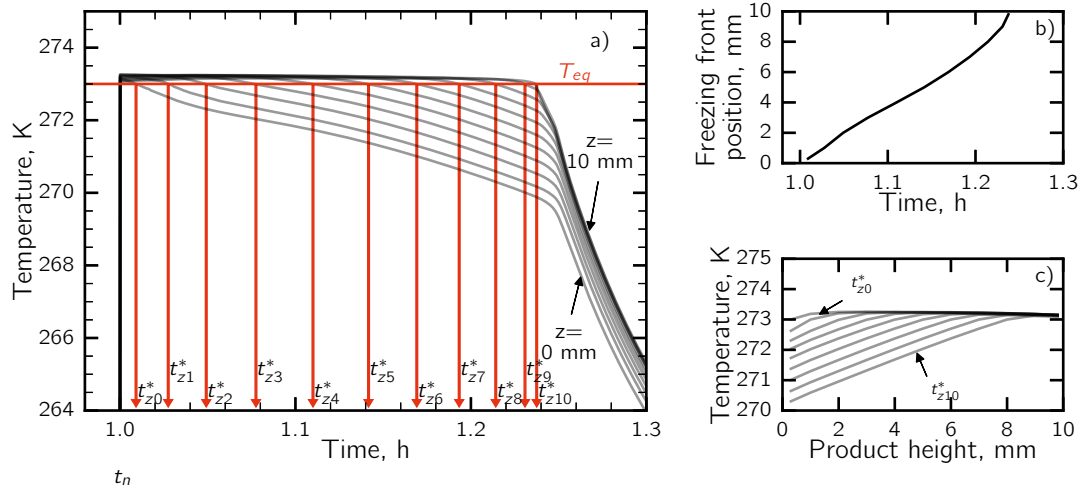
Figure A.6 (a) Temperature profile of the probes placed every 1 mm along the product height and estimation of freezing front position. (b) Freezing front position as a function of time. (c) Temperature profile along product height at heat time t_z^*. Data refer to 5% mannitol (cooling rate of 0.8 K/min, batch configuration).
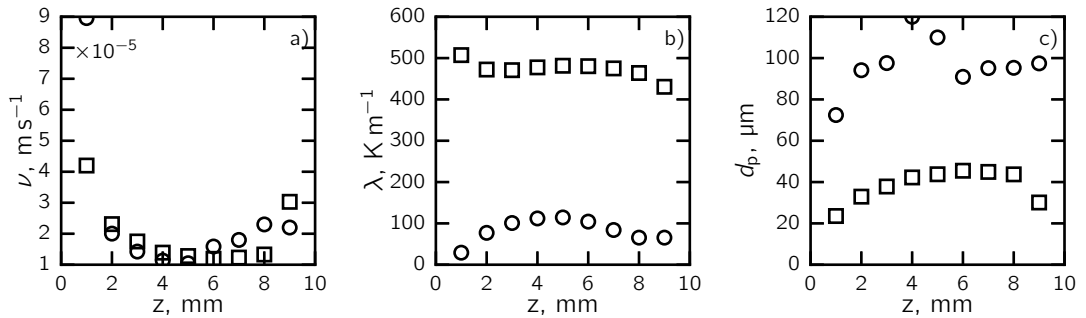
Figure A.7 (a) Freezing front rate ν, (b) temperature gradient λ and (c) the corresponding pore diameter in the case of ($\square$) batch and ($\bigcirc$) suspended-vial configuration ($T_\mathrm{n} = -13\,°C$).

List of symbols

c_p	specific heat capacity, $J\,kg^{-1}\,K^{-1}$
c_p^*	apparent specific heat capacity, $J\,kg^{-1.K^{-1}}$
ΔH_e	enthalpy of evaporation, $J\,kg^{-1}$
ΔH_f	latent heat of crystallization, $J\,kg^{-1}$
k_n	rate constant of nucleation, $kg\,s^{-1}\,m^{-3}\,K^{-1}$
M_w	molecular weight of water, $kg\,kmol^{-1}$
$\dot{Q}_c$	heat of crystallization, $W\,m^{-3}$
$\dot{Q}_n$	heat of nucleation, $W\,m^{-3}$
T_{eq}	equilibrium freezing temperature, K
t_n	nucleation time, s

Greek letters

ν	freezing front rate, $m\,s^{-1}$
ρ	density, $kg\,m^{-3}$
σ_SB	Stefan–Boltz constant, $W\,m^{-2}\,K^{-4}$

Subscript

gl	vial glass
liq	liquid
sol	solid

191

Adimensional numbers

Gr   Grashof number

Nu   Nusselt number

Pr   Prandtl number

References

Lunardini, V. J. (1981). *Heat Transfer in Cold Climates*. New York, USA: Van Nostrand Reinhold Company.

Nakagawa, K., Hottot, A., Vessot, S., and Andrieu, J. (2007). Modeling of freezing step during freeze-drying of drugs in vials. *AIChE Journal* 53 (5), pp. 1362–1372.

B

Introduction to transport phenomena in lyophilization

B.1 Mass transport in vacuum conditions

In standard conditions, in a volume of 1 mm^3, there are about 2.43×10^{16} molecules of a gas, and each molecule collides 10^9 times in one second, traveling for 5×10^{-8} m between two collisions. The enormous number of degrees of freedom that describes such a system requires to move to a different approach which considers differential volumes sufficiently extended to consider the gas as a continuum medium. Continuum regime is, so, the result of the average behavior of the enormous number of particles. On the other hand, for rarefied gas, the number of molecules and collisions decrease dramatically, so that the continuum hypothesis is not valid anymore.

Knudsen number is the adimensional number that determines whether statistical mechanics or the continuum mechanics formulation of fluid dynamics should be used to model a system,

$$\text{Kn} = \frac{\lambda}{l}, \text{ where } \lambda = \frac{k_B T_{\text{gas}}}{\sqrt{2}\pi p d^2} \tag{B.1}$$

where λ is the mean free path and l is the representative physical length scale of the system.

Kn can be used to classify the flow into various regimes, see Figure B.1. For Kn < 0.01, the flow is classified as *continuum flow*, and the Navier-Stokes equations are used to describe it. For $0.01 < \text{Kn} < 0.1$, the flow is known as *slip flow*, and slip velocity boundary conditions have to be accounted for solving the Navier-Stokes equations. When $0.1 < \text{Kn} < 10$, the flow is in the *transition regime*, where molecule-molecule and wall-molecule collisions are equally important. For Kn > 10, the flow is in *free-molecular* (or Knudsen) regimes, and only wall-molecule collisions are statistically relevant (Rathakrishnan, 2013).

During freeze-drying, ice sublimates and water vapor moves from the sublimation interface to the condenser. In its movement, water vapor passes through the porous
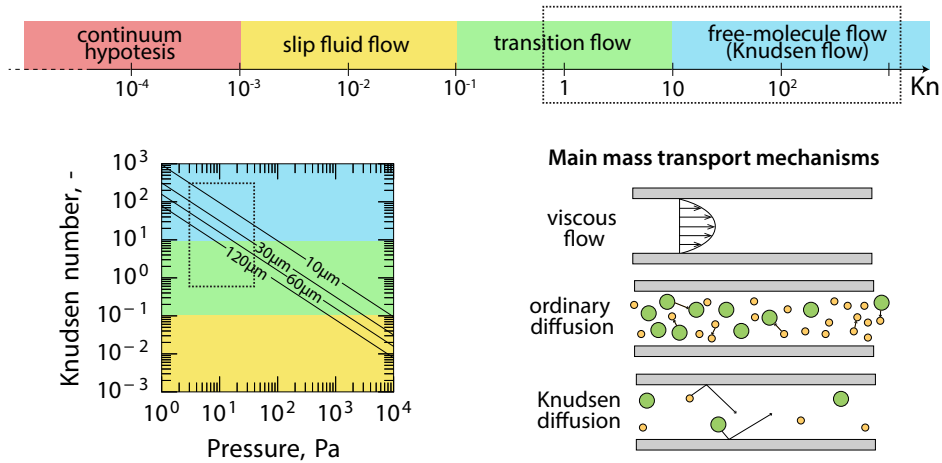
Figure B.1 Transport regimes related to Knudsen number and main mass transport mechanism under vacuum.

cake formed by the part of the product that has been already dried. This porous cake has pores in the micron range so that the flow regime is in the transition or in fully Knudsen regimes, see the plot in Figure B.1.

B.1.1 Mechanism of mass transfer

The main mechanisms of mass transport in porous media that interest freeze-drying are the following,

- Viscous flow: dominated by molecule-molecule collisions, it is due to the total pressure gradient.

- Diffusive flow: dominated by molecule-molecule collisions due to concentration gradients, temperature gradients, or external forces;

- Knudsen flow: dominated by molecule-wall collisions; predominant when the mean-free path of the molecular species is much larger than the pore diameter.

Viscous flow

Viscous flow involves the movement of a gas, in the continuum regime, caused by a pressure gradient. In the context of mass transport of gas under vacuum conditions, viscous flow refers to creeping flow, as inertial terms and turbulence are not included (Cunningham and Williams, 1980). Viscous flow is nonseparative because the gas mixture behaves as a single gas, and follows Darcy's law,

$$\mathbf{N}^{V} = -\frac{B_0}{\mu}\frac{p}{R_{\mathrm{g}}T}\boldsymbol{\nabla}p, \qquad \mathbf{N}_i^{V} = y_i\mathbf{N}^{V} \tag{B.2}$$

where B_0 is the permeability coefficient and strictly depends on the geometry of the system and μ is the coefficient of viscosity.

The permeability coefficient of a porous medium having porosity ε and tortuosity τ can obtained by integrating Poiseuille's law,

$$B_0 = \frac{\varepsilon}{\tau^2} \frac{d_P^2}{32} \tag{B.3}$$

where d_P is the average diameter of the pores.

Diffusive flow

Diffusive flow occurs because of various driving forces. Ordinary diffusion is due to the concentration gradients of species. Barodiffusion is due to total pressure gradients and is the tendency of lighter elements to migrate down a pressure gradient; this mechanism requires a high-pressure gradient as that happens in the centrifugation process. Thermodiffusion is due to temperature gradients, but it is relevant only if gradients are higher than 200 °C. External force, i.g., electric or magnetic forces, can also cause diffusion, usually called forced diffusion. The total diffusive flow reads,

$$\mathbf{N}_i^D = \mathbf{N}_{y,i}^D + \mathbf{N}_{p,i}^D + \mathbf{N}_{T,i}^D + \mathbf{N}_{F,i}^D \tag{B.4}$$

The flow of a mixture of ν species can be described by mean of the generalized Stefan-Maxwell equation (Taylor and Krishna, 1993),

$$\mathbf{d}_i = \sum_{j=1}^{\nu} \frac{y_j \mathbf{N}_i^D - y_i \mathbf{N}_i^D}{c \mathcal{D}_{ij}} \tag{B.5}$$

where $\mathbf{d}_i$ is the total driving force,

$$\mathbf{d}_i = -\boldsymbol{\nabla} y_i - \frac{y_i - \omega_i}{p} \boldsymbol{\nabla} p + \qquad \frac{1}{p}\left(c_i \mathbf{F}_i - \omega_i \sum_{i=1}^{n} c_i \mathbf{F}_i\right) \tag{B.6}$$

where $\boldsymbol{\nabla} y_i$ is the concentration gradient, $\boldsymbol{\nabla} p$ the barodiffusion force and $\mathbf{F}_i$ is a generic external force.

For an isothermal system without external forces applied, Stefan-Maxwell equation reads,

$$-\frac{p}{R_g T} \boldsymbol{\nabla} y_i = \sum_{\substack{j=1 \\ j \neq i}}^{\nu} \frac{y_j \mathbf{N}_{y,i}^D - y_i \mathbf{N}_{y,j}^D}{\mathcal{D}_{ij}} \tag{B.7}$$

For a porous medium having porosity ε and tortuosity τ, the diffusion coefficient can be written as follows,

$$D_{ij}^{eff} = \frac{\varepsilon}{\tau^2} \mathcal{D}_{ij} \tag{B.8}$$

Knudsen flow

Knudsen or free-molecular flow is the maim mass transport mechanism when the free mean path is longer than the scale length of the medium. In that case, molecule-molecule collisions are statistically irrelevant compared to wall-molecule collisions.

The species do not interact with each other and, finally, the flux of each species depends only on their own concentration gradient,

$$\mathbf{N}_{\text{Kn},i}^{\text{D}} = -\text{D}_i^{\text{Kn}} \boldsymbol{\nabla} c_i \tag{B.9}$$

where Knudsen diffusion coefficient is estimated from kinetic theory,

$$\text{D}_i^{\text{Kn}} = \frac{\varepsilon}{\tau^2} \frac{d_{\text{P}}}{3} \sqrt{\frac{8 R_g T}{\pi M_i}} \tag{B.10}$$

B.1.2   Dusty-gas model

Dusty-gas model (DGM) was formalized by Evans, Mason and their colleagues coupling convection and diffusion mechanism, including the effect of porous media (Evans III et al., 1961; Evans III et al., 1962; Mason et al., 1963; Mason and Malinauskas, 1964; Mason and Malinauskas, 1983).

Supposing that the species i is not accelerated on the average, the momentum transferred because of the collisions with the wall and the molecules of the other species have to be balanced by a force, which is ascribed to the gradient of partial pressure $\boldsymbol{\nabla} p_i$. This gradient can be considered as the sum of two contributions,

$$-\boldsymbol{\nabla} p_i \Big|_{\text{molecule}} = \frac{R_g T}{\text{D}_{ij}^{\text{eff}}} (\mathbf{N}_{y,i}^{\text{D}} - y_i \mathbf{N}^{\text{D}}) \tag{B.11}$$

$$-\boldsymbol{\nabla} p_i \Big|_{\text{wall}} = \frac{R_g T}{\text{D}_i^{\text{Kn}}} \mathbf{N}_{\text{Kn},i}^{\text{D}} \tag{B.12}$$

where Eq. B.11 is due to molecule-molecule collisions and Eq. B.12 to molecule-wall collisions. The total gradient of partial pressure of species i reads,

$$-\boldsymbol{\nabla} p_i = \frac{R_g T}{\text{D}_i^{\text{Kn}}} \mathbf{N}_i^{\text{D}} + \frac{R_g T}{\text{D}_{ij}^{\text{eff}}} (\mathbf{N}_i^{\text{D}} - y_i \mathbf{N}^{\text{D}}) \tag{B.13}$$

As shown in Figure B.2a, diffusive and viscous flow are parallel mechanisms, and the two flux can be summed up,

$$\mathbf{N}_i = \mathbf{N}_i^{\text{D}} + \mathbf{N}_i^{\text{V}} \tag{B.14}$$

DGM pictures the porous medium as a collection of large molecules (*dust molecules*), fixed and uniformly distributed in the space, and treats them as an extra component of the gas mixture. As shown in Figure B.2b, a gas mixture of ν components is described as a mixture of $\nu + 1$ components, i.e., the gas species and the dust molecules, and for all of them, the Chapman-Enskog kinetic theory is applied.

The dust molecules are (i) spherical and uniformly distributed in space ($\boldsymbol{\nabla} c_{\nu+1} = 0$), (ii) fixed so that $\mathbf{N}_{\nu+1} = 0$ (iii) much bigger than the other ν components so that $M_{\nu+1} \to \infty$.

The equation of DGM for an isothermal multicomponent system reads,

$$\frac{\mathbf{N}_i}{\text{D}_i^{\text{Kn}}} + \sum_{j=1}^{\nu} \frac{y_j \mathbf{N}_i - y_i \mathbf{N}_j}{\text{D}_{ij}^{\text{eff}}} = -\frac{1}{R_g T} \left(p \boldsymbol{\nabla} y_i + y_i \boldsymbol{\nabla} p + y_i \boldsymbol{\nabla} p \frac{p B_0}{\text{D}_i^{\text{Kn}} \mu} \right) \tag{B.15}$$
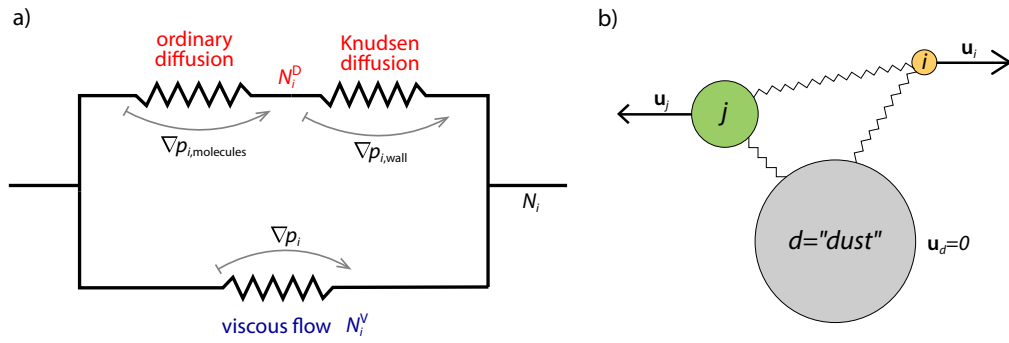
Figure B.2 Dusty-gas Model: (a) electrical analogy of the combined transport mechanisms, (b) representation of the pseudo mixture made of the i gas species and the fictitious "dust" species.

that, in the case of binary mixtures, is reduced to,

$$\mathbf{N}_i = -\frac{p}{R_g T} \left\{ D_i' \boldsymbol{\nabla} y_i + \left(D_i'' + \frac{B_0}{\mu} \right) y_i \boldsymbol{\nabla} p \right\} \qquad i = 1, 2 \tag{B.16}$$

where the coefficient D_i' depends only on concentration gradients,

$$D_i' = \frac{D_i^{Kn} D_{ij}^{eff}}{D_{ij}^{eff} + x_i D_j^{Kn} + x_j D_i^{Kn}} \qquad i = 1, 2 \tag{B.17}$$

and the coefficient D_i'' depends only on pressure gradients,

$$D_i'' = \frac{D_i^{Kn}(D_{ij}^{eff} + D_j^{Kn})}{(D_{ij}^{eff} + x_i D_j^{Kn} + x_j D_i^{Kn})p} \qquad i = 1, 2 \tag{B.18}$$

B.1.3 Tortuosity in flow and diffusion through porous media

Tortuosity is a concept widely used to characterize the structure of porous media, and it refers to the fact the flow does not pass through the medium following a straight path but a "tortuose" one. Although tortuosity appears a straightforward concert it is really not: many definitions of tortuosity are reported in the literature, based on geometric bases or the type of flow or transport process being studied (Ghanbarian et al., 2013).

Further important clarification has to be made when tortuosity is used in the parallel-capillary model. In literature, the concept of tortuosity ($\tau = L_e/L_z$) and tortuosity factor (τ^2) are often confused, leading to incorrect use of the parallel-capillary model (a schematic is shown in Figure B.3). As reported by Epstein (1989), this confusion is originated from the failure to distinguish the capillary velocity (L_e/t) and the interstitial axial velocity (L_z/t), and dates back to Kozeny (1927), then corrected by Carman (1956).

The parallel-capillary model depicts a porous medium as a block of material of volume AL_z and a number of non-interconnected cylindrical pores (n) of diameter d_P (total void volume equal to $n\pi d_P^2 L_e/4$). The porosity reads,

$$\varepsilon = \frac{n\pi d_P^2 L_e}{4AL_z} \tag{B.19}$$
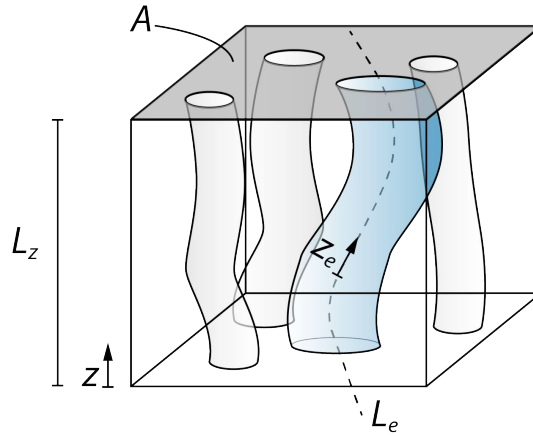
Figure B.3 Schematic of the parallel-capillary model for describing a porous medium.

The viscous flow is given by the Hagen-Poiseuille equation (on molar basis) applied to the n pores of length L_e,

$$\mathbf{N}^V = -\frac{n\pi d_P^4}{128\mu A}\frac{p}{R_g T}\frac{\partial P}{\partial z_e} \tag{B.20}$$

Making a change of variable from z_e to z, where $z_e = z(L_e/L_z)$, and using Eq. B.19, the viscous flow finally reads,

$$\mathbf{N}^V = -\varepsilon\frac{d_P^2}{32}\left(\frac{L_z}{L_e}\right)^2\frac{1}{\mu}\frac{p}{R_g T}\frac{\partial P}{\partial z} = -\frac{\varepsilon}{\tau^2}\frac{d_P^2}{32}\frac{1}{\mu}\frac{p}{R_g T}\frac{\partial P}{\partial z} \tag{B.21}$$

Similar arguments lead to the use of τ^2 in the diffusion coefficients.

B.1.4 Resistance to vapor flow

During primary drying, ice crystals in the product sublimate and the water vapor moves from the product to the condenser where it deposits. During this stage, vapor flow is impeded by three main resistance, i.e., (i) the dried layer of the product being dried, (ii) the stopper and (iii) and the chamber (Pikal, 1985).

The resistance to vapor flow is defined as the ratio between the driving force for mass transfer and the corresponding vapor flow,

$$R_{tot} = \frac{p_{w,int} - p_{w,cd}}{|\mathbf{N}_w|M_w} \tag{B.22}$$

where $p_{w,int}$ and $p_{w,cd}$ are the partial pressure at the sublimation interface and in the condenser chamber, and $\mathbf{N}_w$ the vapor flux from the product. The overall mass transfer resistance R_{tot} is defined as,

$$R_{tot} = R_p + R_{st} + R_{ch} \tag{B.23}$$

where R_p is the resistance due to the product, R_{st} of the vial stopper and R_{ch} of the chamber.

In the last few years, a number of publications has appeared concerning the role of the chamber and its related components on the drying process, revealing that the

chamber has a much more impact on mass transfer than thought in the past (Barresi et al., 2018; Marchisio et al., 2018; Barresi and Marchisio, 2018; Petitti et al., 2013; Rasetto et al., 2010). Although the resistance of the chamber and stopper cannot be neglected in the perspective of an optimal design of a lyophilizer, it is a common practice to consider their contribution negligible compared to the resistance of the product. In that case, $R_{tot} \approx R_p$,

$$R_{tot} \approx R_p = \frac{p_{w,int} - p_{w,c}}{|\mathbf{N}_w| M_w} \tag{B.24}$$

where $p_{w,int}$ and $p_{w,c}$ are the partial pressure at sublimation interface and in the chamber. R_p is usually expressed as a function of the mean pore diameter d_P, tortuosity τ and porosity ε (Rambhatla et al., 2004),

$$R_p = \frac{3}{2} \frac{\tau^2}{\varepsilon} \frac{L_d}{d_P} \sqrt{\frac{\pi R_g T}{2M_w}} \tag{B.25}$$

or by mean of the fitting parameters $R_{p,0}$, Γ_1 and Γ_2,

$$R_p = R_{p,0} + \frac{\Gamma_1 L_d}{1 + \Gamma_2 L_d} \tag{B.26}$$

B.2 Heat transport in vacuum conditions

B.2.1 Mechanism of heat transfer

The main mechanisms of heat transport during freeze-drying are the following,

- Conduction: heat transfer that occurs across a medium due to the molecular motion;

- Convection: heat transfer between a moving fluid and a surface;

- Radiation: electromagnetic mechanism of heat transfer consisting of the emission of thermal energy by a portion of matter at non-zero temperature.

B.2.2 Thermal conductivity of gases in the Knudsen regime

The thermal conductivity of an unconfined gas is independent of its pressure, whereas strongly depends on pressure if the gas is confined in small gaps (*Smoluchowski effect*).

The thermal conductivity of gases in rarefied conditions can be calculated according to the Kaganer model:

$$\kappa_{gas}^{Kn} = \frac{\kappa_{gas}^0}{1 + 2\beta^* \, Kn} \tag{B.27}$$

where κ_{gas}^0 is the thermal conductivity at atmospheric pressure, Kn is the adimensional Knudsen number and β^* is defined as follows:

$$\beta^* = \frac{2 - \alpha}{\alpha} \frac{2\gamma}{\gamma + 1} \frac{1}{Pr} \tag{B.28}$$

α is the so-called accommodation coefficient which takes into account the effectiveness in the energy transfer in the molecule-wall collision, γ is the heat capacity ratio and Pr is the adimensional Prandtl number. β is the temperature jump distance, derived from the Smoluchowsky's temperature jump condition applied to the Fourier's heat conduction equation (Springer, 1971):

$$T_{\text{gas}} - T_{\text{sol}} = \beta^* \frac{\partial T}{\partial z} \tag{B.29}$$

where T_{gas} and T_{sol} are the temperature of the gas and the solid surface respectively.

The thermal accommodation coefficient accounts for the effectiveness of the energy and momentum exchanged because of the interaction between the gas molecules and the solid surface. The accommodation coefficient can be calculated using the Baule formula (Baule, 1914) as modified by Goodman (Goodman, 1980):

$$\alpha = \frac{2.4\mu^*}{(1+\mu^*)^2} \tag{B.30}$$

where μ^* is the ratio of the gas to solid atomic masses.

The thermal conductivity calculated for water vapor at 250 K as a function of its pressure in confined gaps of different size is shown in Fig. B.4.
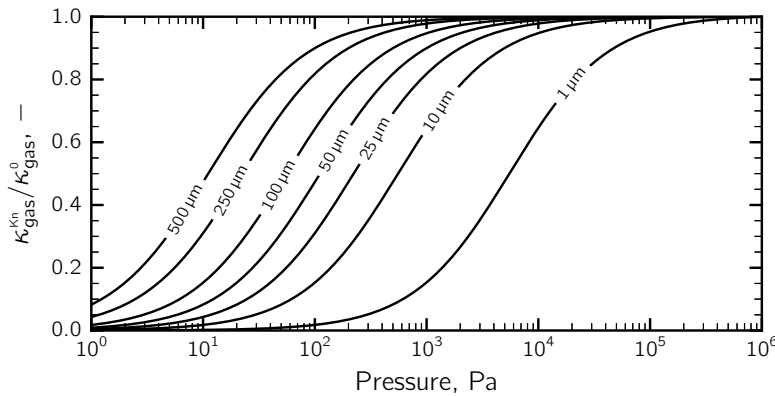
Figure B.4 $\kappa_{\text{gas}}^{\text{Kn}}$ to κ_{gas}^0 ratio as a function of pressure. Gap size is reported over the lines.

B.2.3 Heat transfer through a porous medium

The mathematical model at the macroscale describes the frozen and the dried product as pseudo-homogeneous media, which require the knowledge of effective properties.

The effective thermal conductivity can be depicted as a function of many heat transfer mechanisms (Wang et al., 2006; Carson et al., 2006):

$$\kappa_{\text{s,eff}} = f\left(\kappa_{\text{sol}}, \kappa_{\text{gas}}, \kappa_{\text{conv}}, \kappa_{\text{rad}}\right) \tag{B.31}$$

where κ_{sol} and κ_{gas} are respectively the thermal conductivity of the solid and gas, κ_{conv} is due to the convective contribution and κ_{rad} due to the scattering at interfaces and grain boundaries; these last two terms are considered negligible in the presented simulations.

Table B.1 shows the main models for estimating the effective thermal conductivity through a porous medium (Nield and Bejan, 2006).

Table B.1 Summary of the main models for estimating the effective thermal conductivity through a porous medium.

Model	Schematic	Effective thermal conductivity
Parallel model		$\kappa = \varphi_{\mathrm{sol}}\kappa_{\mathrm{sol}} + \varphi_{\mathrm{gas}}\kappa_{\mathrm{gas}}$
Maxwell-Eucken (continuous solid phase, dispersed gas phase)		$\kappa = \kappa_{\mathrm{sol}}\dfrac{2\kappa_{\mathrm{sol}} + \kappa_{\mathrm{gas}} - 2\varphi_{\mathrm{gas}}(\kappa_{\mathrm{sol}} - \kappa_{\mathrm{gas}})}{2\kappa_{\mathrm{sol}} + \kappa_{\mathrm{gas}} + \varphi_{\mathrm{gas}}(\kappa_{\mathrm{sol}} - \kappa_{\mathrm{gas}})}$
Effective Medium Theory model		$\varphi_{\mathrm{gas}}\dfrac{\kappa_{\mathrm{gas}} - \kappa}{\kappa_{\mathrm{gas}} + 2\kappa} + \varphi_{\mathrm{sol}}\dfrac{\kappa_{\mathrm{sol}} - \kappa}{\kappa_{\mathrm{sol}} + 2\kappa} = 0$
Maxwell-Eucken (continuous gas phase, dispersed solid phase)		$\kappa = \kappa_{\mathrm{gas}}\dfrac{2\kappa_{\mathrm{gas}} + \kappa_{s} - 2\varphi_{\mathrm{sol}}(\kappa_{\mathrm{gas}} - \kappa_{\mathrm{sol}})}{2\kappa_{\mathrm{gas}} + \kappa_{\mathrm{sol}} + \varphi_{\mathrm{sol}}(\kappa_{\mathrm{gas}} - \kappa_{\mathrm{sol}})}$
Series model		$\dfrac{1}{\kappa} = \dfrac{\varphi_{\mathrm{sol}}}{\kappa_{\mathrm{sol}}} + \dfrac{\varphi_{\mathrm{gas}}}{\kappa_{\mathrm{gas}}}$
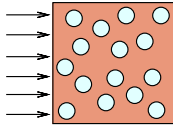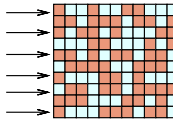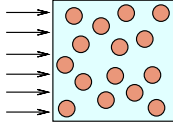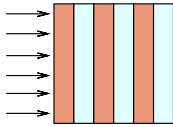
B.3 Thermodynamic and transport properties

B.3.1 Gas viscosity

Chapman-Enskog theory was used to estimate the gas viscosity (Poling et al., 2001),

$$\mu_i = 2.6693 \times 10^{-5}\frac{\sqrt{M_i T}}{d_i^2 \Omega_\mu} \tag{B.32}$$

where the collisional integral reads,

$$\Omega_\mu = \frac{1.16145}{T_*^{0.14874}} + \frac{0.52487}{\exp(0.77320 T_*)} + \frac{2.16178}{\exp(2.43787 T_*)}; \qquad T_* = \frac{k_{\mathrm{B}} T}{\varepsilon_i} \tag{B.33}$$

The formula of Wilke was used to extend the Chapman-Enskog theory to multi-component gas mixtures,

$$\mu_{\mathrm{gas}} = \sum_i \frac{y_i \mu_i}{\sum_j y_j \Psi_{ij}}; \qquad \Psi_{ij} = \frac{1}{\sqrt{8}}\left(1 + \frac{M_i}{M_j}\right)^{-1/2}\left[1 + \sqrt{\frac{\mu_i}{\mu_j}}\left(\frac{M_i}{M_j}\right)^{0.25}\right]^2 \tag{B.34}$$

where y_i is the molar fraction of the i-th component. Figure B.5a shows the gas viscosity μ_{gas} as a function of temperature.
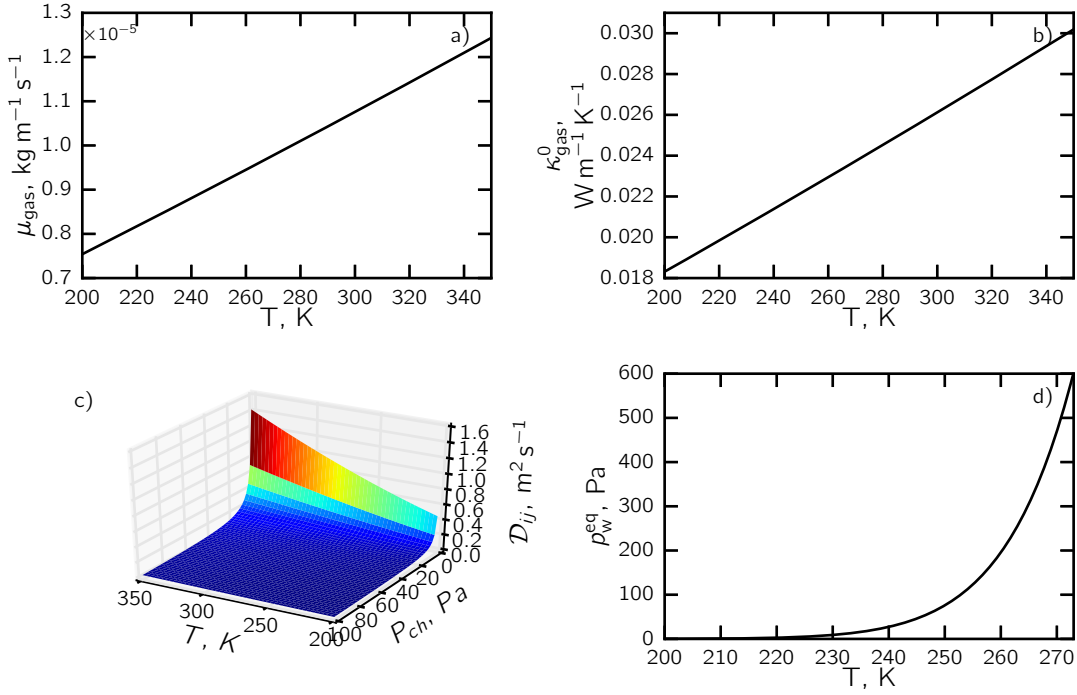
Figure B.5 (a) Gas viscosity, (b) thermal conductivity (c) diffusion coefficient for the binary gas mixtures and (d) saturation vapor pressure over ice.

B.3.2 Thermal conductivity

The thermal conductivity was estimated using the semiempirical method proposed by Eucken (Bird et al., 2007),

$$\kappa^0_{\text{gas}_i} = \left(c_{p,i} \frac{5}{4} \frac{R_g}{M_i} \right) \mu_i \tag{B.35}$$

The thermal conductivities for gas mixture was estimates as follows,

$$\kappa^0_{\text{gas}} = \sum_i \frac{x_i \kappa^0_{\text{gas}_j}}{\sum_j x_j \Psi_{ij}} \tag{B.36}$$

where Ψ_{ij} is identical to that appearing in the viscosity equation. Figure B.5b shows the thermal conductivities for gas mixture κ^0_{gas} as a function of temperature.

B.3.3 Diffusivity

The diffusion coefficient for the binary gas mixtures has been estimated as follows, (Poling et al., 2001)

$$\mathcal{D}_{ij} = \frac{0.00266 T^{3/2}}{p M_{ij}^{1/2} d_i^2 \Omega_D} \tag{B.37}$$

where $M_{ij} = 2[(1/M_i) + (1/M_j)]^{-1}$ and the diffusion collision integral reads,

$$\Omega_D = \frac{1.06036}{T_*^{0.1561}} + \frac{0.19300}{\exp(0.47635 T_*)} + \frac{1.03587}{\exp(1.52996 T_*)} + \frac{1.76474}{\exp(3.89411 T_*)} \tag{B.38}$$

Figure B.5c shows the diffusion coefficient for the binary gas mixture $\mathcal{D}_{ij}$ as a function of pressure and temperature.

B.3.4 Saturation vapor pressure over ice

The saturation vapor pressure over ice has been evaluated using the Goff-Gratch formula (List, 1951),

$$
\begin{aligned}
\log_{10} p_{\text{w}}^{\text{eq}}(T) = &-9.09718\left(\frac{273.15}{T} - 1\right) - 3.56654\log_{10}\left(\frac{273.15}{T}\right) + \\
&+ 0.876793\left(1 - \frac{T}{273.15}\right) + \log_{10} 6.1071
\end{aligned}
\tag{B.39}
$$

Figure B.5d shows the saturation vapor pressure over ice p_{w}^{eq} as a function of temperature.

Acronyms

DGM Dusty-Gas Model.

List of symbols

B_0 permeability coefficient, m^2

c_i molar concentration of the i-component, mol m^{-3}

d molecular diameter, m

D_i', D_i'' transport coefficients of DGM equation for molar flux of specie-i, m^2 s^{-1}

$\mathbf{d}_i$ generalized driving force, m^{-1}

d_i Lennard-Jones parameter, Å

$\mathcal{D}_{ij}$ binary diffusion coefficient, m^2 s^{-1}

D_{ij}^{eff} effective binary diffusion coefficient, m^2 s^{-1}

D_i^{Kn} Knudsen diffusion coefficient, m^2 s^{-1}

d_{P} pore diameter within the dried layer, m

$\mathbf{F}_i$ force acting per mole of species i, N mol^{-1}

k_{B} Boltzmann constant, m^2 kg s^{-2} K^{-1}

l representative physical length scale, m

L_{d} dried thickness, m

L_{e} Effective pore length, m

L_z REV size, m

M molecular weight, kg kmol^{-1}

N molar flux, mol m^{-2} s^{-1}

p total pressure, Pa

p_i partial pressure of the i-component, Pa

p_{w}^{eq} vapor equilibrium pressure, Pa

R ideal gas constant, J mol^{-1} K^{-1}

R_{ch} resistance of the chamber to vapor flow, m s^{-1}

R_{g} universal gas constant, J mol^{-1} K^{-1}

R_{p} resistance of the dried layer to vapor flow, m s^{-1}

R_{st} resistance of the vial stopper to vapor flow, m s^{-1}

T temperature, K

T_* dimensionless tempeture, -

T_{gas} gas temperature, K

y_i molar fraction of component i

Greek letters

α energy accommodation coefficient, -

β constant related to the restitution coefficient, -

γ heat capacity ratio, -

ε_i Lennard-Jones energy parameter, K

ε porosity, -

κ thermal conductivity, W m^{-1} K^{-1}

λ temperature gradient, k m^{-1}

μ viscosity of gas mixture, kg m^{-1} s^{-1}

μ^* ratio of the gas to solid atomic masses, -

τ tortuosity, -

Ω_D collision integral for diffusion, -

$\boldsymbol{\omega}_i$ angular velocity vector, rad s^{-1}

Ω_μ collision integral for viscosity, -

Subscript

c	chamber
cd	condenser
F	externa lforce
int	sublimation interface
p	barodiffusion
T	thermodiffusion
w	wall
y	ordinary diffusion

Superscript

D	diffusive
Kn	Knudsen
V	viscous

Adimensional numbers

Kn	Knudsen number
Pr	Prandtl number

References

Barresi, A. A. and Marchisio, D. L. (2018). Computational Fluid Dynamics data for improving freeze-dryers design. *Data in Brief*.

Barresi, A. A., Rasetto, V., and Marchisio, D. L. (2018). Use of computational fluid dynamics for improving freeze-dryers design and process understanding. Part 1: Modelling the lyophilisation chamber. *European Journal of Pharmaceutics and Biopharmaceutics* 129, pp. 30–44.

Baule, B. (1914). Theoretische Behandlung der Erscheinungen in verdünnten Gasen. *Annalen der Physik* 349 (9), pp. 145–176.

Bird, R. B., Stewart, W. E., and Lightfoot, E. N. (2007). *Transport phenomena*. John Wiley & Sons, New York.

Carman, P. C. (1956). *Flow of Gases through Porous Media*. London: Butterworths Scientific Publications.

Carson, J. K., Lovatt, S. J., Tanner, D. J., and Cleland, A. C. (2006). Predicting the effective thermal conductivity of unfrozen, porous foods. *Journal of Food Engineering* 75 (3), pp. 297–307.

Cunningham, R. E. and Williams, R. (1980). *Diffusion in gases and porous media*. Vol. 1. Buenos Aires: Springer.

Epstein, N. (1989). On tortuosity and the tortuosity factor in flow and diffusion through porous media. *Chemical engineering science* 44 (3), pp. 777–779.

Evans III, R., Watson, G., and Mason, E. (1961). Gaseous diffusion in porous media at uniform pressure. *The journal of chemical physics* 35 (6), pp. 2076–2083.

Evans III, R., Watson, G., and Mason, E. (1962). Gaseous diffusion in porous media. II. Effect of pressure gradients. *The Journal of Chemical Physics* 36 (7), pp. 1894–1902.

Ghanbarian, B., Hunt, A. G., Ewing, R. P., and Sahimi, M. (2013). Tortuosity in porous media: a critical review. *Soil science society of America journal* 77 (5), pp. 1461–1477.

Goodman, F. O. (1980). Thermal accommodation coefficients. *The Journal of Physical Chemistry* 84 (12), pp. 1431–1445.

Kozeny, J. (1927). Uber kapillare leitung der wasser in boden. *Royal Academy of Science, Vienna, Proc. Class I* 136, pp. 271–306.

List, R. J. (1951). Smithsonian meteorological tables. 114 (1), pp. 1–527.

Marchisio, D. L., Galan, M., and Barresi, A. A. (2018). Use of computational fluid dynamics for improving freeze-dryers design and process understanding. Part 2: Condenser duct and valve modelling. *European Journal of Pharmaceutics and Biopharmaceutics* 129, pp. 45–57.

Mason, E. and Malinauskas, A. (1964). Gaseous diffusion in porous media. IV. Thermal diffusion. *The Journal of Chemical Physics* 41 (12), pp. 3815–3819.

Mason, E., Evans III, R., and Watson, G. (1963). Gaseous diffusion in porous media. III. Thermal transpiration. *The Journal of Chemical Physics* 38 (8), pp. 1808–1826.

Mason, E. A. and Malinauskas, A. (1983). *Gas Transport in Porous Media: The Dusty-Gas Model*. Amsterdam: Elsevier, Amsterdam.

Nield, D. A. and Bejan, A. (2006). *Convection in Porous Media*. Vol. 3. New York: Springer.

Petitti, M., Barresi, A. A., and Marchisio, D. L. (2013). CFD modelling of condensers for freeze-drying processes. *Sadhana* 38 (6), pp. 1219–1239.

Pikal, M. (1985). Use of laboratory data in freeze drying process design: heat and mass transfer coefficients and the computer simulation of freeze drying. *PDA Journal of Pharmaceutical Science and Technology* 39 (3), pp. 115–139.

Poling, B. E., Prausnitz, J. M., O'connell, J. P., et al. (2001). *The properties of gases and liquids*. Vol. 5. Mcgraw-hill,New York.

Rambhatla, S., Ramot, R., Bhugra, C., and Pikal, M. J. (2004). Heat and mass transfer scale-up issues during freeze drying: II. Control and characterization of the degree of supercooling. *AAPS Pharmscitech* 5 (4), pp. 54–62.

Rasetto, V., Marchisio, D. L., Fissore, D., and Barresi, A. A. (2010). On the use of a dual-scale model to improve understanding of a pharmaceutical freeze-drying process. *Journal of Pharmaceutical Sciences* 99 (10), pp. 4337–4350.

Rathakrishnan, E. (2013). *Gas dynamics*. PHI Learning Pvt. Ltd.

Springer, G. S. (1971). Heat transfer in rarefied gases. In: *Advances in Heat Transfer*. Vol. 7. New York: Elsevier, pp. 163–218.

Taylor, R. and Krishna, R. (1993). *Multicomponent mass transfer*. Vol. 2. John Wiley & Sons.

Wang, J., Carson, J. K., North, M. F., and Cleland, D. J. (2006). A new approach to modelling the effective thermal conductivity of heterogeneous materials. *International Journal of Heat and Mass Transfer* 49 (17-18), pp. 3075–3083.

Freeze-drying in unit-doses: simulation set-up

C.1 View-factors calculation

The geometrical view factors between the heating sources, i.g., shelves and walls, have been estimated by using Comsol Multiphysics 5.1. The view factors are generally defined as follows,

$$f_{i \to j} = \frac{1}{A_i} \int_{A_i} \int_{A_j} \frac{\cos \phi_i \cos \phi_j}{\pi S_{ij}^2} \, \mathrm{d}A_i \mathrm{d}A_j \qquad (C.1)$$

where A_i and A_i are the area of the surface i and j, $\cos \phi_i$ (or $\cos \phi_i$) is are the angle between the surface normal $\hat{\mathbf{n}}_i$ (or $\hat{\mathbf{n}}_j$) and the line connecting and $\mathrm{d}A_i$ and $\mathrm{d}A_j$ (of length S_{ij}).

The radiative view factors are given as,

$$F_{i \to j} = \frac{1}{\dfrac{1 - \varepsilon_i}{A_i \varepsilon_i} + \dfrac{1}{A_i f_{i \to j}} + \dfrac{1 - \varepsilon_j}{A_j \varepsilon_j}} \qquad (C.2)$$

where ε_i (or ε_j) is the emissivity of surface i (or j) and A_i (or A_j) its surface area.

C.1.1 Batch lyophilizer

In the batch lyophilizer, vials can be arranged in hexagonal or square arrays over the shelves. In the case of the hexagonal arrangement, vials can be roughly divided into five different classes: center vials (C), corner vials (P) and three classes for side vials (L,M,N), see Figure C.1a. In the case of the square arrangement, vials can be divided into central vials (C), corner vials (P) and side vials (L), see Figure C.1b. The presence (or not) of a sideband was also taken into account.

Comsol 5.0 was used to estimate the following geometric view factors,
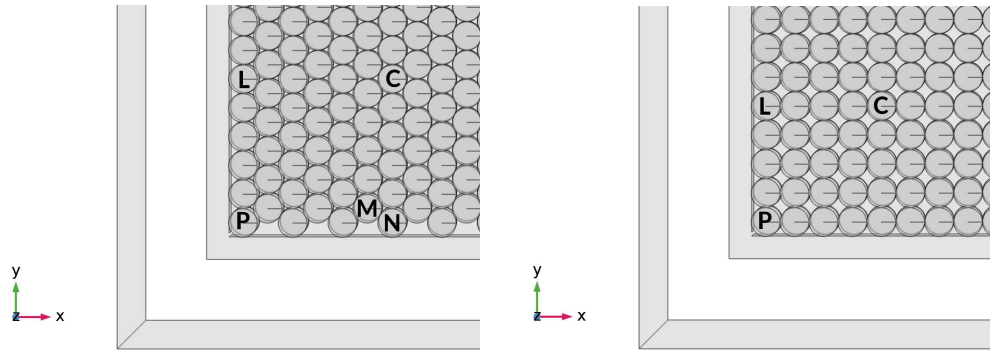
Figure C.1 Geometry used in Comsol 5.0 for calculating the view factors in the case of batch lyophilizer; (a) hexagonal and (b) square arrangement of vials.

- $f_{vs,sh}$, from upper and bottom shelves to vial side;

- $f_{vs,wall}$, from chamber walls to vial side;

- $f_{tp,sh}$, from upper and bottom shelves to product top surface;

- $f_{tp,wall}$, from chamber walls to product top surface;

- $f_{bp,sh}$, from side-band to vial side;

- $f_{bp,wall}$, from side-band to product top-surface.

Table C.1 shows the estimation of the geometric view factors in the case of a batch freeze-drier in which vials are arranged in hexagonal arrays, and Table C.2 in square arrays.

Table C.1 Geometric view factors in the case of a batch freeze-drier; vials in hexagonal configuration.

Vial position	$f_{vs,sh}$	$f_{vs,wall}$	$f_{tp,sh}$	$f_{tp,wall}$	$f_{bp,sh}$	$f_{bp,wall}$
Without band						
C	0.05187	0.00653	0.076728	0.06747	0.0000	0.0000
P	0.26012	0.37528	0.054830	0.57991	0.0000	0.0000
L	0.16190	0.20349	0.055248	0.38366	0.0000	0.0000
N	0.23260	0.25096	0.078639	0.39679	0.0000	0.0000
M	0.12114	0.11149	0.055105	0.33081	0.0000	0.0000
With band						
C	0.05187	0.005467	0.076728	0.056329	0.00098	0.01115
P	0.10199	0.031916	0.053423	0.099605	0.37486	0.53387
L	0.07782	0.010629	0.054139	0.080559	0.17742	0.34233
N	0.13932	0.016937	0.077547	0.092827	0.37817	0.32149
M	0.10512	0.010981	0.055105	0.147240	0.11677	0.19899

Table C.2 Geometric view factors in the case of a batch freeze-drier; vials in square configuration.

Vial position	$f_{vs,sh}$	$f_{vs,wall}$	$f_{tp,sh}$	$f_{tp,wall}$	$f_{bp,sh}$	$f_{bp,wall}$
Without band						
C	0.03488	0.019046	0.143480	0.11122	0.0000	0.0000
P	0.23366	0.35404	0.067003	0.57904	0.0000	0.0000
L	0.20273	0.20919	0.095394	0.40077	0.0000	0.0000
With band						
C	0.03488	0.016602	0.143480	0.099428	0.00246	0.01176
P	0.079675	0.031251	0.065599	0.098492	0.35119	0.53387
L	0.11865	0.015646	0.094249	0.097832	0.17801	0.34242

C.1.2 Continuous lyophilizer

Continuous lyophilizer as proposed in this thesis consists of a certain number of channel, in which suspended-vials move along, following the same path and, finally, experiencing the same conditions. Comsol 5.0 was used to create a portion of a channel and compute the geometric view factors, see Figure C.2. As a matter of fact, these view factors depend on (i) vial-to-shelf clearance, (ii) vial-to-fin width and (iii) vial-to-vial span. The following view factors have been evaluated,

- $f_{vs,sh}$, from upper and bottom shelves to vial side;

- $f_{vs,wall}$, from channel walls (or fin) to vial side;

- $f_{tp,sh}$, from upper and bottom shelves to product top-surface;

- $f_{tp,wall}$, from channel walls (or fin) to product top-surface;

- $f_{bp,sh}$, from upper and bottom shelves to product bottom surface;

- $f_{bp,wall}$, from channel walls (or fin) to product bottom surface.

Table C.3 shows the estimation of the geometric view factors by varying vial-to-shelf clearance, vial-to-fin width, and vial-to-vial span, and Table C.4 of the configuration of the functional prototype used in this thesis.
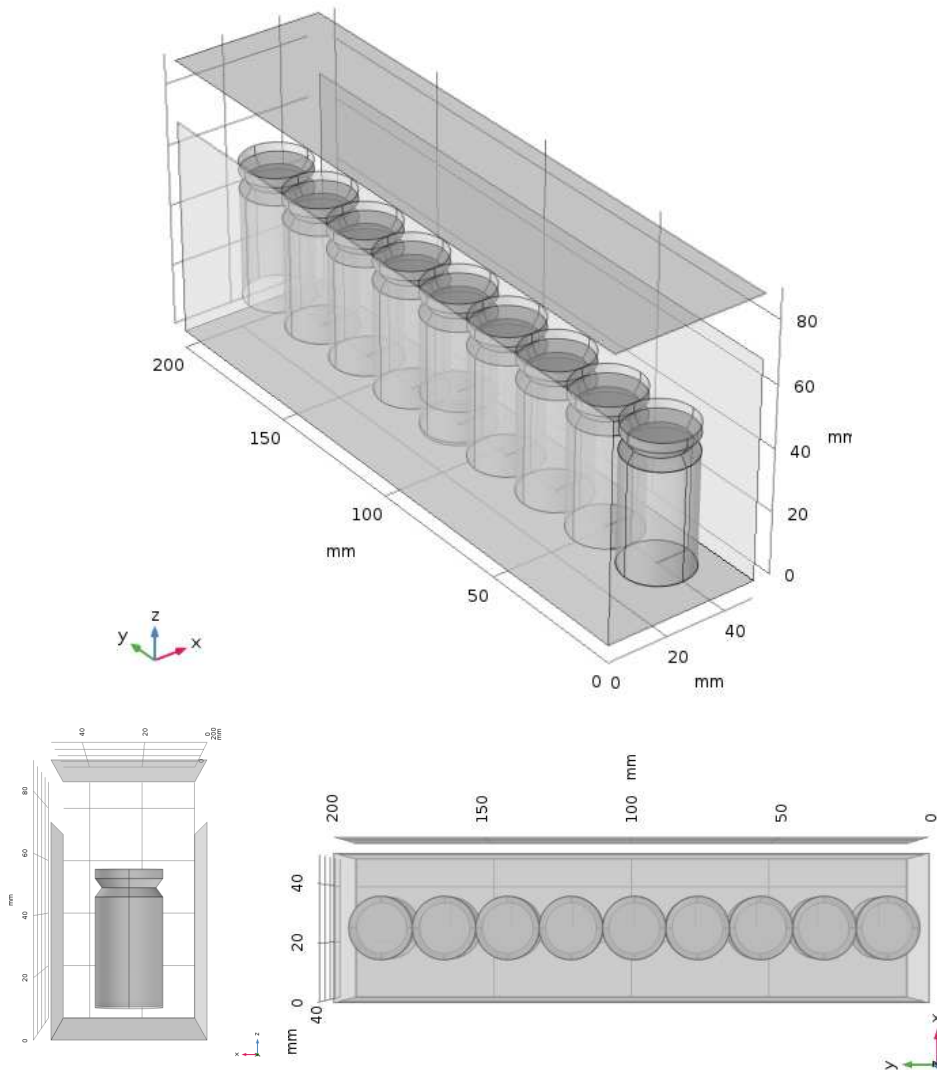
Figure C.2 Geometry used in Comsol 5.0 for calculating the view factors in the case of continuous lyophilizer.

C.2 Heat transfer coefficient of the 1D pseudo-steady state model

C.2.1 Batch freeze-drying

Heat from shelf to the product

The first contribution to consider for all the vial within the bach is due to the direct contact between shelf and vial, which is as usually written as follows,

$$\dot{Q}_d = A_v \left(\frac{1}{K'_v} + \frac{s_{gl}}{\kappa_{gl}} \right)^{-1} (T_{sh} - T_p) \tag{C.3}$$

Table C.3   View-factors in the case of the continuous lyophilizer as proposed in this thesis.

gap, mm	vial-vial span, mm	vial-wall distance, mm	$f_{\text{vs,sh}}$	$f_{\text{vs,wall}}$	$f_{\text{bp,sh}}$	$f_{\text{bp,wall}}$	$f_{\text{tp,sh}}$	$f_{\text{tp,wall}}$
1	0	14	0.24376	0.42266	0.99998	0.0051895	0.46300	0.59175
3	0	14	0.21665	0.45178	0.99210	0.0085821	0.41414	0.58064
6	0	14	0.17911	0.48841	0.96673	0.031906	0.34714	0.56539
10	0	14	0.14050	0.52464	0.91730	0.078960	0.28024	0.54169
20	0	14	0.088478	0.57098	0.76141	0.22912	0.20593	0.46448
30	0	14	0.068194	0.58230	0.61841	0.36206	0.21514	0.36334
10	0	14	0.14050	0.52464	0.91730	0.078960	0.28024	0.54169
10	5	14	0.19551	0.59058	0.91661	0.078887	0.37950	0.54732
10	10	14	0.21919	0.62086	0.91607	0.081298	0.42240	0.54528
10	0	14	0.14050	0.52464	0.91730	0.078960	0.28024	0.54169
10	0	19	0.17731	0.48040	0.94129	0.054652	0.37531	0.47245
10	0	24	0.20827	0.44174	0.95626	0.039860	0.46552	0.41162

Table C.4   Geometric view factors for the functional prototype of the continuous lyophilizer.

gap, mm	vial-vial span, mm	vial-wall distance, mm	$f_{\text{vs,sh}}$	$f_{\text{vs,wall}}$	$f_{\text{bp,sh}}$	$f_{\text{bp,wall}}$	$f_{\text{tp,sh}}$	$f_{\text{tp,wall}}$
3	0	239	0.47615	0.16257	1.00000	0.00055	0.49384	0.12680
6	0	239	0.47861	0.16434	0.99724	0.00184	0.50422	0.11736
10	0	239	0.47555	0.16630	0.99258	0.00543	0.51692	0.10436
30	0	239	0.46155	0.17101	0.94684	0.04501	0.57908	0.044922
10	10	239	0.64876	0.17002	0.99561	0.0027959	0.57689	0.059898

where,

$$K'_{\text{v}} = C_1 + \frac{C_2 P_{\text{c}}}{1 + C_3 P_{\text{c}}} \tag{C.4}$$

The second contribution is due to the extra heat of upper and bottom shelves on vial side,

$$\dot{Q}_{\text{sh,p}} = U_{\text{sh,p}}(T_{\text{sh}}^4 - T_{\text{p}}^4) \tag{C.5}$$

where,

$$U_{\text{sh,p}} = \frac{\sigma_{\text{SB}} A_{\text{vs}}}{\dfrac{1}{f_{\text{sh,p}}} + \left(\dfrac{1}{\epsilon_{\text{gl}}} - 1\right)} \tag{C.6}$$

211

Heat from wall to the product

Peripheral vials receive heat also from the chamber wall as follows,

$$\dot{Q}_{\text{wall,p}} = U_{\text{wall,p}}(T_{\text{wall}}^4 - T_{\text{p}}^4) \tag{C.7}$$

where,

$$U_{\text{wall,p}} = \frac{\sigma A_{\text{vs}}}{\dfrac{1}{f_{\text{wall,p}}} + \left(\dfrac{1}{\epsilon_{\text{gl}}} - 1\right)} \tag{C.8}$$

Heat from band to the product

In the pilot-scale freeze-drier is usually present a band that surrounds the vials, whereas in the industrial scale, when auto-loading systems are used, there are no bands or there is just a thin ridge welded around the shelf. If present supplies heat to the product,

$$\dot{Q}_{\text{bd,p}} = U_{\text{bd,p}}(T_{\text{bd}} - T_{\text{p}}) \tag{C.9}$$

The view factors $U_{\text{bd,p}}$ reads,

$$U_{\text{bd,p}} = \frac{4\sigma_{\text{SB}}\bar{T}^3 A_{\text{vs}}}{\dfrac{1}{f_{\text{bd,p}}} + \left(\dfrac{1}{\epsilon_{\text{gl}}} - 1\right) + \dfrac{A_{\text{vs}}}{A_{\text{bd}}}\left(\dfrac{1}{\epsilon_{\text{bd}}} - 1\right)} + K_{\text{g,bd}}A_{\text{vs}}^* \tag{C.10}$$

where the coefficient related to the gas conduction between the band and the vial reads,

$$K_{\text{g,bd}} = \frac{\dfrac{\alpha}{2-\alpha}\sqrt{\dfrac{273.15}{T}}\Lambda_0 P_{\text{c}}}{1 + \ell_{\text{bd/vs}}\dfrac{\Lambda_0}{\kappa_0}\dfrac{\alpha}{2-\alpha}\sqrt{\dfrac{273.15}{T}}P_{\text{c}}} \tag{C.11}$$

The values of $\ell_{\text{bd/vs}}$ can be calculated as follows,

$$\ell_{\text{bd/vs}} = \frac{\int_0^\theta R_{\text{gl}}(1 - \cos\theta)\mathrm{d}\theta}{\int_0^\theta \mathrm{d}\theta} \tag{C.12}$$

The values of $\ell_{\text{bd/vs}}$ and A_{vs}^* for each class of vial are reported in Table C.5.

At the same time, the band receives heat from direct contact and radiation from the shelf and by radiation from chamber walls. The heat supplied from the shelves to the band reads,

$$\dot{Q}_{\text{sh,bd}} = U_{\text{sh,bd}}(T_{\text{sh}} - T_{\text{bd}}) \tag{C.13}$$

where

$$U_{\text{wall,bd}} = \frac{4\sigma_{\text{SB}}\bar{T}^3 A_{\text{bd}}}{\dfrac{1}{f_{\text{sh,bd}}} + \left(\dfrac{1}{\epsilon_{\text{bd}}} - 1\right) + \dfrac{A_{\text{bd}}}{A_{\text{sh}}}\left(\dfrac{1}{\epsilon_{\text{wall}}} - 1\right)} + K_{\text{c,bd}} \tag{C.14}$$

The heat supplied from the chamber walls to the band reads,

$$\dot{Q}_{\text{wall,bd}} = U_{\text{wall,bd}}(T_{\text{wall}} - T_{\text{bd}}) \tag{C.15}$$

where,

$$U_{\text{wall,bd}} = \frac{4\sigma_{\text{SB}}\bar{T}^3 A_{\text{bd}}}{\dfrac{1}{f_{\text{wall,bd}}} + \left(\dfrac{1}{\epsilon_{\text{bd}}} - 1\right) + \dfrac{A_{\text{bd}}}{A_{\text{wall}}}\left(\dfrac{1}{\epsilon_{\text{wall}}} - 1\right)} \tag{C.16}$$

At steady-state, $\dot{Q}_{\text{bd,p}} = \dot{Q}_{\text{wall,bd}} + \dot{Q}_{\text{sh,bd}}$, eliminating T_{bd} from the equation of $\dot{Q}_{\text{bd,p}}$, so that,

$$\dot{Q}_{\text{bd,p}} = \frac{U_{\text{wall,bd}}T_{\text{wall}} + U_{\text{sh,bd}}T_{\text{sh}} - (U_{\text{wall,bd}} + U_{\text{sh,bd}})T_{\text{p}}}{\left(1 + \dfrac{U_{\text{sh,bd}} + U_{\text{wall,bd}}}{U_{\text{bd,p}}}\right)} \tag{C.17}$$

Table C.5   Values of $\ell_{\text{bd/vs}}$ and A_{vs}^*

Vial position	$\ell_{\text{bd/vs}}$	A_{vs}^*
P	$0.503R_{\text{gl}}$	$5/6A_{\text{vs}}$
L	$0.363R_{\text{gl}}$	$1/2A_{\text{vs}}$
N	$0.59R_{\text{gl}}$	$2/3A_{\text{vs}}$
M	$1.0192R_{\text{gl}}$	$2/6A_{\text{vs}}$

C.2.2   Suspended-vial freeze-drying

In the case of continuous freeze-drying here proposed, the heat is supplied to the heating sources, which for the functional prototype used in this thesis are the shelves and the chamber wall, and will be the upper, bottom source and the lateral fins. The heat power reads,

$$\dot{Q}_{\text{d}} = U_{\text{sh,p}}(T_{\text{sh}}^4 - T_{\text{b}}^4) + U_{\text{wall,p}}(T_{\text{wall}}^4 - T_{\text{b}}^4) + K_{\text{g}}A_{\text{v}}(T_{\text{sh}} - T_{\text{b}}) \tag{C.18}$$

where the first term is related to the heat supplied from upper and bottom shelf, the second to chamber wall and the third to gas conduction from shelf to vial. These coefficients are defined as follows,

$$U_{\text{sh,p}} = \frac{\sigma_{\text{SB}}(A_{\text{vs}})}{\dfrac{1}{f_{\text{vs,sh}}} + \left(\dfrac{1}{\epsilon_{\text{gl}}} - 1\right)} + \frac{\sigma_{\text{SB}}(A_{\text{v}})}{\dfrac{1}{f_{\text{bp,sh}}} + \left(\dfrac{1}{\epsilon_{\text{gl}}} - 1\right)} \tag{C.19}$$

$$U_{\text{wall,p}} = \frac{\sigma_{\text{SB}}(A_{\text{vs}})}{\dfrac{1}{f_{\text{vs,wall}}} + \left(\dfrac{1}{\epsilon_{\text{gl}}} - 1\right)} + \frac{\sigma_{\text{SB}}(A_{\text{v}})}{\dfrac{1}{f_{\text{bp,wall}}} + \left(\dfrac{1}{\epsilon_{\text{gl}}} - 1\right)} \tag{C.20}$$

$$K_{\text{g}} = \frac{\dfrac{\alpha}{2-\alpha}\sqrt{\dfrac{273.15}{T}}\Lambda_0 P_{\text{c}}}{1 + \ell_{\text{b/s}}\dfrac{\Lambda_0}{\kappa_0}\dfrac{\alpha}{2-\alpha}\sqrt{\dfrac{273.15}{T}}P_{\text{c}}} \tag{C.21}$$

C.3   Simulation set-up of the 2D model

Comsol Multiphysics 5.1 (*Heat transfer in porous media*, *Transport of diluted species* and *Deformed Geometry* module) was used to solve the heat and mass balance equations described in Section 6.3.1. The product being dried has meshed with a mapped grid constituted of about 200 cells whereas the vial glass was with a triangular unstructured triangular grid constituted of about 800 cells (see Figure C.3). The mesh is regenerated when the relative element volume in the moving mesh becomes less than 0.92, which means that the mesh was usually regenerate about a hundred times during the simulation. The direct solver PARDISO based on the LU decomposition was used; the implicit time-depended solver BDF (Backward Differentiation Formula) was used with an order of accuracy from 1 to 2, with a conservative step solver and a relative tolerance of 0.01.
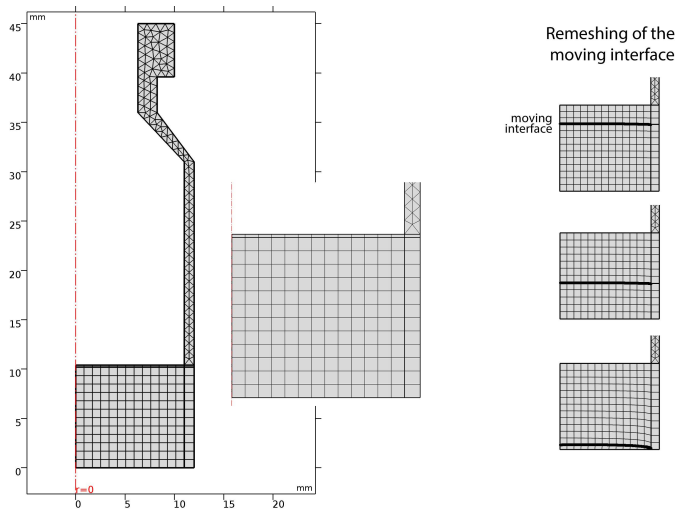
Figure C.3   Computational domain and mesh. Remeshing process is also shown.

C.3.1   Physical properties

The physical properties used for the simulations are shown in Table C.6. Eq. B.27 and the equations in Section B.3.2 were implemented in Comsol to calculate the thermal conductivity of the gas (κ_{gas}). The equations in Section B.3.1 were implemented to calculate the viscosity of the gas (μ_{gas}). The equations in Section B.3.3 were implemented to calculate $\mathcal{D}_{ij}$. The equation in Section B.3.4 was implemented to calculate the vapor pressure over ice (p_w^{eq}).

C.3.2   Validation of 2D model of freeze-drying in the case of pure ice sublimation

Batch freeze-drying

The model for batch freeze-drying has been validated using the experimental data obtained by Zhai et al. (2005), that performed their tests in a laboratory lyophilizer (VirTis Advantage) and used deionized water filled into 7-ml glass vials (VC002-20C Adelphi Tubes) in semi-stoppered configuration (stoppers FDW20 Adelphi Tubes).

214

Table C.6 Physical properties and constants used in the simulations.

Property	Value	Description
κ_{ice}	$2.56\,\mathrm{W\,m^{-1}\,K^{-1}}$	thermal conductivity of ice
κ_{sol}	$1514\,\mathrm{W\,m^{-1}\,K^{-1}}$	thermal conductivity of solid
κ_{gl}	$1.00\,\mathrm{W\,m^{-1}\,K^{-1}}$	thermal conductivity of glass
ρ_{ice}	$920\,\mathrm{kg\,m^{-3}}$	density of ice
ρ_{sol}	$1514\,\mathrm{kg\,m^{-3}}$	density of solid
ρ_{gl}	$2600\,\mathrm{kg\,m^{-3}}$	density of glass
$c_{p,\mathrm{gas}}$	$1616.6\,\mathrm{J\,kg^{-1}\,K^{-1}}$	specific heat of gas
$c_{p,\mathrm{ice}}$	$2100\,\mathrm{J\,kg^{-1}\,K^{-1}}$	specific heat of ice
$c_{p,\mathrm{sol}}$	$1383\,\mathrm{J\,kg^{-1}\,K^{-1}}$	specific heat of solid
$c_{p,\mathrm{gl}}$	$840\,\mathrm{J\,kg^{-1}\,K^{-1}}$	specific heat of glass
M_{w}	$18\,\mathrm{g\,mol^{-1}}$	molecular weight of water
M_{in}	$28\,\mathrm{g\,mol^{-1}}$	molecular weight of inert gas
ΔH_s	$2838\,\mathrm{kJ\,kg^{-1}}$	enthalpy of sublimation
ϵ_{gl}	0.85	emissivity of glass vial
$\epsilon_{\mathrm{steel}}$	0.95	emissivity of steel

Vials were filled with a volume of liquid from 2 to 5 ml and placed in a row on the shelf. The freezing protocol consisted of a cooling ramp of $0.5\,\mathrm{K\,min^{-1}}$ until 233 K, maintaining this value for 1 h to assure perfect uniformity of ice structure within the vial. A thin thermocouple is inserted into the ice, in correspondence of vial bottom, to measure ice temperature during the whole process. Various shelf temperature (in the range 235-263K) and chamber pressure (10-100 Pa) were used. The operative conditions and parameters used in our simulations are detailed in Tab. C.6.

As shown in Table C.7, the simulation outcomes are in good agreement with experimental data.

Table C.7 Comparison of the average ice temperatures and the observed times for ice sublimation as experimentally obtained by Zhai et al. (2005) and the model outcomes. Chamber pressure was set at 10.7 Pa.

T_{sh} (°C)	L_{p} (mm)	Drying time (min)		Average ice temperature (K)	
		Experimental	Simulation	Experimental	Simulation
263	17.6	820 ± 40	890	232.5 ± 0.5	231.7
243	17.6	1170 ± 30	1174	229.8 ± 1.0	231.3
237	10.6	950 ± 10	932	227.5 ± 0.3	230.4
235	6.9	635 ± 35	701	228.6 ± 0.4	229.9

Suspended-vial freeze-drying

The model for suspended-vial freeze-drying has been validated by comparing the product temperature as obtained from the experimental run and the outcome from

the simulation one. Moreover, the mass of ice sublimated in the time interval of the gravimetric test has compared to that predicted by the model.

Gravimetric tests have been performed in the pilot-scale LyoBeta 25 freeze-dryer (Telstar, Terrassa, Spain) adapted so that vials were suspended over the temperature-controlled shelves and underwent similar processing conditions to those that occur in a continuous lyophilizer. 4 ml of water for injection (Fresenius Kabi Italia, Isola della Scala, Italy) was filled into tubing vials (10R 24.0 x 45.0, Nuova Ompi, Piombino Dese, Italy). Miniature thermocouples (T type, Tersid, Milano, Italy) were used to measure the product temperature as well as the temperature of the shelves, chamber walls and the air temperature within the chamber.

In the first run, T_{sh} was set at 273 K, chamber pressure at 10 Pa, and the shelf to vial clearance of 3 mm; the second run was performed at 243 K.
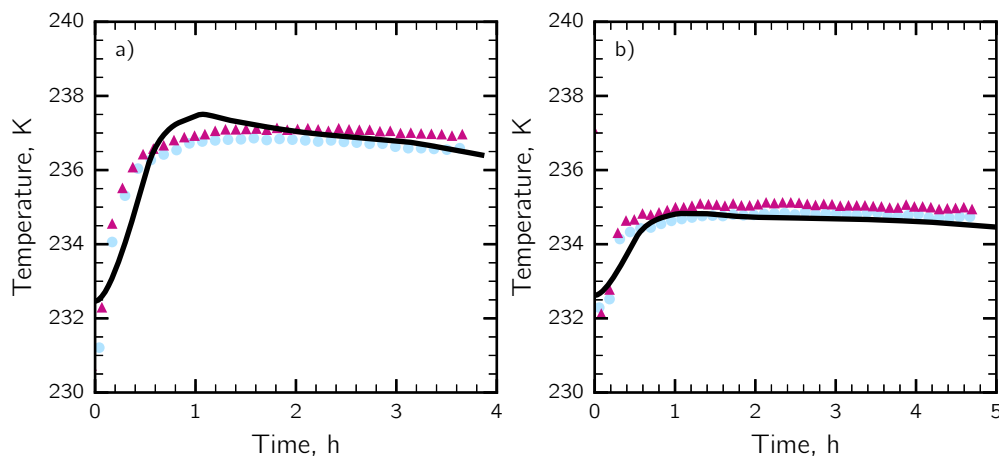
Figure C.4 Ice temperature evolution during the gravimetric test performed at 10 Pa with a shelf-vial clearance of 3 mm and a T_{sh} of (a) 273 K and (b) 243 K.

Table C.8   Comparison of ice mass variation after gravimetric tests.

run	Δm (experimental), g	Δm (simulation), g	relative error, %
1	1.68	1.69	0.7
2	1.28	1.29	0.9

List of symbols

A area, m^2

A_v outer cross-sectional area of the vial, m^2

A_{vs} side area of the vial, m^2

A_{vs}^* effective side area of the vial, m^2

C_1 parameter expressing the dependence of K_v' from radiation and the contact between vial bottom and tray surface, $J\,s^{-1}\,m^{-2}\,K^{-1}$

C_2 parameter expressing the pressure dependence of K_v', $J\,s^{-1}\,m^{-2}\,K^{-1}\,Pa^{-1}$

C_3 parameter expressing the pressure dependence of K_v', Pa^{-1}

F radiation view factor, -

f geometric view factor, -

ΔH_s enthalpy of sublimation, $J\,kg^{-1}$

$K_{g,bd}$ heat transfer coefficient due to conduction in the gas between the band and the vial side, $J\,s^{-1}\,m^{-2}\,K^{-1}$

K_v' heat transfer coefficient between the shelf and the vial bottom, $J\,s^{-1}\,m^{-2}\,K^{-1}$

$\ell_{bd/vs}$ band to vial side clearance, m

216

$\ell_{b/s}$ vial/shelf clearance, m

M molecular weight, $kg\,kmol^{-1}$

P_c chamber pressure, Pa

$\dot{Q}_{bd,p}$ extra heat flow to product from band, W

$\dot{Q}_d$ heat flow supplied to the product during drying, $J\,s^{-1}$

$\dot{Q}_{sh,bd}$ extra heat flow to band from shelf, W

$\dot{Q}_{sh,p}$ Extra heat flow to product from shelves, W

$\dot{Q}_{wall,bd}$ extra to band from chamber wall, W

$\dot{Q}_{wall,p}$ extra heat flow to product from chamber wall, W

T temperature, K

$U_{bd,p}$ band to product extra heat transfer coefficient, $W\,K^{-1}$

$U_{sh,bd}$ shelf to band heat transfer coefficient, $W\,K^{-1}$

$U_{sh,p}$ Shelf to product extra heat transfer coefficient, $W\,K^{-4}$

$U_{wall,bd}$ wall to band heat transfer coefficient, $W\,K^{-1}$

$U_{wall,p}$ wall to product extra heat transfer coefficient, $W\,K^{-4}$

Greek letters

ϵ emissivity, -

κ_0 heat conductivity of the water vapor at ambient pressure, $J\,s^{-1}\,m^{-1}\,K^{-1}$

Λ_0 free molecular heat conductivity at $0\,°C$, $J\,s^{-1}\,m^{-1}\,K^{-1}$

ϕ_S frozen fraction function, see Eq. 8.12

Subscript

bd band

gl vial glass

p barodiffusion

sh shelf

tp product top surface

vs vial sidewall

wall chamber wall

References

Zhai, S, Su, H, Taylor, R, and Slater, N. (2005). Pure ice sublimation within vials in a laboratory lyophiliser; comparison of theory with experiment. *Chemical Engineering Science* 60 (4), pp. 1167–1176.

D

Freeze-drying of microparticles: simulation set-up

This appendix presents a detailed description of methods used in Chapter 8, with particular regards to the discrete element method (DEM), computational fluid dynamics (CFD) simulations and the mathematical modeling of freeze-drying at the macro-scale. Data from DEM simulations are presented, with a particular focus on the influence of the model parameters, packing characteristics and inhomogeneities (wall effect and particles segregation); computational costs and scalability are also taken into account. Data on the properties of packings as modeled at the macroscale are presented with particular regard to the thermal conductivity of gases in the Knudsen regime and effective properties of packed-beds modeled as a pseudo-homogeneous medium. A mathematical model of the freeze-drying of single microparticles and its outcomes are first presented*.

D.1 Set-up of DEM simulations

DEM simulations solve Newton's second law of motion for translation and rotation for any particle i at any time t:

$$m_i \frac{\mathrm{d}^2 \mathbf{r}_i}{\mathrm{d}t^2} = \sum_c \mathbf{F}_{c,i} + m_i \mathbf{g} \tag{D.1}$$

---

*Part of the work described in this chapter has been previously published in "Capozzi, L.C., Barresi, A.A., Pisano, R. (2019) A multi-scale computational framework for modeling the freeze-drying of microparticles in packed-beds. *Powder Technology* 343, pp. 834-846" and "Capozzi, L.C., Barresi, A.A., Pisano, R. (2019) Supporting data and methods for the multi-scale modelling of freeze-drying of microparticles in packed-beds. *Data in Brief*, 22, pp. 722-755". Part of the macro-scale model here presented has been developed by the author in his master thesis "Capozzi, L. C. (2014). Modellazione matematica del processo di liofilizzazione di granuli (en: Mathematical modelling of freeze-drying of particle-based materials). MA thesis. Italy: Politecnico di Torino".

$$I_i \frac{d\boldsymbol{\omega}_i}{dt} = \mathbf{t}_i \tag{D.2}$$

where m_i is the mass of particle i, $\mathbf{r}_i$ its position, $\mathbf{F}_{c,i}$ the total force acting on it. I_i is the moment of inertia, $\boldsymbol{\omega}_i$ the angular velocity, and $\mathbf{t}_i$ the total torque.

D.1.1 Contact model

The Hertz-Mindlin contact algorithm has been used to simulate the falling of microparticle and, so, the generation of random packings (Machado et al., 2012). The basis behind the soft spheres model is that it allows two particles to deform during a collision by means of an overlap. The overlap then allows the calculation of the frictional, plastic and elastic forces resulting from this collision; the magnitude of these forces depends on the size of the deformation or overlap, see Fig. D.1.
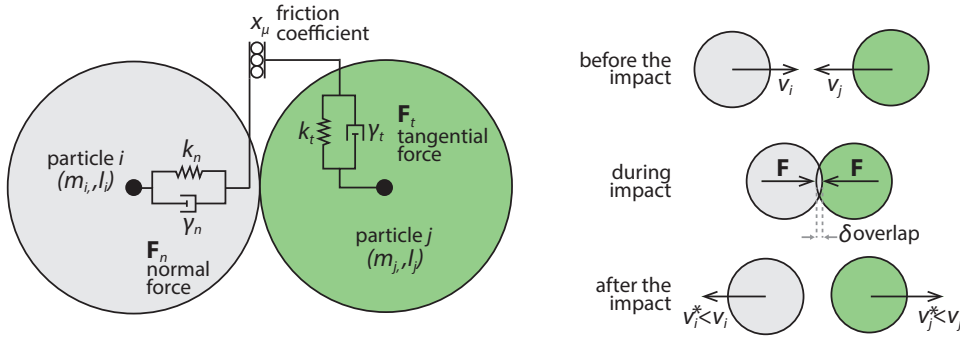
Figure D.1 Schematic of Hertz-Mindlin contact model between two particles

The Hertz-Mindlin model describes the total force on each particle after a collision between particle i and particle j as follows (Smuts et al., 2012):

$$\mathbf{F}_{c,i} = (k_n \delta_n + \gamma_n v_{n,r})\mathbf{n}_{ij} + (k_t \delta_t + \gamma_t v_{t,r})\mathbf{t}_{ij} \tag{D.3}$$

where k_n and k_t are the elasticity constants, γ_n and γ_t are viscoelastic damping constants, $v_{n,r}$ and $v_{t,r}$ are the normal and tangential component of relative velocity, δ_n is the normal displacement and δ_t is the tangential displacement vector between the two particles. The first term in this equation governs the normal force and the second one accounts for the tangential forces. The tangential displacement vector satisfies the Coloumb frictional limit:

$$\mathbf{F}_{t,i} \leq x_\mu \mathbf{F}_{n,i} \tag{D.4}$$

The associated parameters of k_n and k_t are evaluated from the elastic theory:

$$k_n = \frac{4}{3}Y^* \sqrt{R^* \delta_n} \tag{D.5}$$

$$k_t = 8G^* \sqrt{R^* \delta_n} \tag{D.6}$$

where Y^*, G^* and R^* are the equivalent Youngs modulus, the equivalent shear modulus and the equivalent radius of the two contacting bodies.

The values of the viscoelastic parameters γ_n and γ_t are:

$$\gamma_n = -2\sqrt{\frac{5}{6}}\beta\sqrt{S_n m^*} \geq 0 \tag{D.7}$$

$$\gamma_t = -2\sqrt{\frac{5}{6}}\beta\sqrt{S_t m^*} \geq 0 \tag{D.8}$$

where β, S_n and S_t are evaluated from the contact collision theory as follows:

$$S_n = 2Y^*\sqrt{R^*\delta_n} \tag{D.9}$$

$$S_t = 8G^*\sqrt{R^*\delta_n} \tag{D.10}$$

$$\beta = \frac{ln(e_r)}{\sqrt{ln^2(e_r) + \pi^2}} \tag{D.11}$$

where e_r is the coefficient of restitution.

The values of Y^*, G^*, R^* and m^* are:

$$\frac{1}{Y^*} = \frac{1 - v_1^2}{Y_1} + \frac{1 - v_2^2}{Y_2} \tag{D.12}$$

$$\frac{1}{G^*} = \frac{2(2 - v_1)(1 + v_1)}{Y_1} + \frac{2(2 - v_2)(1 + v_2)}{Y_2} \tag{D.13}$$

$$\frac{1}{R^*} = \frac{1}{R_1} + \frac{1}{R_2} \tag{D.14}$$

$$\frac{1}{m^*} = \frac{1}{m_1} + \frac{1}{m_2} \tag{D.15}$$

where v is the Poisson ratio, and m^* is the equivalent mass of the two bodies in contact.

Hertz-Mindlin contact model requires five key parameters, i.e., particle radius R, particle mass m, Young's modulus Y, shear modulus G, Poisson's ratio v and the coefficient of restitution e_r. These parameters are provided in Table D.1. It should also be noted that this contact model was also used to describe both particle-particle and particle-wall collisions.

Table D.1 Parameters used in DEM simulations for particle-particle and wall-particle interactions.

Parameter	Value	Unit	Ref.
Density of particles	926.7	$\mathrm{kg\,m^3}$	
Young's modulus of ice particles	93.3×10^8	$\mathrm{N\,m^{-2}}$	*
Young's modulus of wall	65.0×10^9	$\mathrm{N\,m^{-2}}$	*
Poisson ratio of ice particles	0.325	-	*
Poisson ratio of wall	0.210	-	*
Friction coefficient particle-particle	0.33	-	**
Friction coefficient particle-wall	0.50	-	**
Restitution coefficient particle-particle	0.4	-	***
Restitution coefficient particle-wall	0.5	-	***

* Petrenko and Whitworth, 1999, ** Kietzig et al., 2010, *** Higa et al., 1996.

D.1.2 Computational cost and scalability

DEM simulations were performed on the Galileo supercomputer located in CINECA and equipped with 516 nodes containing two Intel Haswell 8-core processors each, with a clock of 2.40 GHz and a RAM of 128 GB/node (*GALILEO The Italian Tier-1 cluster for industrial and public research*).

LIGGGHTS is an open-source DEM code derived from the molecular dynamics code LAMMPS and used for simulating granular materials. LIGGGHTS supports the addition of mesh geometries and includes granular models for modeling particle-particle and particle-walls collisions. LIGGGHTS can be run as a serial or in a parallel environment through MPI. Dynamic MPI domain decomposition was used to mitigate the load-imbalance of DEM simulations.

The speedup of a parallel implementation reads,

$$\text{speedup} = \frac{\text{serial runtime}}{\text{parallel runtime}} \tag{D.16}$$

Table D.2 reports the test cases used for evaluating the simulation speedup. Table D.3 shows the test cases used for evaluating the computational costs related to the integration timestep adopted for the simulations.

Table D.2 Test case: 100k monodisperse (st.deviation = 0) falling particles of 30 µm as diameter; total simulated time = 1.1 s, no. of cores = 4.

Test case	Integration timestep	No. of timesteps	Runtime	Timesteps/h
1	250	4400000	19.9	241540
2	200	5500000	25.3	237287
3	100	11000000	47.0	255234
4	50	22000000	96.0	250002
5	25	44000000	186.8	256894
6	10	110000000	644.8	186094

Data in Fig. D.2a,b refer to simulation runtime and speedup relative to serial run varying the number of cores from 1 (serial) to 512. The simulations refer to

Table D.3 Test case: 100k monodisperse (st.deviation = 0) falling particles of 30 μm as diameter; integration time step = 25 ns, total simulated time = 1.1 s ($48 \cdot 10^6$ timesteps).

Test case	No. of cores	Runtime	Timesteps/h
1	1	257.0	186747
2	2	252.4	190207
3	4	186.8	256894
4	8	89.5	536471
5	16	43.4	1105375
6	32	34.1	1407494
7	48	21.9	2194135
8	64	16.7	2867110
9	128	12.2	3926460
10	512	3.2	15204827

100,000 monodisperse falling particles of 30 μm and a timestep of 25 ns. Increasing the number of cores from the 1 to 4 did not have a dramatic impact on the runtime, and equivalently on the speedup, because of the geometry of the system. On the other hand, from 4 to 512 cores, the scalability was very good. Data in Fig. D.2c show that the computational cost strongly depends on the integration time step used in the simulation.

D.1.3 Selection of the time-step

For DEM simulations, time step should be small enough to avoid instability and also provide a reliable and stable set of particle spatial location data during the simulation as a whole. A rule of thumb states that the maximum acceptable time step must be set to a value between 0.1 and 0.3 of the minimum value of the semi-empirical parameters, Hertz time and Rayleigh time (Smuts et al., 2012).

The Hertz time can be evaluated from:

$$t_{\text{Hertz}} = 2.87 \frac{4/3 \rho \pi (D_{\text{p}}/2)^3}{(D_{\text{p}}/2) Y^2 v_{\max}} \tag{D.17}$$

The Rayleigh time reads:

$$t_{\text{Rayleigh}} = \frac{\pi (D_{\text{p}}/2)}{0.1631 \nu + 0.766} \sqrt{\frac{\rho}{Y/[2(1+\nu)]}} \tag{D.18}$$

Each simulation has been performed using a time-step equal to 10% of the Rayleigh time; to give you an example, for monodisperse microparticles of 10 μm, the time-step was 8.62 ns, whereas for microparticles of 90 μm, was 77.60 ns. In the case of polydisperse microparticles, the time-step was usually lower, because it was chosen taking into account the smallest particles of the distribution.

D.1.4 Selection of the REV size

REV needs to be chosen sufficiently extended to catch global properties and avoid local fluctuations. If the REV was small, porosity, which was chosen as the reference
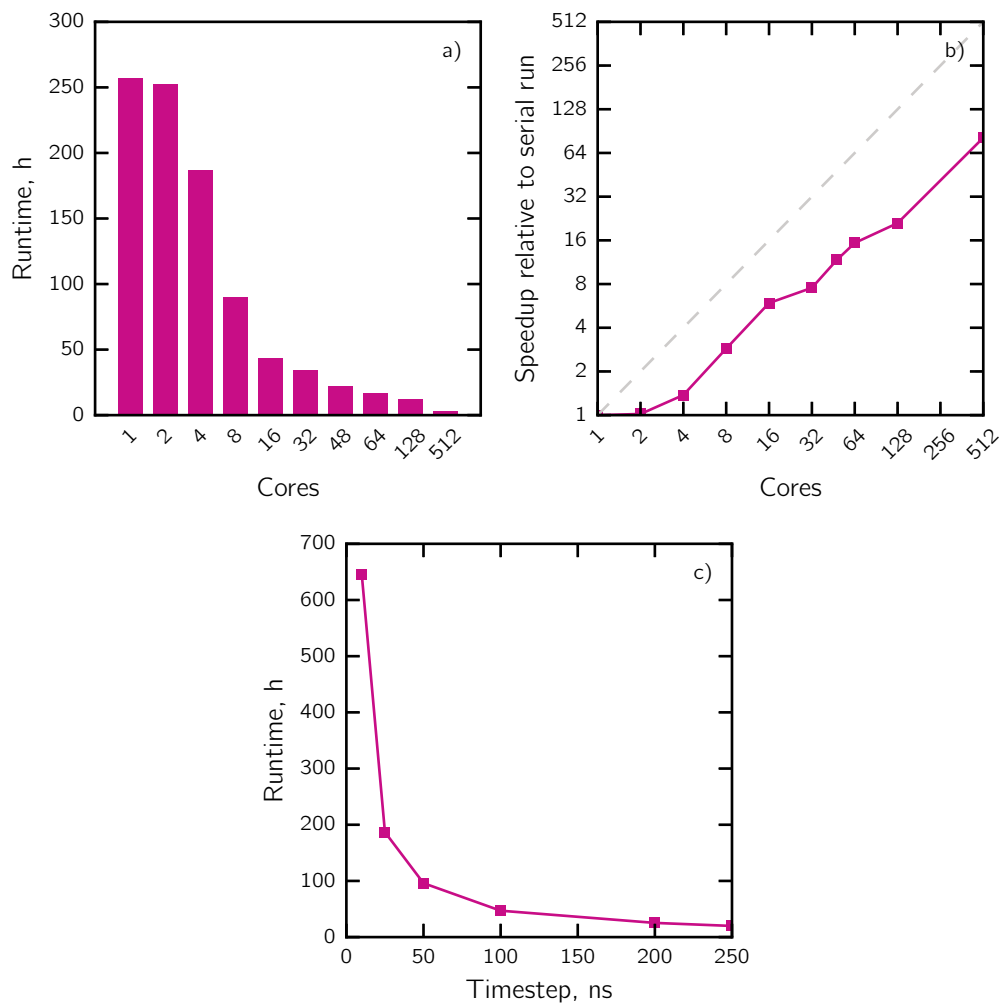
Figure D.2   (a) Simulation runtime. (b) Speedup relative to serial run by varying the number of cores used in the parallelization. Dashed line refers to the ideal speedup. (c) Simulation runtime as a function of the timestep used.

property, fluctuated for different REVs located one near each other. On the other hand, if the REV size is sufficiently large, the fluctuations in the proximity of a certain point in the bed become negligible.

Data shown in Fig. D.3 refer to the case of frozen microparticles consisting of a water mixture 35% w/w of trehalose, mannitol, dextran (10 kDa) and dextran (150 kDa) (TMDD) in the ratio 3:3:3:1 atomized at 48 kHz (sperimental data (Schiffter et al., 2010) and simulation results (Chapter 8).

Data shown in Fig. D.4 refer to the packings of monodisperse and polydisperse microparticles of 50 μm as mean diameter. The data show that REV volume should contain at least 1,000 particles to avoid local fluctuations of the porosity in the proximity of a certain position in the bed, which corresponds to a REV of 0.06 mm^3.

Fig. D.5 show a packing of 100k polydisperse micro-particles and REVs with different volume (from 10×10^{-3} mm^3 to 1×10^{-1} mm^3).
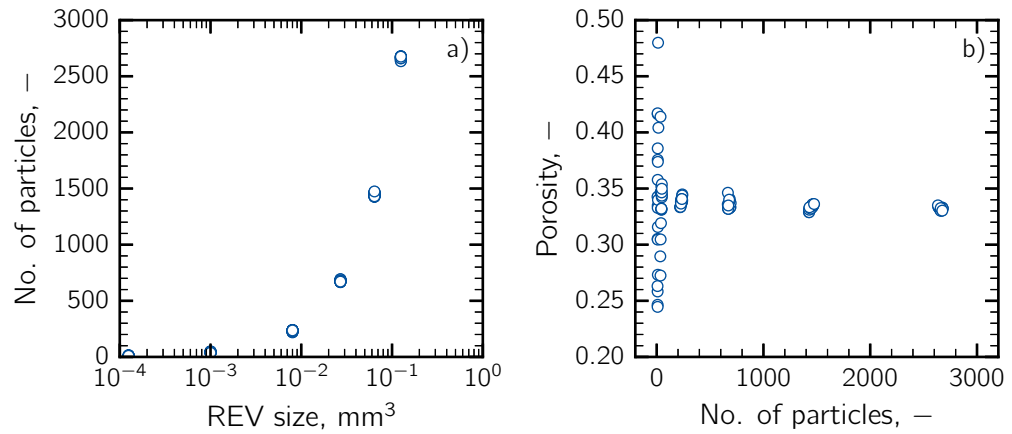
Figure D.3 35 % w/w water-TMDD (3:3:3:1) atomized at 48kHz. (a) Number of particles as a function of REV size and (b) porosity value as a function of the number of particles. REV was chosen in the vicinity of the center of the packing, with small deviations of its center coordinates randomly chosen within the range ± 0.1 mm; each dot represents a value of these neighbors REVs.
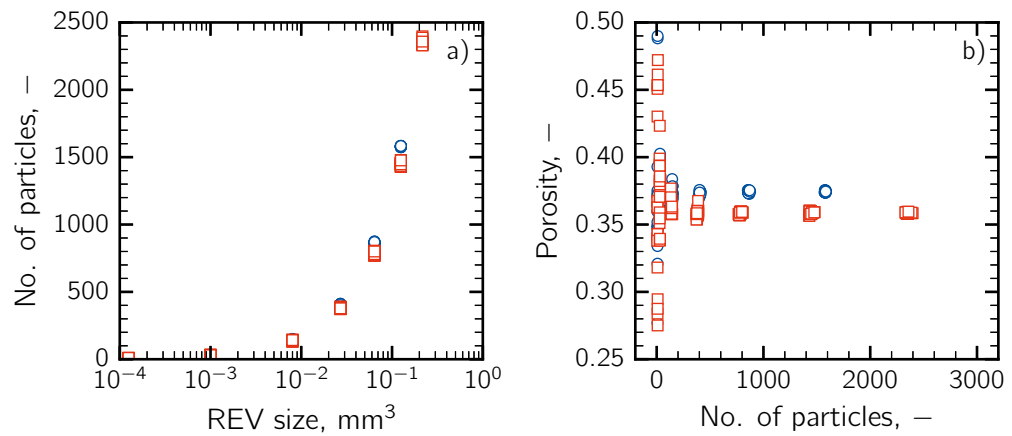
Figure D.4 Microparticles of (O) monodisperse and (□) polydisperse microparticles ($\sigma = 5\,\mu$m) with a mean diameter of 50 μm. (a) Number of particles as a function of the REV size and (b) porosity as a function of the number of particles. REV was chosen in the vicinity of the center of the packing, with small deviations of its center coordinates randomly chosen within the range ± 0.01 cm; each dot represents a value of these neighbors REVs.

D.2   Set-up of CFD simulations for estimating packing properties

In this section, the set-up of CFD simulations used in Chapter 8 for estimating packing properties is presented.

D.2.1   Simulation set-up

The fluid flow within the packed-bed was simulated by solving the continuity and Navier-Stokes equations, imposing a pressure drop in the z-direction between the inlet and outlet sections. The no-slip boundary condition was imposed at the particle
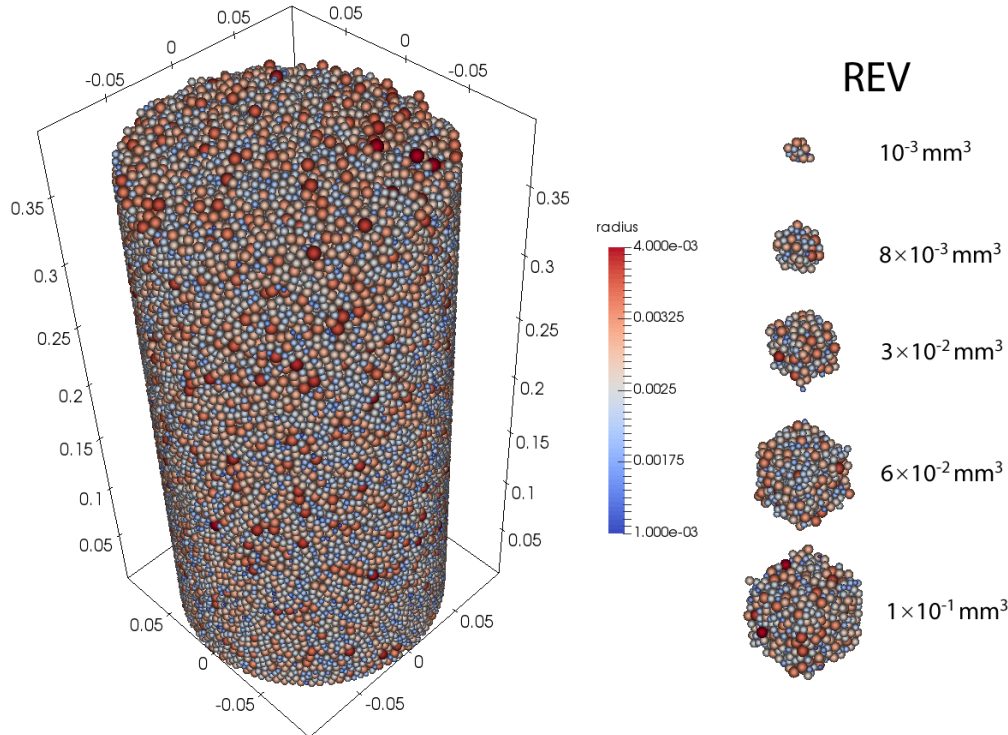
Figure D.5 Packing of polydisperse microparticles ($\sigma = 5\,\mu m$) with a mean diameter of $50\,\mu m$ and extracted REVs of different volumes.

surface and the symmetry condition at the remaining sides of the REV. The pressure drop across the REV was set sufficiently low to guarantee that Re < 0.1, and so Stokes regime occurs. In those conditions, the inertial term is negligible, and the estimated permeability corresponds to the true permeability of the medium.

D.2.2 Mesh refinement

The independence of the solution from the mesh was obtained by successive refinements of the grid within the REV. We performed this analysis by varying the number of cells from about 20,000 to 35,000,000. To give you an example, Fig. D.6 shows the permeability as a function of the number of cells within the computational domain in the case of monodisperse microparticles of $50\,\mu m$. In this case, mesh independence of the solution was reached for a number of cells of about 20,000,000.

D.3 Modeling of freeze-drying of frozen microgranules

D.3.1 Freeze-drying of single microparticles

The heat and mass transfer in a single particle during the primary drying step has been described using a one-dimensional, axisymmetric, unsteady state model (Fig. D.7). The computational domain is divided into two subdomains, namely, the dried layer Γ_α and the frozen layer Γ_β, divided by the sublimation interface $H_p(t)$.
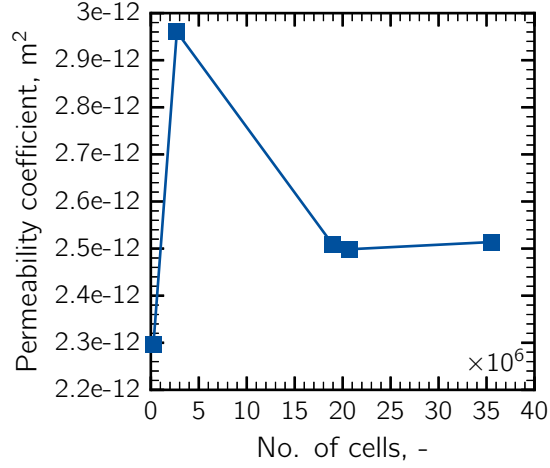
Figure D.6 Value of permeability coefficient as obtained from successive mesh refinement of the REV, in the case of monodisperse microparticles of 50 μm as diameter.
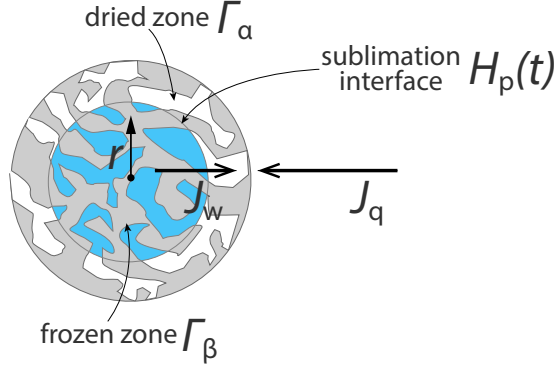
Figure D.7 Schematic of the computational domain for the freeze-drying of a single microparticle.

Heat transfer within the particle

The heat balance equation in the dried layer reads,

$$\rho_{\mathrm{p,d}} c_{p_{\mathrm{p,d}}} \frac{\partial T_\alpha}{\partial t} = \boldsymbol{\nabla} \cdot \left(\kappa_{\mathrm{p,d}} \boldsymbol{\nabla} T_\alpha \right) - c_{p,\mathrm{gas}} \mathbf{M} \cdot \boldsymbol{\nabla} T_\alpha \qquad \text{in} \quad \Gamma_\alpha \tag{D.19}$$

where $\rho_{\mathrm{p,d}}$, $c_{p_{\mathrm{p,d}}}$, and $\kappa_{\mathrm{p,d}}$ are respectively the effective density, heat capacity and thermal conductivity of the dried particle (see Section D.3.2), and $\mathbf{M} = M_\mathrm{w} \mathbf{N}_\mathrm{w} + M_\mathrm{in} \mathbf{N}_\mathrm{in}$ is the total mass flux.

The heat balance equation in the frozen layer is expressed as follows,

$$\rho_{\mathrm{p,f}} c_{p_{\mathrm{p,f}}} \frac{\partial T_\beta}{\partial t} = \boldsymbol{\nabla} \cdot \left(\kappa_{\mathrm{p,f}} \boldsymbol{\nabla} T_\beta \right) \qquad \text{in} \quad \Gamma_\beta \tag{D.20}$$

where $\rho_{\mathrm{p,f}}$, $c_{p_{\mathrm{p,f}}}$, and $\kappa_{\mathrm{p,f}}$ are respectively the effective density, heat capacity and thermal conductivity of the frozen particle (see D.3.2).

The heat transfer initial conditions are,

$$T_\alpha = T_\beta = T_0 \qquad \text{for} \quad t = 0, \quad \forall r \tag{D.21}$$

227

The boundary condition at the surface of the particle can be written as:

$$J_{q,p} = -\mathbf{n} \cdot (-\kappa \nabla T)_{r=D_p/2} = \sigma_B F(T_{sh}^4 - T_{r=D_p/2}^4)$$
$$\text{for} \quad t > 0, \qquad r = D_p/2 \tag{D.22}$$

Mass transfer within the particle

The conservation of species equations on a molar basis for water vapour and inert gas in the dried layer Γ_α can be expressed as:

$$\frac{\partial \varepsilon_p c_{w,\alpha}}{\partial t} = -\nabla \cdot \mathbf{N}_{w,\alpha}$$
$$\qquad \qquad \qquad \text{in } \Gamma_\alpha \tag{D.23}$$
$$\frac{\partial \varepsilon_p c_{in,\alpha}}{\partial t} = -\nabla \cdot \mathbf{N}_{in,\alpha}$$

The frozen core in the particle is considered compact, so that no mass flux occurs within that subdomain.

Rarified conditions and the micrometer magnitude of pores in the particle lead to the transition regime ($0.1 < \text{Kn} < 10$). In this case, the expression of flux of the i-component can be obtained from the Dusty-Gas Model as follows:

$$\mathbf{N}_i = -\frac{1}{R_g T} \left(D'_{p,i} \nabla p_i + D''_{p,i} p_i \nabla p \right) \tag{D.24}$$

where $D'_{p,i}$ and $D''_{p,i}$ ($i = w, in$) are the transport coefficients depending on concentration and pressure gradients respectively, and can be written as:

$$D'_{p,i} = \frac{D_{i,p}^{Kn} D_{ij,p}^{eff}}{D_{ij,p}^{eff} + y_i D_{j,p}^{Kn} + y_j D_{i,p}^{Kn}} \qquad i = w, in \tag{D.25}$$

$$D''_{p,i} = \frac{D_{i,p}^{Kn} (D_{ij,p}^{eff} + D_{j,p}^{Kn})}{(D_{ij,p}^{eff} + y_i D_{j,p}^{Kn} + y_j D_{i,p}^{Kn})P} + \frac{B_{0,p}}{\mu} \qquad i = w, in \tag{D.26}$$

The effective binary diffusion D_{ij}^{eff} is defined as:

$$D_{ij,p}^{eff} = \frac{\varepsilon_p}{\tau_p^2} \mathcal{D}_{ij} \tag{D.27}$$

where ε_p and τ_p are the particle porosity and tortuosity, respectively. The effective Knudsen diffusivity for the i-component is:

$$D_{i,p}^{Kn} = \frac{\varepsilon_p}{\tau_p^2} \frac{d_P^*}{3} \sqrt{\frac{8 R_g T}{\pi M_i}} \tag{D.28}$$

where d_P^* refers to the pore diameter within the particle.

The initial conditions for mass transfer are:

$$c_{w,\alpha}(t_0) = \frac{p_w^{eq}(T_0)}{R_g T_0}$$
$$c_{in,\alpha}(t_0) = \frac{P_c - p_w^{eq}(T_0)}{R_g T_0} \tag{D.29}$$
$$\text{for} \quad t = 0, \quad \forall r$$

The boundary conditions on the particle surface read:

$$c_{w,\alpha} = \frac{0.95 P_c}{R_g T_c}$$

$$c_{in,\alpha} = \frac{0.05 P_c}{R_g T_c}$$

$$\text{for} \quad t > 0, \quad r = D_p/2$$

(D.30)

Mass and heat balance at the moving interface

A moving interface divides the dried layer Γ_α and the frozen layer Γ_β. The mass balance across the interface gives:

$$-\mathbf{n} \cdot \mathbf{N}_w \Big|_{z=H_p(t)} = -v_s(\rho_{p,d} - \rho_{p,f})$$

(D.31)

The heat balance across the moving boundary reads:

$$\mathbf{n} \cdot \left(\kappa_{p,d} \boldsymbol{\nabla} T_\alpha - \kappa_{p,f} \boldsymbol{\nabla} T_\beta\right)\Big|_{z=H_p(t)} +$$
$$+ (\rho_{p,d} c_{p_{p,d}} - \rho_{p,f} c_{p_{p,f}}) v_s T_{int} - \mathbf{n} \cdot (c_{p,gas} T_{int} + \Delta H_s)\mathbf{N}_w\Big|_{z=H_p(t)} = 0 \quad (\text{D.32})$$

Combining Eqs. D.31-D.32 the velocity of the interface is:

$$v_s = \frac{\mathbf{n} \cdot \left(\kappa_{p,d} \boldsymbol{\nabla} T_\alpha - \kappa_{p,f} \boldsymbol{\nabla} T_\beta\right)}{(\Delta c_p T_{int} + \Delta H_s)(\rho_{p,d} - \rho_{p,f})}$$

(D.33)

where $\Delta c_p = c_{p,gas} - (\rho_{II} c_{p,II} - \rho_I c_{p,I})/(\rho_{II} - \rho_I)$.

D.3.2 Parameters of the macro-scale model

Particle properties

The value of physical properties used in the simulation of freeze-drying at the macroscale is shown in Table D.4. The effective properties of the dried layer are considered as an average of solid and gas properties, using the particle porosity ε_p as a weight. Effective density $\rho_{p,d}$, heat capacity $c_{p_{p,d}}$ and thermal conductivity $\kappa_{p,d}$ of the dried particle can be expressed as follows:

$$\rho_{p,d} = \rho_{gas}\varepsilon_p + \rho_{sol}(1 - \varepsilon_p)$$

(D.34)

$$c_{p_{p,d}} = c_{p,gas}\varepsilon_p + c_{p,sol}(1 - \varepsilon_p)$$

(D.35)

$$\kappa_{p,d} = \kappa_{sol} \frac{2\kappa_{sol} + \kappa_{gas} - 2\varepsilon_p(\kappa_{sol} - \kappa_{gas})}{2\kappa_{sol} + \kappa_{gas} + \varepsilon_p(\kappa_{sol} - \kappa_{gas})}$$

(D.36)

where ρ_{gas} is the density of gas mixture in the particle pores, $c_{p,gas}$ its specific heat capacity and $\kappa_{p,d}$ its thermal conductivity. ρ_{sol}, $c_{p,sol}$ and κ_{sol} are respectively the density, the heat capacity and the thermal conductivity of the solid.

The effective properties of the frozen layer are considered as an average of solid and ice properties, using particle porosity ε_p as a weight. The effective density $\rho_{p,f}$,

heat capacity $c_{p_{p,f}}$ and thermal conductivity $\kappa_{p,f}$ of the frozen particle can be expressed as follows:

$$\rho_{p,f} = \rho_{ice}\varepsilon_p + \rho_{sol}(1 - \varepsilon_p) \tag{D.37}$$

$$c_{p_{p,f}} = c_{p,ice}\varepsilon_p + c_{p,sol}(1 - \varepsilon_p) \tag{D.38}$$

$$\kappa_{p,f} = \kappa_{ice}\varepsilon_p + \kappa_{sol}(1 - \varepsilon_p) \tag{D.39}$$

where ρ_{ice}, $c_{p,ice}$ and κ_{ice} are respectively the density, the heat capacity and the thermal conductivity of the ice.

Packed-bed properties

The packed bed can be considered a bidisperse porous medium, as it is characterized by the particle porosity ε_p and bed porosity ε_b. The dried subdomain Ω_I consists of a bed of completely dried particles, thus the total porosity is:

$$\varepsilon_{tot,I} = \varepsilon_b + (1 - \varepsilon_b)\varepsilon_p \tag{D.40}$$

The volume-averaged properties of the dried subdomain Ω_I can be determined from the following expressions:

$$\rho_I = \rho_{p,d}(1 - \varepsilon_b) + \rho_{gas}\varepsilon_b \tag{D.41}$$

$$c_{p,I} = c_{p_{p,d}}(1 - \varepsilon_b) + c_{p,gas}\varepsilon_b \tag{D.42}$$

$$\kappa_I = \kappa_{p,d}(1 - \varepsilon_b) + \kappa_{gas}\varepsilon_b \tag{D.43}$$

where $\rho_{p,d}$, $c_{p_{p,d}}$, $\kappa_{p,d}$ are respectively the effective density, heat capacity and thermal conductivity of dried particles and ρ_{gas}, $c_{p,gas}$ and κ_{gas} the proprerties of gas flowing through the packed-bed.

The subdomain Ω_{II} consists of a bed of particles that can be completely frozen, completely or partially dried, or frozen with condensed ice over the particle surface. Those situations are described using the frozen fraction function ϕ_s (see Eq.12 in Chapter 8), and also the effective particle properties are functions of the frozen fraction function ϕ_s. The total porosity in Ω_{II} can be written as:

$$\varepsilon_{tot,II} = \varepsilon_b + (1 - \varepsilon_b)\varepsilon_p(1 - \phi_s) \tag{D.44}$$

The volume-averaged properties of subdomain Ω_{II} can be determined from the following expressions:

$$\rho_{II} = \rho_p(1 - \varepsilon_b) + \rho_{gas}\varepsilon_b \tag{D.45}$$

$$c_{p,II} = c_{p_p}(1 - \varepsilon_b) + c_{p,gas}\varepsilon_b \tag{D.46}$$

$$\kappa_{II} = \kappa_p(1 - \varepsilon_b) + \kappa_{gas}\varepsilon_b \tag{D.47}$$

where ρ_p, c_{p_p}, κ_p are respectively the effective density, heat capacity and thermal conductivity of dried particles and ρ_{gas}, $c_{p,gas}$ and κ_{gas} the proprerties of gas flowing through the particle bed. The value of ρ_p, c_{p_p} and κ_p depends on the function ϕ_s as follows:

$$\rho_p = \rho_{p,f}\phi_s + \rho_{p,d}(1 - \phi_s) \tag{D.48}$$

$$c_{p_p} = c_{p_{p,f}}\phi_s + c_{p_{p,d}}(1 - \phi_s) \tag{D.49}$$

$$\kappa_p = \kappa_{p,f}\phi_s + \kappa_{p,d}(1 - \phi_s) \tag{D.50}$$

Table D.4 Values of physical properties and parameters.

Parameter	Value	Unit
ρ_{sol}	1514	kg m^{-3}
ρ_{ice}	920	kg m^{-3}
ρ_{gl}	2600	kg m^{-3}
κ_{sol}	0.2014	$\text{W m}^{-1}\text{k}^{-1}$
κ_{ice}	2.56	$\text{W m}^{-1}\text{k}^{-1}$
κ_{gl}	1.0014	$\text{W m}^{-1}\text{k}^{-1}$
$c_{p,\text{sol}}$	1383	$\text{J kg}^{-1}\text{k}^{-1}$
$c_{p,\text{ice}}$	2100	$\text{J kg}^{-1}\text{k}^{-1}$
$c_{p,\text{gas}}$	1617	$\text{J kg}^{-1}\text{k}^{-1}$
$c_{p,\text{gl}}$	840	$\text{J kg}^{-1}\text{k}^{-1}$
M_{w}	18	kg kmol^{-1}
M_{in}	28	kg kmol^{-1}
ΔH_s	2.84	MJ kg^{-1}
R_{g}	8.314	$\text{J kmol}^{-1}\text{K}^{-1}$
σ_{B}	5.67×10^{-8}	$\text{W m}^{-2}\text{K}^{-4}$
R_{gl}	12.0	mm
s_{gl}	1.2	mm
K_{c}	6.354	$\text{W m}^{-2}\text{K}^{-1}$
ℓ_{V}	3.80×10^{-4}	m

D.4   Supporting results

D.4.1   Packing inhomogeneity

Packings of particles can show inhomogeneities due to the wall effects but also to particles segregation; in Fig. D.8 porosity has been mapped within the entire packed-bed.
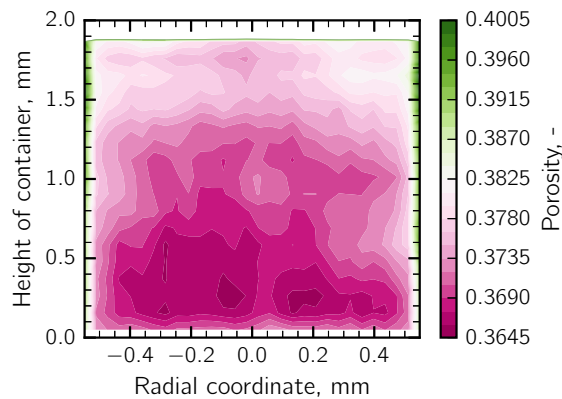
Figure D.8   Value of porosity within the bed for a packed-bed of polydisperse microparticles of 30 μm and $\sigma = 5$ μm.

Wall effects

Data in Fig. D.9 show the typical wall effects that characterize the packing in a confined container. These data refer to the simulation of packings of microparticles in a container with a diameter of 0.4 mm for particles of 10 µm, 1.2 mm for 30 µm, 2 mm for 50 µm, 2.8 mm for 70 µm and 3.6 mm for 90 µm. On the other hand, the freeze-drying of microparticles is usually done in vials with a diameter of 5 to 20 mm; in that context, the wall effects are negligible as the ratio of vial diameter to particle diameter is usually higher than 100.
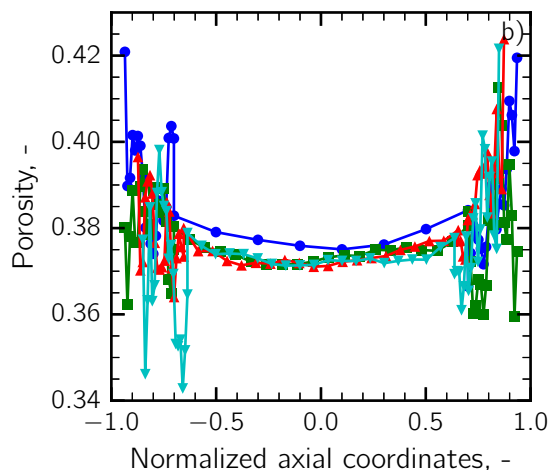
Figure D.9 Porosity value in the axial direction across the diameter of the packed bed for different particle sizes in a monodisperse packed-bed (●— 30 µm, ■— 50 µm, ▲— 70 µm, ▼— 90 µm).

Particles segregation

Particle segregation can occur because of (a) sifting, (b) fluidization, (c) entrainment of particles in the airstream, (d) flotation due to vibration and (e) agglomeration (Carson, 1988). The data in Fig. D.10 and Fig. D.11 show the particle segregation in a packed bed of granules of 50 µm, monodisperse and polydisperse ($\sigma = 5$ µm) respectively; the packings were obtained by simulating 100k particles falling into a cylinder of 2 mm as diameter.

In Fig. D.12 the data of porosity along the packing height are compared for packings obtained by simulating the falling of 100k, 200k and 500k monodisperse particles of 50 µm and polydisperse particles ($\sigma = 5$ µm).

D.4.2   Prediction of a bottom sublimation interface

During primary drying of frozen solutions in a vial, the ice sublimates creating a single sublimation front that recedes downward until the product is completely dried. In that case, the frozen layer is usually compact and there is no formation of further sublimation interfaces, except in the case of shrinkage of the product. If the product shrinks, the cake being dried breaks away from the vial walls, and a new lateral interface might form.
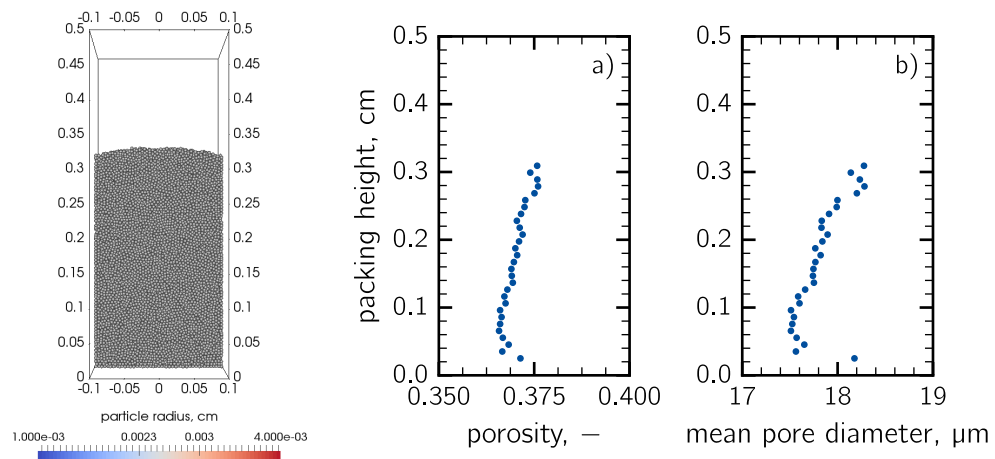
Figure D.10 Packed bed of 100k monodisperse particles of 50 μm as diameter. (a) Porosity and (b) mean pore diameter along packing height.
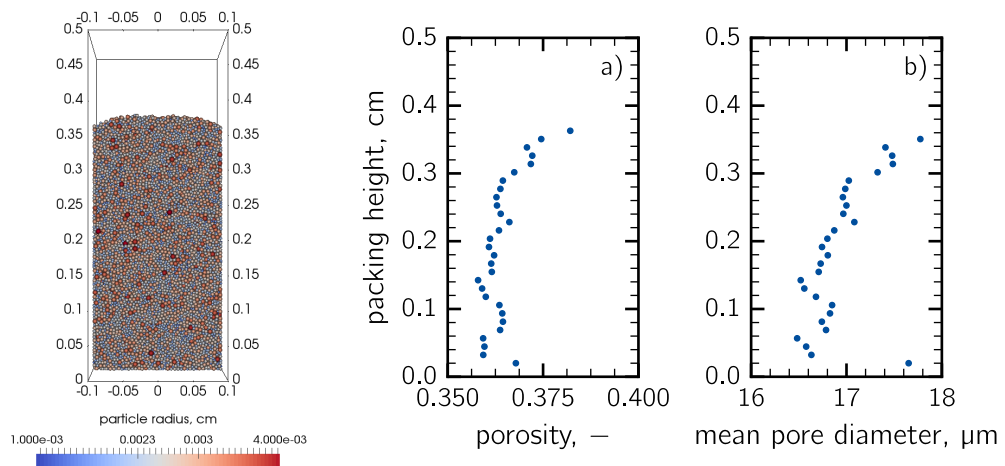
Figure D.11 Packed bed of 100k polydisperse particles of 50 μm ($\sigma = 5$ μm) as diameter. (a) Porosity and (b) mean pore diameter along packing height.

Contrary, a frozen particle-based material is typically a bidisperse medium, where two porosities are present, i.e., bed porosity and particle porosity. In this case, each particle has it own sublimation interface, but sublimation can only occur if the vapor partial pressure at the particle interface is lower than the vapor equilibrium pressure; if the vapor partial pressure is higher than the vapor equilibrium pressure, the deposition of ice over the particles occurs.

The model presented in Chapter 8 describes this behavior through the frozen fraction function. The model predicts the formation of a dried layer at the bottom of the vial, due to the fact the particles at the bottom receive a sufficient amount of heat for sublimation to occur. At the same time, the vapor from the bottom particles moves upwards, increasing the local partial pressure in upper locations in the bed. At that point, the vapor pressure becomes higher than the vapor equilibrium pressure, and the vapor starts depositing over particles; the frozen fraction function is higher than 1. This behavior is clearly shown in Fig. D.13a. Moreover, as a bottom dried layer
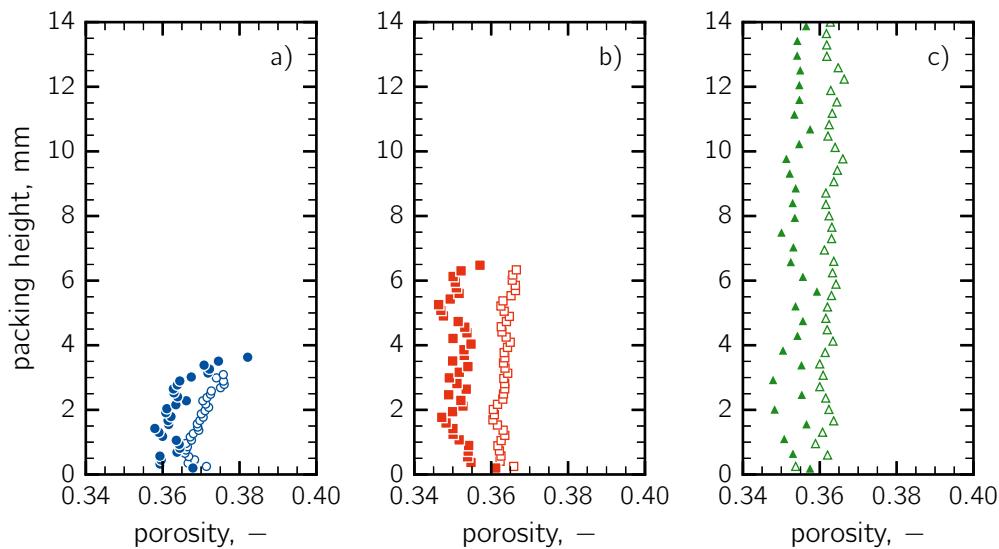
Figure D.12 Porosity (a) 100k (b) 200k and (c) 500k ($\bigcirc$, $\square$, $\triangle$) monodisperse particles of 50 μm as diameter and ($\bullet$, $\blacksquare$, $\blacktriangle$) polydisperse particles ($\sigma = 5$ μm).

is formed, the thermal conductivity decreases, creating a further resistance to heat transferred to the particles being dried, see Fig. D.13b. Figure D.14 shows the contour plot of the product temperature and the frozen fraction during primary drying of microparticles of 50 μm.
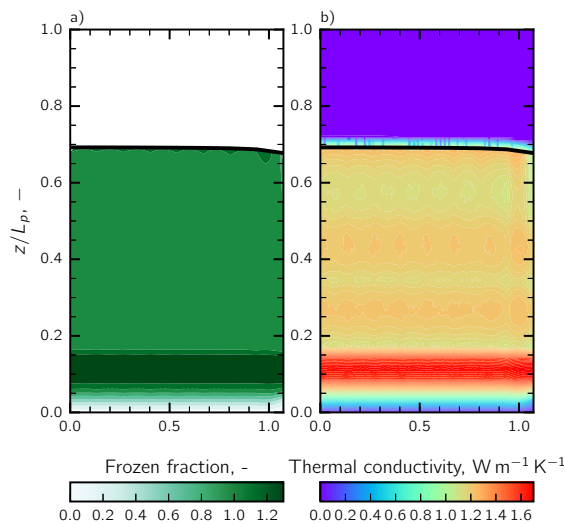
Figure D.13 Contour plot of the (a) frozen fraction function and (b) thermal conductivity in the bed of microparticles in a vial. Data refer to microparticles of 50 μm, $T_{sh} = 253$ K and $P_c = 10$ Pa.

D.4.3 Process design

The effect of shelf temperature and chamber pressure on drying duration of micropar-ticles packed in vials was evaluated for a T_{sh} in the range 238 - 273 K. Three cases
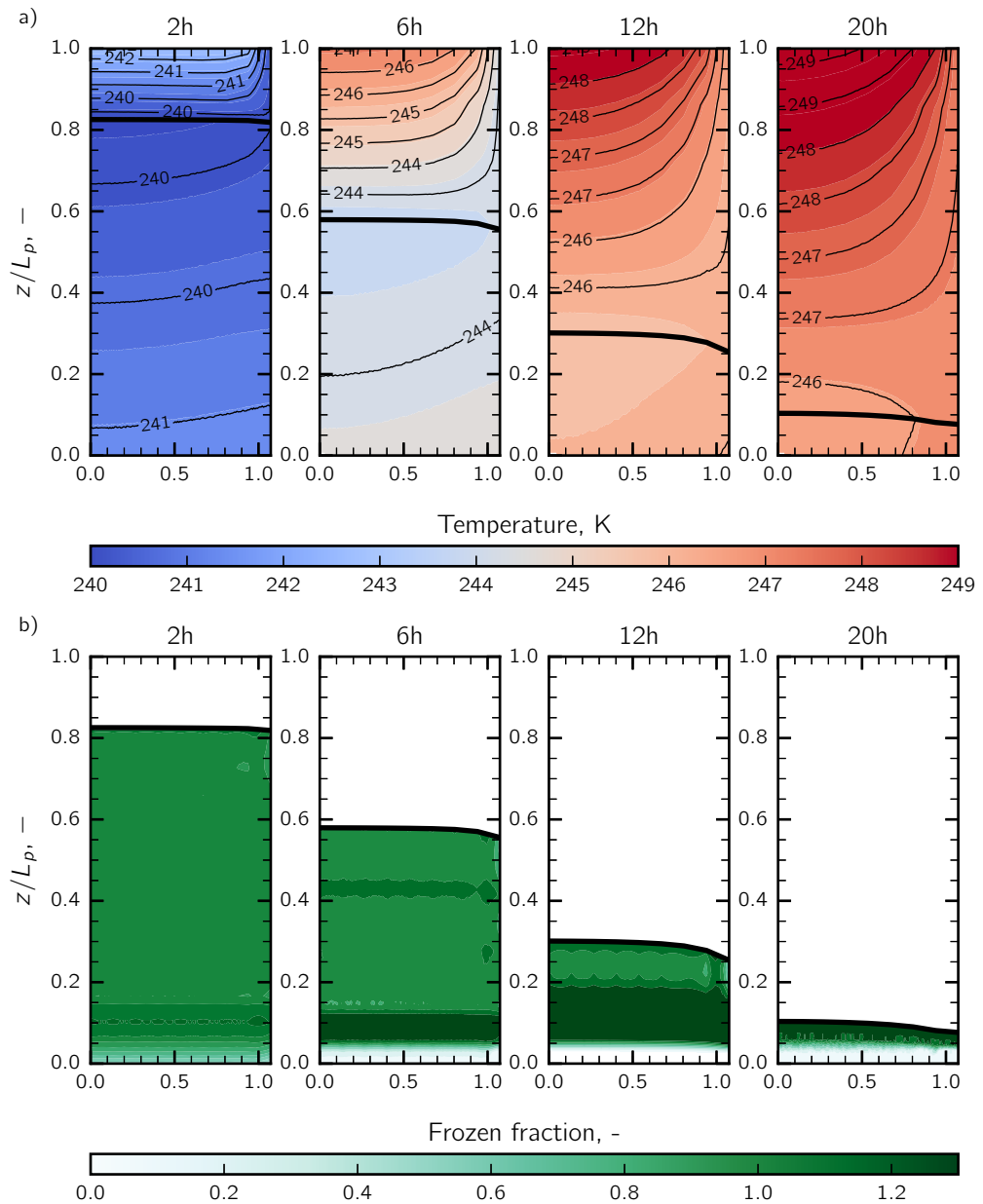
Figure D.14 Contour plot of the (a) product temperature and (b) frozen fraction during primary drying of microparticles of 50 μm. The simulation was performed setting $T_{sh} = 253$ K and $P_c = 10$ Pa.

were analyzed, i.e., monodisperse microparticles having (i) 10 (ii) 50 and (iii) 90 μm as diameter, using the structural parameters shown in the previous section.

As shown in Fig. D.15a, drying time decreased sharply as the shelf temperature increased, especially for the smallest particles. For microparticles having 50 μm as diameter, drying time decreased from 56 to about 13 h as shelf temperature rose from 243 to 273 K. In the same range of temperature, for microparticles of 10 μm, drying time fell from 161 to 23 h, and from 47 to 10 h for microparticles of 90 μm. At higher temperatures, i.g., 273 K, drying time was roughly the same for the case (ii) and (iii), indicating that, at such high-temperature, the mass transfer was not the controlling mechanism in the drying process. Fig. D.15b also shows the effect of shelf temperature on the maximum product temperature during primary drying. As the T_{sh} increased, the maximum product temperature increased as well, and the difference in temperature among the three cases can be imputed to the differences in the product structure.
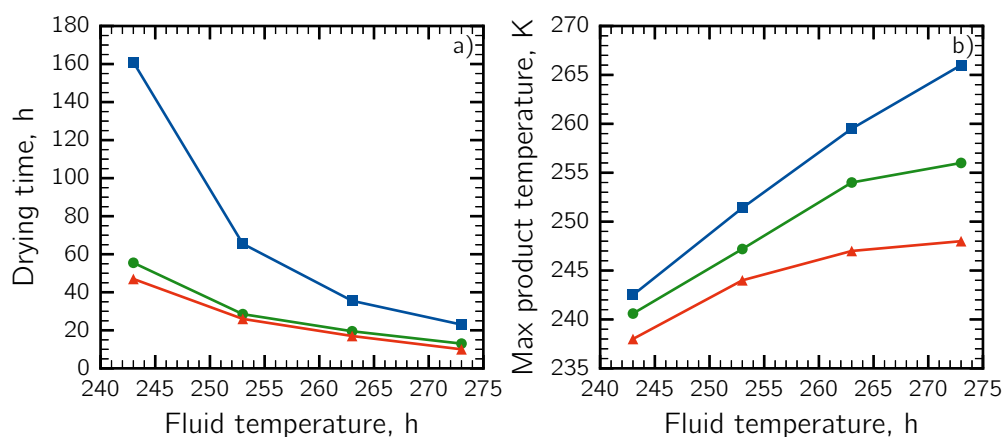
Figure D.15 Effect of shelf temperature on (a) drying time and (b) maximum temperature reached by the product during primary drying of particle-based product within vials and constituted of particles of (■) 10 μm, (●) 50 μm and (▲) 90 μm.

The effect of chamber pressure on drying time is shown in the range 2 - 30 Pa, for a shelf temperature equal to 253 K. As shown in Fig. D.16, case (ii) and (iii) displayed an optimal value of drying time in correspondence of chamber pressure set at 10 Pa. For lower pressures, drying time was slightly longer, i.g., at 2 Pa drying time was about 30 minutes longer than in the case of chamber pressure equal to 10 Pa. On the other hand, increasing the pressure over the optimal pressure of 10 Pa, simulations showed a sharp increase of drying time, i.g., 2 h longer at 15 Pa and 4 h longer at 20 Pa. That is typical behavior in lyophilization of products in vials, where chamber pressure plays a dual role; it affects the driving force for mass transfer within the dried product, but also the heat transfer coefficient for the heat transferred from the shelf to vial bottom. In fact, lowering pressure in the chamber, the pressure difference between the sublimation interface and the upper surface of the product increased. In contrast, decreasing chamber pressure, the value of K_v decreased as well, and the heat flux to the bottom felt down. For instance, K_v, as referred to the central vials simulated in this work, at 2 Pa was about $11.5\,W\,m^{-2}\,K$, $17.8\,W\,m^{-2}\,K$ at 10 Pa, and rose to $23.9\,W\,m^{-2}\,K$ when chamber pressure was 20 Pa. In the case (i), the optimal

value of pressure was 5 Pa; this is due to the fact that the packing of microparticles of 30 μm showed a mass transfer resistance much higher than that of the case (ii) and (iii). In the case (i), the optimal value of pressure was 5 Pa; this is due to the fact that the packing of microparticles of 30 μm showed a mass transfer resistance much higher than that of the case (ii) and (iii) and, although the heat supplied to the product was much lower, a further reduction of pressure was still beneficial for reducing drying duration.
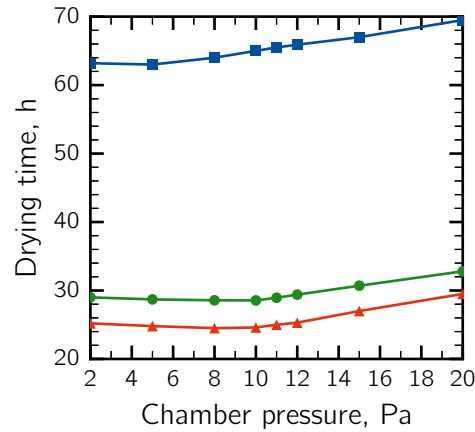
Figure D.16   Effect of chamber pressure on drying time of particle-based product within vials and constituted of particles of (■) 30 μm, (●) 50 μm and (▲) 90 μm.

Acronyms

DEM Discrete Element Method; **REV** Relevant Element Volume.

List of symbols

B_0	permeability coefficient, m^2
c_i	molar concentration of the i-component, $mol\,m^{-3}$
c_p	specific heat capacity, $J\,kg^{-1}\,K^{-1}$
D'_i, D''_i	transport coefficients of DGM equation for molar flux of specie-i, $m^2\,s^{-1}$
$\mathscr{D}_{ij}$	binary diffusion coefficient, $m^2\,s^{-1}$
D_{ij}^{eff}	effective binary diffusion coefficient, $m^2\,s^{-1}$
D_i^{Kn}	Knudsen diffusion coefficient, $m^2\,s^{-1}$
d_P^*	pore diameter within the particle, m
D_P	particle diameter, m
e_r	restitution coefficient, -
$\mathbf{F}_{c,i}$	vector of total force contact acting on particle i, N
$\mathbf{F}_{n,i}$	vector of normal force contact acting on particle i, N

$\mathbf{F}_{t,i}$	vector of tangential force contact acting on particle i, N
$\mathbf{g}$	gravity vector, $m\,s^{-2}$
G^*	equivalent shear modulus, $N\,m^{-2}$
I_i	momentum of inertia of particle i, $kg\,m^{-2}$
J_q	heat flux, $W\,m^{-2}$
k_n	rate constant of nucleation, $kg\,s^{-1}\,m^{-3}\,K^{-1}$
k_t	tangential elastic constant, $N\,m^{-1}$
M	molecular weight, $kg\,kmol^{-1}$
m^*	equivalent mass, kg
m_i	mass of particle i, kg
N	molar flux, $mol\,m^{-2}\,s^{-1}$
$\mathbf{n}$	normal versor
$\mathbf{n}_{ij}$	normal vector, -
p	total pressure, Pa
p_i	partial pressure of the i-component, Pa
p_w^{eq}	vapor equilibrium pressure, Pa
r	radial coordinate, m
R^*	equivalent radius, m

R_g	universal gas constant, $\mathrm{J\,mol^{-1}\,K^{-1}}$		μ	viscosity of gas mixture, $\mathrm{kg\,m^{-1}\,s^{-1}}$
$\mathbf{r}_i$	vector position of particle i, m		ν_i	Poisson ratio of particle i, -
S_n	normal stiffness, $\mathrm{N\,m^{-1}}$		ϕ_S	frozen fraction function, see Eq. 8.12
S_t	tangential stiffness, $\mathrm{N\,m^{-1}}$		ρ	density, $\mathrm{kg\,m^{-3}}$
T	temperature, K		σ_{SB}	Stefan–Boltz constant, $\mathrm{W\,m^{-2}\,K^{-4}}$
t	time, s		τ	tortuosity, -
t_{Hertz}	Herz time, s		$\boldsymbol{\omega}_i$	angular velocity vector, $\mathrm{rad\,s^{-1}}$
$\mathbf{t}_i$	vector of total torque acting on particle i, $\mathrm{N\,m}$			

R_g universal gas constant, $\mathrm{J\,mol^{-1}\,K^{-1}}$

$\mathbf{r}_i$ vector position of particle i, m

S_n normal stiffness, $\mathrm{N\,m^{-1}}$

S_t tangential stiffness, $\mathrm{N\,m^{-1}}$

T temperature, K

t time, s

t_{Hertz} Herz time, s

$\mathbf{t}_i$ vector of total torque acting on particle i, N m

$\mathbf{t}_{ij}$ tangential vector, -

$t_{Rayleigh}$ Rayleigh time, s

T_{sh} shelf temperature, K

v_{max} maximum velocity, $\mathrm{m\,s^{-1}}$

$v_{n,r}$ normal component of relative velocity, $\mathrm{m\,s^{-1}}$

v_s velocity of sublimation front, $\mathrm{m\,s^{-1}}$

$v_{t,r}$ tangential component of relative velocity, $\mathrm{m\,s^{-1}}$

x_μ friction coefficient, -

Y^* equivalent Youngs modulus, $\mathrm{N\,m^{-2}}$

Y_i Young's modulus of particle i, $\mathrm{N\,m^{-2}}$

y_i molar fraction of component i

Greek letters

β constant related to the restitution coefficient, -

γ heat capacity ratio, -

γ_n normal viscoelastic constant, $\mathrm{N\,s\,m^{-1}}$

γ_t tangential viscoelastic constant, $\mathrm{N\,s\,m^{-1}}$

δ_n normal displacement, m

δ_t tangential displacement, m

ε porosity, -

κ thermal conductivity, $\mathrm{W\,m^{-1}\,K^{-1}}$

μ viscosity of gas mixture, $\mathrm{kg\,m^{-1}\,s^{-1}}$

ν_i Poisson ratio of particle i, -

ϕ_S frozen fraction function, see Eq. 8.12

ρ density, $\mathrm{kg\,m^{-3}}$

σ_{SB} Stefan–Boltz constant, $\mathrm{W\,m^{-2}\,K^{-4}}$

τ tortuosity, -

$\boldsymbol{\omega}_i$ angular velocity vector, $\mathrm{rad\,s^{-1}}$

Subscript

0   initial condition

$\parallel$ parallel model

b   vial bottom

d   dried

f   frozen

gas   gas

ice   ice

i, j, k saturation index

in   inert gas

int   sublimation interface

I   layer of completely dried microparticles

II   layer of completely or partially frozen microparticles

p barodiffusion

sol   solid

tot   total

water   water vapor

Superscript

Adimensional numbers

Re   Reynolds number

References

Carson, J. W. (1988). Overcoming particle segregation in the pharmaceutical and cosmetics industries. *Drug Development and Industrial Pharmacy* 14 (18), pp. 2749–2758.

CINECA. *GALILEO The Italian Tier-1 cluster for industrial and public research*. URL: http://www.hpc.cineca.it/hardware/galileo (visited on 10/01/2018).

Higa, M, Arakawa, M, and Maeno, N (1996). Measurements of restitution coefficients of ice at low temperatures. *Planetary and Space Science* 44 (9), pp. 917–925.

Kietzig, A.-M., Hatzikiriakos, S. G., and Englezos, P. (2010). Physics of ice friction. *Journal of Applied Physics* 107 (8), pp. 081101 1–15.

Machado, M., Moreira, P., Flores, P., and Lankarani, H. M. (2012). Compliant contact force models in multibody dynamics: Evolution of the Hertz contact theory. *Mechanism and Machine Theory* 53, pp. 99–121.

Petrenko, V. F. and Whitworth, R. W. (1999). *Physics of Ice*. OUP Oxford.

Schiffter, H., Condliffe, J., and Vonhoff, S. (2010). Spray-freeze-drying of nanosuspensions: the manufacture of insulin particles for needle-free ballistic powder delivery. *Journal of the Royal Society Interface* 7 (4), S483–S500.

Smuts, E. M., Deglon, D. A., and Meyer, C. J. (2012). Methodology for CFD-DEM modelling of particulate suspension rheology. In: *Proceedings of the Ninth International Conference on CFD in the Minerals and Process Industries CSIRO, Melbourne, Australia*.

E

Energetic costs of freeze-drying

This appendix details the energy cost analysis made for the batch and continuous freeze-drying. The model takes into account the energy requirements for freezing and drying the product, the vacuum pumps, condenser, and the energy losses.

E.1 Energetic parameters

Table E.1-E.2 report the parameters of the model and the features of the batch and continuous apparatus. Table E.3-E.4 show the energy consumption breakdown and costs in the case study I and III presented in Chapter 9.

E.1.1 Freezing

Considering the heat exchange 100% efficient and referring the energies to a single vial, the total energy to be removed per vial reads,

$$Q_{\mathrm{F}} = Q_{\mathrm{F,p}} + Q_{\mathrm{F,eq}} + Q_{\mathrm{F,loss}} \tag{E.1}$$

where $Q_{\mathrm{F,p}}$ is the enthalpy change of the product in a single vial during freezing, $Q_{\mathrm{F,eq}}$ is the contribution of the enthalpy change of vials, stoppers, air within the chamber, heat transfer fluid, shelf steel, and $Q_{\mathrm{F,loss}}$ takes into account the thermal losses of the lyophilizer to the external environment.

Batch

$$Q_{\mathrm{F,p}} = m_{\mathrm{p}}((c_{p,\mathrm{liq}}(1 - \varphi_{\mathrm{sol}}) + c_{p,\mathrm{sol}}\varphi_{\mathrm{sol}})(T_{\mathrm{F,ini}} - T_{eq}) + \Delta H_f(1 - \varphi_{\mathrm{sol}}) +$$
$$(c_{p,\mathrm{ice}}(1 - \varphi_{\mathrm{sol}}) + c_{p,\mathrm{sol}}\varphi_{\mathrm{sol}})(T_{eq} - T_{\mathrm{F,fin}})) \tag{E.2}$$

Table E.1 Definition and parameters of the model: general characteristics

Category	Definition	Unit	Symbol	Value
Product	Mass	kg	m_p	0.003
	Solid fraction	-	φ_{sol}	0.05
	Fraction of unfrozen water	-	φ_f	0.05
	Specific heat of water	kJ kg^{-1} K^{-1}	$c_{p,liq}$	4.2
	Specific heat of ice	kJ kg^{-1} K^{-1}	$c_{p,ice}$	2.1
	Specific heat of solute	kJ kg^{-1} K^{-1}	$c_{p,sol}$	1.4
	Latent heat of solidification/fusion	kJ kg^{-1}	ΔH_f	333.5
	Latent heat of sublimation/deposition	kJ kg^{-1}	ΔH_s	2838
	Latent heat of evaporation	kJ kg^{-1}	ΔH_e	2256
Vial	Mass	kg	m_v	0.009
	Specific heat of glass	kJ kg^{-1} K^{-1}	$c_{p,v}$	0.84
	No. of vials	-	n_{vial}	
Stoppers	Mass	kg	m_{stp}	0.001
	Specific heat of rubber	kJ kg^{-1} K^{-1}	$c_{p,stp}$	0.24
Shelves	Specific heat of steel	kJ kg^{-1} K^{-1}	$c_{p,st}$	0.5
Heat transfer fluid	Specific heat of silicon oil	kJ kg^{-1} K^{-1}	$c_{p,st}$	1.5
Air	Specific heat of air	kJ kg^{-1} K^{-1}	$c_{p,air}$	1.3
Nitrogen	Mass	kg	m_{LIN}	
	Specific heat of GAN	kJ kg^{-1} K^{-1}	$c_{p,GAN}$	1.0
	Latent heat of evaporation of LIN	kJ kg^{-1}	$\Delta H_{v,LIN}$	199
	Cost of LIN	EUR kg$_{LIN}^{-1}$		0.13
	Cost of sterilized LIN	EUR kg$_{LIN}^{-1}$		0.26
Electricity	Cost of electricity	EUR kWh^{-1}		0.2
Losses	Environment to lyohphilizer heat transfer coeffient	W m^{-2} K^{-1}	U	1.7
	Average inner/outer temperture gradient	K	ΔT	45
Temperatures	Ambient temperature	K	T_{amb}	298
	Initial cooling temperature	K	$T_{F,ini}$	298
	Final freezing temperature	K	$T_{F,ini}$	223
	Freezing temperaure	K	T_{eq}	273
	Shelf temperature during PD	K	T_{PD}	
	Shelf temperature during SD	K	T_{SD}	
	Temperature of condenser	K	T_{cd}	203
	Temperature of CIP/SIP operation	K	$T_{CIP/SIP}$	373

Table E.2 Definition and parameters of the model: technical characteristics of the equipment

Equipment	Feature	Unit	Symbol	Value
Batch	Chamber volume	m^3		12.4
	Chamber wall surface	m^2	A_{wall}	21.4
	Total shelves area	m^2		28.6
	Useable shelves area	m^2		27.0
	Steel shelves mass	kg	m_{sh}	2,423
	No. of shelves + radiative plate			17 +1
	Condenser surface	m^2		23.7
	Steel Condenser mass	kg	m_{cd}	549
	Heat transfer fluid mass	kg	m_{htf}	587
	Average pump power installed	kW	$\dot{Q}_{pumps}$	9.2
Continuous	Module volume	m^3		0.12
	Module wall surface	m^2	A_{wall}	0.44
	Module surface	m^2		1.2
	Steel mass	kg	m_{sh}	96
	Steel Condenser mass	kg	m_{cd}	316
	Heat transfer fluid mass	kg	m_{htf}	23.3
	Average pump power installed	kW	$\dot{Q}_{pumps}$	3.1
	No. of freezing module		n_{Fmod}	
	No. of drying module		n_{Dmod}	

$$Q_{F,eq} = (m_v c_{p,v} + m_{stp} c_{p,stp} + \frac{1}{n_{vial}}(m_{htf} c_{p,htf} + m_{sh} c_{p,sh} +$$
$$m_{air} c_{p,air}))(T_{F,ini} - T_{F,fin}) + \frac{1}{n_{vial}} m_{sh} c_{p,sh}(T_{CIP/SIP} - T_{F,fin}) \quad \text{(E.3)}$$

$$Q_{F,loss} = \frac{1}{n_{vial}} U A_{wall} \Delta T t_F \tag{E.4}$$

Continuous

$$Q_{F,p} = m_p((c_{p,liq}(1 - \varphi_{sol}) + c_{p,sol}\varphi_{sol})(T_{F,ini} - T_{eq}) + \Delta H_f(1 - \varphi_{sol}) +$$
$$(c_{p,ice}(1 - \varphi_{sol}) + c_{p,sol}\varphi_{sol})(T_{eq} - T_{F,fin})) \quad \text{(E.5)}$$

$$Q_{F,eq} = (m_v c_{p,v} + m_{stp} c_{p,stp} + \frac{1}{n_{vial}}(m_{air} c_{p,air}))(T_{F,ini} - T_{F,fin}) \tag{E.6}$$

$$Q_{F,loss} = \frac{1}{n_{vial}} U A_{wall} \Delta T t_{REF} \tag{E.7}$$

E.1.2 Drying

During primary drying, energy is supplied to sublimate ice and for keeping the drying chamber under vacuum conditions, whereas during secondary drying heat is supplied to desorb bounded water,

$$Q_D = Q_{D,p} + Q_{D,eq} + Q_{D,cd} + Q_{D,pumps} \tag{E.8}$$

where $Q_{D,p}$ is the heat need to sublimate ice and desorb bounded water, $Q_{D,eq}$ is the contribution of the enthalpy change of vials, stoppers, air within the chamber, heat transfer fluid, shelf steel, $Q_{D,cd}$ is the heat remove at the condenser to make ice deposit over its surface, and $Q_{D,pumps}$ is the energy consumption of the vacuum pumps.

Batch

Eq. E.8 can be split in two different terms,

$$Q_D = Q_{PD} + Q_{SD} \tag{E.9}$$

where Q_{PD} accounts for the energy consumption during the primary drying and Q_{SD} for the secondary drying.

The energy consumption during primary drying reads,

$$Q_{PD} = Q_{PD,p} + Q_{PD,eq} + Q_{PD,cd} + Q_{PD,pumps} \tag{E.10}$$

$$Q_{\mathrm{PD,p}} = \Delta H_s m_{\mathrm{p}} (1 - \varphi_{\mathrm{sol}})(1 - \varphi_{\mathrm{f}}) \tag{E.11}$$

$$Q_{\mathrm{PD,eq}} = (m_{\mathrm{v}} c_{p,\mathrm{v}} + m_{\mathrm{stp}} c_{p,\mathrm{stp}} + \frac{1}{n_{\mathrm{vial}}} (m_{\mathrm{htf}} c_{p,\mathrm{htf}} +$$
$$m_{\mathrm{sh}} c_{p,\mathrm{sh}}))(T_{\mathrm{PD}} - T_{\mathrm{F,fin}}) \tag{E.12}$$

$$Q_{\mathrm{PD,cd}} = \Delta H_s m_{\mathrm{p}} (1 - \varphi_{\mathrm{sol}})(1 - \varphi_{\mathrm{f}}) + \frac{1}{n_{\mathrm{vial}}} m_{\mathrm{cd}} c_{p_{\mathrm{cd}}} (T_{\mathrm{amb}} - T_{\mathrm{cd}}) \tag{E.13}$$

$$Q_{\mathrm{PD,pumps}} = \frac{1}{n_{\mathrm{vial}}} \dot{Q}_{\mathrm{pumps}} t_{\mathrm{PD}} \tag{E.14}$$

The energy consumption during secondary drying reads,

$$Q_{\mathrm{SD}} = Q_{\mathrm{SD,p}} + Q_{\mathrm{SD,eq}} + Q_{\mathrm{SD,cd}} + Q_{\mathrm{SD,pumps}} \tag{E.15}$$

$$Q_{\mathrm{SD,p}} = \Delta H_e m_{\mathrm{p}} (1 - \varphi_{\mathrm{sol}}) \varphi_{\mathrm{f}} \tag{E.16}$$

$$Q_{\mathrm{SD,eq}} = (m_{\mathrm{v}} c_{p,\mathrm{v}} + m_{\mathrm{stp}} c_{p,\mathrm{stp}} + \frac{1}{n_{\mathrm{vial}}} (m_{\mathrm{htf}} c_{p,\mathrm{htf}} +$$
$$m_{\mathrm{sh}} c_{p,\mathrm{sh}}))(T_{\mathrm{SD}} - T_{\mathrm{PD}}) \tag{E.17}$$

$$Q_{\mathrm{PD,cd}} = \Delta H_s m_{\mathrm{p}} (1 - \varphi_{\mathrm{sol}}) \varphi_{\mathrm{f}} \tag{E.18}$$

$$Q_{\mathrm{PD,pumps}} = \frac{1}{n_{\mathrm{vial}}} \dot{Q}_{\mathrm{pumps}} t_{\mathrm{SD}} \tag{E.19}$$

Continuous

$$Q_{\mathrm{D,p}} = \Delta H_s m_{\mathrm{p}} (1 - \varphi_{\mathrm{sol}})(1 - \varphi_{\mathrm{f}}) + \Delta H_e m_{\mathrm{p}} (1 - \varphi_{\mathrm{sol}}) \varphi_{\mathrm{f}} \tag{E.20}$$

$$Q_{\mathrm{D,eq}} = (m_{\mathrm{v}} c_{p,\mathrm{v}} + m_{\mathrm{stp}} c_{p,\mathrm{stp}} + \frac{1}{n_{\mathrm{vial}}} (m_{\mathrm{htf}} c_{p,\mathrm{htf}} +$$
$$m_{\mathrm{sh}} c_{p,\mathrm{sh}}))(T_{\mathrm{amb}} - T_{\mathrm{PD}}) \tag{E.21}$$

$$Q_{\mathrm{D,cd}} = \Delta H_s m_{\mathrm{p}} (1 - \varphi_{\mathrm{sol}}) + \frac{1}{n_{\mathrm{vial}}} m_{\mathrm{cd}} c_{p_{\mathrm{cd}}} (T_{\mathrm{amb}} - T_{\mathrm{cd}}) \tag{E.22}$$

$$Q_{\mathrm{D,pumps}} = \frac{1}{n_{\mathrm{vial}}} \dot{Q}_{\mathrm{pumps}} t_{\mathrm{REF}} \tag{E.23}$$

E.1.3 Defrost

At the end of the process, steam is used to defrost the condenser; the energy supplied reads,

$$Q_{\text{dfr}} = m_{\text{p}}(1 - \varphi_{\text{sol}})(\Delta H_f + c_{p,i}(T_{\text{ini}} - T_{\text{fin}})) \tag{E.24}$$

E.2 Energetic costs

E.2.1 Refrigeration

In the batch lyophilizer, the refrigeration apparatus is constituted of a cryogenic heat exchanger that exchanges heat with silicone oil; the silicone oil cools down the shelf in the chamber and, consequently, the product in the vials. Moreover, liquid nitrogen is used for the condenser. The mass of liquid nitrogen required in the refrigeration operations m_{LIN} and its cost reads C_{refr},

$$m_{\text{LIN}} = \frac{Q_{\text{refr}}}{\Delta H_{v,\text{LIN}}}; \qquad C_{\text{refr}} = m_{\text{LIN}}C_{\text{LIN}} \tag{E.25}$$

where Q_{refr} is Q_F during freezing, $Q_{\text{SD,cd}}$ during primary drying and $Q_{\text{SD,cd}}$ during secondary drying.

In the case of continuous lyophilization, the vial comes into contact with the countercurrent flow of sterilized nitrogen gas which extracts heat for cooling down and partially freeze the product, then passes below a spray of liquid nitrogen that completes the freezing. The mass of LIN required is about,

$$m_{\text{LIN}} = \frac{Q_F}{\Delta H_{v,\text{LIN}} + c_p\Delta T_{\text{LIN}}}; \qquad C_{\text{refr}} = m_{\text{LIN}}C_{\text{LIN}^*} \tag{E.26}$$

where C_{LIN^*} is the cost of sterilized LIN per unit weight and ΔT_{LIN} is the difference between the temperature of liquid nitrogen and the temperature of outlet nitrogen gas (ΔT_{LIN} is about $150\,\text{K}$). The refrigeration costs for the condenser are evaluated using Eq.E.25.

E.2.2 Heating

The cost to heat the product for promoting sublimation and desorption, and for defrosting the condenser is calculated as,

$$C_{\text{heat}} = Q_{\text{heat}}C_{\text{elec}} \tag{E.27}$$

E.2.3 Vacuum pumps

The cost to keep the vacuum is calculated as follows,

$$C_{\text{pumps}} = \frac{1}{n_{\text{vial}}}\dot{Q}_{\text{pumps}}C_{\text{elec}}t \tag{E.28}$$

where $\dot{Q}_{\text{pumps}}$ is the average pump power installed in the apparatus and t is the operational time.

Table E.3 Energy consumption and costs for the case study I.

	Batch	Continuous	
$Q_{F,p}$	1.869	1.869	kJ/vial
$Q_{F,eq}$	4.780	0.611	kJ/vial
$Q_{F,loss}$	0.655	0.578	kJ/vial
Q_F	7.304	4.090	kJ/vial
LIN consumption	0.037	0.008	kgLIN/vial
LIN cost	0.005	0.002	EUR/vial
Cost FREEZING	**0.0046**	**0.0021**	**EUR/vial**
$Q_{PD,p}$	7.68		kJ/vial
$Q_{PD,eq}$	1.88		kJ/vial
$Q_{PD,pumps}$	16.64		kJ/vial
$Q_{PD,cd}$	8.53		kJ/vial
Q_{PD}	34.73		kJ/vial
Electricity consumption	0.00728		kWh/vial
Electricity cost	0.00146		EUR/vial
LIN consumption	0.04		kgLIN/vial
LIN cost	0.0053		EUR/vial
Cost PD	0.0068		EUR/vial
$Q_{SD,p}$	0.32		kJ/vial
$Q_{SD,eq}$	1.41		kJ/vial
$Q_{SD,pumps}$	2.47		kJ/vial
$Q_{SD,cd}$	0.40		kJ/vial
Q_{SD}	4.60		kJ/vial
Electricity consumption	0.00117		kWh/vial
Electricity cost	0.00023		EUR/vial
LIN consumption	0.00204		kgLIN/vial
LIN cost	0.0003		EUR/vial
Cost SD	0.0005		EUR/vial
$Q_{D,p}$	8.01	8.01	kJ/vial
$Q_{D,eq}$	3.29	0.74	kJ/vial
$Q_{D,pumps}$	19.10	13.25	kJ/vial
$Q_{D,cd}$	8.93	8.37	kJ/vial
Q_D	39.33	32.30	kJ/vial
Electricity consumption	0.00845	0.00611	kWh/vial
Electricity cost	0.00169	0.00122	EUR/vial
LIN consumption	0.04495	0.04212	kgLIN/vial
LIN cost	0.00557	0.00522	EUR/vial
Cost PD+SD	**0.00726**	**0.00644**	**EUR/vial**
Q_{dfr}	2.40	1.56	kJ/vial
Electricity consumption	0.00067	0.00043	kWh/vial
Electricity cost	0.00013	0.00009	EUR/vial
Cost DEFROST	**0.00013**	**0.00009**	**EUR/vial**
TOTAL COST	**0.01195**	**0.00859**	**EUR/vial**

Table E.4 Energy consumption and costs for the case study III.

	Batch	Continuous (uncontr. nucl.)	Continuous + VISF	
$Q_{F,p}$	1.869	1.869	1.869	kJ/vial
$Q_{F,eq}$	4.780	0.611	0.611	kJ/vial
$Q_{F,loss}$	0.655	0.506	0.506	kJ/vial
Q_F	7.304	3.994	3.994	kJ/vial
LIN consumption	0.037	0.008	0.008	kgLIN/vial
LIN cost	0.005	0.002	0.002	EUR/vial
Cost FREEZING	**0.0046**	**0.0020**	**0.0020**	**EUR/vial**
$Q_{PD,p}$	7.68			kJ/vial
$Q_{PD,eq}$	1.41			kJ/vial
$Q_{PD,pumps}$	12.94			kJ/vial
$Q_{PD,cd}$	8.53			kJ/vial
Q_{PD}	30.56			kJ/vial
Electricity consumption	0.00612			kWh/vial
Electricity cost	0.00122			EUR/vial
LIN consumption	0.04			kgLIN/vial
LIN cost	0.0053			EUR/vial
Cost PD	0.0065			EUR/vial
$Q_{SD,p}$	0.32			kJ/vial
$Q_{SD,eq}$	1.88			kJ/vial
$Q_{SD,pumps}$	2.47			kJ/vial
$Q_{SD,cd}$	0.40			kJ/vial
Q_{SD}	5.07			kJ/vial
Electricity consumption	0.00130			kWh/vial
Electricity cost	0.00026			EUR/vial
LIN consumption	0.00204			kgLIN/vial
LIN cost	0.0003			EUR/vial
Cost SD	0.0005			EUR/vial
$Q_{D,p}$	8.01	8.01	8.01	kJ/vial
$Q_{D,eq}$	3.29	0.57	0.57	kJ/vial
$Q_{D,pumps}$	15.41	11.59	11.59	kJ/vial
$Q_{D,cd}$	8.93	8.35	8.35	kJ/vial
Q_D	35.64	31.23	30.13	kJ/vial
Electricity consumption	0.00742	0.00560	0.00560	kWh/vial
Electricity cost	0.00148	0.00112	0.0012	EUR/vial
LIN consumption	0.04495	0.04204	0.04204	kgLIN/vial
LIN cost	0.00557	0.00521	0.00521	EUR/vial
Cost PD+SD	**0.00706**	**0.00633**	**0.00633**	**EUR/vial**
Q_{dfr}	2.40	1.56	1.56	kJ/vial
Electricity consumption	0.00067	0.00043	0.00043	kWh/vial
Electricity cost	0.00013	0.00009	0.00009	EUR/vial
Cost DEFROST	**0.00013**	**0.00009**	**0.00009**	**EUR/vial**
TOTAL COST	**0.01175**	**0.00843**	**0.00843**	**EUR/vial**

Acronyms

GAN Gaseous nitrogen; **LIN** Liquid nitrogen; **VISF** Vacuum-Induced Surface Freezing.